Synergistically Engineered Hollow Particle and Molecular Amphiphile Systems for Oil Spill Remediation

AN ABSTRACT

SUBMITTED ON THE TWENTY-FIFTH DAY OF FEBRUARY 2016

TO THE DEPARTMENT OF CHEMICAL AND BIOMOLECULAR ENGINEERING

IN PARTIAL FULFILLMENT OF THE REQUIREMENTS

OF THE SCHOOL OF SCIENCE AND ENGINEERING

OF TULANE UNIVERSITY

FOR THE DEGREE OF

DOCTOR OF PHILOSOPHY

BY

Olasehinde Gbenro Owoseni

APPROVED:

Vijay T. John, D. Eng. Sci.

Director

Gary L. McPherson, Ph.D.

Noshir S. Pesika, Ph.D.

Julie N. L. Albert, Ph.D.

ABSTRACT

Oil spill accidents represent an inherent occupational, environmental, economic, and community health disaster associated with the transformation of petroleum resources into products that help meet our world's energy need. Dispersants are applied to break the oil spill into sufficiently small droplets and mitigate oil spill impacts by reducing the possibility of shoreline impact, lessening the impact on marine life and significantly increasing the oil-water interfacial area available for remediation processes.

Existing dispersants are liquid solutions of surfactant in hydrocarbon solvents. There are several concerns with the existing dispersant systems including the large volume of hydrocarbon solvents introduced into the ecosystem; waste due to spray drift during application; ineffectiveness on heavy and weathered oils; low dispersant contact with oil due to miscibility with ocean water; lack of buoyancy; and easy removal of the dispersant by ocean currents.

In this dissertation, an alternative, benign and efficient dispersant technology is developed based on principles of particle stabilized emulsions. Naturally occurring halloysite clay nanotubes (HNTs) adhere to the oil-water interface to stabilize oil-in-water emulsions. Additionally, the internal tubular structure allows the loading and delivery of oil spill treating agents such as surfactant to the oil-water interface. The halloysite surface is functionalized with magnetic iron oxides for oil mobilization. Synergistic emulsion stabilization is also achieved using the HNT and hydrophobically modified chitosan (HMC), an amphiphilic derivative of chitosan biopolymer. A selective

surface carbonization technique is developed to optimize the partitioning of the halloysite to the oil-water interface. The carbonization concept is extended to a rapid aerosol process for the synthesis of hollow structured silica-carbon composite particles as particulate emulsifiers.

The mesocrystalline gel system consisting of the innocuous phospholipid, l-α-phosphatidylcholine (PC); anionic surfactant, dioctyl sulfosuccinate sodium salt (DOSS), and nonionic surfactant, polyoxyethylene (20) sorbitan monooleate (Tween 80), is developed as an effective gel dispersant for oil spill treatment. The gel dispersant effectively lowers the crude oil-saline water interfacial tension, is positively buoyant, breaks down on contact with surface oil layers and releases surfactant components that stabilize oil-in-water emulsions for extended periods. Particles such as halloysite may be incorporated into the gel for oil spill remediation.

Synergistically Engineered Hollow Particle and Molecular Amphiphile Systems for Oil Spill Remediation

A DISSERTATION

SUBMITTED ON THE TWENTY-FIFTH DAY OF FEBRUARY 2016

TO THE DEPARTMENT OF CHEMICAL AND BIOMOLECULAR ENGINEERING

IN PARTIAL FULFILLMENT OF THE REQUIREMENTS

OF THE SCHOOL OF SCIENCE AND ENGINEERING

OF TULANE UNIVERSITY

FOR THE DEGREE OF

DOCTOR OF PHILOSOPHY

BY

Olasehinde Gbenro Owoseni

APPROVED:

Vijay T. John, D. Eng. Sci.

Director

Gary L. McPherson, Ph.D.

Noshir S. Pesika, Ph.D.

Julie N. L. Albert, Ph.D.

ACKNOWLEDGEMENTS

Support from the Gulf of Mexico Research Initiative (GoMRI), National Science Foundation (Grant 1049330 and Grant 1236089), the U.S. Department of Energy under EPSCoR Grant No. DE-SC0012432 and the Louisiana Board of Regents are gratefully acknowledged.

I thank my research advisor, Prof. Vijay T. John for his invaluable guidance and investment. I am deeply grateful to Prof. Gary L. McPherson, Prof. Noshir Pesika and Prof. Julie Albert for their input and advice as my thesis committee members. I appreciate the members of my research group. I thank Dr. Jibao He, Michael Drenski and Dr. William Heller for being immensely helpful instrument scientists. I am grateful for the input of Dr. Arijit Bose into my research. I enjoyed collaborating with Jasmin Athas, David Riehm and Emmanuel Nyankson from the research groups of Dr. Srinivasa Raghavan, Dr. Alon McCormick and Dr. Ram Gupta respectively. I thank Moses Oguntoye for the collaboration on carbon nanotubes. Samantha Adams, Joyce Ward, Julie Kaiga and Rebecca Tamayo were great summer research interns. I appreciate all the faculty, staff and students in the Chemical and Biomolecular Engineering Department.

I am sincerely grateful for the immense sacrifice and instruction of my parents, Mr. Olugbenga Owoseni and Mrs. Titilayo Owoseni. The love, support and encouragement of my wonderful brothers, Ibiwumi Owoseni and Oluwaseye Owoseni, and my beautiful sister, Oluwanifemi Owoseni, is a priceless blessing.

TABLE OF CONTENTS

LIST OF TABLES

LIST OF FIGURES

CHAPTER 1

GENERAL INTRODUCTION

1.1 The Challenge of Crude Oil Spills

The exploration, development, production, and transportation of petroleum resources are significant in meeting our world's energy need. The benefits derived from these operations are accompanied by an inherent occupational, environmental, economic, and community health disaster in form of oil spill accidents.[4, 5] Oil spills can adversely affect the health of plants and animals in the coastal ecosystem if there is no adequate clean-up response.[5] The spill oil impacts the health of marine associated bird species by fouling their feathers, damaging the skins or eyes, producing internal physiological harm on ingestion or inhalation and significantly impacting reproduction by suppressing the sex steroid hormone production.[1] The Exxon Valdez oil spill and Apex Houston oil spills were reported to have killed thousands of seabirds.[1] Oil spills have also resulted in the widespread death of marine mammals such as sea otters, sea cows, polar bears, seals and sea lions, whales, dolphins and porpoises.[1, 6] There is evidence that the MC-252 Deepwater Horizon (DWH) oil spill in 2010 affected the reproduction and health of coastal bottlenose dolphins in the Gulf of Mexico.[6]

The impact of an oil spill depends on the circumstances of the spill including the spill source, spill cause, oil type, spill volume, spill location with respect to proximity to sensitive resources, and environmental conditions such as the season in which spill

occurs.[1, 6] In the event of an oil spill, the oil can spread into a film on water, evaporate, emulsify into oil mousse, be transported by winds and ocean waves, or dissolve into the water column.[5, 6] Table 1.1 summarizes the effects of oil type on the persistence and characteristic impacts of an oil spill.[1]

Oil spill risk can be mathematically described using the equation:[1]

$$Risk_{oil\ spill} = Probability_{oil\ spill} \times Consequences_{oil\ spill} \qquad (1.1)$$

Approaches to minimize the probability of oil spill accidents include using fault tree analysis, event trees from historical data and engineering studies, analysis of weather and seismic data.[1] The concept of zero probability for oil spills is desirable but may not be attainable with current practices and technologies.[1] The dissertation exploits the fundamental principles of colloidal and interfacial phenomena of particles, surfactant molecules and polymer macromolecules in the development of alternative, cheaper, and environmentally-benign technologies for mitigating the consequences of oil spills.

1.2 Oil Spill Response Procedures

The response to an oil spill may involve mechanical containment and recovery of the spilled oil from water (Figure 1.1a)[2], application of solidifiers, chemical herding, in-situ burning (Figure 1.1b)[2], bioremediation and oil dispersion.[6, 7] Containment equipment such as booms are used to restrict the spread of the oil for recovery by skimmers or sorbents.[6] However, this approach can be time-consuming, expensive and have low oil recovery rates. Mechanical removal of the spilled oil also leaves behind a thin layer of oil that is inaccessible to native oil degrading microbes and creates a barrier to oxygen transport from the atmosphere to the water.[5]

Table 1.1 Effects of oil type on the persistence and impacts of an oil spill[1]

Oil Type	Examples	Spill Characteristics and Impacts
Volatile Distillates	Jet fuel, kerosene, gasoline	highly volatile, contains high concentration of toxic soluble compounds, high potential to impact surface and subsurface resources including drinking water, difficult to clean using conventional tools
Light Fuels	Diesel fuels, No. 2 fuel, home heating oil, marine diesel	contains toxic soluble compounds, leaves about one-third of spill as residue, potential long-term contamination of surface and subsurface resources, possible to clean with effective oil spill response
Lube Oils Crude Oil	Lubricating Oils Medium Crude oil	about one-third of oil evaporates after 24 hours, severe and long-term contamination, severe impact on marine life, quick clean-up response can be effective
Heavy Oils	Heavy fuel oils, intermediate fuel oils, No. 4 fuel, No. 5 fuel, No. 6 fuel, residual oil	little or no evaporation or dissolution, heavy and long term contamination of sediments, severe impacts of coating and ingestion of waterfowl and fur-bearing mammals, weathers slowly, difficult shoreline and substrate clean-up

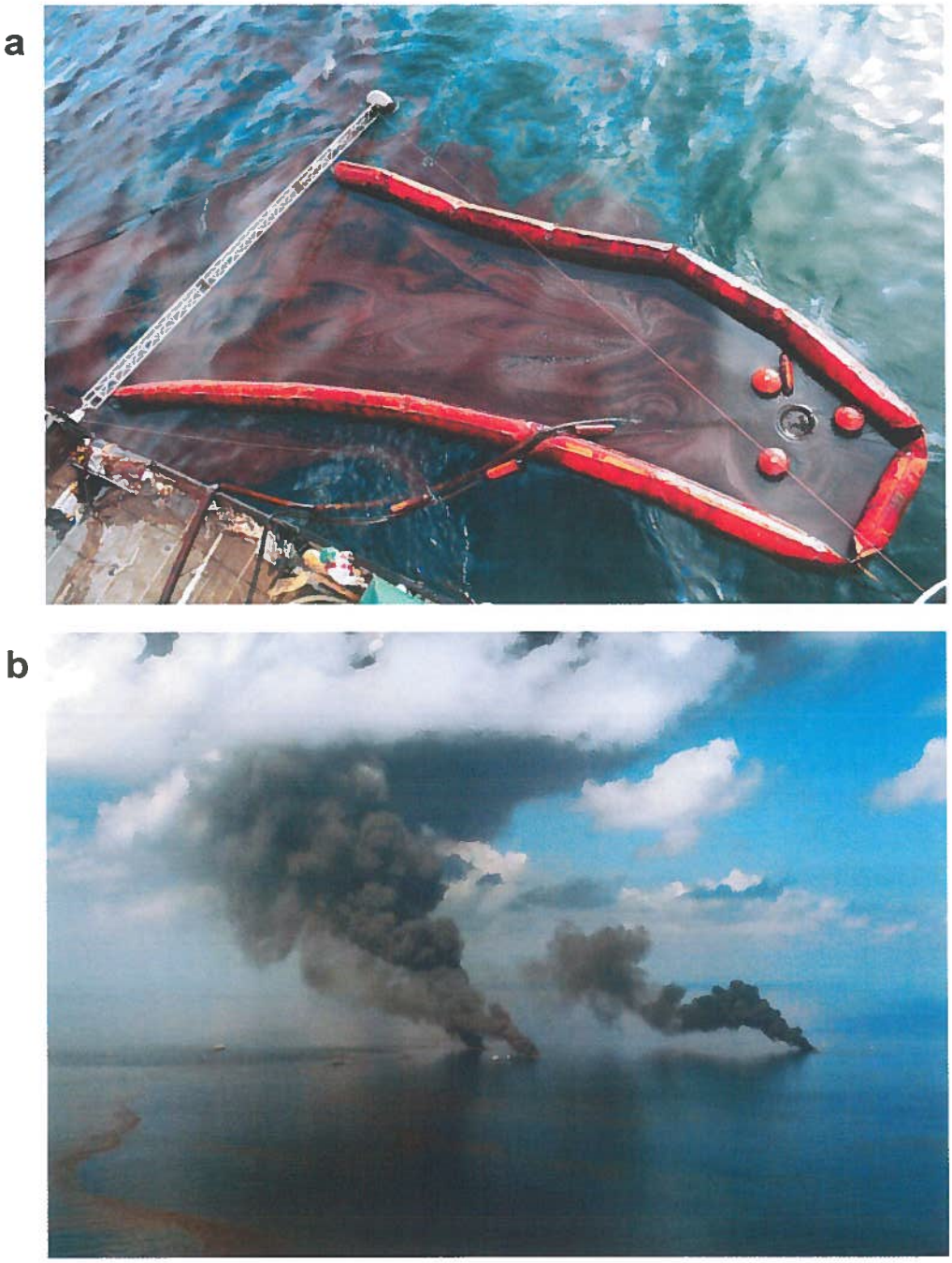

Figure 1.1: (a) Photograph of oil spill recovery using skimmer and boom. (b) Photograph showing the in situ burning of surface oil layers.[2]

In chemical herding, water insoluble surfactants are applied around the periphery of oil slicks to generate Marangoni flows that compact and thicken the slick.[8] The increased thickness of the oil facilitates in-situ burning or skimming operations. Typically, oil thicknesses greater than 3mm are required to sustain the in-situ burning process. Herding is especially useful for cold water spills such as in the Arctic where ice floes dampen the utility of wave action for oil spill dispersion and results in dispersant waste when sprayed onto the ice.

Solidifiers may also be applied to convert the oil into a solid mass and reduce the spread of oil in the marine environment.[6] Solidifier types include polymer sorbent, crosslinking agents and polymers with cross linking agents. Several challenges have restricted the use of solidifiers to small, thin and near shore spills. The challenges encountered in several steps of solidifier use include difficulties in delivering large amount of solidifier material required, attaining complete mixing of the solidifier with the oil, recovering solidified oil, as well as potential for toxic and long term effects of the solidifier itself.[6]

The application of dispersants to break spill oils into tiny droplets for subsequent biodegradation is often an efficient approach for the treatment of oil spills (Table 1.2).[6, 7, 9] Typical oil spills dispersants are a blend of surfactants with organic solvents such as glycol and light petroleum distillates.[7] Surfactant, the active ingredients in existing dispersants, diffuse to the crude oil-seawater interface and reduce the interfacial tension, allowing oil to mix into water column as tiny droplets.[7] Corexit 9500 and Corexit 9527 are the most common dispersants considered for use in the United States. Application of dispersants may reduce the possibility of shoreline impact, lessen the impact on birds and

mammals, and promote the biodegradation of oil (Figure 1.2).[6] In instances where mechanical recovery is employed to remove the bulk of the spilled oil, dispersants are used to break the thin oil film left into droplets promoting oxygen transport to oil degrading organisms in the water.[5]

Table 1.2 Description of major oil spills[3]

Oil Spill Accident	Year	Oil Spill Characteristics				Dispersant Application
		Duration	Depth (m)	Distance Offshore (km)	Volume of Oil Released (m^3)	
Torrey Canyon	1967	12 days	Surface	25	14000	9500 m^3 of BP1002 plus 11 other dispersants
Santa Barbara Blowout	1969	11 days, reduced flows for more than 1 year	57	9.5	13000-16000	294 m^3 of Polycomplex A-11, Corexit 7664
Ixtoc I blowout	1979 - 1980	10 months	50	80	580000	5600m^3 of Corexit 9527
Exxon Valdez	1989	< 1 day	Surface	2	42000-120000	15m^3 of Corexit 9580, 7664, BP1100X
Deepwater Horizon Blowout	2010	87 days	1,544	73	780000	7000m^3 of Corexit 9500A

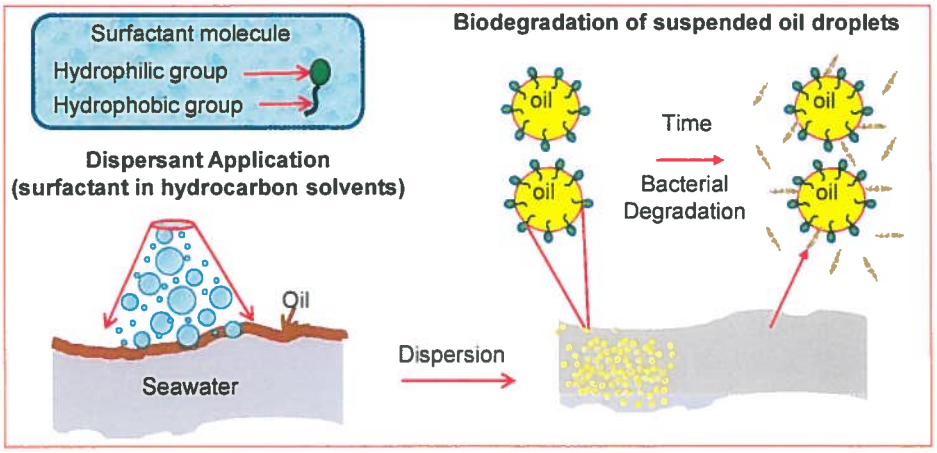

Figure 1.2: Oil dispersion and biodegradation of suspended oil droplets

A challenge often encountered in the bioremediation process is the low concentration of inorganic nutrients that are utilized by the oil-degrading microorganisms.[10] Enhanced bioremediation of spill oils typically involves the addition of materials to accelerate the microbial degradation of oil.[10] Nitrogen and phosphorus containing nutrient formulations are usually added. However, added nutrients may be highly diluted in open water systems. Current approaches require the use of oleophilic formulations to improve nutrient contact with the spill oil.[10]

1.3 Significance of Developing New and Effective Spill Remediation Technologies

The Deepwater horizon oil spill generated concerns within the scientific and technological community for several reasons including the impacts of the large volume and subsurface injection of dispersant. A key area of concern is the volume of hydrocarbon solvents[11] introduced into the marine ecosystem, with potential toxic effects.[5] Existing dispersants are liquid formulations that are sprayed onto spill oils to break them into tiny droplets that are suspended in the water column. Due to the large volume of water in the ocean, solubility and miscibility of dispersant components in

ocean water and spray drift during application, a significant amount of dispersant may not come into contact with the oil. These factors make it imperative to apply large amounts of dispersant formulations to treat oil spills. In addition liquid dispersants such as Corexit 9500 does not work effectively on weathered oil and is easily washed away by ocean waves when applied onto heavy or weathered oils.[12] This has significant economic and environmental consequences.

Therefore it is important to develop environmentally benign dispersants with more efficient delivery methods that can minimize the use of organic solvents. This will significantly improve the net environmental benefit of dispersant application in the treatment of oil spills. The development of multifunctional dispersants systems that can allow the controlled delivery of nutrients and facilitate bacteria colonization at the oil water-interface will enhance the bioremediation of spill oils especially in conditions where nutrient availability is a limiting factor. In addition, the wastage of dispersant in the treatment of surface oil spills can be significantly reduced by developing buoyant dispersants systems that effectively contact surface oil layers.

The current challenges with dispersant technologies can be overcome by leveraging the existing fundamental understanding of dispersant activity in the development of alternative dispersant systems using environmentally benign materials and synergistic properties of emulsifying agents.

1.4 Classification and Design of Emulsifying Agents

Emulsifying agents such as surfactant, surface active polymers or particles are needed to stabilize emulsions against processes such as sedimentation, creaming, flocculation and coalescence. The origins of the inherent instability of the pristine

emulsion system may be thermodynamically described by the free energy change generated on emulsification:[13]

$$\Delta G^{emulsion} = \Delta G^{interfacial\ area} - T\Delta S^{configuration} \qquad (1.2)$$

which is the sum of the free energy associated with the oil-water interfacial area increase and configurational entropy of the oil droplets.[13] Typically, the entropy term ($T\Delta S^{configuration}$) is negligible and equation 1.2 reduces to:

$$\Delta G^{emulsion} = \Delta G^{interfacial\ area} = \sigma \Delta A \qquad (1.3)$$

where σ is the interfacial tension and ΔA is the increase in interfacial area. The spontaneous breakdown of emulsions with a high interfacial area to the parent bulk phases is therefore thermodynamically favorable necessitating the addition of emulsifying agents as stabilizers. The classes of emulsifiers (Figure 1.3) are described in the subsequent subsections.

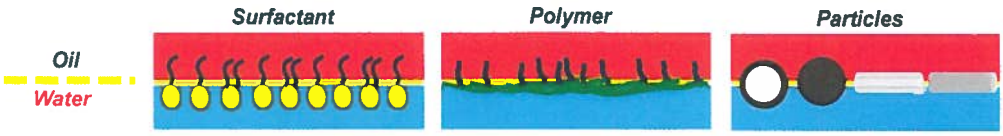

Figure 1.3: Classes of emulsifiers

1.4.1 Low Molecular Weight Amphiphiles

Amphiphiles such as surfactant and lipid molecules stabilize emulsions by physicochemical and mechanical mechanisms.[13, 14, 15] Surfactant adsorbs and orients at the oil-water interface to lower the interfacial tension and reduce the thermodynamic work of emulsification (equation 1.3). The reduction in interfacial tension may be

characterized using geometric methods such as capillary rise, sessile drop, pendant drop, spinning drop, oscillating jet, contracting circular jet or force methods such as the Du Nüoy ring detachment, Wilhelmy plate, Langmuir barrier, drop weight and maximum bubble pressure.[13]

Surfactant also stabilizes the interfacial layer by imparting elastic-like properties, resisting shear and dilatational distortion. The thermodynamic expression for the Gibbs elasticity (E_G), which describes the surface tension gradients generated by the surfactant to oppose thinning and rupture of the interfacial film, is given by:

$$E_G = \frac{d\sigma}{dlnA} \qquad (1.4)$$

The integration of hydrophobic tail and hydrophilic headgroups into the surfactant molecule drives surfactant adsorption at the oil water interface and imparts self-assembly characteristics. The relative composition of the hydrophilic and hydrophobic portions of the surfactant molecule may be quantified in terms of the hydrophilic lipophilic balance (HLB) or molecular packing parameter ($P = v/a_0 l_c$) which is the ratio of the molecular volume occupied by the surfactant tail (v) to the product of the contour length (l_c) and effective cross-sectional area of the hydrophilic headgroup (a_0).[16] When $P > 1$ the oil tends to be on the concave side of the surfactant laden interface and when $P < 1$ water tends to be on the concave side.[13]

A crude application of the HLB concept is that stable oil-in-water emulsions can be produced when the HLB of the surfactant is same at that of the oil.[13] Surfactant of various HLB can be blended to attain a suitable weighted average HLB for emulsion stabilization.[15] This synergism concept is applied in the formulation of surfactant based

emulsifiers in food, cosmetics, paints and oil spill dispersant products. Corexit 9500A dispersant is a blend of 48% nonionic surfactant derivatives of polyethoxylated sorbitan and oleic acid with 35% of dioctyl sodium sulfosuccinate as the anionic surfactant in light hydrocarbon distillate and 1-(2-butoxy-1-methylethoxy) propanol solvent.[17]

1.4.2 Surface Active Polymers

Polymers are large macromolecules composed of smaller and repeating chemical units. Polymers span the range of natural macromolecules such as proteins and polysaccharides and synthetic macromolecules such as elastomers, thermosets, thermoplastics and fibers. Polymers may stabilize emulsions by lowering the interfacial tension, imparting viscoelastic properties to the oil water, and/or by steric and electrostatic stabilization mechanisms.[14, 18, 19] These surface active polymers may be designed by grafting hydrophobic side chains to a hydrophilic backbone, grafting hydrophilic side chains to a hydrophobic polymer or alternating hydrophilic and hydrophobic polymer blocks.[14, 19] The combination of these basic architectures allows the design of polymeric surfactant with more complex architectures. Similar to surfactant molecules, the integration of hydrophilic and hydrophobic moieties into the polymer molecule imparts self and interfacial assembly properties to the polymer.

The broad availability, environmentally benign characteristics and easily functionalized groups of polyelectrolytes such as chitosan provides a major route for synthesizing hydrophobically modified water soluble polymers as emulsion stabilizers.[19] Chitosan, an abundantly available cationic biopolymer extracted from crustacean shells, may be modified into an amphiphilic derivative by grafting hydrophobic alkyl groups to the polymer backbone.[18] As a polymeric emulsifier, the hydrophobically modified

chitosan (HMC) is positively charged and anchors its hydrophobic residues into oil droplets, stabilizing emulsions by electrosteric mechanisms.[17]

1.4.3 Particulate Emulsifiers

Particles can adhere to the soft deformable oil-water interface to stabilize emulsions against coalescence.[20] These solid-stabilized emulsions are often referred to as Pickering emulsions in recognition of the pioneering efforts of Spencer Umfreville Pickering.[21] Several experimental and theoretical studies have been carried out on solids-stabilized emulsion especially on the key factors that affect stability and the structure of drop interfaces.[22, 23] The attachment of the particle at the oil-water interface with energies that are several orders of magnitude higher than the thermal energy is a key mechanism for the high stability of particle stabilized emulsions.[22] This energy depends on factors such as particle shape, size and wettability. The roles of these factors in the design of particle based dispersant systems are elucidated in this dissertation using free energy analysis of particles attached at the oil-water interface.

Most solid stabilized emulsions are prepared with solid, non-porous particles of various shapes including spherical, cylindrical, sheet-like and ellipsoidal particle.[22] However, particles with porous or hollow structured internal morphologies may be synthesized with the aid of sacrificial templates.[24, 25, 26, 27, 28, 29] Hollow particles are a unique class of particles because the significant pore volume in the particles may be exploited in energy storage, catalysis and controlled delivery applications.[30, 31, 32]

When dealing with solid particles at liquid interfaces, the three-phase contact angle is an important parameter.[22, 23] The contact angle is the angle, conventionally

measured through the liquid, at which a liquid/vapor interface meets a solid surface. This is the angle between the tangents to the solid surface and the fluid-fluid interface measured through one of the fluids. It is conventionally measured through the more polar liquid. The contact angle (θ) for an oil-water interface is related to the tension of particle-water, γ_{pw}, particle-oil, γ_{po}, and oil-water, γ_{ow} by the Young's equation:[23]

$$\gamma_{po} - \gamma_{pw} = \gamma_{ow} \cos \theta \qquad (1.5)$$

Relevant to oil spill remediation, the association of oil with solid particles such as fine clay minerals in the aqueous seawater medium results in the formation of oil-mineral aggregates.[33] This natural interaction enhances the physical removal of spill oils from low-energy shorelines and facilitates the dispersion of the oil into coastal waters. The formation of oil-mineral aggregates also enhances the biodegradation of spill oils. This approach has been observed facilitate the process of oil-spill clean-up especially in aspects of oil dispersion and natural recovery of oiled shorelines.[33]

1.4.4 Design of Mixed Emulsifier Systems

The design of mixed emulsifier systems is attainable by exploiting covalent and non-covalent interactions between the various classes of materials. The overall goal is to obtain a system with the appropriate interfacial activity for emulsion stabilization. Particles can be functionalized with hydrophobic groups using strong chemical bonds to optimize their wettability and partitioning to the oil water interface.[23] Based on the charge structure of their hydrophilic headgroups, surfactant may be classified as anionic, cationic, nonionic or zwitterionic.[13] The adsorption of oppositely charged surfactant on solid particles by electrostatic interaction can facilitate oil emulsification.[34] Non-ionic or

zwitterionic surfactant may also be physisorbed on particles for improved emulsification.[35]

The formation of a surfactant–polyelectrolyte complex (SPEC) by electrostatic interaction between chitosan polyelectrolyte and an oppositely-charged surfactant has also been reported to facilitate oil emulsification properties of the polyelectrolyte.[18] The adsorption of polymer onto the surface of particles may also modify the particle wettability[36] and lock particles together thereby strengthening the interfacial layer.[37] These previous works demonstrate that effective emulsifier systems can be designed by a systematic synergy of the attractive characteristics of a range of materials using the fundamental principles of colloidal and interfacial phenomena.

1.5 Brief Description and Novelty of Dissertation Research

1.5.1 Integration of Particle-Stabilized Emulsions with Surfactant Delivery using Halloysite Clay Nanotubes (HNT)

Hollow particles possess a significant void volume that can be exploited for the targeted delivery and controlled release of materials.[30] We hypothesize that using hollow particles, the concept of particle stabilized emulsions can be integrated with the delivery of spill treating agents, such as surfactants and nutrients, directly at the oil-water interface. Here we focus on halloysite, a naturally occurring aluminosilicate nanotube[38] with characteristic dimensions of about 10 - 70 nm in internal diameter, 90nm - 250nm in external diameter and up to 1.0μm in length. The void volume of halloysite nanotubes has previously been explored for the controlled release of materials such as anti-corrosion agents, biocides and drugs.[39]

In this dissertation, the halloysite lumen is exploited for the loading and delivery of surfactant components to the oil water interface for effective oil emulsification. Functionalization of the HNT surface with superparamagnetic iron oxide nanoparticles is demonstrate to impart magnetic responsiveness to the oil-water interface with potential multifaceted applications in oil spill dispersion, mobilization of surfactant-herded surface oil layers and remote oil spill detection using magnetic fields.

Optimum wettability of the HNT by oil and water phases is crucial for the efficient delivery of spill treating agents, such as surfactants and nutrients, directly at the oil-water interface. In addition to the available pore volume and open ended nanotubular morphology, halloysite nanotubes (HNT) possess a negatively charged outer silica surface and a positively charged inner alumina surface.[38, 40] The interaction of the negatively charged external HNT surface with the positively charged chitosan biopolymer followed by a carbonization step is developed as a novel approach for tuning particle wettability in the preparation of particle-stabilized emulsions. Based on the interaction of chitosan and halloysite, the mechanisms of synergistic emulsion stabilization using the HNT and hydrophobically modified chitosan (HMC) derivative is clearly investigated. The hollow nanotubular morphology of the HNT is further exploited in the unique design of an effective clay nanotube, hydrophobic surfactant, and cationic biopolymer mixed dispersant system having tubular inorganic micelle architecture.

1.5.2 Formation Mechanism and Emulsion Stabilization Characteristics of Hollow Microspheres Synthesized in a Scalable Aerosol Process

As demonstrated with the naturally occurring halloysite nanotubes, hollow particles have potential applications as emulsion stabilizers and release vehicles for oil

spill treating agents. Common approaches for synthesizing hollow particle synthesis are difficult to scale up to commercially viable quantities due to the multistep operations and complex components involved.[30] We elucidate the colloidal mechanism of hollow particle synthesis using a rapid and scalable aerosol process. Relevant to the carbonization concept for tuning particle wettability aforementioned in section 1.5.1, hollow structured silica-carbon particles produced using the scalable aerosol process are exploited for oil emulsification applications.

1.5.3 Development of Nanostructured Gel Dispersants

Gel dispersants have attractive characteristics such as (a) improved adherence to heavy or weathered oils without being washed off by ocean waves (b) significantly reduced spray drift during delivery (c) improved contact with spills oils due to buoyancy for extended periods (d) lower hydrocarbon solvent content and (e) provision of some degree of visible feedback on dispersion to spill responders. We develop an effective mesocrystalline gel dispersant containing the innocuous phospholipid, l-α-phosphatidylcholine (PC), and surfactant components of Corexit 9500, dioctyl sulfosuccinate sodium salt (DOSS, 98%) and polyoxyethylene (20) sorbitan monooleate (Tween 80) for the treatment of oil spills. The influence of Tween 80 content on the gel microstructure is elucidated using small angle neutron scattering (SANS), electron microscopy and nuclear magnetic resonance spectroscopy. The effectiveness of the gel dispersant is characterized using the standard baffled flask test.

CHAPTER 2

RELEASE OF SURFACTANT CARGO FROM INTERFACIALLY-ACTIVE HALLOYSITE CLAY NANOTUBES FOR OIL SPILL REMEDIATION

Based on: Owoseni, O.; Nyankson, E.; Zhang, Y. H.; Adams, S. J.; He, J. B.; McPherson, G. L.; Bose, A.; Gupta, R. B.; John, V. T. Release of Surfactant Cargo from Interfacially-Active Halloysite Clay Nanotubes for Oil Spill Remediation Langmuir 2014, 30 (45) 13533– 13541

2.1 Introduction

Oil spills are often major occupational, environmental, and community health disasters.[4] Crude oil spills can adversely affect the health of plants and animals in the ecosystem if adequate spill remediation procedures are not deployed.[41] The addition of surface-active materials or dispersants to disperse spill oils into tiny droplets is often an efficient approach for the treatment of oil spills.[17] Such surface-active materials, such as dispersants and lipophilic fertilizers, can facilitate the biodegradation process at the oil-water interface.[7] Typical oil spill dispersants are a blend of surfactants with organic solvents such as glycol and light petroleum distillates.[17] The dispersant is sprayed onto the spill oils to break them into tiny droplets that are suspended in the water column. Application of dispersants can reduce the possibility of shoreline impact, lessen the impact on birds and mammals, and promote the biodegradation of oil.[7] Approximately 2.1 million gallons of dispersant was applied during the Deepwater Horizon Oil Spill.[42] Surfactants which are the active ingredients in existing dispersants, diffuse to the

oil/water interface and reduce the oil-water interfacial tension, allowing oil to mix into water column as tiny droplets.[7]

There are concerns over the potential impact of existing dispersants on the ecosystem.[11, 43] Key areas of concern include the volume of dispersants and hydrocarbon solvents introduced into the marine ecosystem.[11] The active surfactant components are in dynamic equilibrium between the oil-water interface and the bulk phases.[44] Due to the large volume of water in the ocean a significant amount of dispersant may not come into contact with the oil. The solubility and miscibility of dispersant components coupled with the ocean waves often makes it imperative to apply large amounts of the dispersant with significant economic and environmental consequences. Therefore it is important to develop environmentally benign dispersants with more efficient delivery methods that can minimize the use of organic solvents.

Emulsions are a dispersion of one liquid in another immiscible liquid in the form of small droplets typically stabilized by the addition of emulsifiers. While such emulsifiers are typically surfactants, it is known that interfacially-active solid particles can function as emulsifiers for stabilizing oil-in-water emulsions.[45] Following the pioneering studies by Ramsden and Pickering,[21, 46] several experimental and theoretical studies have been carried out on solids-stabilized emulsions to understand the factors that affect stability and the structure of the interface.[23, 47] The synergy of particles and surfactants in stabilizing emulsions has also been exploited in designing optimally stable emulsions in food and material science applications.[48, 49]

This paper describes the use of a naturally occurring clay mineral, halloysite, with the morphology of hollow tubules, in stabilizing oil-in-water emulsions. The additional

aspect is that the pore volume in the tubules can sequester surfactants, thereby allowing a release of surfactant to the oil-water interface. Halloysite has been used in the controlled release of pharmaceutical and agricultural compounds.[50, 51, 52, 53, 54, 55] Halloysite has also been utilized in the fabrication of composite polymer microparticles via suspension and emulsion-based routes, for drug delivery applications.[56, 57, 58] Its use in stabilizing emulsions together with the delivery of surfactants to the oil-water interface is the specific novelty of the concepts advanced in this paper.

Halloysite is a naturally occurring aluminosilicate with a chemical formula $Al_2[Si_2O_5(OH)_4].2H_2O$. It is formed from the rolling of kaolinite sheets into tubes due to the lateral misfit of the smaller gibbsitic octahedral sheet and the larger silica tetrahedral sheet.[59, 60] In addition to the nanocylindrical geometry, halloysite possesses a predominantly negatively charged outer silica surface and a positively charged inner alumina surface at the pH of the marine environment.[54] In recent and pioneering work, Cavallaro and coauthors have shown that charge-mediated adsorption of surfactants to the lumen and external surfaces of halloysite facilitates the dispersion of halloysite in aqueous media and also enables the capture of hydrophobic compounds, including hydrocarbons.[40, 61] These concepts are relevant to our work with encapsulating surfactants in HNTs, which when released will reduce the oil-water interfacial tension.[27, 28]

Our objective in this work is to encapsulate surfactants representative of COREXIT 9500, the commonly used dispersant in oil spill remediation, into the tubular voids of halloysite. We show that halloysite stabilizes oil-in-water emulsions and subsequently releases the surfactants thereby reducing the interfacial tension significantly allowing much smaller droplets to form leading to enhanced dispersion of oil.

2.2 Experimental Procedures

2.2.1 Materials

Dioctyl sulfosuccinate sodium salt (DOSS, 98%), polyoxyethylene (20) sorbitan monooleate (Tween 80), sorbitan monooleate (Span 80), dodecane, methanol, chloroform, methylene blue , cobalt(II) nitrate hexahydrate ($Co(NO_3)_2$) and ammonium thiocyanate (NH_4SCN, ≥97.5%) were purchased from Sigma-Aldrich. Halloysite nanotubes (HNT) were obtained from NaturalNano. Inc. (Rochester, NY, USA). Sodium tetraborate decahydrate ($Na_2B_4O_7 \cdot 10H_2O$) was obtained from J. T. Baker. Deionized (DI) water, produced from an Elga water purification system (Medica DV25), with resistance of 18.2 MΩ was used in all experiments. 0.6 M sodium chloride (Certified ACS grade, Fisher Scientific) solution in deionized water was used as a substitute for seawater. Louisiana sweet crude oil with a viscosity of 0.01 Pa s and specific gravity 0.85 at 15 °C was obtained from British Petroleum's Macondo prospect (SOB-20100617032).[17] All chemicals were used as received.

2.2.2 Loading of Halloysite Nanotubes (HNT) with Surfactants

In a typical loading experiment, 0.2g of HNT was weighed into a round bottom flask. A known amount of surfactant(s) dissolved in methanol was then added to the flask. The halloysite nanotubes were then dispersed by magnetic stirring and brief ultrasonication (Cole-parmer 8890). Vacuum suction was applied to the contents of the flask to displace the air in the HNT and suck the surfactant solution into the HNT. The pressure was then cycled back to atmospheric pressure, typically after 15minutes. This cycling process was repeated two times and then the remaining methanol was allowed to

evaporate under vacuum in a rotary evaporator to allow the loaded surfactants to crystallize inside the halloysite nanotubes.[62]

The surfactants used in the vacuum loading experiments were DOSS, Tween 80 and Span 80. Native HNT and the surfactant-loaded HNT were characterized by transmission electron microscopy (TEM) on a FEI Tecnai G2 F30 Twin Transmission Electron Microscope operated at 300 kV. Thermogravimetric analysis (TGA) of the native and surfactant-loaded HNT was carried out on a TA Instruments SDT 2960 Simultaneous DTA-TGA. The analysis was performed in an air environment at a heating rate of 10°C/min. The surfactant loading is simply expressed as the mass percentage of surfactant in the surfactant-loaded HNT samples.

2.2.3 Emulsion Preparation and Characterization

The nanotubes were uniformly dispersed in water by ultrasonication (Cole-parmer 8890) for 1 minute. Dodecane was then added to the HNT dispersion at a dodecane to water ratio of 1:3. Emulsions were then prepared by vortex mixing at 3000rpm (Thermolyne Maxi Mix II) for 2 minutes. Crude oil (BP-MC 252) in saline water emulsion was also prepared using this procedure.

A small aliquot of the oil-in-water emulsion was removed using a Pasteur pipet and diluted with water prior to imaging on a Leica DMI REZ optical microscope. The images were analyzed using Image ProPlus v.5.0 software to obtain the droplet sizes. Emulsion stability in a centrifugal field was characterized by carefully transferring the emulsions into 15ml polypropylene centrifuge tubes followed by centrifugation at 1000rpm for 2minutes on an Eppendorf 5810 Centrifuge.

The three-phase contact angle of the HNT-water-dodecane interface was measured using a standard goniometer (Rame-Hart model 250). The HNT powder was pressed into a tablet and placed in a glass cell (Starna Cells Inc.) containing dodecane as the external phase.[39] Water was injected from a 21 gauge needle onto the HNT tablet for contact angle measurement.

The structure of drop interfaces were imaged by Cryo-scanning electron microscopy (Cryo-SEM) imaging on a Hitachi S-4800 field emission Scanning Electron Microscope operated at a voltage of 3 kV and a working distance of 8mm. The emulsion sample was first plunged into liquid nitrogen, followed by fracturing at −130 °C using a flat-edge cold knife and sublimation of the solvent at −95 °C for 5 min. The sample was sputtered with a gold–palladium composite at 10 mA for 88 s before imaging.

2.2.4 Characterization of Surfactant Release Kinetics

Briefly, 5mg of DOSS-loaded HNT was added to 100ml of saline water in a glass beaker. The DOSS loading from TGA analysis was 12.4wt%. 5ml samples were withdrawn at several time intervals and analyzed for DOSS release. 5ml of saline water was added back to the beaker immediately after each sampling to replace the saline water that was withdrawn. The system was continuously stirred at 200rpm using a magnetic stirrer. The release kinetics of DOSS into the saline water was characterized by the simplified methylene blue active substances (MBAS) spectrophotometric method.[63]

Briefly, 200 µl of a 50mM sodium tetraborate solution at pH 10.5 was added to the 5ml samples in a 20ml vial. 100 µl of a solution containing 3.1mM methylene blue and 10mM sodium tetraborate was then added to the vial. This was followed by vortex

mixing for 1minute. 4 ml of chloroform was then added and the system was vigorously stirred on a vortex mixer at 3000rpm for 30 seconds. After equilibration for 5 minutes, the absorbance of the blue chloroform phase resulting from the transfer of the DOSS-methylene blue (DOSS-MB) complex was measured at 650 nm against air using a Shimadzu UV-1700 PharmaSpec UV-VIS Spectrophotometer.

The release of Tween 80 into saline water was also characterized by UV-spectroscopy using the cobalt thiocyanate active substances (CTAS) method.[64, 65] The CTAS reagent was prepared by dissolving 3g of $Co(NO_3)_2$ and 20g of NH_4SCN in 100 mL of water. 500mg of Tween 80-loaded HNT were added into 100ml of saline water and continuously stirred at 200rpm. The Tween 80 loading from TGA analysis was 13.0wt%. 0.75ml samples were withdrawn at intervals of time. 0.75ml of the CTAS reagent and 3mL of chloroform were then added to the samples followed by vortex mixing at 3000rpm for 1 minute. Absorbance of the chloroform phase containing the cobalt thiocyanate-polyethoxylate complex was measured at 620nm. The amounts of surfactant released over time were extracted from calibration curves prepared using known concentrations of the surfactants in saline water.

2.2.5 Measurement of Oil-water Interfacial Tension

The dynamic reduction in the dodecane-saline water interfacial tension was measured by the pendant drop method using a standard goniometer (Ramé-Hart, model 250). 5mg of the surfactant-loaded HNT was weighed into 4ml of dodecane in a glass cell. A drop of water of about 15μL was then quickly injected from a syringe. The dynamic interfacial tension was measured by drop shape analysis using the DROPimage Advanced Software.

Low crude oil-saline water interfacial tensions obtainable with surfactant-loaded HNT dispersants were measured using the spinning drop tensiometer (Grace Instruments model M6500).[17] The spinning drop tensiometer has a rotating capillary of 2mm inner diameter with total volume of 0.292cm^3. The surfactant-loaded HNT dispersants were thoroughly mixed with crude oil by vortex mixing and sonication at various dispersant to oil mass ratios. A small drop, approximately 0.0005 cm^3, of the dispersant-oil mixture was injected into the capillary filled with saline water using a micro syringe. The capillary tube was sealed and rotated at a velocity in the range of 5000–6000 rpm. The temperature of the tube was maintained at 25°C by circulating cold water around the capillary tube. The radius of the oil drop was measured using an optical microscope fitted with a digital output.

The interfacial tension values were then obtained by the Vonnegut's formula:[66]

$$\gamma = \frac{\Delta\rho\omega^2 R^3}{4} \qquad (2.1)$$

where γ (mN m^{-1}) is the interfacial tension, $\Delta\rho$ (g cm^{-3}) is the density difference between the drop and the surrounding fluid, ω (rad s^{-1}) is the angular velocity, and R (cm) is the drop radius. The crude oil-saline water interfacial tension without the dispersant was measured by the pendant drop method.

2.3 Results and Discussion

2.3.1 Interfacial activity of halloysite nanotubes

Figure 2.1 shows optical micrographs of dodecane-in-water emulsions stabilized by various concentrations of HNT without surfactant.

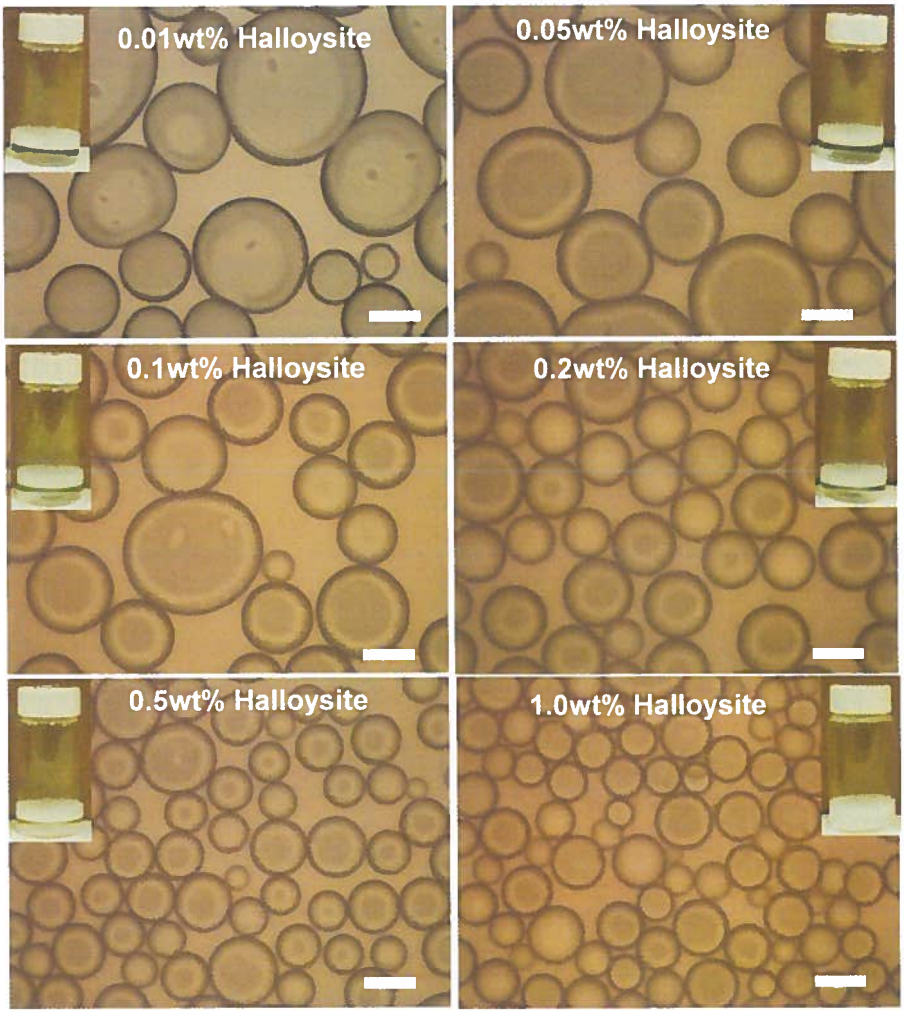

Figure 2.1: Optical microscopy images of dodecane-in-water emulsions showing the interfacial-activity of HNT. HNT concentrations in water were 0.01wt%, 0.05wt %, 0.1wt %, 0.2wt %, 0.5wt % and 1wt % respectively. Smaller droplets are obtained with increasing concentration of HNT adsorbed at the oil-water interface. The emulsions are stable for months. The insets are photographs of vials containing the emulsions prepared with varying HNT concentrations. Scale bars = 100μm.

The emulsions are creamy-white in appearance and stable for more than 3months at room temperature. Increasing the concentration of HNT leads to emulsions with progressively smaller droplet sizes. There is no significant reduction in droplet size beyond 0.5wt% HNT concentration, likely due to complete coverage of the interface by the particles.

The effect of increasing HNT concentration on the stability of the oil-in-water emulsions was characterized by centrifugation. In a centrifugal field, the denser aqueous phase collects at the end of the tube furthest from the axis of rotation while the halloysite stabilized oil-in-water emulsion phase forms a concentrated cream at the other end.[45] This procedure forces the droplets together, thereby deforming the droplets into polyhedra separated by thin water films. The rupture of the thin oil-water-oil films leads to the formation of a clear oil layer which provides a reasonable measure of emulsion stability.[23, 45] Figure 2.2 shows the effect of increasing halloysite concentration on the fraction of oil resolved on centrifugation and the average droplet sizes. There is a significant impact of increasing halloysite concentration on emulsion stability and average droplet sizes between halloysite concentrations of 0.05wt% and 0.5wt%. The average droplet size decreases by 53% and the fraction of oil resolved decreases from 38% to 0% for the 10-fold increase in particle concentration from 0.05wt% to 0.5wt%.

It is evident that the increased adsorption of halloysite nanotubes at higher concentrations, leads to the formation of more stable emulsions. The formation of a rigid and protective interfacial film by the adsorption of HNTs at the oil-water interface provides steric hindrance to drop coalescence leading to high emulsion stability. [67]

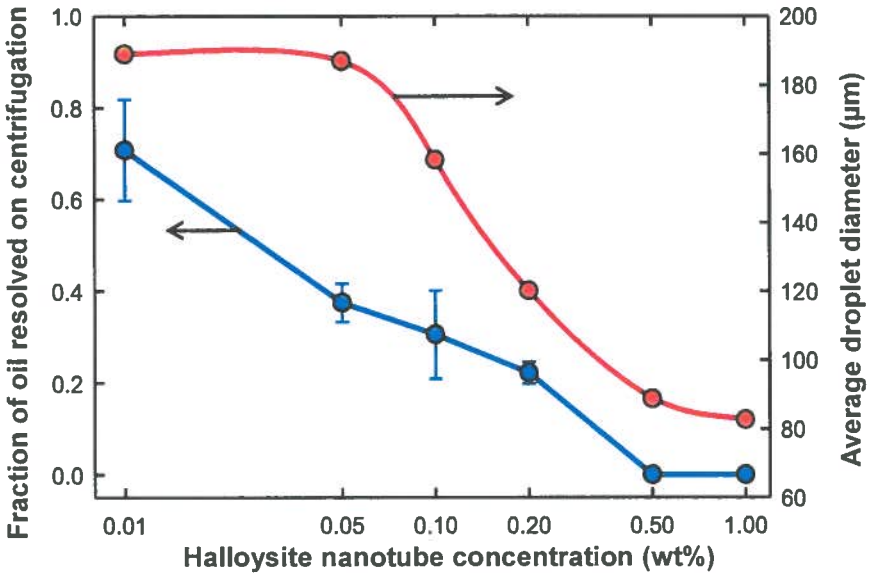

Figure 2.2: Relationship between HNT concentration, emulsion stability and average droplet size. Emulsion stability increases with HNT concentration.

Cryo-SEM imaging of the oil-in-water emulsion shows the morphology of the oil droplet-water interface (Figure 2.3). At 0.1wt% HNT concentration in water, the oil droplet is covered by network-like aggregates of HNT (Figure 2.3 a-d). Cryo-SEM imaging shows the interconnected nanotubes trapped together at the oil-water interface. A denser network of HNT is observed at the oil water interface at the higher 1wt% concentration (Figure 2.3 e-h). The HNTs assemble in a side-on orientation at the oil-water interface at both concentrations.[68]

The contact angle is an important parameter in understanding the adsorption of solid particles at liquid interfaces. The contact angle is the angle between the tangents to the solid surface and the fluid-fluid interface measured through one of the fluids.[22] It is conventionally measured through the more polar liquid. The contact angle (θ) is related to

the tension of particle-water, γ_{cw}, particle-oil, γ_{co}, and oil-water, γ_{ow}, interfaces by the Young's equation[22]

$$\gamma_{co} - \gamma_{cw} = \gamma_{ow} \cos\theta \qquad (2.2)$$

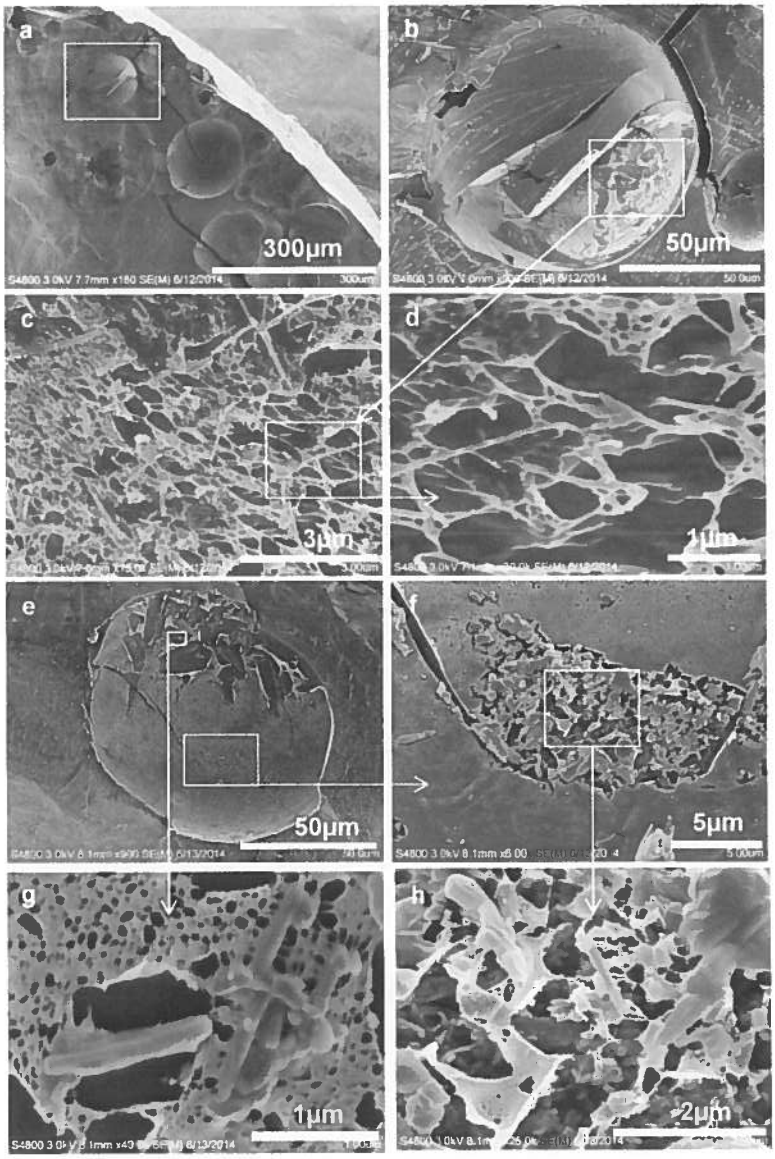

Figure 2.3: Cryo-SEM images of dodecane-in-water emulsion stabilized by HNT. HNT concentrations are 0.1wt% (a,b,c,d) and 1wt% (e,f,g,h). The emulsion is stabilized by the adsorption of halloysite nanotubes network at the oil water interface. A denser network of halloysite nanotube is trapped at the oil water interface at the higher 1wt% concentration.

Free energy analysis of particle positioning at the interface provides useful insights into the mechanisms governing the stability of particle-stabilized emulsions.[22] At the low Bond numbers (low ratio of gravitational forces to surface tension forces), the deformation of the fluid interface by small particles due to gravity can be neglected.[22, 68] Here, we assume the geometry of a solid cylinder with flat faces and with a three-phase contact angle (θ) as shown in Figure 2.4. The analysis for a solid cylinder is approximate, given that the morphology of halloysite is tubular. Due to capillary action, however, the lumen is likely to be filled with liquid and the three phase contact is essentially on the exterior surface of the material, validating the analysis to the exterior surface.

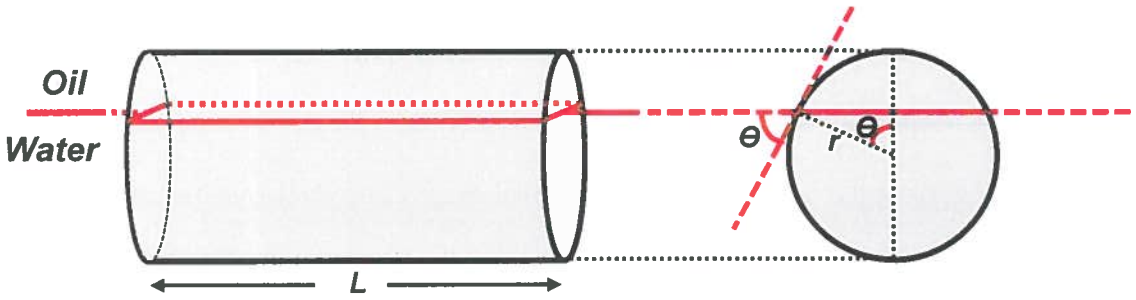

Figure 2.4: Cylindrical particle in a side-on orientation at a planar oil-water interface

The surface free energy (G^{int}) can be expressed as:

$$G^{int} = \gamma_{ow} A_{ow}^{int} + \gamma_{pw} A_{pw}^{int} + \gamma_{po} A_{po}^{int} \qquad (2.3)$$

$$A_p = A_{pw}^{int} + A_{po}^{int} \qquad (2.4)$$

where A_p is the area of the cylindrical particle, A_{ow}^{int} is the area of the oil-water interface when the particle is adsorbed at the interface, A_{pw}^{int} is the area of the particle in contact with the aqueous phase and A_{po}^{int} is the area of the particle in contact with the oil phase.

The emulsion will be destabilized if the particles are detached into either of the bulk phases. The contact angle of the particle at the oil-water interface defines the phase into which the particle will be detached. The three phase contact angle of the halloysite-water-dodecane interface was measured through the water phase as 25.6 ± 0.1^0 using the compressed HNT tablet method.[39] This value of the contact angle indicates that the particles are more hydrophilic than lipophilic and will therefore stabilize emulsions where water is the bulk phase.[22, 23] We analyze the detachment of the hydrophilic HNTs from the oil-water interface into water as this scenario will be thermodynamically more favorable than detachment into the oil phase.[22] The surface free energy when the particle is detached from the interface and fully submerged into the aqueous phase (G^w) is:

$$G^w = \gamma_{ow} A_{ow}^w + \gamma_{pw} A_p \qquad (2.5)$$

where A_{ow}^w is the area of the oil water interface when the particle has been detached into water.

Therefore, the free energy change (ΔG) on removing the particle from the oil-water interface into water is:

$$\Delta G = G^w - G^{int} \qquad (2.6)$$

$$\Delta G = \gamma_{ow} [A_p^{int} - A_{po}^{int} \cos\theta] \qquad (2.7)$$

where A_p^{int} is the area of the oil-water interface occupied by the cylindrical particle. Simple analysis of the cylindrical geometry for the areas A_p^{int} and A_{po}^{int} gives:

$$\Delta G = 2rL\gamma_{ow}(\sin\theta - \theta\cos\theta - \frac{r\theta\cos\theta}{L} + \frac{r\cos^2\theta\sin\theta}{L}) \qquad (2.8)$$

For a 1μm long cylindrical particle with radius of 50nm, three-phase contact angle of 25.6^0 and a dodecane-water interfacial tension of 49±1mN/m, the energy of particle attachment at the interface is calculated to be 3.45×10^4kT. The particle is trapped at the interface with an energy that is four orders of magnitude greater than the thermal energy, kT. At such high energy levels for detachment, the particles can be considered to be irreversibly adsorbed at the oil-water interface.[22, 45] Small particles adsorbed at fluid interfaces experience net attractive capillary forces due to formation of an asymmetric menisci between particles located at the interface.[68] The forces act when the distance between particles at the interface is less than the characteristic capillary length of the system.[22, 68] The capillary length (q) determines the range of action of the capillary forces and can be expressed as:[22, 44]

$$q = \left(\frac{\gamma_{ow}}{\Delta\rho g}\right)^{\frac{1}{2}} \qquad (2.9)$$

where γ_{ow} is the interfacial tension, $\Delta\rho$ is the difference between the mass densities of the two fluids and g is the gravitational acceleration. Capillary interactions between the particles will influence the network assembly and interconnection of HNT at the oil-water interface, leading to the observed aggregates and to network formation.[69] Typically, these attractive capillary interactions greatly exceed the thermal energy kT and can strongly chain the particles together.[70] A chain of cylindrical particles at the oil-water interface can be represented as having a length (L') which is greater than the individual length (L) of each particle. For HNT, while it is clear that L > r, when the particles aggregate to chains, the assumption of L' >> r is valid, leading to the simplification of equation (2.8) to

$$\Delta G = 2rL'\gamma_{ow}(\sin\theta - \theta\cos\theta) \qquad (2.10)$$

Figure 2.5 shows that the free energy of particle detachment (ΔG) calculated from equation 2.7 increases with the number of contacting particles jammed together at the oil-water interface. The energy required for detaching an assembly of ten interconnected 1μm long cylindrical particles with a radius of 50nm from the oil-water interface into the aqueous phase is about eleven times the energy required to detach a single particle. Capillary interactions between HNTs allow end-to-end linkages into aggregates with an increased energy of attachment at the oil-water interface. The analysis is distinct from that of a single rod of equivalent length since the linkages allow the multiple cylindrical particles to conform to the interface. In general, the energies also increase with particle radius (equations 2.8 and 2.10).

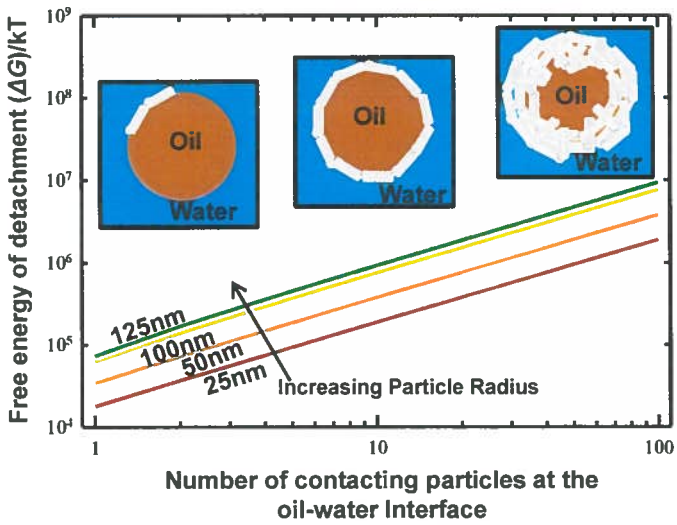

Figure 2.5: Variation of free energy of detachment with number of contacting cylindrical particles in capillary aggregates trapped at the oil-water interface. Curves are for a 1μm long cylindrical particles with radius ranging from 25nm to 125nm. The free energy of particle detachment (ΔG) is several orders of magnitude greater than the thermal energy (kT) and increases with the number of particles jammed together into a capillary aggregate.

2.3.2 Synergistic Effects of Surfactant Loaded HNT

In practical oil spill remediation applications, the reduction in interfacial tension aids the dispersion of spill oils into small droplets. This will expose a large oil-seawater interfacial area for the effective bioremediation of oil spills by indigenous bacteria in the ocean.[7] Surfactants and interfacially-active particles can act synergistically to stabilize the emulsion.[48] The adsorption of surfactant molecules at the interface serves to lower the interfacial tension while the adsorption of particles provides a steric barrier to drop coalescence.[11, 22, 48] With this objective in mind, HNTs were loaded with surfactant(s) by vacuum suction and solvent evaporation.[62]

Figure 2.6 shows TEM images and thermogravimetric curves for native HNT and DOSS-loaded HNT. Figure 2.6a reveals the hollow nanotubular structure of the native halloysite clay particle with an empty lumen. The characteristic dimensions of the HNT range from about 0.33μm - 1.5μm in length, 90nm-250nm in external diameter and 10nm – 70nm in lumen. Loading of the surfactant, DOSS, fills the lumen with the surfactant resulting in a higher electron density from the TEM imaging (Figure 2.6b).

Figure 2.6c shows the TGA curves for halloysite and DOSS-loaded halloysite at various DOSS loadings. The TGA curve for native HNT (curve i) shows two distinct mass losses centered at 64^0C and 510^0C respectively. The first mass loss is due to the loss of water molecules adsorbed on the external surface of halloysite nanotubes while the second mass loss is due to the dehydroxilation of halloysite.[71] The TGA curve for surfactant-loaded HNT has an additional distinct mass loss centered at 290^0C due to the thermal degradation of the loaded surfactant. The degree of mass loss increases accordingly with the amount of surfactant loaded into the HNTs (curves ii-v).

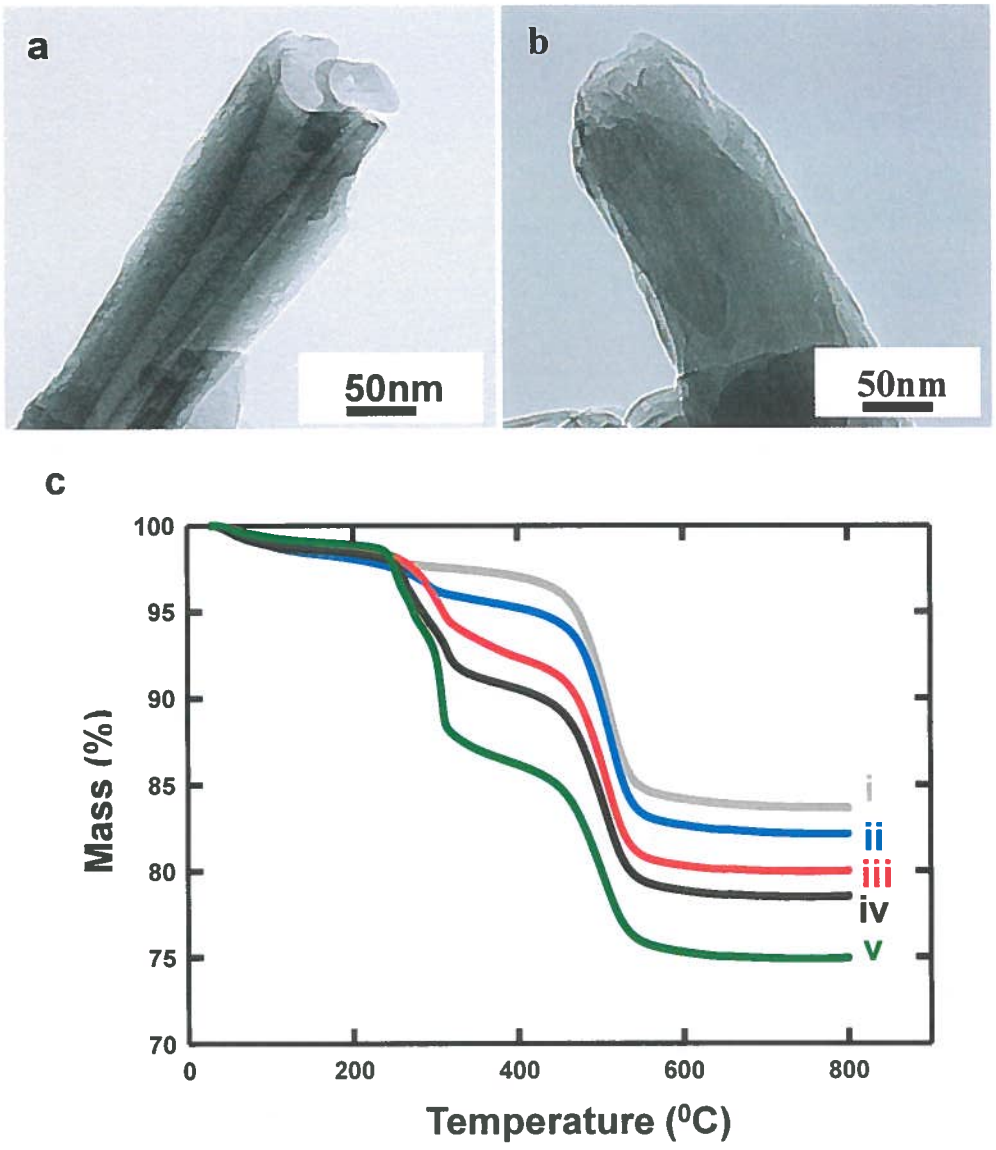

Figure 2.6: TEM images of native HNT (a) and HNT loaded with 12.4wt% DOSS (b); Panel (c) shows TGA analysis of HNT with various DOSS loadings. DOSS loadings are 0wt% (curve i), 2.83wt% (curve ii), 5.55wt% (curve iii), 7.70wt% (curve iv) and 12.4wt% (curve v) respectively. The higher mass loss observed for the DOSS-loaded HNT is due to the thermal degradation of DOSS.

Figure 2.7 shows the kinetics of release for DOSS and Tween 80 from HNT into saline water. Based on TGA analysis and mass balance calculations on the surfactant-loaded HNT samples, about 80% of the surfactant cargos were typically released from the HNT over the time period of the experiments. The kinetics of release for Tween 80 are significantly higher than for DOSS due to the higher water solubility of Tween 80.[72] With DOSS an initial burst release over the first 5 minutes or so due to surface adsorption is followed by a much slower release as the sparingly water soluble surfactant slowly partitions out of halloysite into the aqueous phase. Electrostatic interactions between the anionic surfactant DOSS and the positively charged inner surface of the HNT lumen may also contribute to the more sustained release of DOSS compared to the non-ionic surfactant Tween 80.

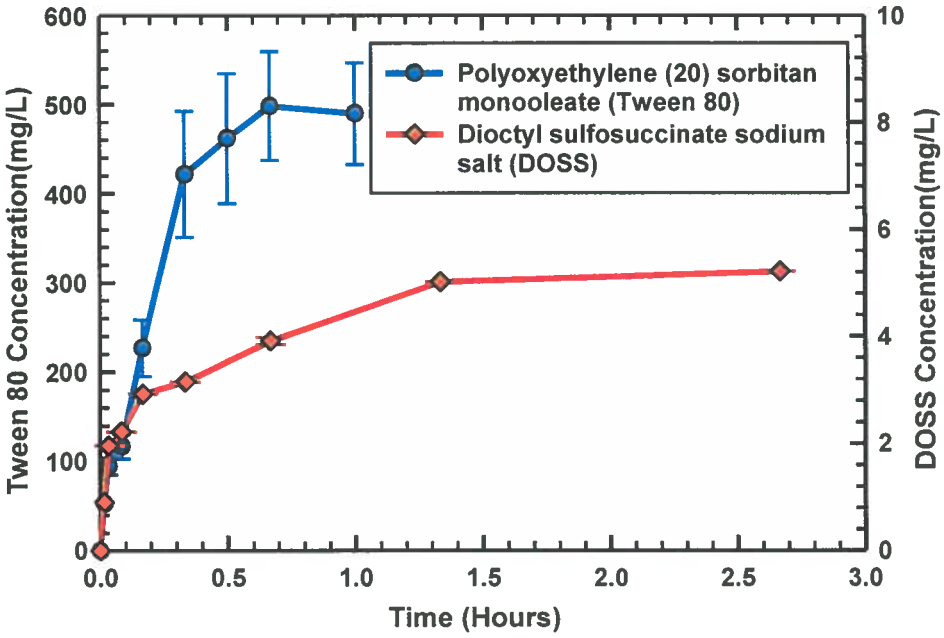

Figure 2.7: Kinetics of surfactant release into saline water. DOSS and Tween 80 release into the saline water was characterized by the methylene blue active substances (MBAS) and the cobalt thiocyanate active substances (CTAS) spectrophotometric method.

Figure 2.8a shows the effect of synergistic emulsion stabilization by halloysite nanotubes and DOSS. At constant halloysite concentration, the average droplet size decreases with increasing surfactant loading and release from halloysite nanotubes. Neglecting configurational entropy contributions, the overall free energy change (ΔG) for emulsification can be expressed as:[73]

$$\Delta G = \gamma_{ow} * \Delta A \qquad (2.11)$$

where ΔA is the change in interfacial area and γ is interfacial tension. Reduction of the interfacial tension therefore allows a significantly greater surface area generation (smaller droplets) for the same work done to the system.

Using pendant drop tensiometry, we characterized the interfacial tension dynamics when DOSS is released from the HNT into the dodecane phase. Curve i in Figure 2.8b is the dynamic interfacial tension measurements for HNT without any surfactant loaded. Without surfactant loading into the HNT, there is no significant reduction in interfacial tension. For the surfactant loaded-HNT samples (Figure 2.8b, curve ii and iii), the release of DOSS molecules from HNT into the dodecane phase results in a dynamic reduction in the dodecane-saline water interfacial tension. We note that the DOSS will create water-in-oil microemulsions in the dodecane phase.[74]

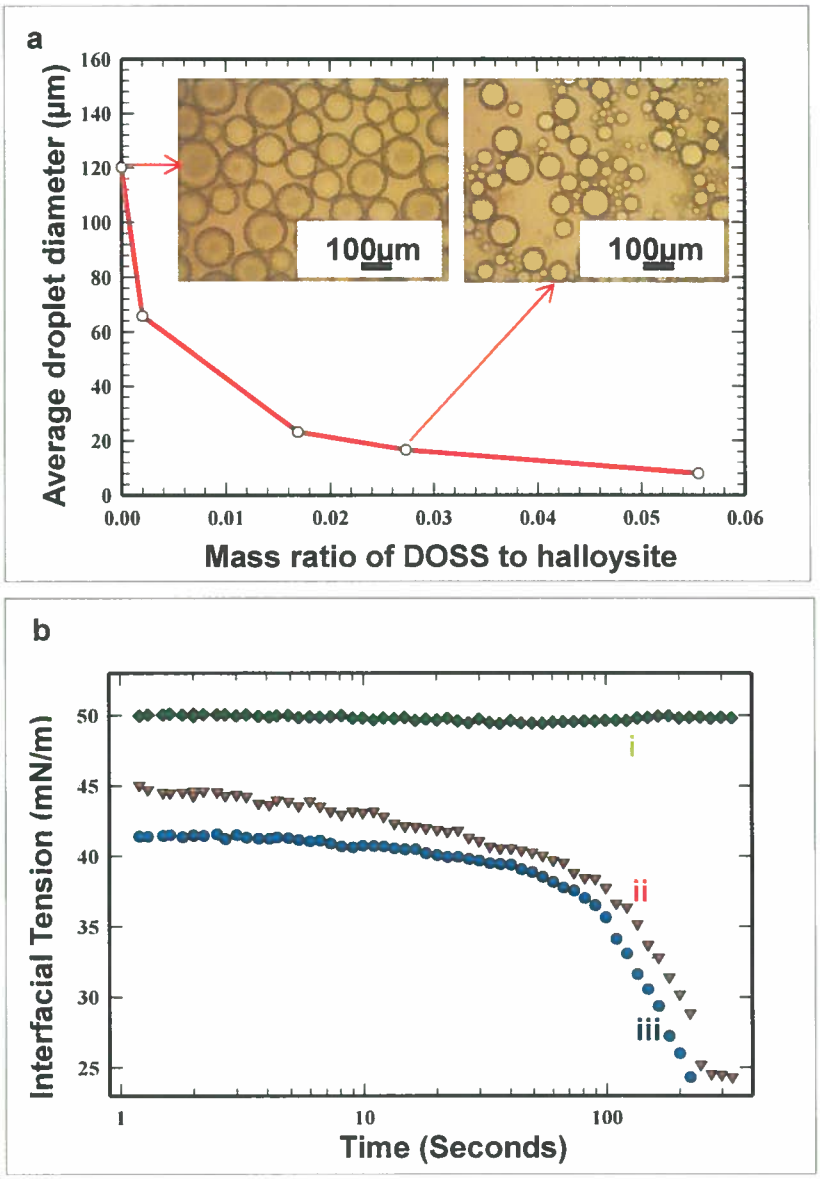

Figure 2.8: (a) Influence of surfactant loading and release from HNT on the average droplet size of dodecane in water emulsions. Emulsions were prepared at dodecane to water ratio of 1:3 and at constant HNT concentration of 0.2wt% in water. Inset shows optical microscopy image of dodecane-in-water emulsion stabilized by HNT alone and DOSS-loaded HNT at 2.83wt% DOSS loading. (b) Dynamic interfacial tension of the dodecane-saline water interface for native HNT (i), HNT loaded with 2.83wt% DOSS (ii), and HNT loaded with 5.55wt% DOSS (iii).

Figure 2.9 shows cryo-SEM images of an oil-in-water emulsion prepared with DOSS-loaded HNT as the emulsifier. The low resolution cryo-SEM images show that droplets sizes are significantly smaller for the emulsion stabilized by HNT and DOSS (Figure 2.9a-b) compared to the emulsion stabilized by 0.1wt% HNT alone (Figure 2.3a). The adsorption of DOSS molecules and HNTs at the dodecane-water interface (Figure 2.9c-d) synergistically reduces the net interfacial energy and stabilizes the emulsion.

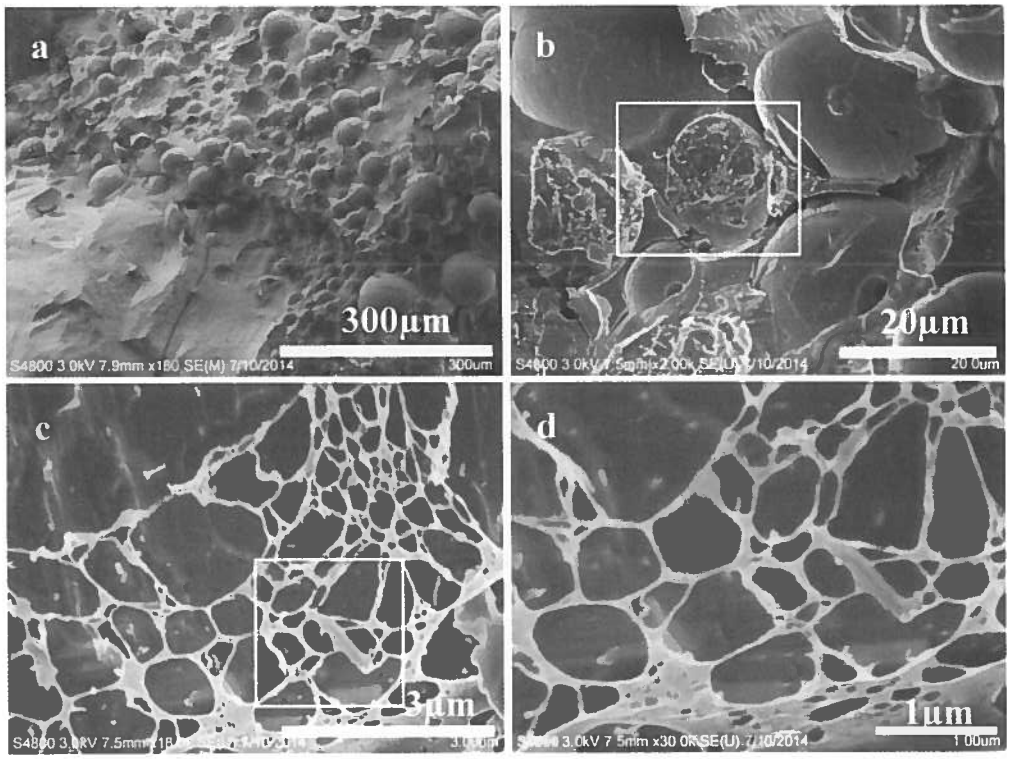

Figure 2.9: Cryo-SEM images of dodecane-in-water emulsion stabilized by DOSS-loaded HNT at 12.4wt% DOSS loading. Emulsions were prepared at dodecane to water ratio of 1:3 and 0.1wt% HNT concentration. DOSS molecules and HNT synergistically adsorb at the interface to stabilize the emulsion.

The ability of dispersants to significantly lower the crude-oil water interfacial tension is an important criterion in effectively dispersing spill oils. Synergism in mixtures of surfactants can reduce the interfacial tension to levels appropriate for the dispersion of spills oils.[43, 75] When surfactants act in synergy the interfacial tension can be reduced beyond the level obtainable with the individual surfactants. Blends of surfactants such as DOSS, Tween 80 and Span 80 are commonly used in dispersant formulation.[17, 43]

Recently, Reihm and McCormick have expanded on earlier work by Brochu, and correlated the effectiveness of dispersants containing DOSS, Tween 80 and Span 80 to the initial and dynamic oil-water interfacial tension.[72, 75] These authors found that DOSS helps stabilize the interface formed during the breakup of dispersant treated oil, while Tween 80 and Span allow formation and retention of low interfacial tensions. [72, 75]

To test the combined effects of the three surfactants used in the formulation of COREXIT 9500, HNTs were loaded with one or more combinations of DOSS, Tween 80 and Span 80. Figure 2.10 shows the crude-oil saline water interfacial tension values obtained at various dispersant-to-oil mass ratios (DORs). The dispersants were HNT loaded with DOSS; HNT loaded with a binary mixture of DOSS and Tween 80 (ratio of 80:20) and HNT loaded with a ternary mixture of DOSS, Tween 80 and Span 80 (ratio of 48:32:20). In all experiments, methanol was used as the solvent for the surfactants to infiltrate the halloysite lumen. The surfactant compositions were chosen to span the three levels of interfacial tension reduction effectiveness for blends of DOSS, Tween 80 and Span 80.[72, 75] The release of surfactant cargo from halloysite nanotubes lowers the crude oil-saline water interfacial tension to levels appropriate for the dispersion of spill oils.[17, 43, 72] The inset to Figure 2.10 is an optical micrograph of crude oil-in-saline water

emulsion stabilized by HNT loaded with a ternary mixture of DOSS, Tween 80 and Span 80 at dispersant to oil ratio of 1:10.

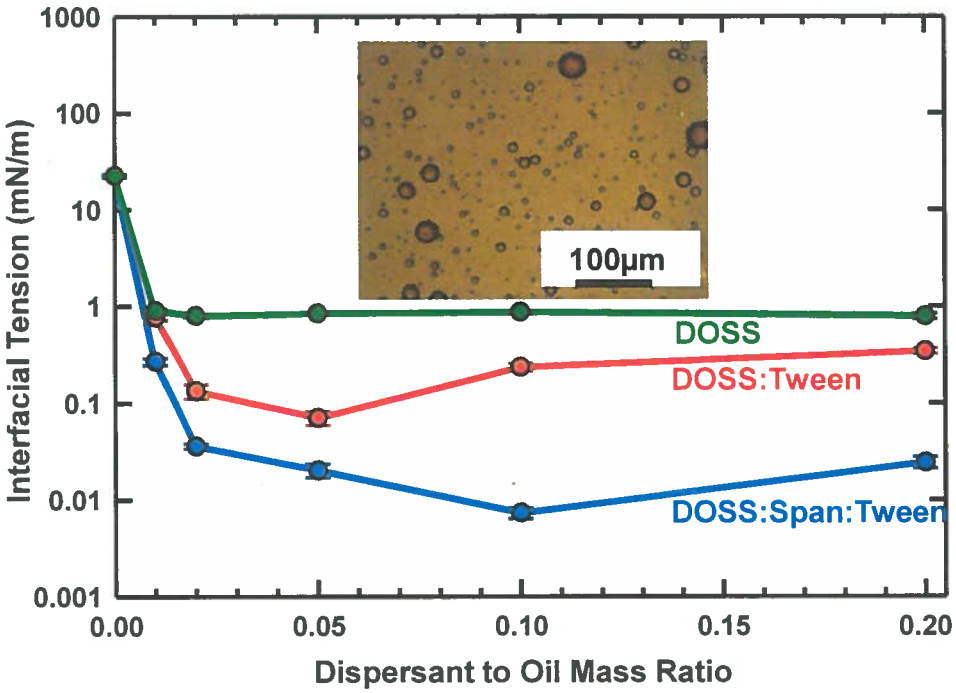

Figure 2.10: Crude oil-saline water interfacial tension measurements by the pendant drop and spinning drop method. HNT was loaded with DOSS, a binary mixture of DOSS and Tween 80(ratio of 80:20) and a ternary mixture of DOSS, Tween 80 and Span 80 (ratio of 48:32:20). The surfactant loadings in HNT from TGA analysis were 12.4wt%, 11.0wt% and 11.9wt% respectively. The inset shows optical micrograph of crude oil in saline water emulsion prepared with HNT loaded with a ternary mixture of DOSS, Span 80 and Tween 80 at dispersant to oil ratio of 0.10 (blue curve). Surfactant release from halloysite nanotubes lowers the crude oil-water interfacial tension to levels appropriate for the dispersion of spill oils into small droplets that can be suspended in the water column.

It is noteworthy that the crude oil-saline water interfacial tension is significantly reduced with the dry surfactant-loaded HNTs dispersants without the use of any hydrocarbon solvents. The low cost, ready availability, biocompatibility, very low cytotoxicity and interfacial activity of halloysite nanotubes makes this concept very promising for oil spill remediation applications. It is important to recognize however, that the halloysite particulate system must be delivered to the oil phase so that they migrate to the oil-water interface and become attached to the interface upon natural agitation (wave energy for surface spills or turbulence in deep sea oil release).

2.4 Conclusions

The release of surfactants from interfacially-active hollow particles is proposed as a new technology for the treatment of oil spills. The key concepts are based on principles of emulsification using naturally occurring halloysite clay nanotubes and the delivery of surfactants from the halloysite nanotubes to the oil-water interface. This concept eliminates the use of organic solvents in existing dispersants. The adsorption of the halloysite nanotubes (HNT) provides a steric barrier to drop coalescence and the release of surfactant molecules lowers the oil-water interfacial tension. It is also found that the nanotubes adopt a side-on orientation and form networks on the interface through end-to-end linkages. The synergistic stabilization of emulsions by halloysite and surfactants generates oil droplets that are smaller than with halloysite alone as a particulate emulsifier. Interfacial tension measurements show that the application of the surfactant loaded-HNT dispersant lowers the crude oil-water interfacial tension to levels appropriate for oil spill dispersion. In practical applications, the dispersion of spill oils into small

droplets will expose a large oil-seawater interfacial area for the ultimate bioremediation of oil spills by indigenous bacteria in the sea.

We note that the halloysite stabilized emulsions have the potential for several other applications relevant to oil spill remediation, based on the fact that these materials become stabilized at the oil water interface. In addition to the encapsulation of surfactants, the nanotubes can be fabricated to contain hydrophobic fluorescent markers that will partition into the oil phase to help identify oil spills in nighttime conditions. The nanotubes can be made to contain magnetic markers to mobilize oil spills. These are aspects of our continuing research. The availability of halloysite nanotubes in tonnage levels from natural deposits [54] additionally enables translation to large scale industrial applications feasible.

CHAPTER 3

INTERFACIAL ADSORPTION AND SURFACTANT RELEASE CHARACTERISTICS OF MAGNETICALLY FUNCTIONALIZED HALLOYSITE NANOTUBES FOR RESPONSIVE EMULSIONS

Based on: Owoseni, O.; Nyankson, E.; Zhang, Y.; Adams, D. J.; He, J.; Spinu, L.; McPherson, G. L.; Bose, A.; Gupta, R. B.; John, V. T. Interfacial adsorption and surfactant release characteristics of magnetically functionalized halloysite nanotubes for responsive emulsions J. Colloid Interface Sci. 2016, 463, 288– 298

3.1 Introduction

The adsorption of solid particles at the oil-water interface is useful in variety of applications including materials synthesis, interfacial catalysis and emulsion stabilization.[22, 37] The magnetic functionality of iron oxide nanoparticles have stimulated their application in the preparation of magnetically responsive emulsions, oil mobilization and remote detection of the oil-water interface.[47, 76, 77] In particle stabilized emulsions, the partial wetting of particles by both the oil and aqueous phases drives the partitioning of the particles to the oil-water interface.[23, 78] The underlying concept behind the stabilization of emulsions by particles is the fact that the particles are held at the oil-water interface with energies that are several orders of magnitude higher than the thermal energy thereby providing a large steric hindrance to droplet coalescence.[22, 23, 49, 79]

Free energy analysis on a particle at a planar oil-water interface gives the work required to desorb the particle from the interface into a bulk phase in terms of the free

energy change (ΔG).[22] For instance, the free energy change (ΔG) on removing a cylindrical particle from the interface into the bulk aqueous phase can be expressed as:[80]

$$\Delta G = 2rL\gamma_{ow}\left[\sin\theta - \theta\cos\theta\left(1+\frac{r}{L}\right)+\frac{r\cos^2\theta\sin\theta}{L}\right] \quad (3.1)$$

where γ_{ow} is the oil-water interfacial tension, r is the radius of the cylindrical particle, L is the particle length and θ is the contact angle.[80] Using equation 3.1, the work required to detach a 1μm long cylindrical particle with a radius of 50nm at a 30^0 contact angle and interfacial tension of 49mN/m is calculated to be 5.54×10^4kT.

Similar analysis for the detachment of a spherical particle into the aqueous phase gives:[22]

$$\Delta G = \pi r_s^2\gamma_{ow}(1-\cos\theta)^2 \quad (3.2)$$

where γ_{ow} is the oil-water interfacial tension, r_s is the radius of the spherical particle, and θ is the contact angle.[22] From equation 3.2, the work required to detach a spherical particle of the same volume as the cylindrical particle above (r_s=123.3nm) at a 30^0 contact angle and interfacial tension of 49mN/m is calculated to be 1.12×10^4kT.

The high energy of attachment at the oil-water interface makes particulate emulsifiers effective in preventing droplet coalescence. However, the adsorption of the particles at the interface does not reduce interfacial tensions sufficiently for optimal emulsification.[45, 81] The lowering of the oil-water interfacial tension can be achieved by the combination of particle and surfactant emulsifiers.[35, 48, 82] Pichot et. al. investigated the synergistic mechanisms of emulsion stabilization by hydrophilic silica particles added to the aqueous phase and monoolein surfactant added to the oil phase.[83] The monoolein surfactant was reported to play key roles of lowering the interfacial tension, inducing droplet break-up during emulsification and delaying droplet coalescence until the silica particles assemble at the oil/water interface.[83]

The methods employed in treating oil spills include physical containment with booms, mechanical recovery with skimmers, chemical herding, in-situ burning, dispersion and biodegradation.[6] In calm ocean conditions and in arctic conditions in the presence of ice floes, chemical herding can be used to thicken oil slicks to for easy recovery or in-situ burning without the need for mechanical containment.[8] In the dispersion of oil spills into the water column, surfactant solutions are typically applied to lower the oil-water interfacial tension and break up oil spills into droplets with minimal wave energy, thereby providing a large oil-water interfacial area for biodegradation. [9,5] The energy required to create droplets and thereby increase interfacial area can be expressed as:

$$\Delta G = \gamma_{ow} * \Delta A \qquad (3.3)$$

the product of the oil-water interfacial tension (γ_{ow}) and interfacial area (ΔA).[22] Dispersant formulations contain a significant amount of solvents such as propylene glycol and there is considerable interest in reducing solvent levels and effectively delivering surfactant components.[84]

We recently exploited the unique nanotubular morphology of halloysite nanotubes (HNT) for the loading and release of surfactant from the pore volume of the tubes, lowering the crude oil-saline water interfacial tension to values of 10^{-2} mN/m.[80] The nanotubes attach to the oil-water interface, thereby allowing a release of surfactant to the oil–water interface and dispersion of oil into small droplets. Here, we functionalize the HNT surface with superparamagnetic iron oxide nanoparticles for the preparation of magnetically responsive oil-in-water emulsions. We characterize the release of surfactant from the magnetically-functionalized halloysite nanotubes (M-HNT), synergistic particle-

surfactant stabilization of emulsions over extended time periods and the structure of the oil-water interface. The integration of superparamagnetic nanoparticles within the hollow scroll-like nanostructure of halloysite (HNT) and the interfacial activity of the resulting magnetic nanotubes may find potential applications in oil spill dispersion, interfacial release of spill treating agents, magnetic mobilization and as magnetic contrast agents for enhanced oil spill detection.[85, 86]

3.2 Experimental Procedures

3.2.1 Materials

Iron (III) chloride hexahydrate ($FeCl_3.6H_2O$), dioctyl sulfosuccinate sodium salt (DOSS, 98%), polyoxyethylene (20) sorbitan monooleate (Tween 80), sorbitan monooleate (Span 80), methanol and dodecane were purchased from Sigma-Aldrich. Iron (II) sulfate heptahydrate ($FeSO_4.7H_2O$, ≥99.0 %), sodium chloride (NaCl, certified ACS grade) and ammonium hydroxide solution (ACS reagent, 28.0-30.0% NH_3 basis) were obtained from Fisher Scientific. Halloysite nanotubes (HNT) were obtained from NaturalNano. Inc. (Rochester, NY, USA). The characteristic dimensions of the HNT range from about 0.33 - 1.5 μm in length, 90 -250 nm in external diameter and 10 – 70 nm in lumen. All materials were used as received. Deionized (DI) water, produced from an Elga water purification system (Medica DV25), with resistivity of 18.2 MΩ cm was used in all experiments. 0.6M sodium chloride solution in deionized water was used as a substitute for seawater.

3.2.2 Synthesis of Halloysite-Supported Iron Oxide Nanoparticles (M-HNT)

HNT supported magnetite nanoparticles were prepared by a modification of a previously reported co-precipitation method.[87] In a typical synthesis, 0.50g of HNTs was dispersed in 200ml of deionized water in a 250ml Buchner Flask by stirring. The HNT

suspension was purged with N_2 under vacuum conditions for 20 minutes, to remove dissolved oxygen. 0.332g of $FeSO_4 \cdot 7H_2O$ and 0.645g of $FeCl_3 \cdot 6H_2O$ were then added to the flask to give a molar ratio of Fe^{2+} to Fe^{3+} of 1:2. The mixture was further purged with N_2 under vacuum conditions for 20 minutes. The temperature of the mixture was then raised to 80 °C. This was followed by the slow addition of 0.5M NH_4OH to the mixture using a syringe pump operating at 0.1ml/min. The final molar ratio of OH^- to iron (Fe^{2+} and Fe^{3+}) was 16:1. The mixture was then aged at 80^0C under N_2 bubbling, vigorous stirring and vacuum conditions for 4 hours. The particles were recovered by magnetic decantation and then washed 4 times with deionized water. After the final washing step, the particles were dried in a vacuum oven at 80°C for 12 hours.

3.2.3 Particle Characterization

The morphology of the particles was characterized by transmission electron microscopy (TEM) imaging using a FEI Tecnai G2 F30 Twin Transmission Electron Microscope operated at 300 kV, and X-ray diffraction (XRD) on a Siemens D500 diffractometer using Cu KR radiation at 1.54 Å. The magnetic properties of the particles were measured using a vibrating sample magnetometer (VSM).

3.2.4 Loading of M-HNT with Surfactant

The M-HNT was loaded with surfactant following a previously reported procedure.[80] In a typical loading experiment, the M-HNT was weighed into a round bottom flask. A known amount of surfactant dissolved in methanol was then added to the flask. The halloysite nanotubes were then dispersed by stirring, followed by ultrasonication for 1 minute (Cole-Parmer 8890). Vacuum suction was applied to the contents of the flask and the pressure was then cycled back to atmospheric pressure,

typically after 15minutes. This cycling process was repeated two times and then the remaining methanol was allowed to evaporate under vacuum in a rotary evaporator to allow the loaded surfactant to crystallize inside the halloysite nanotubes.[62] The surfactant loading is simply expressed as the mass ratio of surfactant to M-HNT added into the methanol expressed as a percentage. The surfactant-loaded M-HNT was characterized by transmission electron microscopy (TEM) imaging on a FEI Tecnai G2 F30 Twin Transmission Electron Microscope operated at 300 kV. Surfactant loadings were determined by thermogravimetric analysis (TGA) using a TA Instruments SDT 2960 Simultaneous DTA-TGA. The analysis was performed in an air environment at a heating rate of 10°C/min.

3.2.5 Emulsion Preparation

A 1wt% stock suspension of M-HNT was prepared by stirring the M-HNT in water until a uniform dispersion was obtained. Various concentrations of M-HNT in water were prepared by diluting appropriate quantities of the uniformly dispersed 1wt% M-HNT stock suspension in water. Emulsions prepared with surfactant-loaded M-HNT were prepared by directly weighing the particles into a glass vial and adding the appropriate volume of the aqueous phase. Dodecane was then added to the nanotube dispersion at a dodecane to water ratio of 1:3. Emulsions were prepared by mixing the aqueous dispersion of particles with the dodecane for 2 min using a Thermolyne Maxi Mix II vortex mixer operating at 3000rpm. For the centrifugation stability studies, emulsions were carefully transferred into 15mL polypropylene centrifuge tubes and centrifuged at 1000rpm for 5minutes. The magnetic responsiveness of the emulsions was

demonstrated by applying a magnetic field of a 7mT magnet to an aliquot (about 200μL) of the M-HNT stabilized emulsion on a glass slide.

3.2.6 Emulsion Characterization

Emulsions were characterized by Optical Microscopy and Cryogenic Scanning Electron Microscopy (Cryo-SEM) techniques. A small aliquot of the emulsions were placed on a glass slide and imaged on a Leica DMI REZ optical microscope. The images were analyzed using Image ProPlus v. 5.0 software. Cryo-SEM imaging was performed using a Hitachi S-4800 field emission Scanning Electron Microscope operated at a voltage of 3 kV and a working distance of 8 mm. The emulsion sample was first plunged into liquid nitrogen, followed by fracturing at −130 °C using a flat-edge cold knife and sublimation of the solvent at −95 °C for 5 min. The sample was sputtered with a gold–palladium composite at 10 mA for 88 s before imaging.

3.2.7 Surfactant Release and Interfacial Tension Measurements

Interfacial tension measurements were made on a standard goniometer (Ramé-Hart, model 250). 5mg of DOSS-loaded HNT was weighed into 4ml of dodecane in a glass cell. The DOSS loading in M-HNT was 4.05% from TGA analysis. A pendant drop of water of about 10μL was then quickly injected from a syringe. The dynamic interfacial tensions were measured by drop shape analysis using the DROPimage Advanced Software. For the release of Tween 80 from M-HNT, 5mg of Tween 80-loaded M-HNT was weighed into 4ml of saline water. The Tween-80 loading in M-HNT was 3.96% from TGA analysis. An inverted pendant drop of dodecane was quickly injected through the water phase for interfacial tension measurements.

3.3 Results and Discussion

3.3.1 Particle Characteristics

Figure 3.1(a, b) shows representative SEM images of the native HNT. SEM images of the M-HNT indicate that iron oxide nanoparticles are supported on the HNT (Figure 3.1c, d). The iron oxide nanoparticles are about 10nm in size. Nanoclusters consisting of magnetite nanoparticle as subunits are also observed on the HNT. Figure 3.1(e-f) shows TEM images of the M-HNT sample. TEM imaging reveals that the magnetite nanoparticles are supported both on the external and inner lumen surfaces of the HNT. A plausible route for the incorporation of the iron oxide nanoparticles in the HNT lumen is the infiltration of iron precursors into the HNT lumen by capillary action resulting in the precipitation of iron oxide nanoparticles inside the lumen on addition of NH_4OH.[51] The capillary pressure driving the infiltration of water into the HNT lumen is about 200atm.[51] Energy-dispersive X-ray spectroscopy (EDS) analysis confirms the presence of Fe atoms from the nanoparticles supported on the aluminosilicate HNT (Figure 3.1g). A key observation from the TEM imaging (Figure 3.1f) is that there is available lumen volume in the M-HNT for the loading of materials such as surfactant.

Figure 3.2a shows XRD patterns of native HNT and the M-HNT. Using Bragg's law, the sharp diffraction peak at 2θ angle of 12.0^0 corresponds to a 001 basal spacing of 7.37Å which is indicates a dehydrated form of the HNT.[88] The key observation is that the XRD curve for M-HNT shows characteristic peaks of HNT in addition to peaks from the magnetite.[87, 89] Figure 3.2b shows the magnetization curve for M-HNT obtained using a VSM at room temperature in an applied magnetic field sweeping from -20 to 20 kOe. The magnetization curve shows no remanence indicating the superparamagnetic properties of

the material. The superparamagnetism results from the effective stabilization of the magnetite nanoparticles on the HNT. Competition between the magnetocrystalline anisotropy and thermal energies in the nanoparticles leads to a transition from the ferromagnetic property of the bulk iron oxide to the observed superparamagnetic property of the small magnetic nanoparticles.[90] The photograph to the right of the magnetization curve (Figure 3.2b) shows the magnetic responsiveness of the M-NHT powder the externally applied field of a 7mT bar magnet.

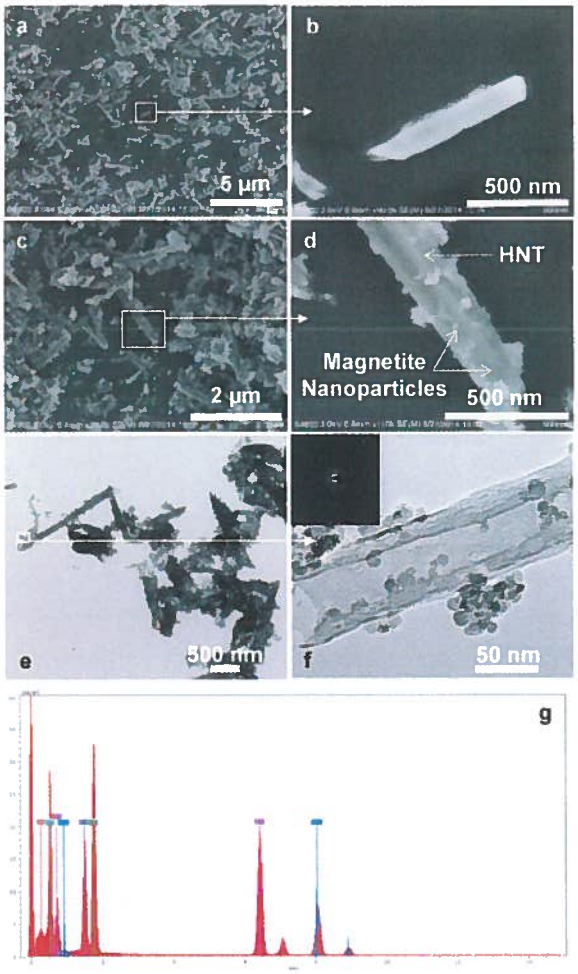

Figure 3.1: SEM images of native HNT (a,b) and M-HNT(c,d) showing magnetite nanoparticles supported on HNTs. Panels e and f shows TEM images of M-HNT. Inset to Figure 3.1f is the electron diffraction pattern of the crystalline iron oxide nanoparticles. Panel g is the EDS spectrum of the M-HNT.

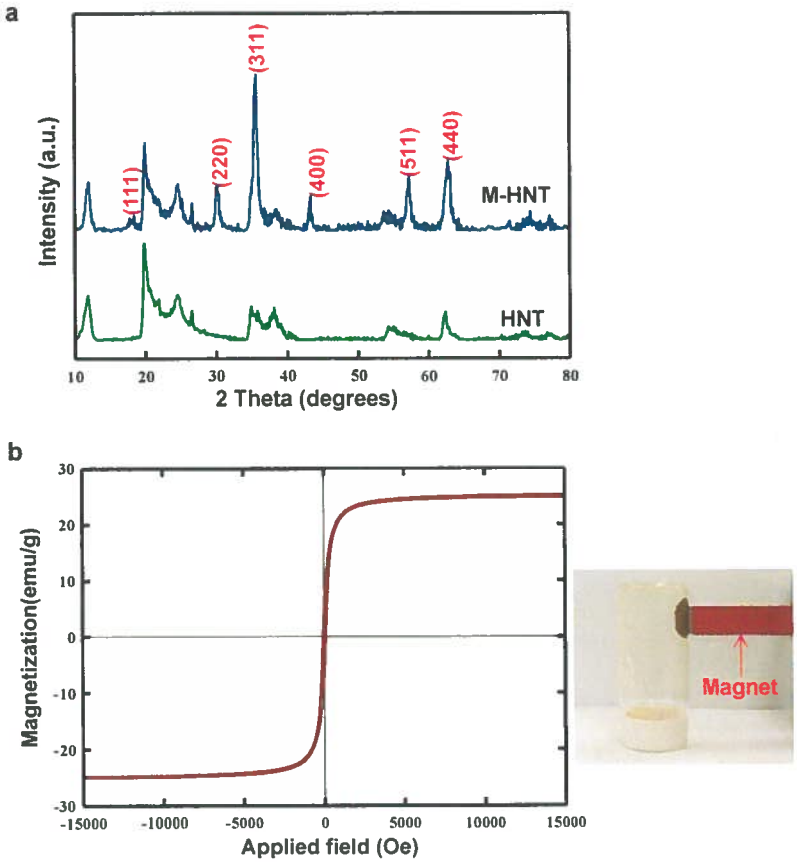

Figure 3.2: (a) XRD patterns of HNT and M-HNT. XRD curve for M-HNT shows characteristic peaks of HNT in addition to peaks from the magnetite. The peaks indexed to magnetite are shown in red Miller indices in Figure 3.2a. (b) Magnetization curve of M-HNT. The magnetization curve shows the superparamagnetic property of M-HNT. The photograph to the right shows the magnetic responsiveness of the M-NHT powder.

3.3.2 Stability and Interfacial Structure of M-HNT stabilized Emulsions

Figure 3.3 shows the stability in a centrifugal field, optical microscopy images and magnetic mobilization of dodecane-in-water emulsions stabilized by the M-HNT. Stability of the emulsions was characterized under forced coalescence in a centrifugal field. In a centrifugal field, the critical de-emulsification pressure (P_c) required to break

the film of the continuous phase between two approaching solid-stabilized droplets provides a quantitative basis for comparing the stability of solid-stabilized emulsions.[45, 91]

The critical de-emulsification pressure (P_c) is expressed as:[45, 91]

$$P_c = \Delta\rho g_k(V_{oil} - V_{rel})/A \qquad (3.4)$$

where $\Delta\rho$ is density difference between the aqueous and oil phases, g_k is the centrifugal acceleration, V_{oil} is the volume of oil used in preparing the emulsion, V_{rel} is volume of oil released on centrifugation, and A is the cross-sectional area of the centrifuge tube.[45]

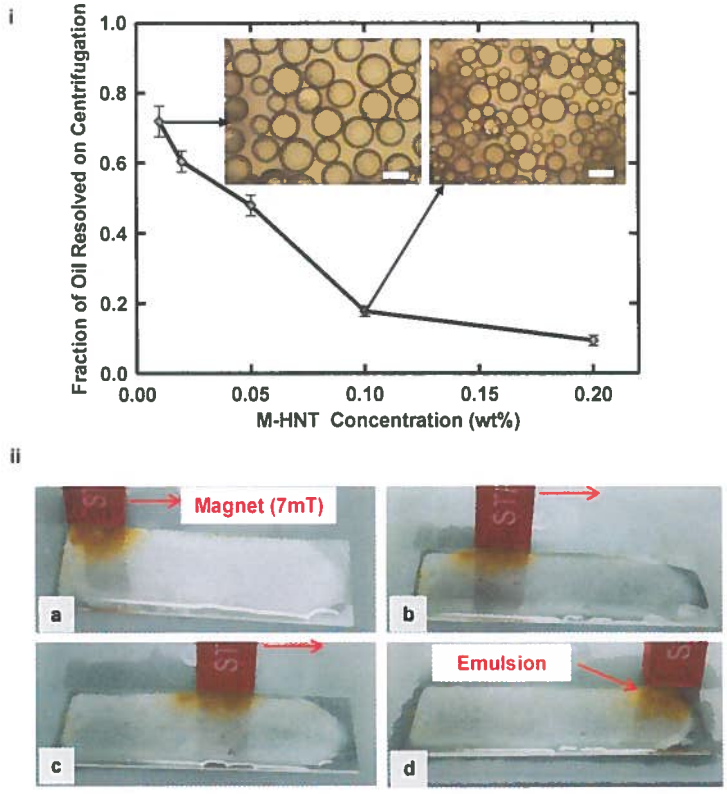

Figure 3.3: (i) Fraction of oil resolved on centrifugation for dodecane-in-water emulsions stabilized by various concentrations of M-HNT. Inset shows optical microcopy images of emulsions stabilized by 0.01wt% and 0.1wt% M-HNT (scale bars = 100μm). (ii) Magnetic mobilization of M-HNT stabilized oil-in-water emulsion from left to right (a-d). Attachment of M-HNT at the oil-water interface stabilizes the emulsion and imparts magnetic responsiveness to an externally applied filed of a 7mT magnet.

In all experiments, the centrifugal acceleration, cross-sectional area of the centrifuge tube as well as volumes of the oil and water phases were kept constant at the various M-HNT concentrations. The ratio of P_c for emulsions prepared at two conditions of different particle concentrations (1) and (2) can then be expressed as:

$$\frac{P_c^1}{P_c^2} = \frac{1 - \varphi_{rel}^1}{1 - \varphi_{rel}^2} \qquad (3.5)$$

where P_c^1 is the critical de-emulsification pressure at condition 1, P_c^2 is the critical de-emulsification pressure at condition 2, φ^1_{rel} is the fraction of oil released on centrifugation at condition 1 (0.17 at 0.1wt% M-HNT from Figure 3.3, Panel i) and φ^2_{rel} is the fraction of oil released on centrifugation at condition 2 (0.72 at 0.01wt% M-HNT from Figure 3.3). Using equation 3.5, the increase of M-HNT concentration from 0.01wt% to 0.1wt% triples the pressure required to rupture the film between two approaching oil droplets under forced coalescence in a centrifugal field. The attachment of M-HNT at the oil-water interface provides the steric barrier to droplet coalescence and stabilizes the emulsion.[22] The particles impart magnetic responsiveness to the stabilized oil droplets (Figure 3.3, Panel ii). The emulsion is mobilized by the application of an external magnetic field of a 7mT magnet.

Cryo-SEM imaging reveals the interfacial structure of the M-HNT-stabilized emulsion (Figure 3.4a-d). Cryo-SEM images of the emulsion shows that the M-HNT particles are attached to the oil-water interface in a side-on orientation and are networked together into aggregates at the oil-water interface (Figure 3.4c). This is in agreement with the orientation of nanocylindrical HNT at the oil oil-water interface.[80] Figure 3.4d is a high resolution image of magnetic nanotubes lying in a side-on orientation at the

interface. The HNT simultaneously acts as a support for the superparamagnetic iron oxide nanoparticles and imparts interfacial-activity to the M-HNT.

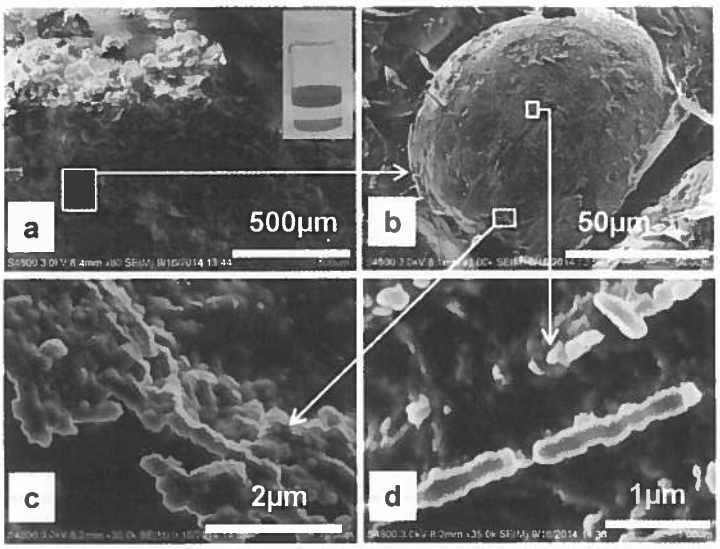

Figure 3.4: Cryo-SEM imaging of the interfacial structure of dodecane-in-water emulsion stabilized by magnetically functionalized halloysite clay nanotubes

3.3.3 Surfactant Release and Synergistic Emulsion Stabilization

Figure 3.5a is a representative SEM (a) image of Tween 80-loaded M-HNT at 11.31wt% Tween loading. Surfactant loading into the M-HNT lumen results in a higher electron density from the TEM imaging (Figure 3.5b).[80]

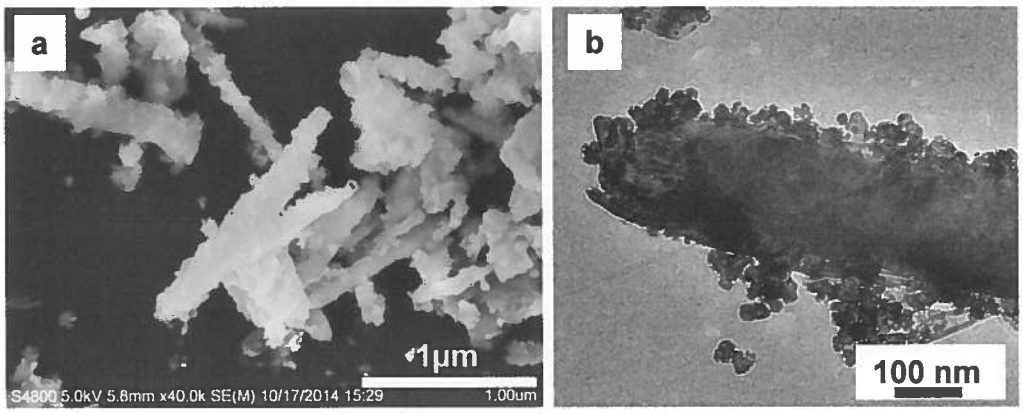

Figure 3.5: (a) SEM image of M-HNT loaded with Tween 80. Tween 80 loading is 11.31% from TGA. (b) TEM image of a surfactant-loaded M-HNT.

Figure 3.6 shows representative TGA curves for M-HNT and surfactant-loaded M-HNT. The mass loss for the M-HNT is due to the loss of water molecules adsorbed on the external surface and the dehydroxilation of the nanotubes centered at 50^0C and 519^0C respectively.[80] The higher mass loss for the surfactant-loaded M-HNT is due to the thermal decomposition of the surfactant in addition to the loss of water and dehydroxilation of the M-HNT.[80]

Figure 3.6b presents the differential thermal analysis (DTA) curves for M-HNT loaded with increasing amounts of DOSS. At lower surfactant loadings (curves i and ii), the mass loss due to surfactant decomposition is sharply centered around 280^0C. At a higher surfactant loading of 9.63%, the surfactant decomposition peak is a broader compared to the peak at lower surfactant loadings. A rough calculation based on filling the lumen exclusively with DOSS indicates a maximum loading of about 6.25wt% for a nanotube having a 30nm lumen diameter, a 90 nm external diameter and a length of 1 micron. At low surfactant loading, the surfactant is predominantly loaded into the M-HNT lumen, enhancing the thermal stability of the surfactant. Once the lumen is filled, the remaining surfactant adsorbs on the external surface of the M-HNT. As the surfactant loading increases, the amount of surfactant adsorbed on the external surface of the M-HNT increases resulting in the broader surfactant decomposition peak.

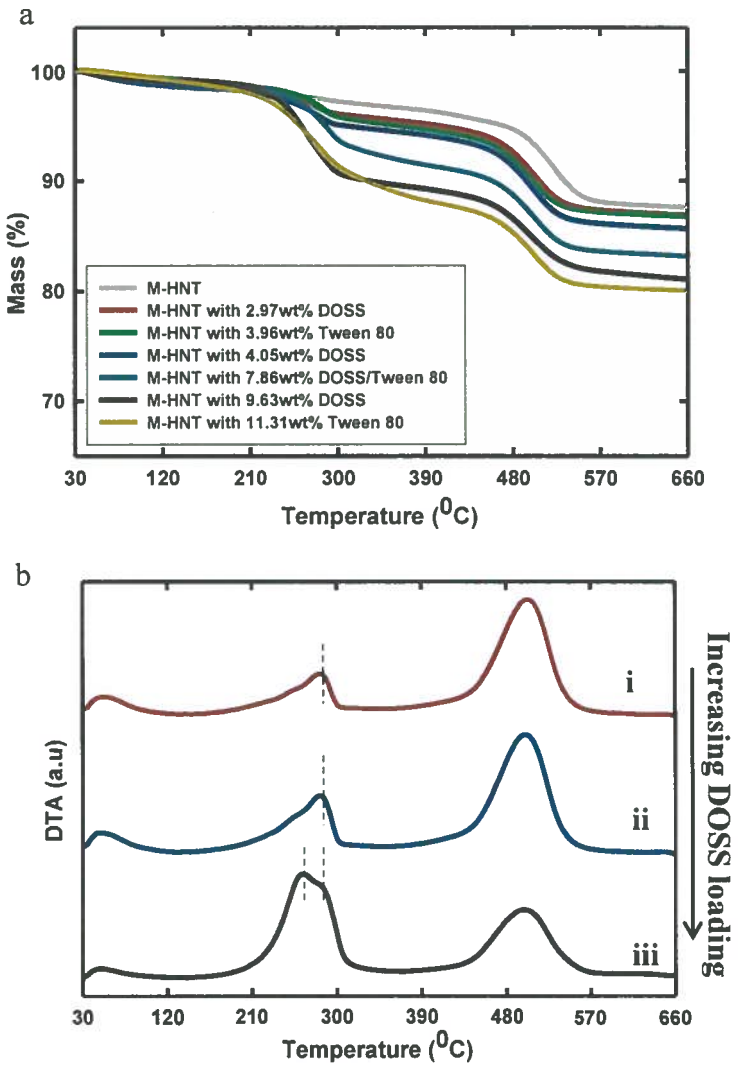

Figure 3.6. (a) Thermogravimetric curves of M-HNT with various surfactant loadings. (b) Differential thermal analysis (DTA) curves for M-HNT loaded with increasing amounts of DOSS. The DOSS loadings are 2.97wt% (i), 4.05wt% (ii) and 9.63wt% (iii).

Figure 3.7 shows optical micrographs of emulsions stabilized by M-HNT and surfactant-loaded M-HNT. The release of surfactants from the M-HNT leads to significant reduction in droplets sizes compared to emulsions stabilized by M-HNT alone. Figure 3.7 (b-d) shows optical micrographs of emulsions stabilized by DOSS-loaded M-HNT with increasing DOSS loadings while Figure 3.7e is a representative optical micrograph of emulsion prepared with Tween 80 loaded-M-HNT.

Surfactant release and adsorption at the oil-water interface lowers the interfacial tension leading to a reduction in emulsion droplet sizes compared to the emulsion stabilized by M-HNT without surfactant loading for the same energy input to the system. The interaction of ionic surfactants with oppositely charged particles is typically employed in the synergistic particle-surfactant stabilization of emulsions and foams. An interesting aspect of the tubular halloysite is the negatively charged outer layer surface and positively charged inner lumen surface. This is attractive for the synergistic stabilization of emulsions with M-HNT and surfactants, including ionic and non-ionic surfactants as well as surfactant blends used in dispersant formulation. Figure 3.7f show optical micrographs of dodecane-in-water emulsions stabilized by 0.1wt% M-HNT loaded with a blend of the anionic surfactant, DOSS, and the non-ionic surfactant, Tween 80, at DOSS to Tween 80 ratio of 60:40. The synergistic delivery of the surfactants, DOSS and Tween 80 from M-HNT in Figure 3.7f facilitates oil emulsification into very small droplets.

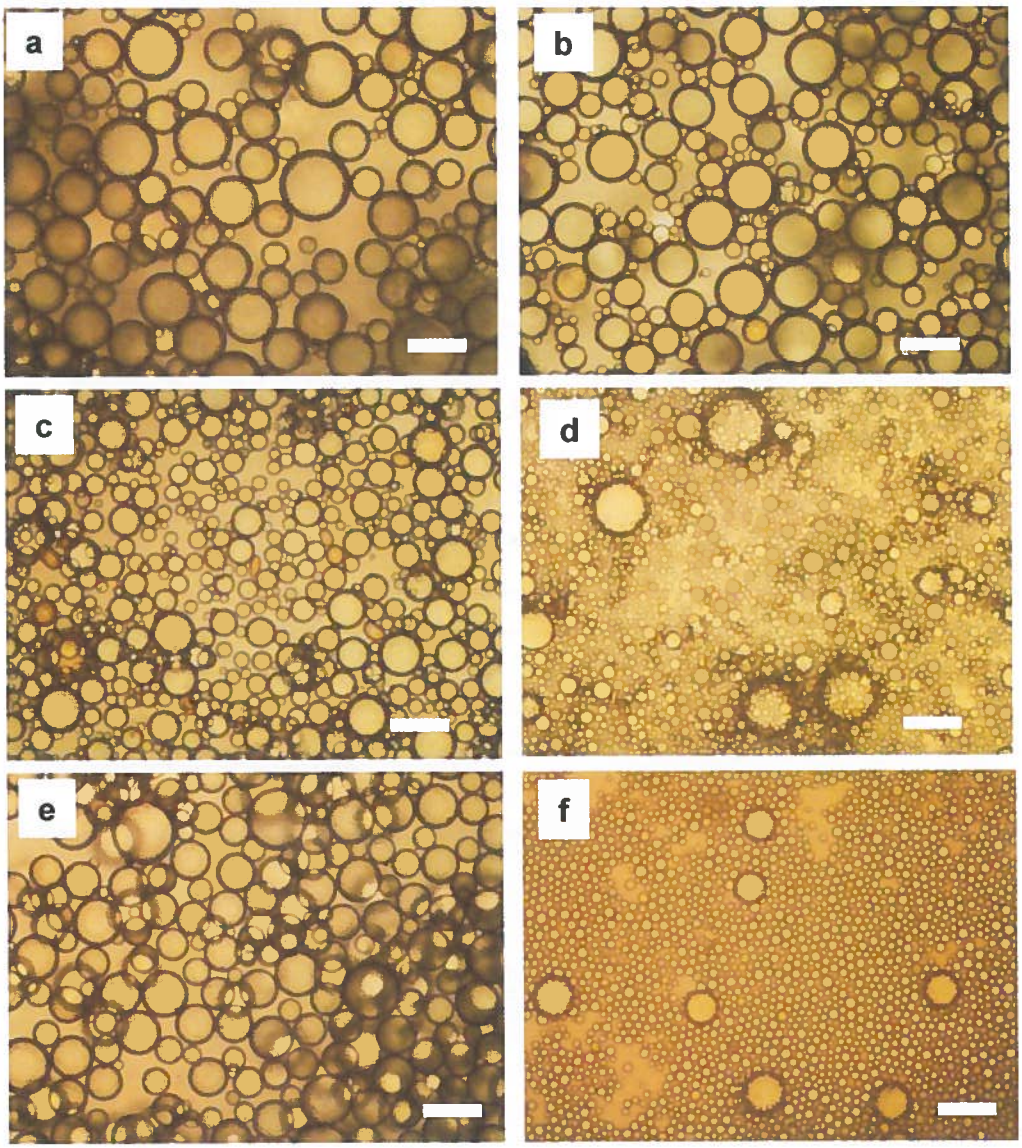

Figure 3.7: Optical Microscopy of emulsions stabilized by 0.1wt% M-HNT and 0.1wt% M-HNT with various surfactant loadings. Surfactant loading in M-HNT were 0 wt % (a) 1.50 wt% DOSS (b), 4.05 wt% DOSS (c), 9.63 wt% DOSS (d), 3.96 wt% Tween 80 (e) and 7.86wt% DOSS-Tween 80 blend (f) respectively. DOSS to Tween 80 ratio in the blend was 60:40. Scale bars = 100μm.

Figure 3.8(a-d) shows representative cryo-SEM images of an oil-in-water emulsion prepared with DOSS-loaded M-HNT as the emulsifier. The emulsion system is stabilized by the adsorption of DOSS and M-HNT at the oil water interface. The M-HNT are attached to the oil-water interface in a side-on orientation (Figure 3.8c). The high resolution Cryo-SEM image in Figure 3.8d shows the magnetite nanoparticle and native HNT components in the interfacially-active M-HNT. Figure 3.8e shows the reduction in the dodecane-saline water interfacial tension (IFT) on release of DOSS and Tween 80 from M-HNT. The IFT curves suggest an initial burst release of surfactant resulting in a sharp reduction in the interfacial tension. The initial burst release region is directly followed by a less rapid reduction in IFT suggesting a more gradual release of the surfactant. Over time, the IFT curves exhibit the characteristic rapid fall and meso-equilibrium regions of dynamic surface tension reduction by surfactant.[92] The reduction in interfacial tension lowers the energy required to create new oil-water interface leading to the formation of small droplets (Figure 3.8).[80] In practical remediation applications, the dispersion of oil into tiny droplets translates into the creation of a large oil-water interfacial area for the enhanced bioremediation of oil spills by oil-degrading microorganisms.[7, 43]

The stability of emulsions stabilized by M-HNT and DOSS-loaded M-HNT with time were characterized by analyzing a number of optical micrographs to obtain the droplet size distribution over a period of 5 weeks. Figure 3.9 shows the droplet size distributions immediately after emulsion preparation and after 5 weeks. To the best of our knowledge, these results provide the first detailed characterization of the stability over time for emulsions stabilized by the clay nanotubes alone and in combination with

surfactant. The droplet size distributions progressively decrease with increasing loading and release of DOSS from the M-HNT. The M-HNT provides steric hindrance to droplet coalescence over time while the released surfactant facilitates oil emulsification into smaller droplets.

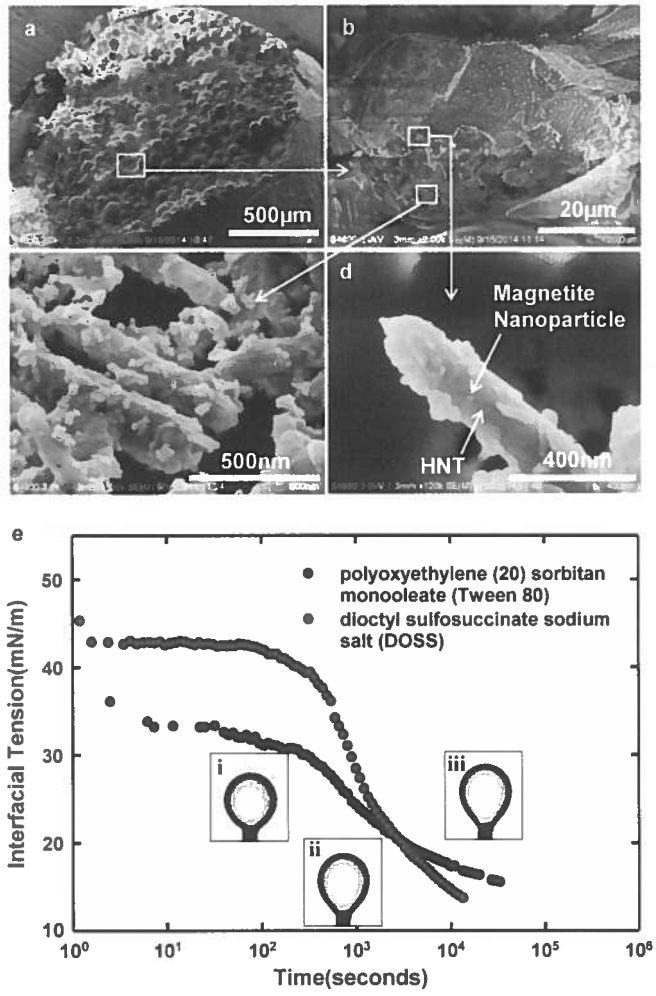

Figure 3.8: Cryo-SEM images of dodecane-in-water emulsion stabilized by DOSS-loaded M-HNT (a-d). M-HNT concentration is 0.1wt%. DOSS loading in M-HNT is 9.63%. Panels (a) to (d) are in order of increasing magnification. Panel e shows the dynamic reduction in the dodecane-saline water interfacial tension for M-HNT loaded with DOSS and Tween 80. Surfactant loadings in M-HNT were 4.05wt% DOSS and 3.96wt% Tween 80 from TGA. The inserts are snapshots of the progressively elongated inverted pendant drop of dodecane in saline water on release of Tween 80 from the Tween 80-loaded M-HNT. Images were taken at 240s (i), 5220s (ii) and 17400s (iii) respectively.

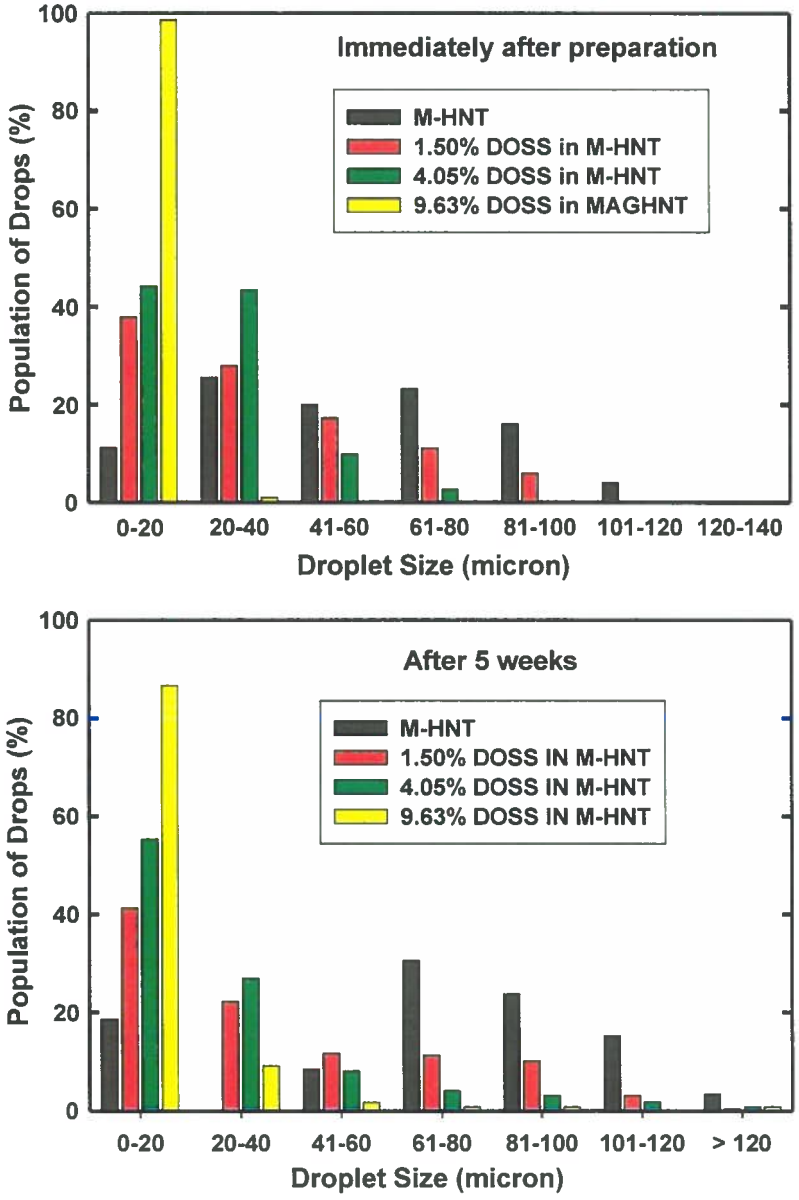

Figure 3.9: Droplet size distributions of emulsions stabilized by M-HNT and DOSS. The droplet size distribution immediately after preparation and after 5 weeks shows emulsion stability with time.

3.4 Conclusions

A magnetically responsive iron oxide nanoparticle system supported on halloysite clay nanotubes has been successfully developed for oil emulsification and magnetic mobilization of oil. Attachment of the magnetic particles at the oil-water interface makes the oil-in-water emulsions responsive to an externally applied field. The anionic surfactant, dioctyl sulfosuccinate sodium salt and the non-ionic surfactant, polyoxyethylene (20) sorbitan monooleate are effectively loaded and released to reduce the interfacial tension and thus the oil droplet size. Droplet size analysis over a period of 5 weeks reveals the high stability of emulsions stabilized by the magnetic particles and released surfactant. The attachment of the nanotubes at the oil-water interface stabilizes the oil-in-water emulsions and provides an efficient dispersant delivery method that can minimize the use of organic solvents.

The simple synthesis procedure and the synergy of biocompatible HNT and magnetite components make the M-HNT materials, an attractive multifunctional and environmentally-benign material for practical oil spill remediation applications.[50, 93, 94, 95] It is demonstrated that development of multifunctional particulate emulsifiers can effectively provide combined properties of surfactant delivery,[84] emulsion stabilization[80] and magnetic field response[76] with potential applications in oil spill detection.[85, 86] Aspects of our continuing work include exploiting the unique oppositely charged surfaces of the HNT for selective surface modification of the nanotubes for chemical herding and selective recovery of surface oil layers.

CHAPTER 4

TUNING THE WETTABILITY OF HALLOYSITE CLAY NANOTUBES BY SURFACE CARBONIZATION FOR OPTIMAL EMULSION STABILIZATION

Based on: Owoseni, O.; Zhang, Y.; Su, Y.; He, J.; McPherson, G. L.; Bose, A.; John, V. T. Tuning the Wettability of Halloysite Clay Nanotubes by Surface Carbonization for Optimal Emulsion Stabilization. Langmuir, 2015, 31 (51), 13700 - 13707

4.1 Introduction

Emulsions stabilized by fine solid particles are relevant in a wide range of processes such as in the food, pharmaceutical and petroleum industries.[22] Solid stabilized emulsions have also attracted interest in environmental remediation applications including the treatment of crude oil spills.[35, 45, 80, 96] A key characteristic of an effective emulsifier, including particles used as oil spill dispersants, is the ability to adsorb at the oil-water interface, inhibit droplet coalescence and phase separation.[17, 43, 97] The particle wettability can be quantitatively expressed in terms of the three phase contact angle which the particle makes at the oil-water interface.[23]

The attachment of particles to the oil-water interface with energies that are several orders of magnitude higher than the thermal energy provides a large steric hindrance to droplet coalescence and is one of the key underlying concepts behind particle-stabilization of emulsions.[98] Analysis on a spherical particle at a planar oil-water interface gives the work required to desorb the particle from the interface (ΔG) as:[23, 45]

$$\Delta G = \pi r_s^2 \gamma_{ow} (1 \pm cos\,\theta)^2 \qquad (4.1)$$

where γ_{ow} is the oil-water interfacial tension, r_s is the particle radius, and θ is the equilibrium contact angle measured through the water phase. The sign in the bracket

(equation 4.1) is negative for particle desorption into water ($0 \leq \theta \leq 90^0$) and positive for particle desorption into oil ($90^0 \leq \theta \leq 180^0$).[22]

Similar free energy analysis on a cylindrical particle at a planar oil-water interface gives the free energy change (ΔG_w) on removing the particle from the interface into the water as:[80, 97]

$$\Delta G_w = 2rL\gamma_{ow}\left[\sin\theta - \theta\cos\theta\left(1+\frac{r}{L}\right)+\frac{r\cos^2\theta\sin\theta}{L}\right] \quad for\ 0 \leq \theta \leq 90^0 \qquad (4.2)$$

and the free energy change to remove the particle from the interface into the oil phase as:

$$\Delta G_o = 2rL\gamma_{ow}\left[\sin\theta + (\pi-\theta)\cos\theta\left(1+\frac{r}{L}\right)+\frac{r\cos^2\theta\sin\theta}{L}\right] for\ 90^0 \leq \theta \leq 180^0 \qquad (4.3)$$

where γ_{ow} is the oil-water interfacial tension, r is the radius of the cylindrical particle, L is the particle length and θ is the contact angle.

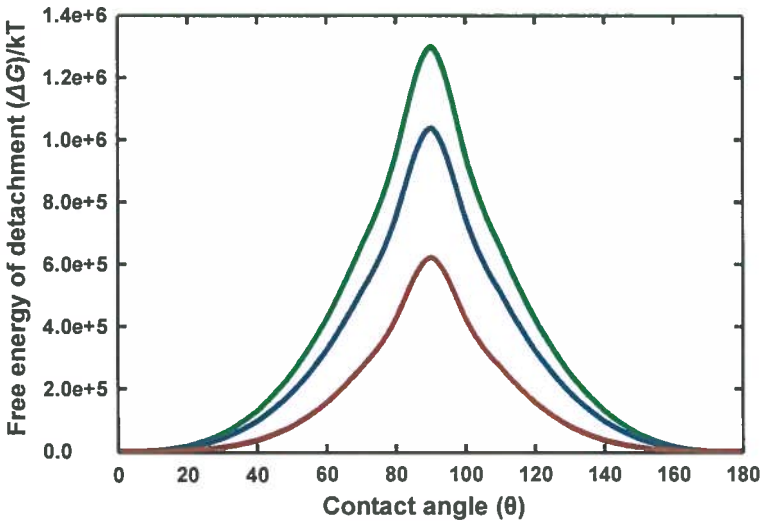

Figure 4.1: Free energy of particle detachment from the oil-water interface as a function of contact angle for a spherical particle (red curve) and cylindrical particles with aspect ratio of 5.0 and 10.0 (blue and green curves respectively). All particles have the same volume of $7.85*10^{-21}$ m^3, oil-water interfacial tension was 49mN/m and the cylinder aspect ratio is defined as the length to diameter ratio.

Figure 4.1 shows the free energy of detachment from the oil-water interface for spherical and cylindrical particles of the same volume as a function of contact angle. A first observation is that the energy of attachment of the cylindrical particle at the oil-water interface is higher than for a spherical particle of the same volume, underscoring the role of particle shape on emulsion stabilization by the particles.[22, 99] For instance at $\theta = 90^0$, the work ΔG in equations 4.1 and 4.2 reduces to the product of the interfacial tension (γ_{ow}) and the area of the oil-water interface occupied by the particle corresponding to the area of the mid-section of the particles. For a cylindrical particle with 50.0nm radius and length of 1.0μm, a spherical particle of equal volume will have a radius of 123.3nm. The area of the mid-section is calculated to be $1.0*10^{-13}m^2$ and $4.8*10^{-14}m^2$ for the cylindrical and spherical particles respectively, yielding a higher $\Delta G/kT$ value of $1.3*10^6$ for the cylindrical particle compared to $6.2*10^5$ for the spherical particle. The energy of attachment at the interface is higher for cylindrical particles with aspect ratio of 10 relative to cylindrical particles with an aspect ratio of 5.

Madivala et al. experimentally characterized the role of particle shape and aspect ratio on emulsion stabilization and viscoelastic properties of the oil-water interface.[99] The authors discovered that emulsion stability and the magnitude of the interfacial viscoelastic properties depends strongly on the aspect ratio of the particles.[99] Strong attractive capillary interactions that are induced based on particle shape also facilitate particle assembly into networks at the oil-water interface.[99]

For both cylindrical and spherical particles the work required to detach a particle from the interface into a bulk phase increases from 0^0 to 90^0, reaches a maximum at 90^0 and then decreases from 90^0 to 180^0.[22] Therefore, tuning the surface chemistry of particles

to intermediate wettability provides a means to prepare optimally stable particle-stabilized emulsions because of the improved propensity of the particles to partition the oil-water interface.[22, 23] Traditionally, hydrophilic solids can be modified by chemisorption of hydrophobic moieties such as silane coupling agents,[23, 100] carboxylic acids[101] and polymer grafts;[102, 103, 104] or physisorption of oppositely charged surfactant,[34, 105, 106] polymer[36, 107] and asphatlenes.[108, 109] Relevant to the treatment of subsea oil spills, the synergy of the hydrophobic surfactant Span 20 and hydrophilic silica particles in dispersing oil into small droplets has been demonstrated in high shear energy jet experiments.[110] The adsorption of Span 20 onto the surface of the silica particles was proposed to make the particles more hydrophobic and enhance their interfacial activity for oil emulsification.[110]

Recently we have advanced the use of naturally occurring halloysite aluminosilicate clay nanotube (HNT) for oil emulsification.[80] An interesting aspect of the HNT, is that it has a predominantly negatively charged outer silica surface and a positively charged inner alumina surface.[61, 80] The nanotubular morphology of the HNT has been exploited for the loading and delivery of surfactant to the oil-water interface. The effectiveness of particles in emulsion stabilization and interfacial delivery of materials are largely dependent on the partitioning of the HNT to the oil-water interface. Here we propose a new concept to optimize the attachment of the particles to the oil-water interface and tune the wettability of the hydrophilic native HNT by the systematic carbonization of the external surface of the particles. We exploit the selective binding of the readily available cationic biopolymer, chitosan, onto the negatively charged external surface of HNT[55] to carbonize the HNT on pyrolysis in an inert atmosphere. We

demonstrate that this is an effective route to tune the wettability of the nanotubes for optimal emulsion stabilization.

4.2 Experimental Procedures

4.2.1 Materials

Medium molecular weight chitosan (190 - 310 kDa) was obtained from Sigma-Aldrich. The reported degree of deacetylation is 75 - 85%. Dodecane and sodium hydroxide were obtained from Sigma-Aldrich. Acetic acid (glacial, ≥99.7%) was purchased from Fisher Scientific. All materials were used as received. Halloysite nanotubes (HNT) were purchased from NaturalNano Inc. (Rochester, NY, USA). Deionized (DI) water, produced from an Elga water purification system (Medica DV25) with a resistivity of 18.2 MΩ cm was used in all experiments. Acetic acid solutions were prepared by diluting the glacial acetic acid in DI water.

4.2.2 Synthesis and Characterization of Carbonized Halloysite Nanotubes (CHNT)

Stock solutions of 2wt% HNT in deionized water and 0.5wt% medium molecular weight chitosan in acetic acid were first prepared. Appropriate amounts of medium molecular weight chitosan and HNT were then pipetted from stock solutions and added to a vial. The mass ratios of chitosan to halloysite used in particle synthesis were 0.002, 0.01, 0.02, 0.025, 0.05, 0.2, 0.5 and 1. To ensure homogeneous solubilization of chitosan and protonation of the amine groups in the solvent medium, the pH was adjusted to ~ 3.7 by adding acetic acid solution. The pH was measured using a Thermo Scientific Orion 3-star benchtop pH meter. The mixture was stirred for 24hours to facilitate the adsorption of the positively charged chitosan biopolymer on the negatively charged external surface of the HNT.[53] The pH was then adjusted by the addition of 1M NaOH solution to

deionize the chitosan and form a non-dissolvable chitosan coating on the HNT.[111] The chitosan coated halloysite particles were recovered by centrifugation and washed twice with deionized water. The recovered samples were then pyrolyzed at 700 °C for 1 h under the flow of N_2 gas to convert the chitosan adsorbed on the HNT to carbon.[112] The carbonized halloysite samples are hereafter referred to as CHNT1 to CHNT8 with the numbers assigned in order of increasing level of carbonization.

The morphology of the particles was characterized by field emission scanning electron microscopy (SEM, Hitachi S-4700) and transmission electron microscopy (TEM, JEOL 2010, operated at 200 kV). Energy dispersive X-ray spectroscopy (EDS) was carried out on the Hitachi S-4700 scanning electron microscope operating at 20kV and a working distance of 15mm. The sample was placed on a Cu/Zn substrate and the EDS spectrum was acquired with the oxford INCA software. Thermogravimetric analysis (TGA) of the CHNT samples was performed in an air environment at a heating rate of 10°C/min using a TA Instruments SDT 2960 Simultaneous DTA-TGA. Similar to the CHNT synthesis procedure, the native HNT was heated at 700^0C for 2 hours in N_2 and used in the control TGA experiment.

Zeta potential of halloysite-chitosan mixtures in acetic acid solution (pH ~ 3.7) were determined by measuring the electrophoretic mobility using the Phase Analysis Light Scattering (PALS) technique (Nanobrook ZetaPALS, Brookhaven Instrument). 2 ml of the samples were transferred into a disposable polystyrene cuvette that was connected to the solvent resistant electrode and the zeta potential was measured at 25^0C. Fourier transform infrared spectroscopy (FTIR) was performed on a Thermo Nicolet Nexus 670 FT-IR Spectrometer. FTIR analysis was carried out with KBr pellets of the

native HNT, chitosan, chitosan coated HNT and carbonized HNT. The chitosan coated-HNT was dried at 50^0C for the FTIR analysis.

4.2.3 Emulsion Preparation and Characterization

1wt% stock particle suspensions were prepared by uniformly dispersing the particles in water by magnetic stirring followed by ultrasonication (Cole-Parmer 8890) for 1 minute. Appropriate amounts of the stock suspension were diluted in 20ml glass vials containing the aqueous phase. Emulsions were prepared at dodecane to water ratio of 1:3 by vortex mixing the aqueous particle dispersion with the dodecane. Mixing was carried out for 2 minutes on a Thermolyne Maxi Mix II operating at 3000 rpm.

The emulsion was characterized by Optical Microscopy and Cryogenic Scanning Electron Microscopy (Cryo-SEM). In the optical microscopy imaging, a small aliquot of the emulsion was placed on a glass slide prior to imaging on a Leica DMI REZ optical microscope. The images were analyzed using Image ProPlus v. 5.0 software. Cryo-SEM imaging was performed using a Hitachi S-4800 field emission Scanning Electron Microscope operated at a voltage of 3 kV and a working distance of 9 mm. The emulsion sample was first plunged into liquid nitrogen, followed by fracturing at −130 °C using a flat-edge cold knife and sublimation of the solvent at −95 °C for 5 min. The sample was sputtered with a gold–palladium composite at 10 mA for 88 s before imaging. Photographs of the emulsions were taken with a Pentax K10D Digital Camera. In the partitioning experiments, the particles were initially dispersed in dodecane by magnetic stirring at a 0.5wt% particle concentration. 2ml of the particle suspension was placed in a vial followed by the addition of 2ml of water. The contents were mixed for 2minutes (Thermolyne Maxi Mix II) at a low speed (~ 1000rpm) to prevent emulsion formation.

4.2.4 Interfacial Tension and Contact Angle Measurement

Interfacial tension was measured using the pendant drop method on a standard Ramé-Hart model 250 goniometer. About 15μL of 0.01wt% particle dispersions in water were injected into an external dodecane phase and the drop shape was analyzed using DROPimage Advanced Software to obtain the interfacial tensions. Contact angle was measured on a Ramé-Hart contact angle goniometer using compressed discs of the particles.[39, 106, 108] The contact angle measured on compressed discs is not fully representative of the contact angle of particles distributed on an interface. However, the method does provide an indirect estimation of the wettability and has been used to characterize particles at the oil-water interface.[22, 108] The particles were compressed into 10mm discs in an evacuable pellet die (Specac) at a pressure of 30Mpa (Riken High Pressure Hydraulic Equipment). The compressed discs were immersed in dodecane contained in a rectangular cell and water was then injected from a 21 gauge needle onto the particle discs using the automated Ramé-Hart dispenser. The contact angle was measured at 25^0C through the aqueous phase at the dodecane, water and particle interface.

4.3 Results and Discussion

4.3.1 Particle Characterization

Figure 4.2a shows a schematic for the synthesis of the carbonized halloysite nanotubes (CHNT). Figure 4.2b presents FTIR analysis of adsorption of chitosan onto halloysite and the synthesized CHNT. Chitosan is solubilized in acidic aqueous solution as a positively charged biopolymer due to the protonation of its primary amine groups below its pKa of 6.5.[113] On the other hand, the isomorphic substitution of Al^{3+} for Si^{4+} in

the external tetrahedral sheet imparts a net negative charge on the external surface of the HNT.[38] Figure 4.2a is a schematic of the adsorption of positively charged chitosan polymer on the negatively charged HNT yielding the carbonized HNT on pyrolysis in an inert atmosphere. We carried out FTIR to gain insights on the mechanisms of adsorption and subsequent pyrolysis of chitosan (Figure 4.2b).

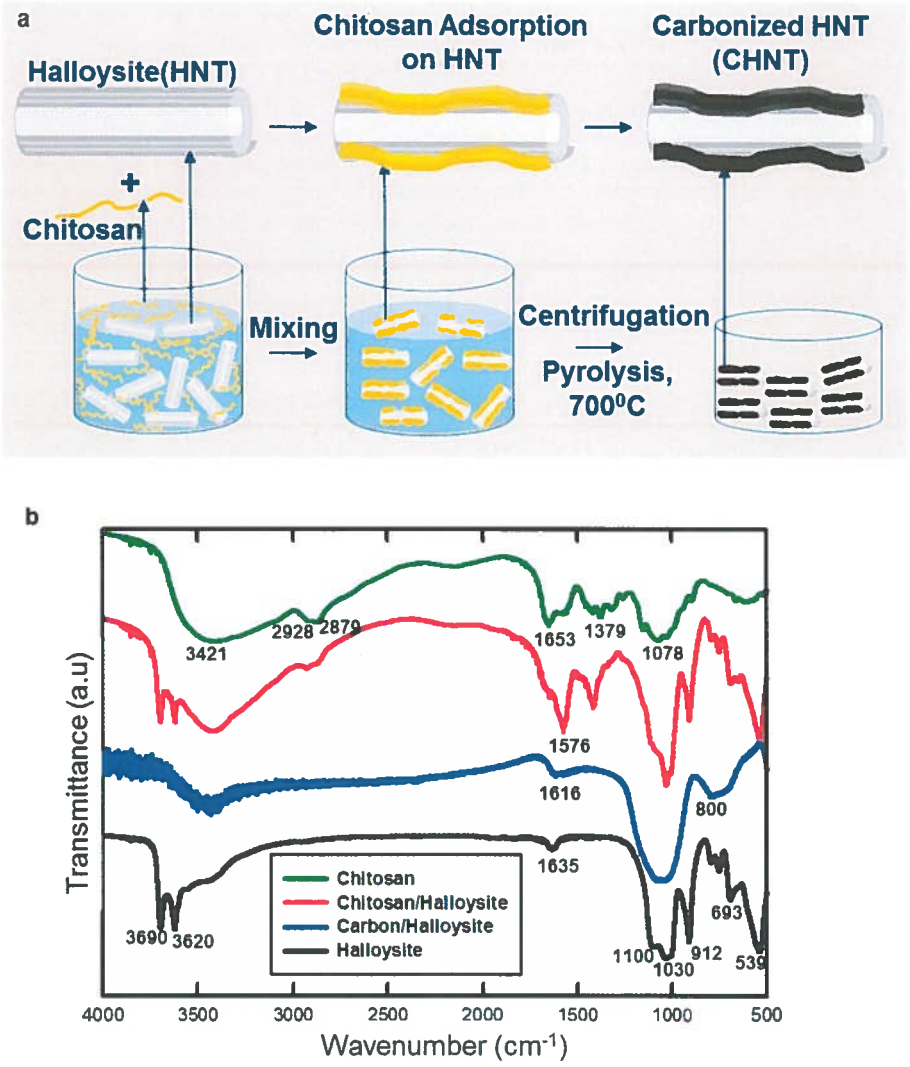

Figure 4.2: Synthesis of the carbonized halloysite nanotubes (a), FTIR analysis of chitosan adsorption and carbonization mechanisms on halloysite nanotubes (b). Chitosan adsorbs on halloysite by electrostatic attraction and hydrogen bonding, yielding carbonized halloysite nanotubes on pyrolysis in an inert atmosphere.

The FTIR spectrum of the chitosan shows key characteristic absorption peaks at 3421 cm^{-1}, 2928 cm^{-1} - 2879 cm^{-1}, 1653 cm^{-1}, 1078 cm^{-1} attributable to OH stretching, C–H stretching vibrations, amide I (-CONH-) and skeletal vibration involving the COO stretching respectively.[112, 114, 115] The FTIR for the native HNT shows the characteristic peaks at 1635 cm^{-1}, 1100 cm^{-1}, 1030 cm^{-1},912 cm^{-1}, 693 cm^{-1} and 539 cm^{-1} corresponding to the O-H deformation vibration of the interlayer water, Si-O stretching vibration, in-plane Si-O-Si stretching vibration, O-H deformation of inner surface hydroxyl groups, perpendicular Si-O stretching vibration and Al-O-Si deformation respectively.[100] The peaks at 3690cm^{-1} and 3620 cm^{-1} are assigned to the Al_2-OH stretching bands of the HNT.[53] The key observation in the spectrum for the chitosan/HNT system is that the amide I band of chitosan is perturbed from 1653 cm^{-1} to a lower frequency of 1576 cm^{-1}, corresponding to a frequency shift ($\Delta\nu$) of 77cm^{-1}. The frequency shift is attributable to hydrogen bonding interactions between the chitosan and the HNT.[53, 116]

The zeta potential of chitosan/halloysite mixtures at pH of 3.7 (Table 4.1) transitioned from negative (- 3.06 mV) to positive, reaching a relatively constant value (~ +70 mV) with increasing mass ratio of chitosan to halloysite. Thus, the adsorption of chitosan onto the HNT is driven by electrostatic attraction and hydrogen bonding interactions. Pyrolysis leads to loss of the aliphatic C-H peaks (2928 cm^{-1} - 2879 cm^{-1}) indicative of the decomposition of aliphatic structures[117] and the loss of Al_2-OH stretching bands in the CHNT suggesting dehydration of the HNT on heat treatment at 700^0C. The FTIR spectra of the CHNT indicates the appearance of absorption bands at 1616 cm^{-1} attributable to C=C stretching and 800 cm^{-1} region attributable to aromatic C-H out-of-plane bending vibrations.[118]

Table 4.1: Zeta Potential of Chitosan/Halloysite Mixtures

Mass Ratio of Chitosan to Halloysite	Zeta Potential (mV)
0	-3.06 ± 1.62
0.002	4.24 ± 0.95
0.01	23.41 ± 3.5
0.025	55.47 ± 2.14
0.05	61.28 ± 0.85
0.1	70.24 ± 2.29
0.5	71.73 ± 2.67
1	67.37 ± 1.03

Figure 4.3 presents a photograph of the HNT with increasing levels of carbonization and representative TGA curves of the particles. Table 4.2 lists the mass percent of carbon coating on halloysite nanotubes for samples reported in this work as obtained from the TGA. The level of carbonization increases with the increasing mass ratio of chitosan to HNT in the precursor solution used for synthesizing the CHNT (Figure 4.2a and Figure 4.3). Accordingly, the particles transition from white to grey and ultimately to black in appearance with increasing levels of carbonization (Figure 4.3b). The mass losses observed in the thermogravimetric curves of the CHNT samples are due to the oxidation of the carbon coating on the HNT and it increases with the level of carbonization.

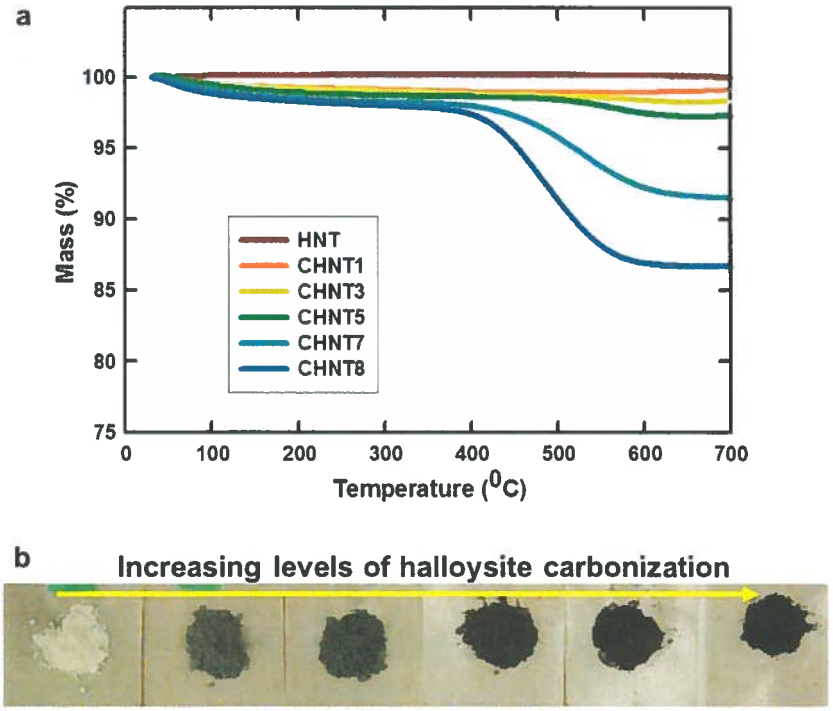

Figure 4.3: Representative thermogravimetric curves (a) and photograph of HNT with increasing levels of carbonization (b).

Table 4.2: Thermogravimetric Analysis (TGA) of Carbonized Halloysite

Sample	Mass Percent of Carbon Coating on Halloysite Nanotube (%)
CHNT1	0.84
CHNT2	1.19
CHNT3	1.63
CHNT4	2.57
CHNT5	3.51
CHNT6	4.65
CHNT7	8.76
CHNT8	13.43

The SEM images in Figures 4.4a and 4.4b reveals the smooth external surface of the native HNT. SEM imaging provides direct evidence of the carbon coating on the native HNT in the synthesis of the partially carbonized CHNT5 sample (Figure 4.4c and 4.4d) and the CHNT7 particles with a higher level of carbonization (Figure 4.4e). The TEM image shows that the CHNT retains an overall tubular nanostructure (Figure 4.4f).

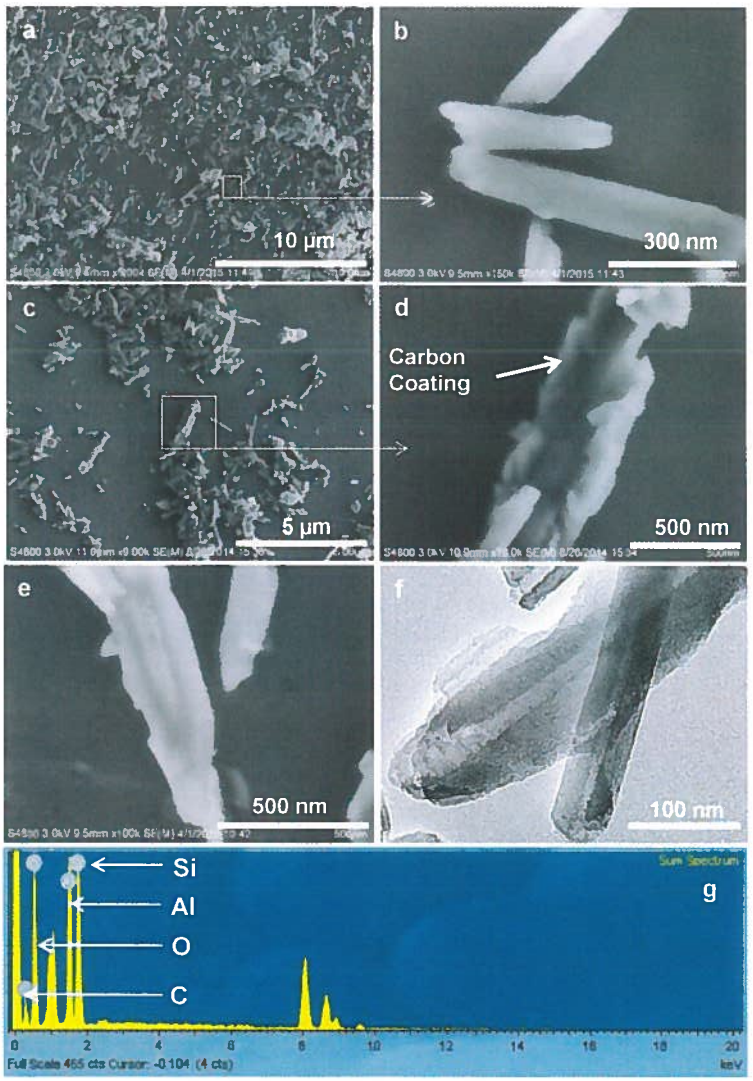

Figure 4.4: SEM images of the native HNT (a, b) and carbonized halloysite nanotubes CHNT5 (c, d) and CHNT7 (e). Panel f is the TEM image showing the retention of the nanotubular structure in the carbonized halloysite (CHNT5) and g is the SEM EDS confirming the formation of the carbon coating on the aluminosilicate HNT.

The carbonization procedure allows for the selective hydrophobic modification of the external surface of the HNT while preserving the native positively charged internal alumina surface and lumen volume. The available lumen volume in the clay nanotubes allows the loading and release of materials such as surfactant from the nanotubes in oil spill remediation applications.[80] Elemental mapping by SEM/EDS on the CHNT7 sample confirms the formation of the carbon coating on the native aluminosilicate HNT (Figure 4.4g).

4.3.2 Particle Partitioning and Oil Emulsification Characteristics

The oil-water partitioning characteristics of the HNT with varying levels of carbonization are presented in Figure 4.5. The native HNT partitions largely into the bottom aqueous phase (Figure 4.5a). The greater affinity of the native HNT for the aqueous phase compared to the oil phase indicates a relatively hydrophilic surface property. The aqueous HNT suspension is stable as shown by the turbidity of the bottom aqueous phase in the photograph taken after 1 hour (Figure 4.5b).

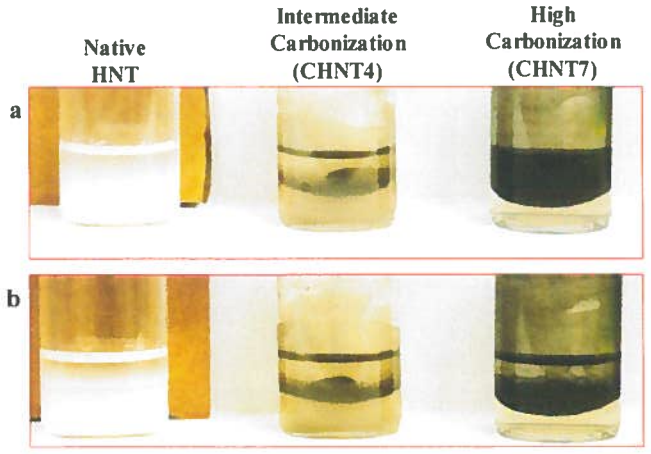

Figure 4.5: Influence of surface carbonization on the wettability and partitioning characteristics of halloysite clay nanotubes. Photographs a and b were taken immediately after gentle mixing and after 1 hour respectively.

On the other hand, HNT with a high level of carbonization (CHNT7) is retained in the upper dodecane phase. Over time the CHNT7 particles sediment towards the oil-water interface under gravity.[35] The particles are trapped at the oil-water interface and do not transfer into the bottom aqueous phase. Hydrophobic modification of the HNT by surface carbonization effectively imparts a greater affinity for the upper oil phase. The key observation is that at intermediate level of carbonization (CHNT4), the particles preferentially partition to the oil-water interface compared to either the bulk oil or water phase. The partial wetting of particles by both the oil and aqueous phases drives the location of the particles at the oil-water interface.[23]

Figure 4.6 shows optical microscopy images and photographs of emulsions stabilized by 0.1wt% of the native HNT and the carbonized halloysite nanotubes (CHNT1 to CHNT7). The appearance of the emulsions range from creamy white for the native HNT to light grey for HNT with intermediate levels of carbonization and ultimately to black for emulsions prepared with HNT at high levels of carbonization. This is in line with the transition in the appearance of the particles illustrated in Figure 4.3b. Figure 4.6 presents the average droplet sizes and corresponding interfacial tension measurements for the clay nanotube laden dodecane-water interfaces. A key observation is that relative to the native HNT, the average droplet sizes decreases with increasing level of carbonization up to the CHNT4 sample and then increases at much higher levels of carbonization. The broad minimum in average droplet size is centered on the emulsion stabilized by the CHNT4 particles, having a 2.57wt% carbon coating on the HNT surface (Table 4.2). Based on the oil-emulsification characteristics, the samples may be classified

into four categories; the native HNT, HNT at very low level of carbonization (CHNT1), HNT at intermediate levels of carbonization (CHNT2 - CHNT5) and HNT at high level of carbonization (CHNT6 – CHNT8).

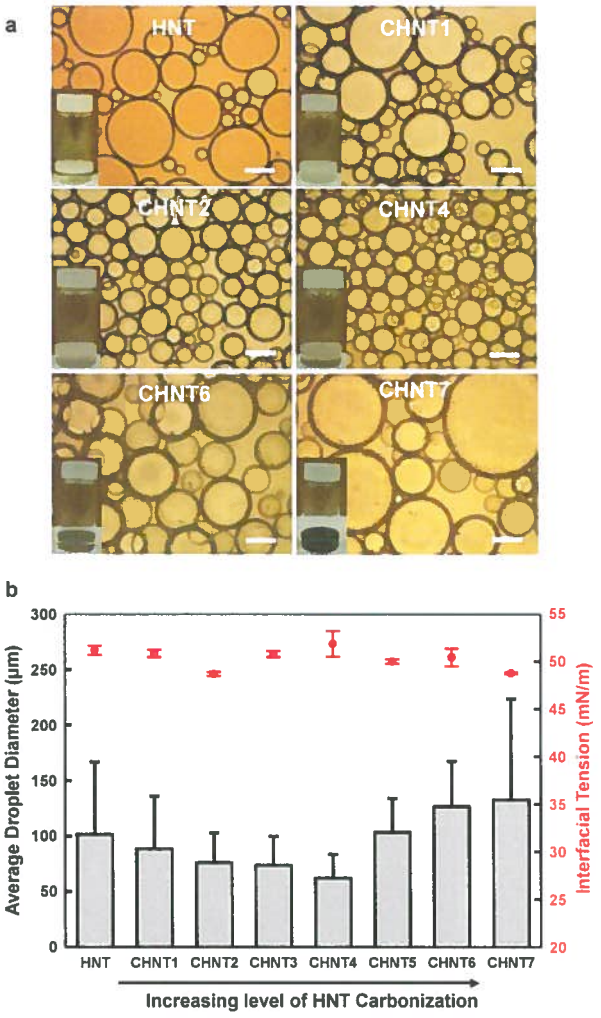

Figure 4.6: (a) Optical microscopy images of dodecane-in-water emulsions stabilized by HNT with increasing level of carbonization. Particle concentrations are 0.1wt%. Smaller droplets are obtained at intermediate levels of HNT carbonization (CHNT2, CHNT4). The insets are photographs of vials containing the emulsions. Scale bars = 100 μm. (b) Average emulsion droplet sizes and corresponding dodecane-water interfacial tensions measured using the pendant drop technique by injecting about 15μL of 0.01wt% particle suspensions into an external dodecane phase.

Figure 4.6b indicates that the dodecane-water interfacial tension does not change significantly with the varying level of HNT carbonization. For the same amount of energy input and comparable interfacial tension values for all the particle types, the smaller average droplet sizes obtained at intermediate levels of halloysite carbonization can be attributable to an increased partitioning of the particles to the oil-water interface.[22, 119, 120] The enhanced interfacial activity of the particles at intermediate level of carbonization necessitates the creation of more oil-water interfacial area in form of small droplets to accommodate the particles at the interface.[22] Once the particles are attached to the oil-water interface, they provide steric hindrance to the coalescence of the small droplets into larger ones.

Figure 4.7a presents the variation of the dodecane-water-particle contact angles with the level of HNT carbonization. The three-phase contact angle for the CHNT4 sample is 89.8^0. This contact angle value is the closest to 90^0 of all particle types and coincides with the minimum in average droplet sizes centered on the emulsions stabilized by the CHNT4 (Figure 4.6). However, we note that the compressed disc method is an indirect way to characterize the change in hydrophobicity of the nanotubes. The representative photographs in Figure 4.7b illustrate the variation of the three-phase contact angle with increasing level of HNT carbonization. Regression analysis shows that the contact angle (θ) varies logarithmically with the level of HNT carbonization (m_c) according to the equation:

$$\theta = 37.27 \ln(m_c) + 54.52 \qquad (4.4)$$

with the coefficient of determination (R^2) = 0.97. At HNT surface carbonization (m_c) levels of 0.84wt%, 2.57wt% and 13.43 wt%; the contact angle which the particle makes

at the oil-water interface are calculated to be 48.0^0, 89.7^0 and 151.3^0 respectively. Thus, carbonization of the external surface of the native hydrophilic halloysite particles effectively tunes the wettability of the particles for emulsion stabilization.

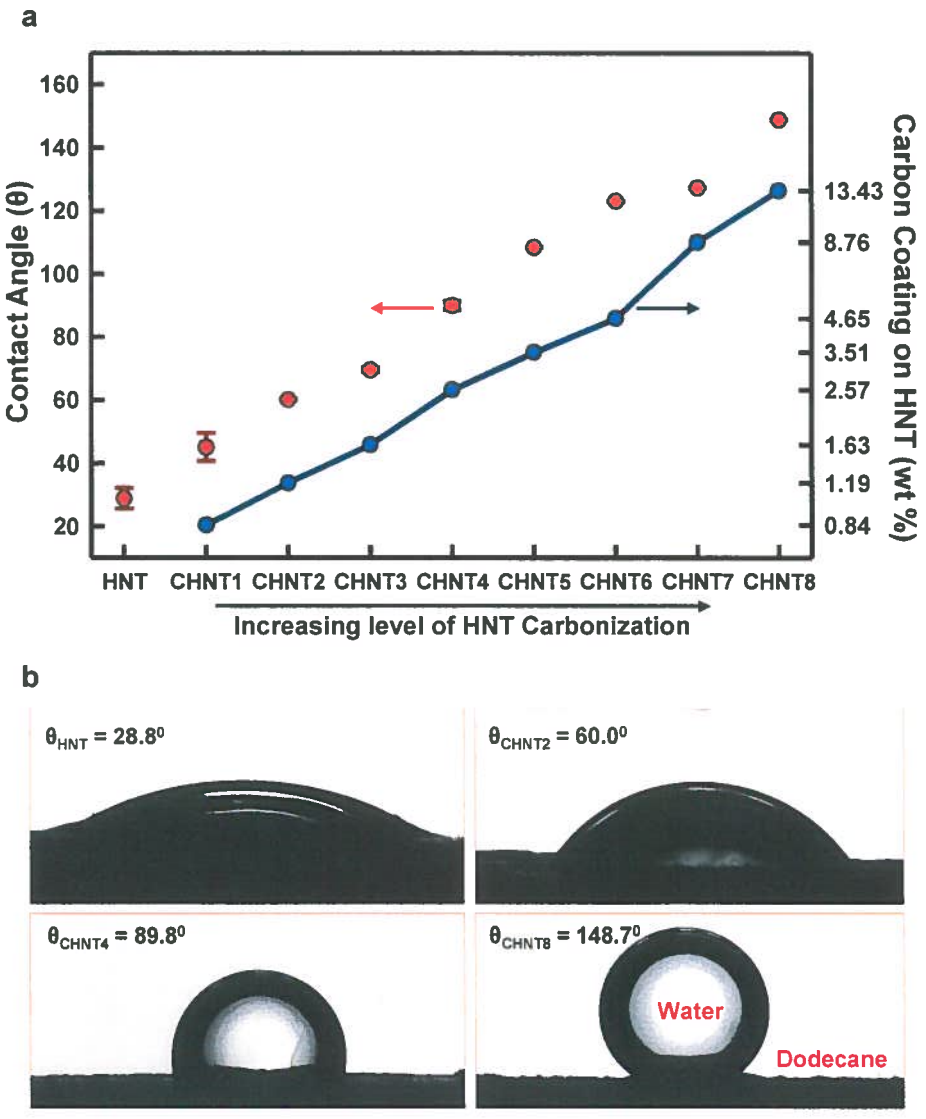

Figure 4.7: (a) Variation of the three-phase contact angle with level of HNT carbonization. Red symbols are contact angle measurements while the blue curve with blue symbols corresponds to the mass percentage of carbon coating on halloysite. (b) Photographs showing contact angle of water drops on particle surfaces in an external dodecane phase.

The cryo-SEM imaging (Figure 4.8) shows that networks of the CHNT are adsorbed at the oil-water interface. The CHNT stabilizes the oil-droplets by providing a steric barrier to droplet coalescence due to the high energy of attachment of the particles at the oil-water interface.[80] Coalescence of solid-stabilized emulsion droplets can occur when the particles are detached from the interface into a bulk phase or the particles are displaced laterally along the interface. The lateral displacement of the particles at the oil-water interface could result in the contact of exposed oil-water interfacial areas on adjacent droplets leading to coalescence.[22] In particle-stabilized emulsions, the strength of the particle network adsorbed at the oil-water interface prevents lateral displacement of particles away from droplet contact areas, providing stability against coalescence.[22] The energy required to detach network aggregates of particles at the oil-water interface is also much higher than for an individual particle as it scales with the overall size of the adsorbed particle aggregates (equation 4.1 – 4.3).[45, 80] These mechanisms are fundamental to emulsion stabilization by solids such as the CHNT.

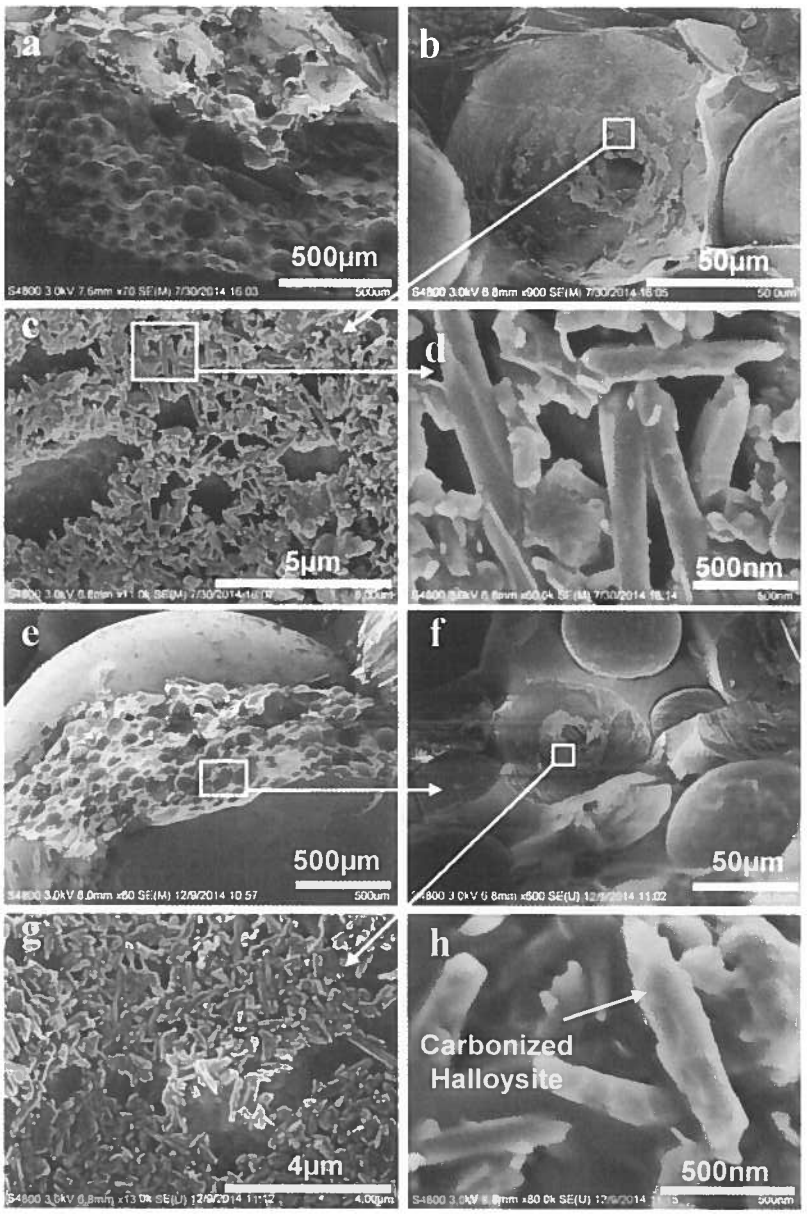

Figure 4.8: Cryo-SEM images of dodecane-in-water emulsion stabilized by carbonized halloysite nanotubes (CHNT). Panels (a) to (d) are prepared with CHNT2 with low level of carbonization while (e) to (f) are stabilized by CHNT6 with high level of carbonization. Emulsion is stabilized by the adsorption of network of particles at the oil water interface. Particle concentration is 0.1wt% in water.

4.4 Conclusions

Naturally occurring halloysite nanotubes have been hydrophobized by the selective carbonization of the external surface of the HNT. The level of carbonization of the HNT determines the relative wettability of the particles by the oil or water phases. Smaller droplet sizes are obtained at intermediate levels of carbonization compared to the hydrophilic native HNT due to an increased propensity of the particles to partition to the oil-water interface. The lowest average droplet sizes are obtained for emulsions stabilized by the CHNT4 particles prepared at a chitosan to halloysite mass ratio of 0.025, yielding a carbon coating of about 2.57wt%. Droplet size analysis indicates that at high levels of carbonization the HNT are less effective in oil emulsification into small droplets. The driving force for oil emulsification into smaller droplets at intermediate levels of carbonization is the improved preference of the particles to reside at the oil-water interface. The experimental observations with increasing levels of HNT carbonization are in agreement with free energy analysis on the attachment of cylindrical particles at the oil-water interface. The energy required to detach a cylindrical particle from the oil water interface is much higher at intermediate particle wettability compared to the more hydrophilic or hydrophobic regimes. The concept of tuning the wettability of solids by surface carbonization can be extended to other inorganic materials such as titania or iron oxides as well as other carbon sources including sugars, polymers and organic molecules. The lumen volume in the clay nanotubes can be exploited for the smart delivery of materials such as surfactant[80, 95], fluorescent markers or nutrients in oil spill remediation applications.[6]

CHAPTER 5

SYNERGISM OF HALLOYSITE NANOTUBE WITH POLYMERIC AND SMALL MOLECULE AMPHIPHILES IN A TERNARY MIXED EMULSIFIER SYSTEM

5.1 Introduction

Emulsions are stabilized by the adsorption of emulsifying agents such as solid particles, surface active polymer macromolecules and surfactant molecules at the interface between the dispersed and continuous phases.[13, 14] The synergy of the inherent characteristics of various emulsifying agents can facilitate the preparation of optimal emulsion systems.[14, 17, 35, 80, 102] A key mechanism by which the emulsifiers preserve emulsion stability is by resisting the coalescence of the droplets.[14] Low molecular weight surfactant adsorb at the oil-water interface to lower the interfacial tension and stabilize emulsions.[14] The surfactant molecules are typically in a dynamic equilibrium between the interface and the bulk phases and may desorb from the interface into the bulk phase.[80]

Polymeric surfactant have several attractive properties including excellent retention at the interface compared to low molecular weight surfactant, effectiveness at low concentrations as well as little sensitivity to salt and temperature changes.[14] These surface active polymers are used in conjunction with low molecular amphiphiles as they diffuse less rapidly to newly created interfaces.[14] Surface active polymers can be designed by grafting hydrophobic chains to a hydrophilic backbone polymer, grafting hydrophilic side chains to a hydrophobic backbone polymer or alternating hydrophilic

and hydrophobic polymer blocks.[14, 19] In these architectures the hydrophobic polymer segments have a strong affinity for an apolar phase with the hydrophilic segments exposed to a polar phase. Chitosan, a readily available polysaccharide extracted from crustacean shells, can be hydrophobically modified into an amphiphilic derivative by grafting hydrophobic alkyl groups to the chitosan backbone by reductive amination.[17, 121]

Driven by the hydrophobic effect, the hydrophobically modified chitosan (HMC) biopolymer assembles at the oil-water interface to enhance the stability of oil droplets dispersed using the commercial oil spill dispersant (Corexit 9500) and prevents rapid resurfacing of the oil droplets.[17] The HMC also anchors its hydrophobic residues into the oil phase as well as hydrophobic domains of vesicle bilayers and onto the surface of solid particles.[17, 113, 122, 123] The formation of hydrophobic crosslinks between the chains of HMC leads to the formation of a transient macromolecular network.[122, 123] The hydrophobic alkyl groups attached to the chitosan backbone anchors to the surface of particles such as carbon microspheres and latex nanoparticles, connecting the particles together into a self-supporting, three-dimensional gel matrix.[113, 123] The native chitosan shows negligible interfacial activity and is not able to form gels with solid particles.[17, 122, 123]

Solid particles that are partially wettable by oil and water attach to the oil-water interface to stabilize emulsions primarily by providing a steric hindrance to droplet coalescence.[22] Particles are held at the interface with energies that are several orders of magnitude in thermal energy, kT.[22] Mixed emulsifier systems incorporating particles, polymers and/or surfactant can be formulated for the synergistic stabilization of emulsions using covalent or non-covalent interactions between the individual

components.[23, 35, 124, 125] Hybrid particle-polymer materials have been designed for optimal emulsion stabilization and emulsion templated materials synthesis.[36, 102] The coadsorption of polymers and particles at the oil-water interface is proposed to improve the mechanical strength of the particle layer in the fabrication of microcapsules.[36, 37, 126] Relevant to the treatment of oil spills, hydrocarbon degrading bacteria that is electrostatically complexed with chitosan biopolymer have been exploited as particulate oil emulsifiers.[127, 128]

The use of naturally occurring halloysite aluminosilicate clay nanotube (HNT) in oil emulsification and interfacial surfactant delivery has recently been advanced for the treatment of crude oil spills.[80, 97, 129] The lumen volume of the HNT allows the loading and release of representative surfactant components of dispersants.[80] In addition to the anisotropic nanotubular morphology of the HNT, it has a predominantly negatively charged outer silica surface and a positively charged inner alumina surface.[80] The binding of the readily abundant cationic chitosan biopolymer onto the negatively charged external surface of HNT followed by pyrolysis in an inert atmosphere has recently been exploited for tuning the particle wettability by a selective surface carbonization technique.[129]

In this work, the colloidal interaction and mechanisms of synergistic emulsion stabilization of negatively charged HNT with the cationic biopolymer, HMC, is investigated. The bulk emulsion systems and the oil-water interfacial structure were characterized to elucidate the synergistic roles of HMC and HNT in oil emulsification. The design of a ternary, mixed emulsifier system with inorganic tubular micelle based architecture is demonstrated by exploiting the unique nanotubular morphology of the HNT.[130, 131] Based on our recent work, the water insoluble surfactant, sorbitan monooleate

(Span 80), is loaded on the HNT core and the cationic HMC interacts with the negatively charged external surface of the HNT from the continuous aqueous phase. The nanotubular morphology and elemental composition of the HNT, basic repeat units of the HMC biopolymer as well as the chemical structure of Span 80 are presented in Figure 5.1.

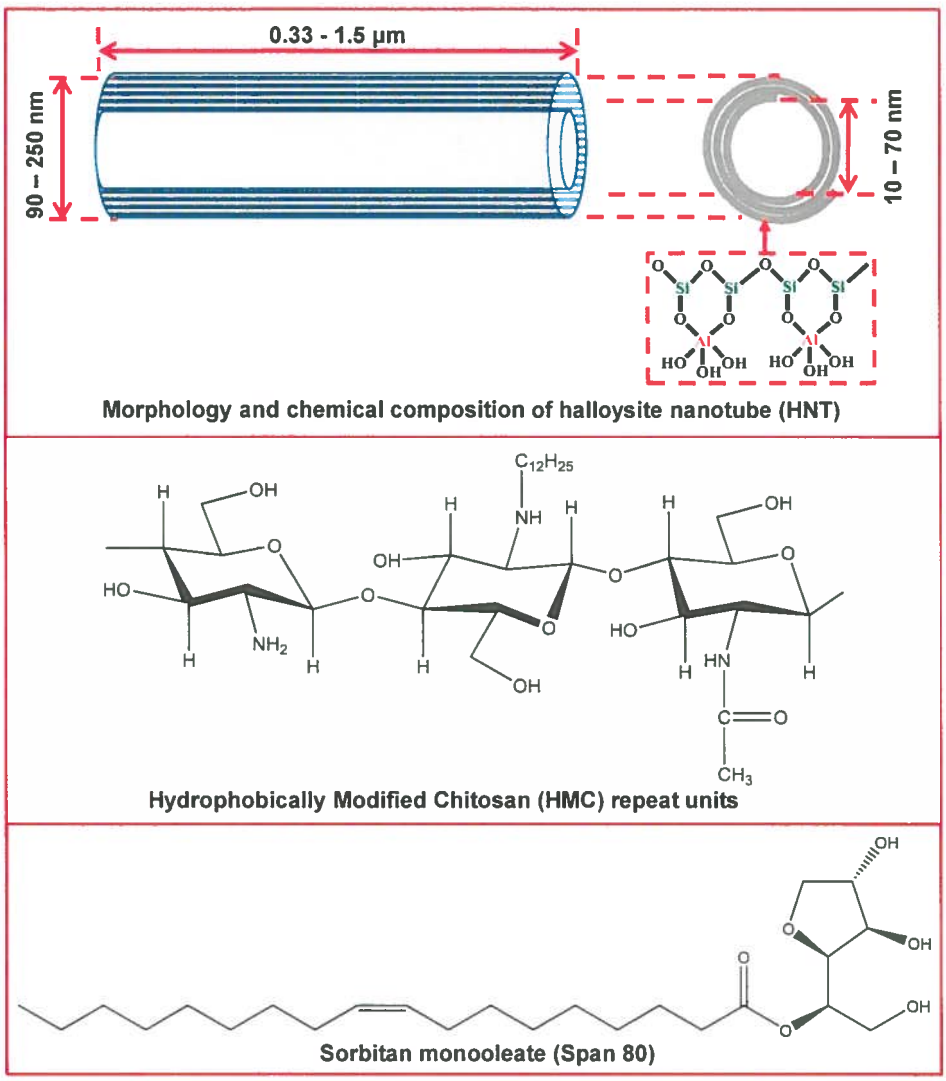

Figure 5.1: Structure of the halloysite nanotube (HNT), representative repeat units of hydrophobically modified chitosan (HMC) biopolymer and sorbitan monooleate (Span 80) surfactant

5.2 Experimental Procedures

5.2.1 Materials

Low molecular weight chitosan (50,000 - 190,000 Da) with a reported deacetylation degree of 75% - 85%, dodecane, dodecyl aldehyde, sodium cyanoborohydride, sodium hydroxide, sodium chloride and sorbitan monooleate (Span 80) were obtained from Sigma-Aldrich. Acetic acid (glacial, ≥ 99.7%) was purchased from Fisher Scientific. Halloysite nanotube (HNT) was purchased from NaturalNano Inc. (Rochester, New York, USA). All materials were used as received. Acetic acid solution was prepared by diluting glacial acetic acid in deionized water produced from an Elga water purification system (Medica DV25, 18.2 MΩ cm resistivity). A saline water solution of 0.6M sodium chloride concentration was used a surrogate for seawater. Louisiana sweet crude with viscosity of 0.01 Pa.s and specific gravity 0.85 at 15 °C was obtained from British Petroleum's Macondo prospect (SOB-20100617032).[17, 80]

5.2.2 Synthesis and Characterization of Hydrophobically Modified Chitosan (HMC)

Hydrophobically modified chitosan (HMC) was synthesized using a previously reported procedure involving the reaction of the amine groups of chitosan with n-dodecyl aldehyde.[17, 123, 132] Briefly, 4 g of low molecular chitosan was first dissolved in 220 mL of 1% (wt/v) acetic acid. 150 mL of ethanol was then added to allow for the solvation of the n-dodecyl aldehyde when it is added to the chitosan solution. The pH was adjusted to 5.1 by the addition of sodium hydroxide, followed by a solution of dodecyl aldehyde in ethanol containing a 2.5% molar ratio of the aldehyde to the amine groups in chitosan.[132]

An excess of sodium cyanoborohydride was then added to the mixture. The mixture was subsequently stirred at room temperature for 24 hours. The final product was precipitated with ethanol and sodium hydroxide solution. The precipitate was then washed with ethanol and deionized water 3 times followed by freeze drying. Attachment of the dodecyl hydrophobes to the chitosan backbone was confirmed by ^{1}H NMR spectroscopy conducted on a Bruker Avance 500 MHz NMR spectrometer (Appendix A). The HMC is soluble in acidic medium below the parent chitosan pKa of 6.5.[113] The amine groups of the parent chitosan are protonated in acidic media, imparting a positive charge to the solubilized HMC.[113]

5.2.3 Preparation and Characterization of Span 80 loaded HNT

HNT was loaded with the lipophilic surfactant, Span 80 following the vacuum suction and solvent evaporation procedure employed in our previous work.[80, 97] 0.1g of HNT was weighed into a round bottom flask. The HNT was uniformly dispersed by magnetic stirring and brief ultrasonication (Cole-Parmer 8890) in 2ml of ethanol containing 0.03g of Span 80. Vacuum suction was then applied to the mixture in the flask to displace the air in the HNT and suck the surfactant solution into the HNT. The pressure was cycled back to atmospheric pressure after about 15minutes. This pressure cycling process was repeated twice and then the remaining ethanol solvent was evaporated under vacuum in a rotary evaporator.

The loading of Span 80 onto the HNT was confirmed by Fourier transform infrared (FTIR) spectroscopy analysis carried out on a Thermo Nicolet Nexus 670 FT-IR Spectrometer and transmission electron microscopy (TEM) imaging on a FEI Tecnai G2

F30 Twin transmission electron microscope operated at 300 kV. The native HNT and Span 80 loaded HNT were pressed into KBr pellets for the FTIR analysis.

5.2.4 Emulsion Preparation and Optical Microscopy Imaging

Halloysite nanotube (HNT) was uniformly dispersed in deionized water by magnetic stirring followed by brief ultrasonication (Cole-Parmer 8890) for 1 minute. HMC solutions were prepared by dissolving the dried polymer in a 1wt% acetic acid solution. Emulsions were prepared by adding known amounts of a 0.5% (wt/v) HMC stock solution in acetic acid and/or 1wt % HNT dispersion in water into the aqueous phase. The contents of the aqueous phase were ultrasonicated (Cole-Parmer 8890) for 1 minute before emulsion preparation. Emulsions were prepared in 20ml glass vials by vortex mixing dodecane with the aqueous phase containing the HMC and/or HNT at dodecane to water ratio of 1:3. Mixing was carried out on a Thermolyne Maxi Mix II operating at 3000 rpm for 2 minutes. In all the emulsions, the pH of the aqueous phase was adjusted to ~ 3.7 by adding acetic acid. The pH was measured using a Thermo Scientific Orion 3-star benchtop pH meter. Crude oil in saline water emulsion was also prepared with span 80 loaded HNT following the same procedure.

The emulsions were imaged on a Leica DMI REZ optical microscope to characterize droplet shape and sizes. A small aliquot of the emulsion was transferred onto a glass slide prior to imaging and analysis using the Image ProPlus v. 5.0 software. To characterize emulsion stability to forced coalescence, the emulsions were centrifuged in 15ml Polypropylene Centrifuge Tubes at 1000rpm for 2min on an Eppendorf 5810 Centrifuge.

5.2.5 Scanning and Cryogenic-Scanning Electron Microscopy Imaging

The morphology of the native HNT and HNT with adsorbed HMC was characterized by field emission scanning electron microscopy (SEM, Hitachi S-4800). Cryogenic Scanning Electron Microscopy (Cryo-SEM) imaging of the interfacial structure of the emulsions was performed on the Hitachi S-4800 field emission Scanning Electron Microscope operated at a working distance of 9 mm and voltage of 3 kV. In cryo-SEM experiments, the emulsion samples were plunged into liquid nitrogen followed by fracturing at −130 °C using a flat-edge cold knife and sublimation of the solvent at −95 °C for 5 min. The sample was then sputtered with a gold–palladium composite at 10 mA for 88 s.

5.2.6 Zeta Potential and Turbidity Measurements

Zeta potential of the suspension and emulsion samples was obtained by measuring the electrophoretic mobility of the systems using Laser Doppler Velocimetry (Zetasizer Nano, Malvern Instruments). 800 μL of the samples were transferred to a polypropylene electrode cell and the measurements made after temperature equilibration at 25 °C for 2 min. The colloidal stability of halloysite and HMC mixtures at pH of ~ 3.7 was characterized by measuring the percentage light transmittance through the sample as a function of time using a UV–vis Spectrophotometer (Shimadzu UV-1700) operated at a wavelength of 400 nm.

5.2.7 Contact Angle and Interfacial Tension Measurement

In the contact angle measurements, compressed tablets of HNT and HNT with adsorbed HMC were immersed in dodecane contained in a rectangular cell.[80, 129] The

HNT samples with adsorbed HMC were recovered by centrifugation from HMC and HNT mixtures and were subsequently dried at 50^0C. The samples were compressed into 10mm discs in an evacuable pellet die (Specac), using a Riken High Pressure Hydraulic Equipment at a pressure of 30MPa.[129] Water was then injected from a 21 gauge needle onto the compressed tablets using the automated dispenser of the standard Ramé-Hart model 250 goniometer. The contact angle was measured through the aqueous phase at the dodecane, water and solid interface.[129] Dynamic interfacial tensions were measured using the pendant drop method on the standard Ramé-Hart model 250 goniometer. About 15µL of a water drop containing HMC, HNT and/or Span 80 loaded HNT were injected into an external dodecane phase. The drop shape was analyzed using DROPimage Advanced software to obtain the interfacial tensions.

5.3 Results and Discussion

5.3.1 Interfacial Adsorption of HMC in Oil Emulsification

Figure 5.2 shows optical microscopy images, average droplet sizes and stability to forced coalescence in a centrifugal field of dodecane-in-water emulsions stabilized solely by HMC. The emulsions are white in appearance. Progressively smaller droplet sizes are obtained with increasing HMC concentration (Figure 5.2a – 5.2d). An order of magnitude increase in HMC concentration from 0.005 wt% to 0.05 wt% results in a 61.4% decrease in average droplet size from 89.35µm to 34.47µm respectively (Figure 5.2e). Increase in the concentration of the interfacially-active HMC biopolymer necessitates the creation of more oil-water interfacial area in the form of smaller droplets to accommodate the HMC at the oil-water interface.

Figure 5.3a presents the zeta potential of HMC solutions and HMC stabilized emulsions. There is no significant increase in the zeta potential of the HMC solutions with increasing concentration (red plot, Figure 5.3a). The zeta potential of the solutions is higher than for the emulsions at all HMC concentrations. The lower zeta potential measured for the emulsions compared to the HMC solutions is likely due to the negative charge of the pristine oil-water interface.[133] The cationic polymer layer at the oil-water interface imparts a positive charge on the oil droplets inducing electrostatic repulsion between the HMC stabilized droplets. The charge imposed on the droplets increases with the concentration of the cationic HMC[17] as observed in the zeta potential of 40.68mV at 0.005wt% HMC that plateaus to 48.82mV at a higher 0.05wt% HMC (green plot, Figure 5.3a).

Cryo-SEM imaging reveals the interfacial structure of dodecane-in-water emulsion stabilized solely by HMC (Figure 5.3b). The HMC adsorbs at the oil-water interface with the hydrophobic residues preferentially anchored in the oil droplets.[17, 134] The HMC also show non-covalent networks in the adjoining aqueous phase by the self-association of the hydrophobes (Figure 5.3b).[135] The zeta potential and cryo-SEM imaging reveals that the hydrophobic modification of chitosan integrates cationic and hydrophobic functionalities in the HMC, imparting interfacial activity as well as hydrophobic assembly properties.[18, 113] The polymer chains attach at the oil-water interface and likely stabilizes the oil droplets through steric and electrostatic mechanisms.[17, 136]

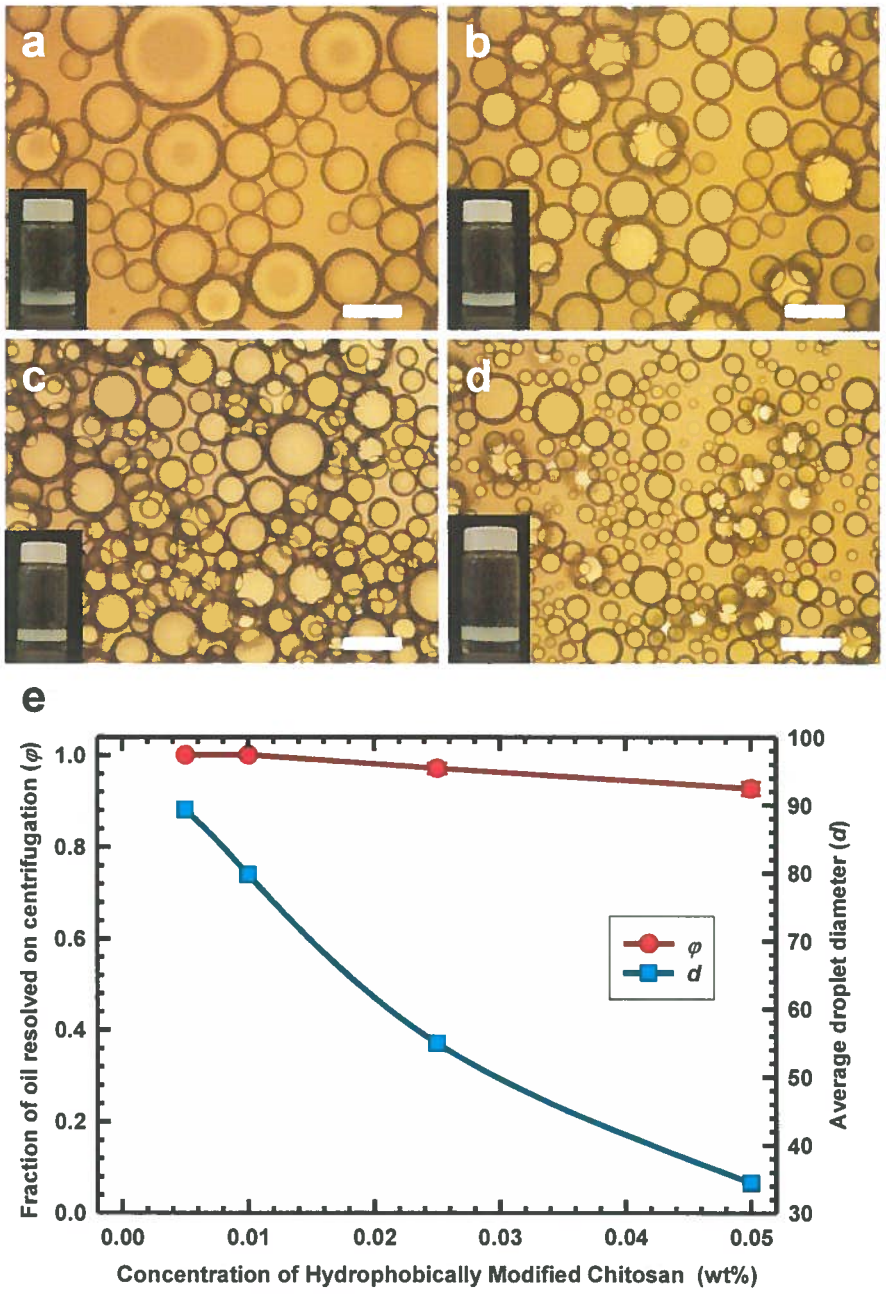

Figure 5.2: (a – d) Optical microscopy images of dodecane-in-water emulsions stabilized by increasing amounts of HMC. The pH of the aqueous phase was adjusted to about 3.7 for all the samples by adding acetic acid. The insets are photographs of vials containing the emulsions. Scale bars = 100 μm. (e) Average droplet sizes and emulsion stability to coalescence.

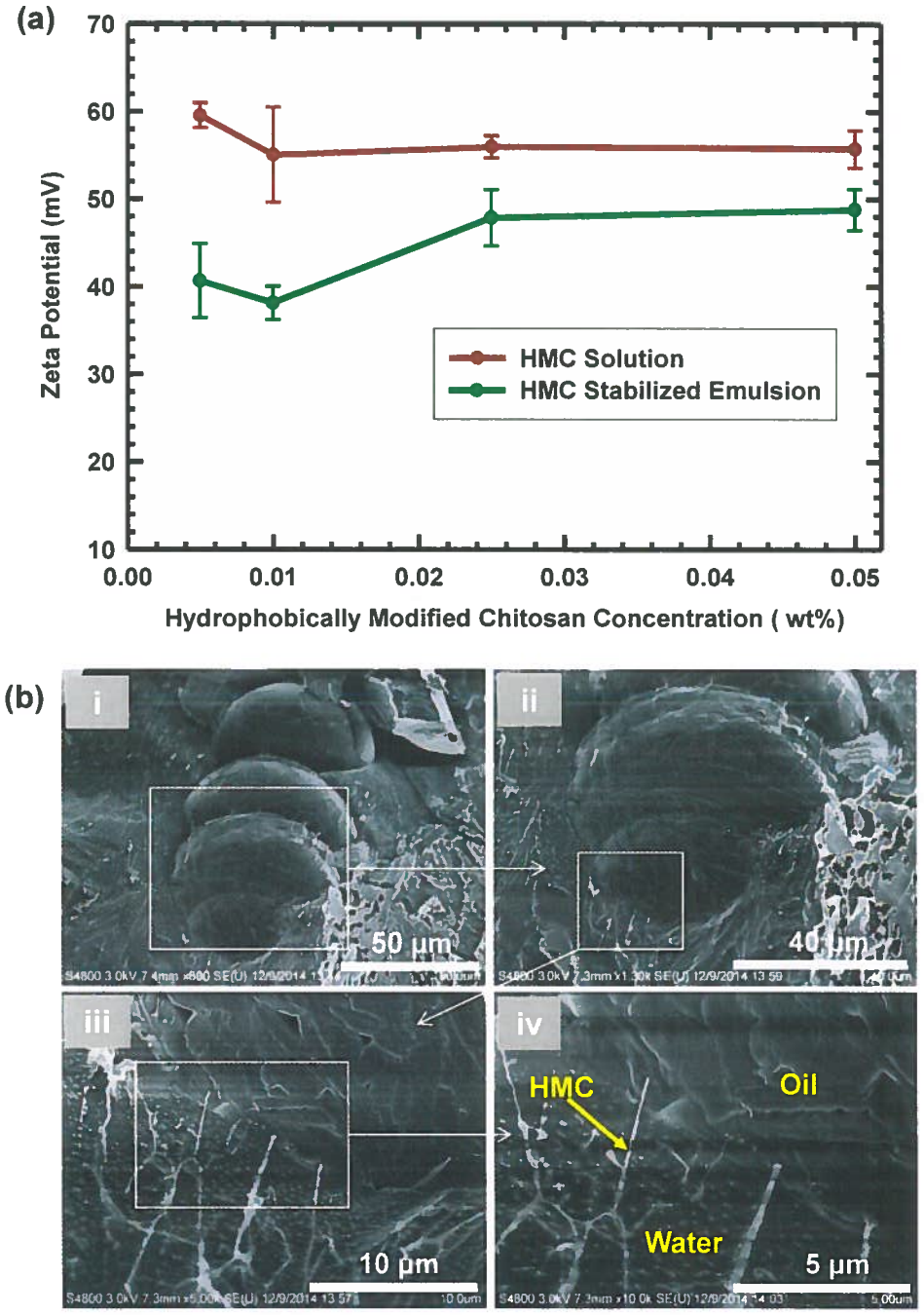

Figure 5.3: (a) Zeta potential of hydrophobically modified chitosan (HMC) solutions and dodecane-in-water emulsions stabilized by HMC. (b) Cryo-SEM images of dodecane-in-water emulsions stabilized by HMC. Images (i) to (iv) in panel b are in increasing order of magnification.

The stability of the emulsion against droplet coalescence and phase separation is ultimately dependent on the resistance of the stabilizing interfacial layer to droplet coalescence. The resistance of the interfacial layer to coalescence can be quantitatively characterized by applying a centrifugal field.[45, 80] In a centrifugal field, the oil droplets are forced together and deformed into polyhedra separated by thin water films.[45] Rupture of the thin oil-water-oil films around the droplets results in the formation of a clear oil layer. The experimentally measured fraction of oil resolved on centrifugation (φ_{rel}) is related to the critical de-emulsification pressure (P_c) required to rupture the stabilizing interfacial layer of the emulsion by:[45, 91]

$$P_c = \Delta\rho g_k V_{oil}(1 - \varphi_{rel})/A \qquad (5.1)$$

where $\Delta\rho$ is density difference between the aqueous and oil phases, g_k is the centrifugal acceleration, V_{oil} is the volume of oil used in preparing the emulsion and A is the cross-sectional area of the centrifuge tube.

A key observation in Figure 5.2e is that the emulsions stabilized by HMC have very low resistance to coalescence as the fraction of oil resolved on centrifugation range from 0.93 to 1 at the various HMC concentrations. Motivated by the propensity of particles such as halloysite nanotubes (HNT) to provide a large hindrance to coalescence, we exploit synergistic emulsion stabilization mechanisms of HMC and the HNT.[22, 129]

5.3.2 Colloidal Interaction and Synergistic Emulsion Stabilization of HMC and HNT

Zeta potential measurements of HMC and HNT mixtures are listed in Table 5.1. The HNT concentration was fixed at 0.1 wt% for all the systems listed in Table 5.1. The HMC concentrations were 0 wt%, 0.005 wt%, 0.01 wt%, 0.025 wt% and 0.05 wt% corresponding to HMC to HNT mass ratios of 0, 0.05, 0.1, 0.25 and 0.5 respectively.

Table 5.1 shows that the positively charged HMC polyelectrolyte adsorbs onto the negatively charged external surface of the halloysite tubules, reversing the net surface charge from negative to positive.[129] In the adsorption of a polyelectrolyte onto an oppositely charged surface, the counter ions from the polymer and the surface are released into the bulk solution increasing the entropy in the system.[14] This thermodynamic driving force brings the system to a lower free energy state on adsorption of the polymer to the solid surface.[14] The zeta potential increases and plateaus to a relatively constant value of about 60mV beyond HMC concentration of 0.01wt %.

Table 5.1: Zeta potential HMC and HNT mixtures

HMC Concentration	Zeta Potential (mV)
0	-6.83 ± 0.44
0.005	12.00 ± 1.01
0.01	58.57 ± 1.59
0.025	60.39 ± 1.38
0.05	60.48 ± 4.68

Figure 5.4 presents the colloidal stability of the HNT/HMC system as characterized by turbidity measurements. At low HMC concentrations of 0.005 wt% and 0.01 wt%, there is a rapid increase in transmittance of the HNT/HMC system (green and yellow curves, Figure 5.4b) relative to the HNT colloidal dispersion (purple curve, Figure 5.4b). This may be attributable to strong bridging flocculation of the HNT at low polymer

coverage, producing large HNT aggregates that sediment rapidly (photographs in Figure 5.4a).[13] At higher HMC to HNT mass ratios, the colloidal system becomes more stable (blue and red curves, Figure 5.4b). This is likely a result of the electrosteric stabilization of the HNT at higher concentrations of the cationic HMC biopolymer.[13] We hypothesize that beyond HMC concentration 0.01 wt%, the nanotubes are stabilized in the aqueous phase by the transient network[122, 123] formed from hydrophobic associations of HMC chains.

Figure 5.5a – 5.5b shows the SEM of native HNT while Figure 5.5c – 5.5f shows HNT with HMC adsorbed on the surface. Figure 5.5g shows the influence of HMC adsorption on the contact angle of water on the solid HNT surface in an external dodecane phase. The adsorption of HMC increases the three-phase contact angle of the native HNT from about 26.2 ± 0.13^0 to 61.10 ± 0.01^0 at HMC to HNT mass ratio of 0.1. The adsorption of the HMC with hydrophobic alkyl residues onto the HNT makes the surface of the native hydrophilic HNT more hydrophobic.[132] In agreement with the zeta potential measurements, there is no further increase in the contact angle beyond HMC to HNT mass ratio of 0.1 (panel iv, Figure 5.5g). The zeta potential and contact angle measurements suggests that the ionic sites on the negatively charged HNT surface is electrostatically saturated with the cationic polymer at HMC to HNT mass ratio of 0.1, and at higher concentrations the additional HMC interacts via hydrophobic interactions with the exposed hydrophobes of HMC that is electrostatically adsorbed onto the HNT.

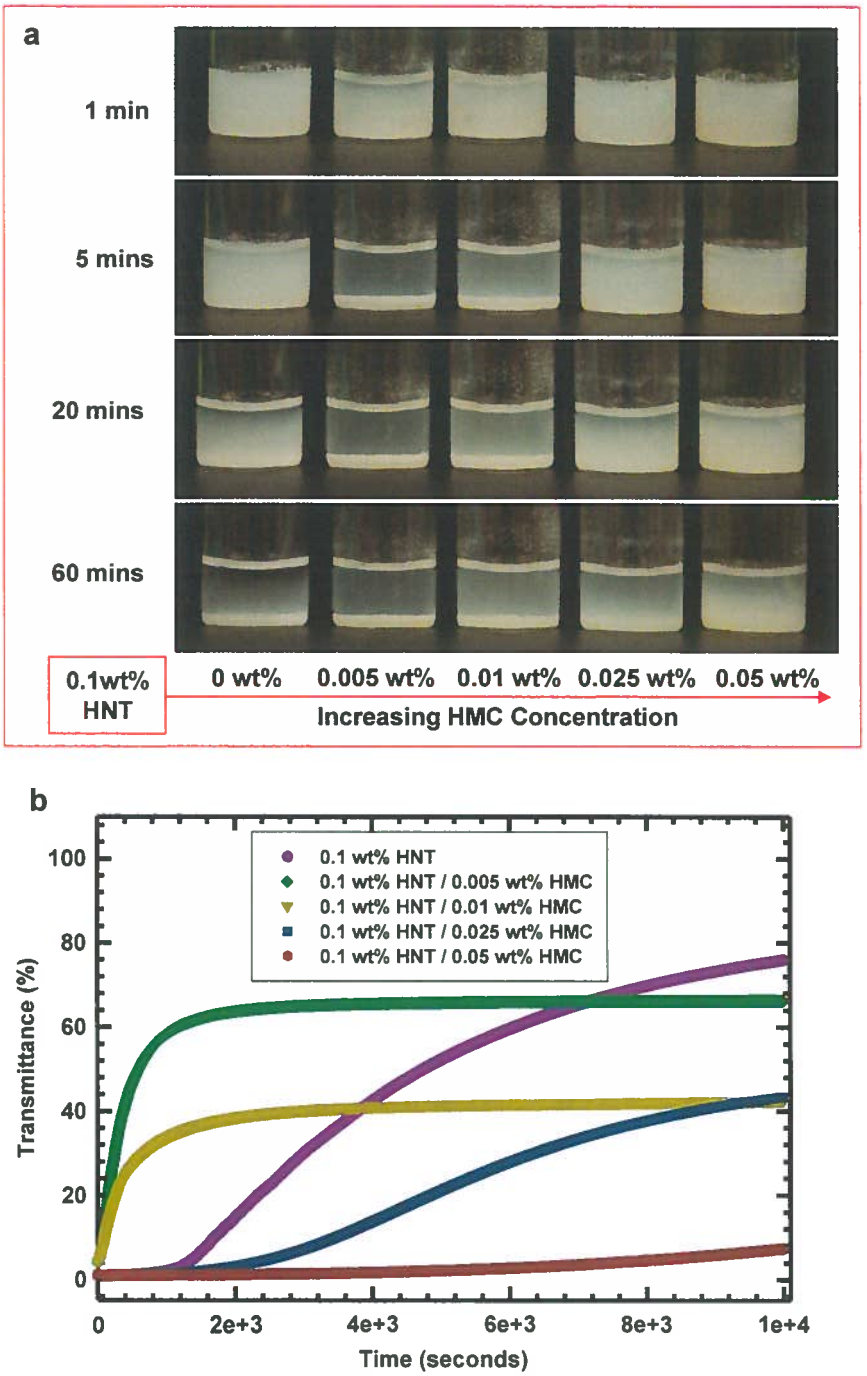

Figure 5.4: Colloidal stability of halloysite nanotubes (HNT) as a function of hydrophobically modified chitosan (HMC) concentration. Figure 5.4a shows photographs while Figure 5.4b is turbidity measurements over time at 400nm.

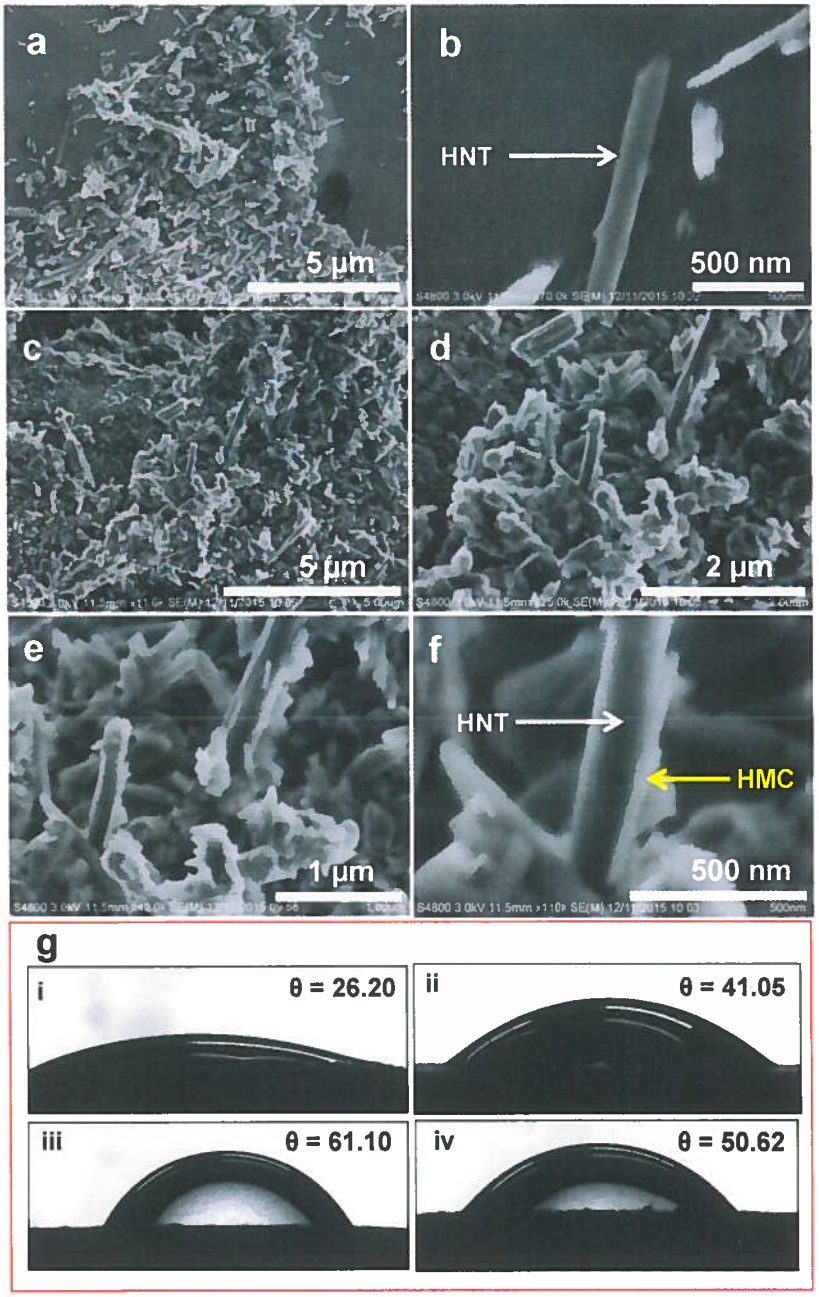

Figure 5.5: SEM images of HNT (a,b) and HNT with adsorbed HMC (c-f). Photographs showing contact angle of water in an external dodecane phase on the surface of native HNT and HNT with adsorbed HMC (g). In panel g, the compressed tablets were made from dried particles initially recovered by centrifugation from systems with HMC to HNT mass ratios of 0 (i), 0.05 (ii), 0.1 (iii) and 0.25 (iv) respectively.

Figure 5.6a – 5.6d shows representative optical micrographs of emulsions stabilized by the HNT and increasing HMC concentrations and Figure 5.6e shows emulsion stability to coalescence. Synergistic oil emulsification of the HNT and HMC produces emulsions with smaller droplet sizes and a significantly improved stability to coalescence. To understand the synergistic emulsion stabilization mechanisms of the HMC and HNT, the zeta potential of the emulsions were first measured and listed in Table 5.2. The zeta potential increases with HMC concentration and plateaus to about 60mV beyond HMC concentration of 0.01wt%. The charge imparted on the oil droplets by the interfacial coadsorption of HMC and HNT will generate electrostatic repulsion that limits the close approach of the positively charged droplets and facilitates emulsion stabilization.

In the emulsion stability experiments reported in Figure 5.6e, the centrifugal acceleration, cross-sectional area of the centrifuge tube, volume of oil and volume of the aqueous phase were kept constant. The HNT concentration is fixed at 0.1 wt% and the conditions vary only with the HMC concentration. Using equation 5.1, the ratio of P_c for emulsions prepared at two conditions (1) and (2) can be expressed as:[97]

$$\frac{P_c^1}{P_c^2} = \frac{1 - \varphi_{rel}^1}{1 - \varphi_{rel}^2} \qquad (5.2)$$

where $P_c{}^1$ is the critical de-emulsification pressure at condition 1, $P_c{}^2$ is the critical de-emulsification pressure at condition 2, $\varphi^1{}_{rel}$ is the fraction of oil released on centrifugation at condition 1 and $\varphi^2{}_{rel}$ is the fraction of oil released on centrifugation at condition 2.

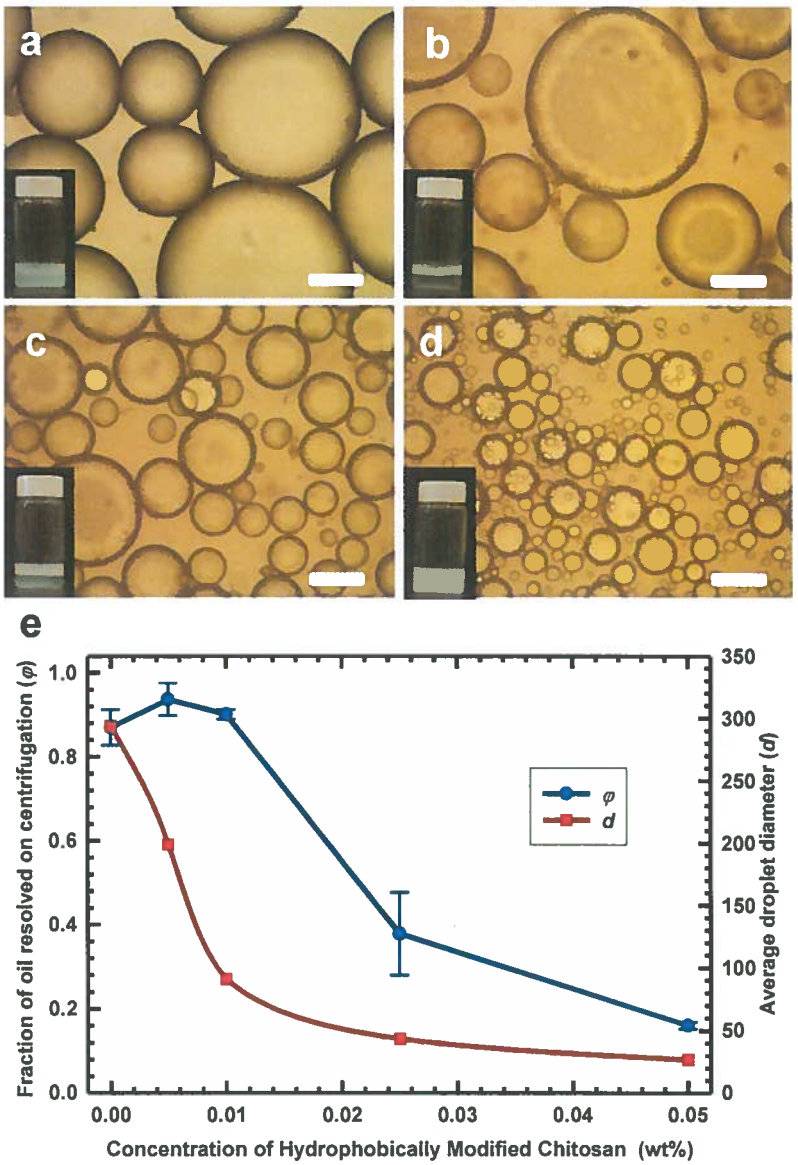

Figure 5.6: Optical microscopy images of dodecane-in-water emulsions stabilized by 0.1wt% HNT and increasing HMC concentrations of 0wt% (a), 0.01wt % (b), 0.025wt % (c) and 0.05wt % (d) respectively. Scale bars = 100μm. The pH of the aqueous phase was adjusted to about 3.7 for all the samples by adding acetic acid. Emulsion stability to coalescence and average droplet sizes (e).

Table 5.2: Zeta potential of oil-in-water emulsions stabilized by HMC and HNT

HMC Concentration	Zeta Potential (mV)
0	-8.15 ± 0.86
0.005	46.42 ± 2.08
0.01	51.77 ± 4.26
0.025	60.14 ± 1.67
0.05	57.29 ± 1.89

For instance, emulsions stabilized by 0.1wt% HNT with HMC concentrations of 0.005wt% and 0.025wt% may be considered as conditions 1 and 2 respectively. Figure 5.6e shows that the fraction of oil released decreases from 0.94 at HMC concentration of 0.005 wt% and to 0.38 at 0.025 wt% HMC. From equation 5.2, there is about a 10-fold increase in the pressure required to rupture the interfacial layer containing the HNT with the increase of HMC concentration from 0.005 wt% and 0.025 wt%. We hypothesize that the interfacially-active HMC biopolymer anchors the particles at the oil-water interface and strengthens the resistance of the interfacial layer to coalescence. Although this mechanism has been suggested to increase the mechanical strength of particle layers in the synthesis of emulsion templated capsules,[37] the analysis here provides quantitative characterization of the strengthening of interfacial HNT layer on coadsorption with the HMC biopolymer.

The addition of very small HMC amounts (0.005wt % - 0.01 wt %) does not lead to a considerable increase in emulsion stability to coalescence. This may be due to the charge-patch flocculation of oil droplets[136] or strong flocculation[137] of the HNT into large aggregates at small HMC concentrations. The enhanced emulsion stability appears correlated with conditions in which the HNT is effectively stabilized by the HMC in the aqueous phase (0.025wt% and 0.05 wt%) unlike systems where the HNT is strongly flocculated by the HMC (0.005wt% and 0.01 wt%). The correlation of strong particle flocculation with reduced emulsion stability has been reported in emulsions stabilized by silica and laponite particles.[137, 138] Strong particle flocculation may lower the availability of dispersed particles that can adsorb at freshly created oil-water interfaces during emulsifcation.[138]

Figure 5.7 shows cryo-SEM images of dodecane-in-water emulsion synergistically stabilized by the HNT and HMC. The imaging of the oil-water interfacial structure reveals domains of the HNT locked together by the HMC biopolymer (Figure 5.7d, 5.7e and 5.7f) at the oil-water interface. The cryo-SEM imaging provides direct evidence that HMC anchors the particles together at the oil-water interface to strengthen the interfacial particle layer.[37, 126] The 'connecting' HMC chains (yellow arrow, Figure 5.7f) likely locks the nanotubes at the oil-water interface, by hydrophobic interactions with the hydrophobic residues of HMC that is electrostatically adsorbed on the HNT surface (red arrows, Figure 5.7f).[123]

To induce droplet coalescence the emulsifier stabilizing the oil-water interface has to be detached from the oil-water interface into a bulk phase. Free energy analysis on a cylindrical particle at a planar oil-water interface gives the work of detachment or free

energy change (ΔG_w) on removing the particle from the oil-water interface into water as:[80]

$$\Delta G_w = 2rL\gamma_{ow}\left[\sin\theta - \theta\cos\theta\left(1+\frac{r}{L}\right)+\frac{r\cos^2\theta\sin\theta}{L}\right] \quad for\ 0 \le \theta \le 90^0 \qquad (5.3)$$

where γ_{ow} is the oil-water interfacial tension, r is the radius of the cylindrical particle, L is the particle length and θ is the contact angle.

From equation 5.2, the thermodynamic propensity of particles to remain attached to the oil-water interface as quantified by ΔG_w is dependent on the particle size and wettability.[23] The network aggregate of the HNT locked together by the HMC may be pictured as a particle unit with a larger size compared to a single HNT at the oil-water interface. The energy required to remove particle aggregates from the oil-water interface is higher than for a single particle, as ΔG_w scales with size.[45] From Figure 5.5, the adsorption of HMC onto the HNT surface also modifies the HNT wettability. For a 1 μm long cylindrical particle with a radius of 50 nm at interfacial tension of 49 mN/m, increase of the three-phase contact angle from 26.20^0 to 50.62^0 translates to an increase in the work of detachment from 3.70×10^4 kT to 2.60×10^5 kT. The locking of the HNT together at the oil-water interface and modification of HNT wettability by the HMC increases the thermodynamic propensity of the particles to remain attached to the oil-water interface, significant enhancing emulsion stability to coalescence.[17, 37]The synergistic oil emulsification of HMC and HNT is driven by:

i) hydrophobic interaction of HMC with the oil phase through hydrophobic alkyl residues (Figure 5.3b, Figure 5.7)

ii) adsorption of the HMC onto the halloysite nanotube (HNT) by electrostatic attraction (Figure 5.5c – 5.5f, Figure 5.7)

iii) locking of HNT together at the oil-water interface by hydrophobic associations between HMC chains (Figure 5.7).

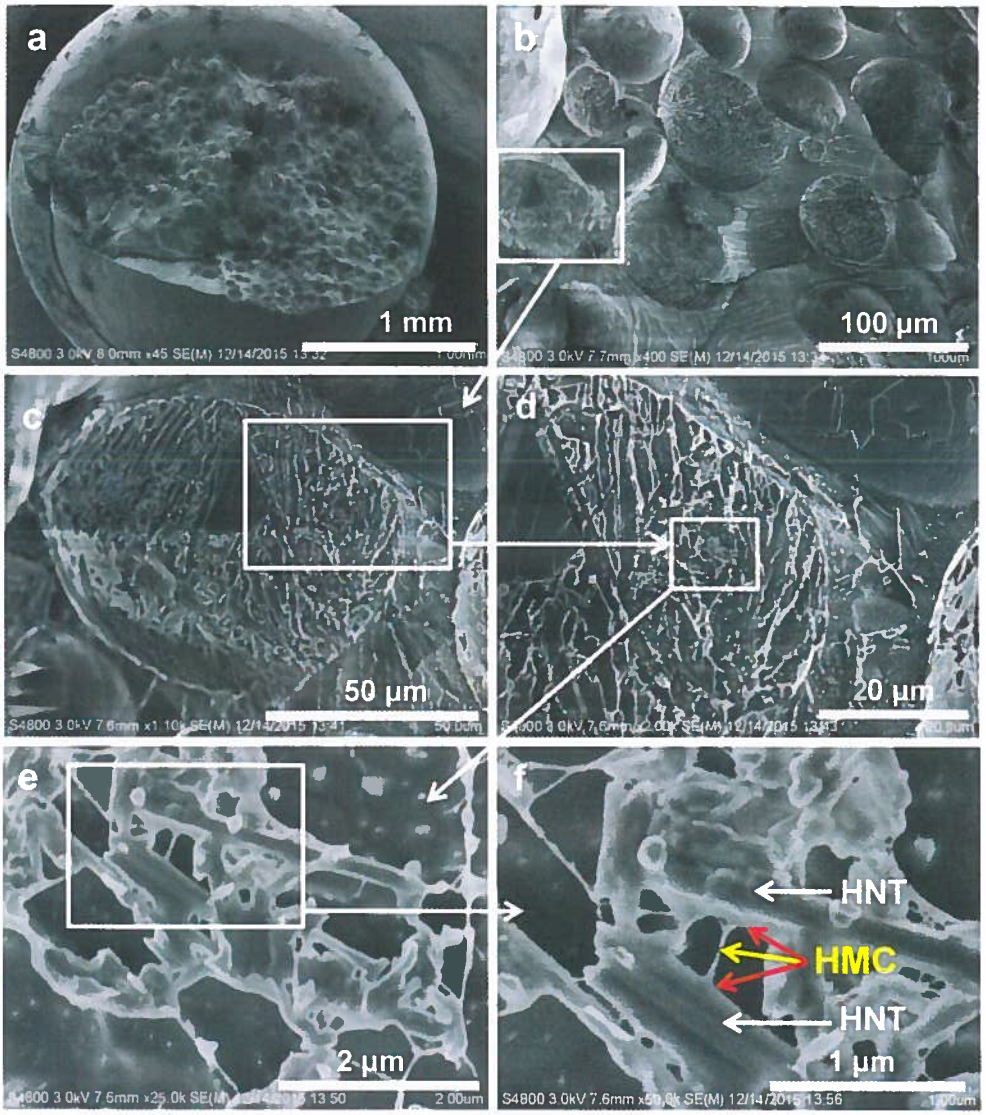

Figure 5.7: Cryo-SEM images of dodecane-in-water emulsions stabilized by the HNT and HMC. Panels (a) to (f) are in increasing order of magnification.

In practical applications, such as in the treatment of oil spills, the interfacial tension reduction is crucial for oil emulsification with minimal input of ocean wave energy.[3, 9] The thermodynamic work for emulsification (W) can simply be expressed as a product of two contributions:[73]

$$W = \gamma_{ow} * \Delta A \qquad (5.4)$$

where ΔA is the change in interfacial area and γ_{ow} is interfacial tension. Emulsification involves the creation of more oil-water interfacial area, making W positive and requiring the input of work into the system. Using equation 5.4, the work of emulsification can be minimized by the lowering of interfacial tension, typically by the adsorption of surfactant at the oil-water interface. The nanotubular morphology of the HNT allows for the loading and release of surfactant for the lowering of the oil-water interfacial tension.[80, 97]

Figure 5.8a is the FTIR of the native HNT and Span 80 loaded HNT. The inset to Figure 5.8a shows a representative high resolution TEM image of the Span 80 loaded HNT. The FTIR spectrum of the Span 80 loaded HNT shows characteristic absorption peaks at 535, 911, 1008, 3696 - 3621 cm^{-1} corresponding to the Al–O–Si deformation, O–H deformation of inner surface hydroxyl groups, in-plane Si–O–Si stretching vibration and Al_2–OH stretching bands of the HNT respectively.[95, 129] In addition to peaks attributable to the HNT, the FTIR analysis of the span 80 loaded HNT revealed infrared absorption bands at 1742, 2854 and 2925 cm^{-1} attributable to C=O stretching vibration, symmetric stretching of CH_3 and asymmetric stretching of CH_2 of the Span 80 (Figure 5.1).

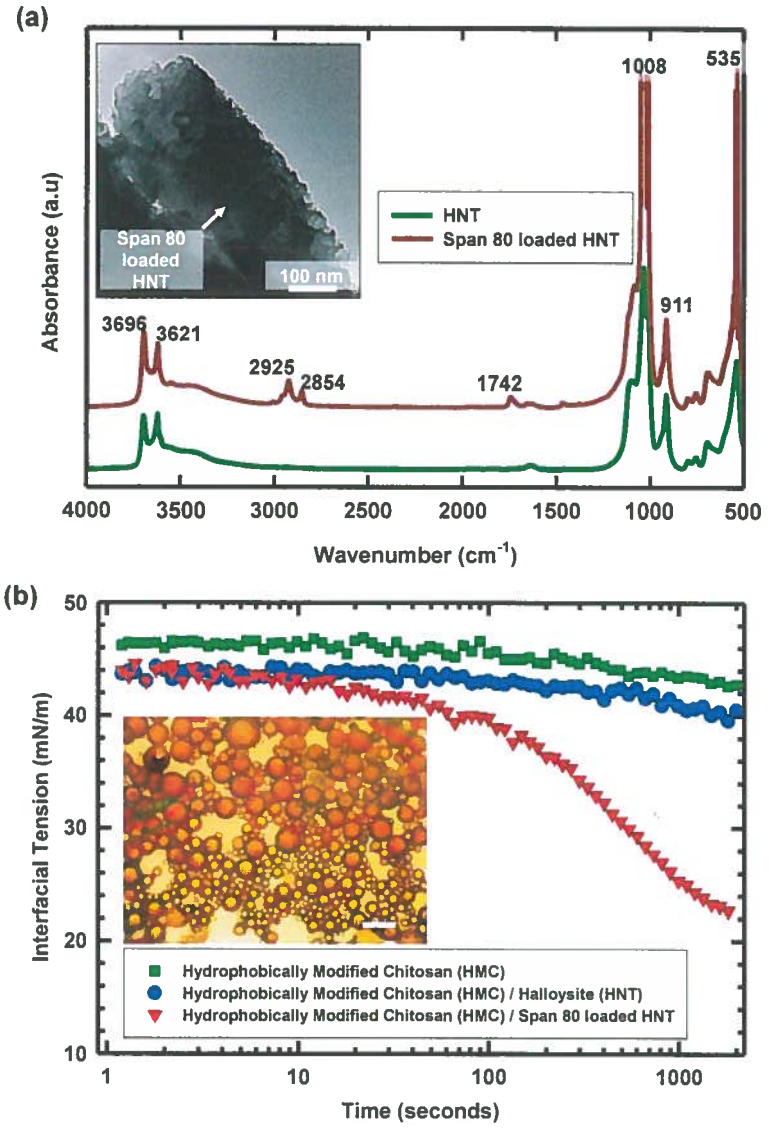

Figure 5.8: (a) FTIR spectra of native HNT and Span 80 loaded HNT. The inset shows a representative TEM image of a Span 80 loaded HNT. (b) Dynamic interfacial tension measurements for dodecane–water interface laden with HMC (green squares), HMC/HNT (blue circles), and HMC/Span 80 loaded HNT (red triangles). The HMC, HNT and Span 80 loaded HNT concentrations in the aqueous droplet were 0.05 wt%, 0.1wt% and 0.1 wt% respectively. The inset shows optical micrograph of crude oil in saline water emulsion prepared with span 80 loaded HNT (0.1 wt%) and HMC (0.05wt%). Scale bar is 100μm.

Figure 5.8b presents dynamic interfacial tension measurements showing the influence of the low molecular weight surfactant, Span 80 in lowering the interfacial tension. The HMC/HNT/Span 80 system has inorganic tubular micelle architecture with the water insoluble surfactant, Span 80, loaded onto the HNT core and the HMC macromolecule in the external domain. Figure 5.8b reveals that the HMC and HNT show negligible interfacial tension reduction ability. This observation is in agreement with previous report that the HMC does not significantly lower the oil-water interfacial tension.[17] The synergistic effect of HMC and the clay nanotubes in enhancing emulsion stability is also not due to a reduction in interfacial tension but by providing an electrosteric barrier to droplet coalescence. However, the release of the small molecule surfactant Span 80 from the HNT at the oil-water interface, results in a significant reduction in interfacial tension. The unique nanotubular morphology of halloysite facilitates the integrative application with the polymeric surfactant, HMC, and the low molecular weight surfactant, Span 80 for effective oil emulsification.

5.4 Conclusions

Integrative electrostatic and hydrophobic effects drives the interfacial co-adsorption of the cationic HMC biopolymer and the particulate HNT resulting in improved emulsion stability to coalescence and oil emulsification into much smaller droplets. The HMC biopolymer adsorbs on the negatively charged HNT by electrostatic attraction and hydrophobic associations between the hydrophobic residues of HMC chains. The anchoring of the HNT together at the oil-water interface and modification of HNT wettability by the hydrophobically modified biopolymer HMC are key mechanisms that increase the energy barrier required to detach the particles from the interface, leading

to enhanced emulsion stability. The cationic HMC biopolymer adsorbs on the negatively charged HNT by electrostatic attraction and cryo-SEM imaging revealed that the HMC anchors its hydrophobic residues into oil droplets by the hydrophobic effect. Smaller droplet sizes are obtained with increasing HMC concertation but the attachment of the particulate HNT at the oil-water interface is crucial in providing sufficient steric resistance to coalescence. The concepts advanced in this work can be exploited for anchoring hydrocarbon degrading bacteria onto nutrient loaded HNT using the simultaneous electrostatic attraction of the cationic HMC to the negatively charged HNT and the hydrophobic interaction of HMC with the hydrophobic domains of bacterial cell bilayer membranes.[139] This is significant in oil emulsification and nutrient enhanced bioremediation processes[10] at the oil-water interface. A multifunctional amphiphile system consisting of Span 80 loaded HNT and high molecular weight HMC[17] may find applications in the herding, gelation[17] and mobilization[97] of surface oil layers.

CHAPTER 6

FORMATION MECHANISM AND EMULSION STABILIZATION CHARACTERISTICS OF HOLLOW PARTICLES SYNTHESIZED IN A SURFACTANT AIDED AEROSOL PROCESS

6.1 Introduction

Hollow particles have attractive properties such as their low density and high capacity for guest compounds facilitating applications such as sensor technologies,[140] catalysis,[141, 142] controlled release,[24, 143] materials synthesis.[26, 32, 144] and oil spill remediation.[80, 97] The hollow morphology of particles such as naturally occurring halloysite aluminosilicate mineral has been exploited in the encapsulation and delivery of surfactant to the oil water interface for oil spill remediation applications.[80] In addition to the use of naturally occurring hollow materials, the rapid and scalable synthesis of particles with a hollow morphology has huge scientific and technological significance.[145]

Typically, the synthesis of such hollow particles requires building a desirable material layer around a core, followed by removal of the core by dissolution or high temperature calcination.[25, 27, 145, 146] Consequently, these synthetic approaches involve multistep operations and complex components, leading to difficulties in scale up to commercially viable quantities.[30] However, using a rapid and scalable surfactant-aided aerosol process, we are able to synthesize hollow silica microspheres encapsulating ferromagnetic iron oxide nanoparticles. This potentially eliminates the difficulties in

scale up to commercially viable quantities often encountered in the synthesis of hollow silica particles.

Our work described here deals with the introduction of a templating surfactant such as the cationic surfactant, cetyl trimethylammonium bromide (CTAB), into a solution containing a silica precursor such as tetraethylorthosilicate (TEOS) which leads to the rapid formation of ordered mesoporous silica in an aerosol-based process.[29, 147] In our previous work[31] we explored the possibility of incorporating iron oxide in mesoporous silica particles. On doping increasing amounts of $FeCl_3$ into the precursor solution, the silica particles gradually lost their ordered mesostructure leading to particles with disordered structure. Surprisingly, further increase of the $FeCl_3$ loading resulted in a significant morphological transformation to hollow silica spheres encapsulating iron oxide nanoparticles. Hollow structured particles with a silica-carbon shell have also been synthesized by the introduction of sucrose into the precursor solution as a carbon source.[30]

However, a translucent solution appearance is observed that upon mixing of $FeCl_3$ and CTAB in solution. This translucent appearance was not observed in the absence of $FeCl_3$. Our hypothesis is that, the translucent solution appearance is a result of the formation of colloidal aggregates by salt bridging between iron chloride and CTAB. We envisage that this will disrupt the co-assembly of CTAB with silicate species by the preferential partitioning of CTAB to the iron chloride salt. During the aerosol process, this salt bridging effect locks the surfactant (CTAB) within the interior of the rapidly forming silica shell as aerosol droplets pass through the heating zone. Subsequent

calcination removes CTAB from the core of the spheres leading to the formation of hollow silica spheres encapsulating iron oxide nanoparticle.

The objective here is to understand the colloidal nature of the solution that produces hollow silica microspheres through the aerosol-based process. Furthermore, we will explore if adding molar equivalents of other salts into the precursor solution will bring about the structural transition from mesoporous to hollow silica particles. Light scattering, NMR spectroscopy and conductometry techniques are used to elucidate how salts influence the aggregation properties of the CTAB template in solution. Relevant to potential applications as particulate oil spill dispersants, we demonstrate the interfacially activity of hollow structured silica-carbon composite particles synthesized using the scalable aerosol process.[30]

6.2 Experimental Procedures

6.2.1 Materials

Cetyl trimethylammonium bromide (CTAB), ferric chloride ($FeCl_3$), ferric nitrate ($FeNO_3$), chromium chloride ($CrCl_3$), sucrose, isooctane and tetraethylorthosilicate (TEOS) were purchased from Sigma-Aldrich. Deuterium oxide (99.9%) and ethanol-d6 (CD_3CD_2OD, 99.9%) were purchased from Cambridge Isotope Laboratories. All compounds were used as received.

6.2.2 Synthesis of Silica Particles

In a typical synthesis, 1.0 g of $FeCl_3$ was dissolved in 15 mL of ethanol with stirring followed by the addition of 1.1 g of CTAB. 4.5 mL of TEOS was then added to

the solution, followed by 1.8 mL of 0.1 M HCl solution. The resulting solution was aged for 30 minutes under stirring. The salt concentration in the ethanol-water solvent was 0.22M and the concentration of H^+ was 0.1 M. Silica particles were then produced using the aerosol apparatus which was described in detail in our previous work.[30] In brief, the precursor solution was atomized to form aerosol droplets, which was then sent through a quartz tube placed in a furnace where preliminary solvent evaporation and silica condensation occurred. The temperature of the heating zone was held at 400 °C, and the entering gas pressure of N_2 was adjusted to yield a droplet residence time of about 15s through the furnace.

The resulting particles were collected on a filter maintained at 80 °C. The as-synthesized particles were calcined in air at 500 °C for 3 hours to remove the surfactant and solvent. Similarly, this procedure was employed to synthesize silica particles from solutions containing 0.22 M of $Fe(NO_3)_3$ and $CrCl_3$ respectively. Silica particles were also synthesized without addition of salt. The quantity of ethanol, CTAB, TEOS and 0.1M HCl was same for all the experiments.

Silica-carbon particles were synthesized following the same procedure but with the addition of 1 g sucrose into the precursor solution.[30] The precursor solution was atomized and sent through the furnace where preliminary solvent evaporation, sucrose carbonization and silica condensation occurred. The particles were then pyrolyzed at 500 °C for 3 h under the flow of N_2 gas.[30]

6.2.3 Particle characterization

The morphology of the particles was characterized using transmission electron microscopy (FEI Tecnai G2 F30 Twin Transmission Electron Microscope operated at

300 kV), and X-ray diffraction (XRD, Siemens, D 500, using Cu KR radiation at 1.54 Å.). The porosity of the particles was measured by the nitrogen sorption technique at 77 K (Micromeritics, ASAP 2010).

6.2.4 Light Scattering Experiments

Static light scattering experiments were carried out at 25^0C using the Simultaneous Multiple Sample Light Scattering (SMSLS)[148] instrument using a 35 mW diode laser emitting vertically polarized light at a wavelength of 660 nm. Evolution of light scattering intensity was monitored in real time for CTAB alone and mixtures of CTAB with each salt. The first set of light scattering experiments was carried out with same concentrations of CTAB and salts in ethanol/0.1M HCl used in synthesizing the particles. The second set of experiments was carried out using same concentration of CTAB but with increasing $FeCl_3$ concentrations of 0M, 0.06M, 0.13M, 0.17M and 0.22M in the ethanol/0.1M HCl solvent.

6.2.5 ^{1}H NMR and Conductivity Measurements

^{1}H NMR spectra were obtained with a Bruker 500 MHz NMR spectrometer operating at 25^0C. Solutions of CTAB and salts were prepared in ethanol-d6. 0.1M HCl was prepared in D_2O and added to the surfactant solution. NMR experiments were carried out at salt concentrations of 0.0247M. NMR experiment of CTAB in the acidified ethanol-d6/D_2O served as the control experiment. About 1 ml of each solution was transferred to a 5 mm NMR tube and chemical shifts were recorded on the δ scale.

Conductivity was measured at 298K as a function of CTAB molality at fixed salt and HCl content using a Fisher Scientific Traceable Bench Conductivity Meter. The conductivity cell was calibrated with standard KCl solution. Stock solutions of CTAB

and salts were prepared in ethanol and then desired mole fractions of surfactant were prepared by mixing pre-calculated volumes of stock solutions.

6.2.6 Oil Emulsification using Silica-Carbon Particles

0.30wt% particle suspension was prepared by uniformly dispersing 0.0067g of the particles in 2.25ml of water by ultrasonication (Cole-parmer 8890) for 2 minutes. Emulsions were prepared at isooctane to water ratio of 2:3 by mixing the aqueous dispersion of particles with 1.5ml of isooctane for 2 min using an IKA Ultra-Turrax T-18 homogenizer with a S10N-5G dispersing element operating at 30000 rpm. Crude oil (BP-MC 252) in seawater emulsion was also prepared using this procedure.

6.2.7 Emulsion Characterization

The emulsion was characterized by Optical Microscopy and Cryogenic Scanning Electron Microscopy (Cryo-SEM) techniques. For optical imaging, a small aliquot of the isooctane-in-water emulsion stabilized by the silica-carbon particles was removed using a Pasteur pipet and diluted with water prior to imaging on a Leica DMI REZ optical microscope. The images were analyzed using Image ProPlus v. 5.0 software to obtain the droplet size distribution.

Cryo-SEM imaging was performed using a Hitachi S-4800 field emission Scanning Electron Microscope operated at a voltage of 3 kV and a working distance of 9 mm. The emulsion sample was first plunged into liquid nitrogen, followed by fracturing at −130 °C using a flat-edge cold knife and sublimation of the solvent at −95 °C for 5 min. The sample was sputtered with a gold–palladium composite at 10 mA for 88 s before imaging. Interfacial tension measurements were made using the pendant drop

method on a standard goniometer (Ramé-Hart, model 250) with analysis carried out using DROPimage Advanced Software.

6.2.8 Contact Angle Measurement

Thin films were synthesized by spray deposition[149] of the precursor solution on a silicon wafer for 10 minutes using the aerosol setup but without operating the furnace. The silicon wafer was fixed on the filter setup by a double-sided tape. Formation of the continuous thin film occurs via droplet coalescence (Aerosol assisted formation of mesostructured thin films) on the silicon substrate. The film is allowed to dry for 24hours before pyrolysis at 500 °C for 3 h under the flow of N_2 gas to produce the silica-carbon composite film. The silica-carbon thin film was imaged on a FEI Tecnai G2 F30 Twin Transmission Electron Microscope operated at 300 kV by scratching off the film on the surface of the silicon wafer onto the TEM grid using a razor blade. The flat film was used for contact angle measurement on a Rame-Hart contact angle goniometer. The thin-film coated silicon wafer was immersed in isooctane contained in a rectangular cell. A drop of water, about 5µL, was then placed onto the film. The contact angle was measured at 25^0C through the aqueous phase at the isooctane, water and silica-carbon thin film interface.

6.3 Results and Discussion

6.3.1 Salt Effects on Silica Particle Morphology

The morphology of the calcined silica particles was examined using transmission electron microscopy (TEM) and X-ray diffraction (XRD). Figure 6.1 shows TEM images of silica particles synthesized with and without the addition of salts into the precursor solutions. Figure 6.2 is the low angle XRD data for particles synthesized without addition

of salt (curve a) and with addition of 0.22M $CrCl_3$ (curve b), $Fe(NO_3)_3$ (curve c) and $FeCl_3$ (curve d) respectively. The inset to Figure 6.2 is the high angle XRD data for particles synthesized with addition of salts.

Figure 6.1a – 1b are low and high resolution TEM images of mesoporous MCM 41-type, silica particle prepared without adding salts and is the control experiment to clearly demonstrate the ability of CTAB to template silica particles with well-ordered hexagonal pore mesostructure. Low angle XRD of the MCM 41-type, silica particle prepared without adding salts (curve a in Figure 6.2) clearly shows a highly ordered hexagonal structure through the presence of the (100), (110), and (200) peaks.[31, 150] The characteristic d-spacing for the (100) planes is 3.34 nm, and the material has a high surface area of 1020 m^2/g (Table 6.1).

Figure 6.1c - d, 6.1e – f and 6.1g – h are representative TEM images of particles synthesized with the addition of 0.22M $CrCl_3$, $Fe(NO_3)_3$ and $FeCl_3$ respectively. The addition of $CrCl_3$ resulted in particles that are closest to the ordered mesoporous silica obtained without the addition of salt. However, the lower intensity in the low-angle XRD (Figure 6.2) indicates it has a lower degree of order compared to the mesoporous silica. Nanoparticles about 20nm in size are formed mainly on the surface of the silica particles. High angle XRD confirms that the nanoparticles were chromium oxide (Cr_2O_3) nanoparticles (inset to Figure 6.2, curve i). Moreover, it is clear that silica particles synthesized with $CrCl_3$ show a more ordered mesostructure compared to particles made with $Fe(NO_3)_3$ or $FeCl_3$.

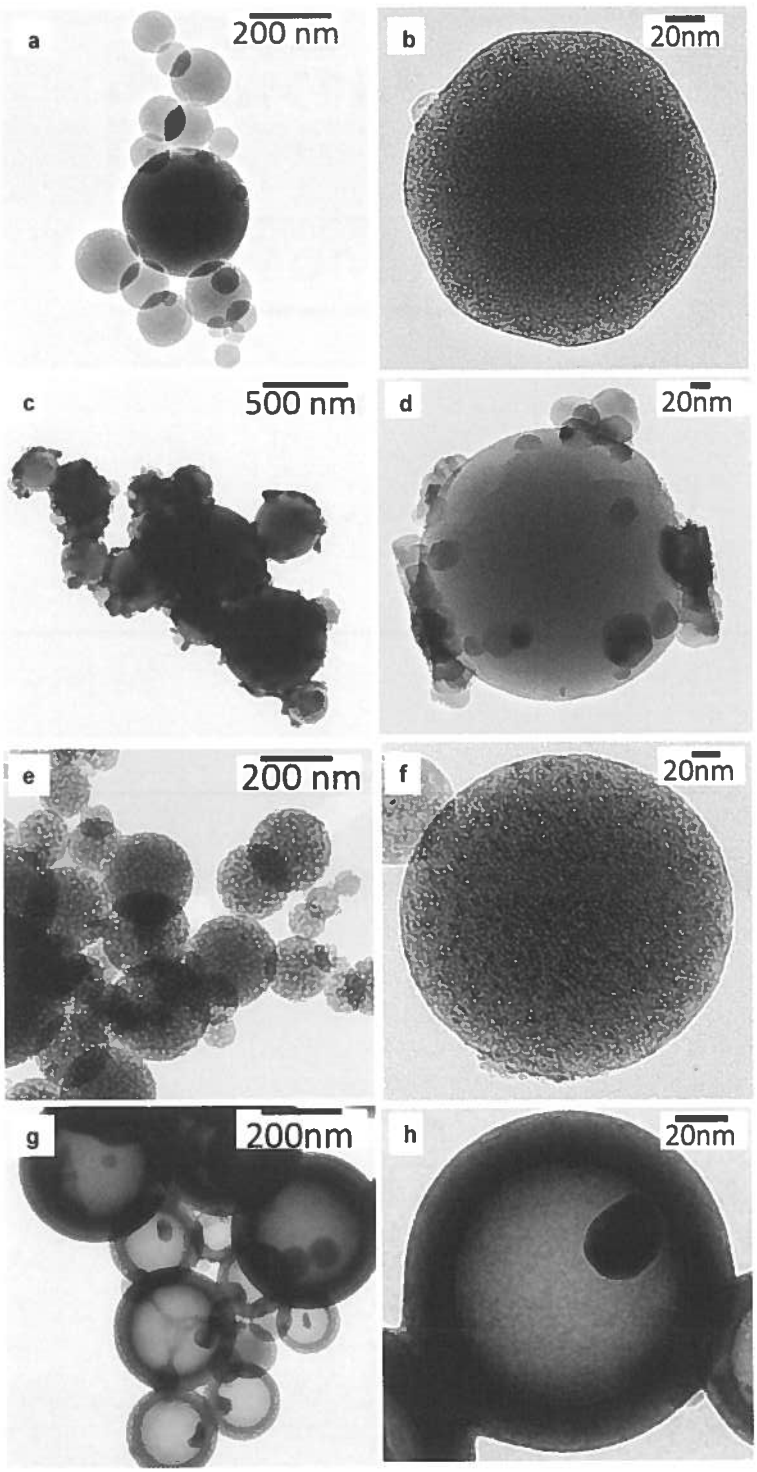

Figure 6.1: TEM images of particles synthesized with 1.1g of CTAB without addition of salt (a, b) and with 0.22M of $CrCl_3$ (c, d), $Fe(NO_3)_3$ (e, f), and $FeCl_3$ (g, h).

With addition of $Fe(NO_3)_3$, silica microspheres having a fairly homogeneous distribution of darker spots corresponding to a higher electron density, throughout the particles. High-angle XRD (inset to Figure 6.2, curve ii). confirms that the formation of hematite, the most thermodynamically stable polymorph of iron oxide[151] in the in the silica particle. However, Figure 6.1d shows that the addition of $FeCl_3$ to the precursor solution results in the structural transition from mesoporous to hollow silica spheres encapsulating iron oxide nanoparticle. High angle XRD (inset to Figure 6.2, curve iii) reveals that the encapsulated nanoparticle is hematite. Unlike with $FeCl_3$, hollow particles are not produced with molar equivalents of either $Fe(NO_3)_3$ or $CrCl_3$ (Figure 6.1c – 1f).

In general, the (100) XRD peaks are broadened and have reduced intensities upon the addition of salts (Figure 6.2) showing the loss of crystalline order. In addition, BET area measurements shows that the surface area of the particles decreases with the degree of deviation from ordered mesoporous silica (Table 6.1). The TEM images, XRD and BET data all indicate that the addition of salts results in varying degree of deviation from the well-ordered mesoporous silica. The addition of salt clearly decreases the structured-order of the hexagonal channels[152] in the silica particles, and implies a disruption of the co-assembly of silicate and surfactant species. However, it is only with $FeCl_3$ that there is a unique transition to hollow microspheres produced only with $FeCl_3$. More importantly, we can infer that the structural transition from mesoporous to hollow silica microspheres in the surfactant-aided aerosol process is not achieved by Fe^{3+} or Cl^- ion independently, but by the combination of both ions in $FeCl_3$. Moreover, the addition of $CrCl_3$ produces significant deposition of the resulting chromium oxide on the particle surface while the

iron salts produces iron oxides that are largely retained on the inside of the silica particles.

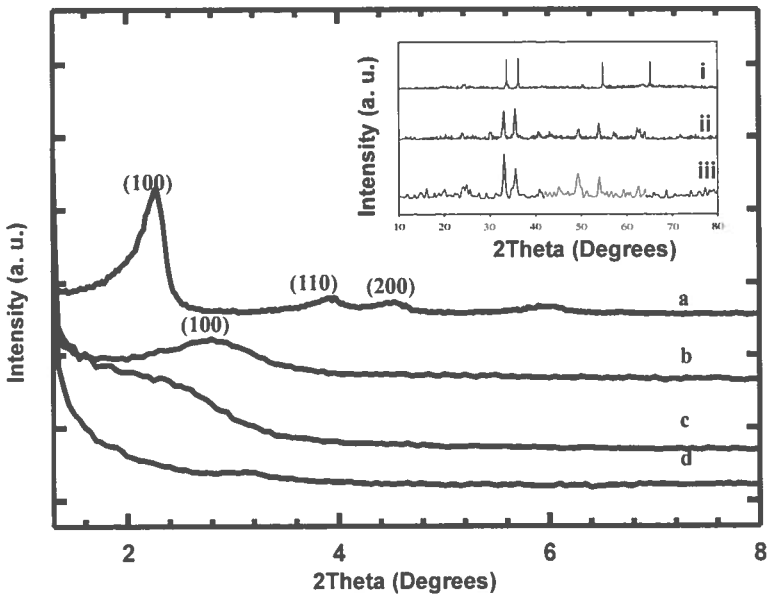

Figure 6.2: Low-angle XRD of (i) silica particles synthesized without salt (a), and with 0.22M of $CrCl_3$ (b), $Fe(NO_3)_3$ (c), and $FeCl_3$ (d) respectively. The inset shows the high-angle XRD of showing metal oxide peaks for silica particles synthesized with $CrCl_3$ (i), $Fe(NO_3)_3$ (ii), and $FeCl_3$(iii).

Table 6.1: Surface areas of particles synthesized with and without addition of salts

Silica Particles	BET surface area (m^2/g)
Without salt	1020
With $CrCl_3$	644
With $Fe(NO_3)_3$	40
With $FeCl_3$	20

6.3.2 Colloidal Assembly in Precursor Solution

Light scattering, NMR and conductivity measurement techniques were carried out to further understand the effect of salt addition on the aggregation behavior of CTAB species in solution. Figure 6.3a shows the time evolution of the normalized scattered intensity for mixtures of CTAB with salts in the acidified ethanol/water solvent. Raw light scattering intensity data were normalized for each system by dividing with the intensity at zero time. As can be seen, the extent of CTAB aggregation is significantly greater in the presence of $FeCl_3$, likely due to the formation of colloidal aggregates. The plot shows that the scattering intensity increases rapidly initially and then plateaus with time. Results of the control experiments are shown in Figure 6.3b where scattering intensities of solutions with CTAB alone, or $FeCl_3$ alone are compared to the system with both CTAB and $FeCl_3$. In both controls, there is no evidence of aggregate formation in solution. Therefore, the observed evolution of light scattering intensity with time appears to be the result of the interaction of $FeCl_3$ and CTAB in solution.

In addition, there appears to be a correlation between the extent of aggregation observed for a salt-CTAB system in the light scattering experiment and the deviation from the ordered mesoporous structure of the resulting silica particles it templates. The strong aggregation effect on the addition of $FeCl_3$, implies that the concentration of free CTAB will likely not be high enough to drive their co-assembly with silicate, significantly preventing the formation of mesoporous silica. Figure 6.4 shows the evolution of light scattering intensity with increasing levels of $FeCl_3$. Increasing $FeCl_3$ concentration enhances the degree of light scattering due to the increased formation of colloidal aggregates.

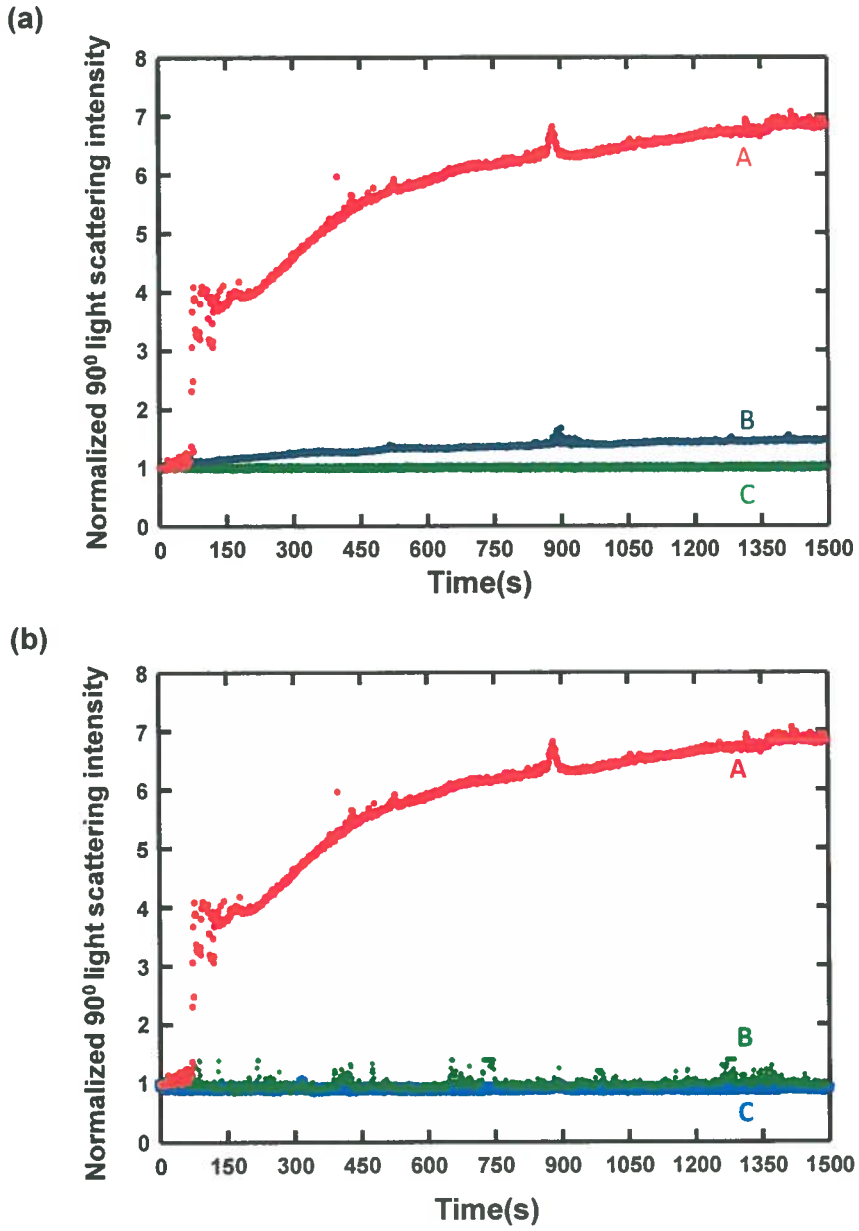

Figure 6.3: (a) Evolution of normalized light scattering intensity with time for CTAB and $CrCl_3$ (green curve), CTAB and $Fe(NO_3)_3$ (blue curve) and CTAB and $FeCl_3$ (red curve) in ethanol/0.1M HCl solvent at 0.22M salt concentration. The enhanced scattering seen for $FeCl_3$ is the result of the formation of colloidal aggregates. (b) Evolution of normalized light scattering intensity with time for CTAB (blue curve), $FeCl_3$ (green curve) and CTAB and $FeCl_3$ (red curve) in ethanol/0.1M HCl solvent.

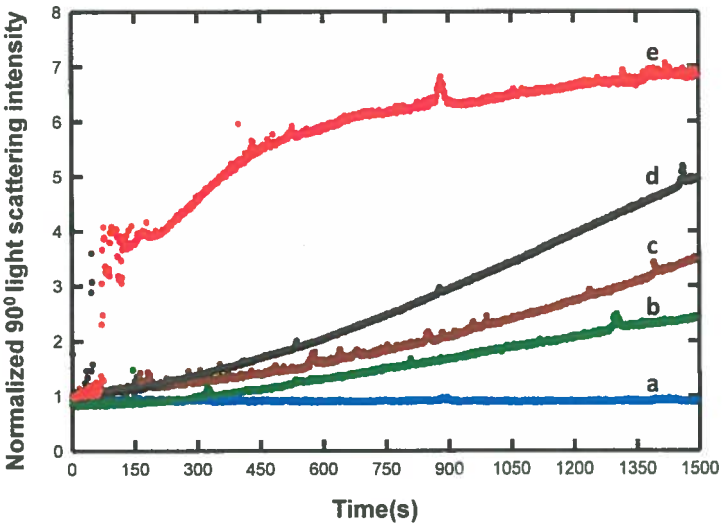

Figure 6.4: Evolution of normalized light scattering intensity with time for CTAB with 0M(a), 0.06M (b), 0.13M (c), 0.17M (d) and 0.22M (e) $FeCl_3$ in ethanol/0.1M HCl solvent. Raw scattering intensity data were normalized for each system by dividing with the intensity at zero time.

The ^1H NMR spectra of CTAB and CTAB-salt systems in deuterated ethanol-water solvent at 25^0C are shown in Figure 6.5a. The NMR experiment was carried out at a lower salt concentration due to the paramagnetic nature of the salt ions. CTAB proton assignments are indicated on the control NMR experiment for CTAB (spectra I). Figure 6.5a shows that addition of salts results in an upfield shift of CTAB proton signals, indicating that the protons are shielded on addition of salts. The surfactant signals in the NMR spectra are also broadened. Typically, addition of inorganic salts to surfactant solutions promotes surfactant aggregation by reducing the electrostatic repulsion among the surfactant headgroups. This changes the microenvironment of surfactant protons causing chemical shifts of proton signals.

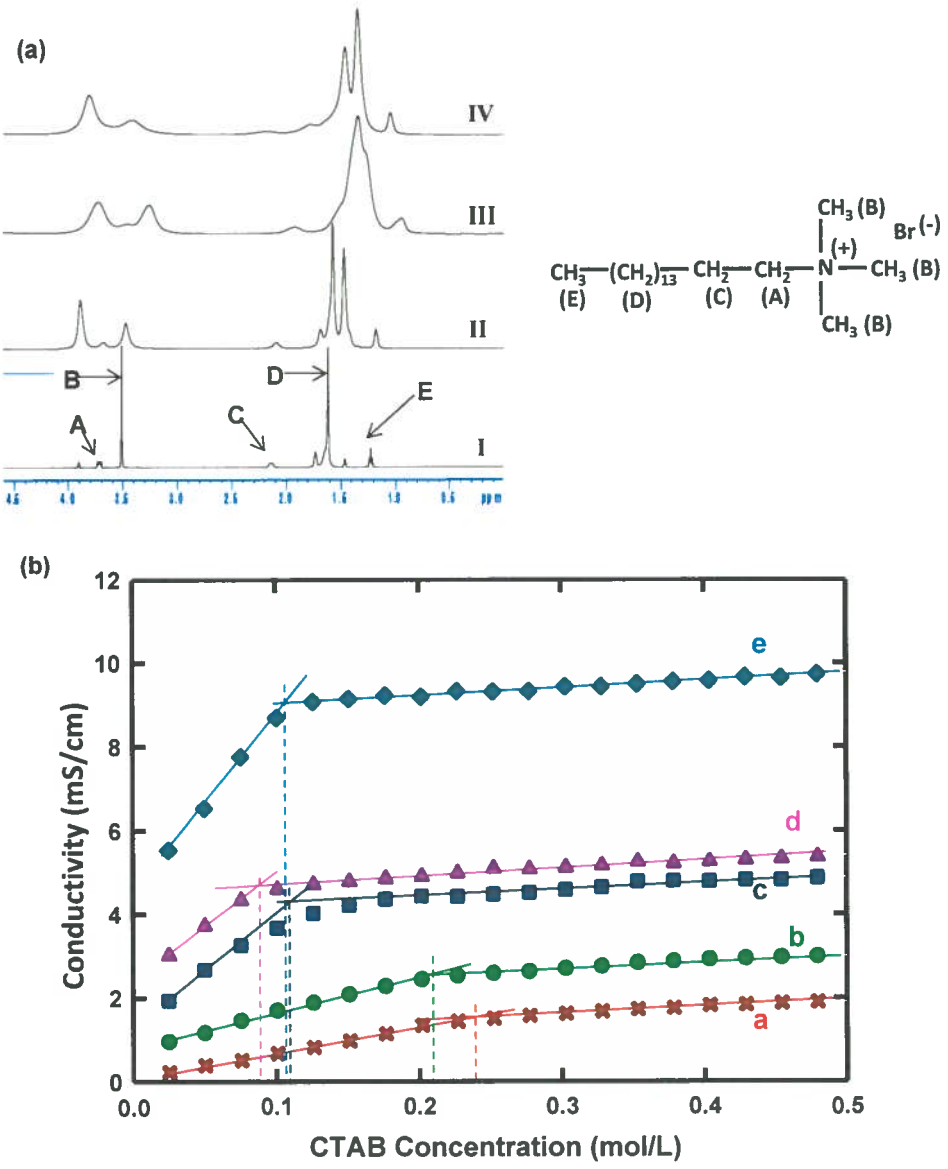

Figure 6.5: (a) ^{1}H NMR spectra of CTAB (I), CTAB and $CrCl_3$ (II), CTAB and $Fe(NO_3)_3$ (III), CTAB and $FeCl_3$(IV) in CD_3CD_2OD/0.1M HCl in D_2O solvent. (b) Plots of conductivity as a function of CTAB concentration. Plot a is the control experiment for CTAB in ethanol. Plot b is without addition of salt in the ethanol/0.1M HCl solvent while plot c, d and e are at fixed salt concentration of 0.22M for $CrCl_3$, $Fe(NO_3)_3$ and $FeCl_3$ and respectively.

However, we observe that the signals are downfield with the chloride salts relative to the nitrate salt. This suggests that the salt anions play a key role in the interaction of the cationic surfactant, CTAB and cationic ferric or chromic species. The anion mediated $S^+X^-I^+$ route has been proposed for the interaction of a cationic surfactant S^+, intermediate anion X^-, and cationic inorganic species I^+ in solution.[31, 153] The NMR spectra with iron salts are broader compared to the chromium salt. This suggests the iron salts are in closer proximity to CTAB compared to the chromium salt and may explain why addition of iron salts produced iron oxides that were largely retained on the inside of the particles. With $CrCl_3$ on the other hand, there is significant formation of the resulting chromium oxide on the surface of the silica particles.

Moreover, surfactant aggregation will generate species that are much larger than surfactant monomers. These aggregates should diffuse more slowly through solution and so become less efficient charge carriers. Therefore, conductivity measurements as a function of CTAB concentration at fixed salt concentrations are expected to show how the salts affect the aggregation behavior of CTAB.[154] Figure 6.5b shows plots of conductivity as a function of surfactant concentration while Table 6.2 summarizes the critical micelle concentration (CMC) obtained from each plot. From Figure 6.5b and Table 6.2, the CMC of CTAB in ethanol is 0.24M and this value agrees with the reported value determined by steady-state fluorescence measurements.[155] This CMC of CTAB in ethanol is about 266 times greater than the CMC in water.[155] The dielectric constant of ionic surfactant systems is lower in ethanol, as a result, the electrostatic repulsion among the ionic surfactant head groups would increase.[156] The relationship between the CMC of a surfactant and the dielectric constant of the solvent is expressed in the equation:[15]

$$\log CMC = K_g/Z_i \left[log \frac{2000\pi\sigma^2}{\varepsilon_r RT} - logC_i \right] + \left[\frac{\Delta G(-CH_2)}{2.3RT} \right] N + constant \qquad (6.1)$$

where (K_g/Z_i) is the slope of the plot of CMC versus total concentration C_i, in equivalents per liter, of the counterions of charge Z_i in the solution, σ is the charge density on the micelle surface, ε_r is the dielectric constant of the solvent, K_g is the effective coefficient of the electrical energy of micellization, R is gas constant, T is temperature, $\Delta G(-CH_2-)$ is the free energy change involved in the transfer of a methylene unit in the hydrophobic group from the aqueous solution to the interior of the micelle, and N is the total number of carbon atoms in the hydrophobic group. The dielectric constant of water is 78.39 while that of ethanol is 24.55.[155] Consequently, the decrease in the dielectric constant of the solvent medium will increase the CMC of the surfactant.[15, 156] Furthermore, the hydrophobic interaction between hydrophobic groups of surfactants is reduced. These two effects decrease the potential for micellization in ethanol resulting in a higher CMC for the surfactant.[156] As expected with higher water content, the CMC of CTAB in the acidified ethanol/water solvent reduces to 0.21M.

Table 6.2: Critical Micelle Concentration (CMC) obtained from conductivity plots

Plot	Component(s)	Solvent	CMC(M)
A	CTAB	Ethanol	0.24
B	CTAB	Ethanol/ 0.1M HCl	0.21
C	$CTAB/CrCl_3$		0.11
D	$CTAB/Fe(NO_3)_3$		0.107
E	$CTAB/FeCl_3$		0.09

However, addition of inorganic salts to ionic surfactant solutions further promotes surfactant aggregation, causing a change in the CMC of the surfactant. The decrease in CMC is due mainly to the decrease in the thickness of the ionic atmosphere surrounding the ionic head groups in the presence of additional electrolyte. This reduces the electrostatic repulsion among surfactant head groups in the micelle. In essence, salt ions acts as a bridge[157] between nearest-neighbor surfactant head groups. Conductivity measurements were carried out to compare the bridging effect of each salt on the aggregation of CTAB. It can be seen that at the same molar concentration, the salts enhance the aggregation of CTAB, but to different extents. For the same cation Fe^{3+}, the effect of anions on the CMC follows the order $Cl^- > NO_3^-$. This clearly follows the ion-surfactant binding strength in the Hofmeister series.[158] The stronger binding Cl^- counter-ion will be more efficient at promoting surfactant aggregation.[159] However, for the same anion Cl^-, the effect of cations is in the order $Fe^{3+} > Cr^{3+}$. This suggests that although the anions play a key role, the interaction of salts with CTAB is not a simple anion exchange reaction. The high hydration of certain structure-making ions, which includes Fe^{3+}, has been considered to cause further reduction in surfactant hydration, promoting micelle formation at lower surfactant concentrations[160, 161]

The aerosol-based process that produces the ordered mesoporous silica starts with a precursor solution with initial surfactant concentration of 0.18M which is less than 0.21M, the CMC of CTAB in the acidified ethanol/water solvent. However, the addition of salts drives the assembly of the templating surfactant, CTAB from the pre-micellar to the micellar region (Figure 6.5b, Table 6.2) leading to changes in morphology of the resulting silica particles. In agreement with light scattering and NMR results, the

conductivity data indicates additive effects of the anion and cation in each salt on the aggregation of surfactant species in solution. Addition of $FeCl_3$ strongly enhances the aggregation of the templating surfactant CTAB, disrupting its co-assembly with silicate species. Salt bridging between iron chloride and CTAB leads to the formation of colloidal aggregates. CTAB is preferentially adsorbed onto ferric colloids and coagulates the colloids to form larger clusters. This essentially locks the surfactant (CTAB) within the interior of the rapidly forming silica shell during the passage of the aerosol droplets through the heating zone of the tube furnace (Figure 6.6). The silica shell is formed by preferred silicate condensation on the gas–liquid interface of the aerosol droplet, with the core rich in iron and CTAB species. Calcination removes CTAB in the core of the spheres[28] leading to the formation of hollow silica spheres encapsulating iron oxide nanoparticle. Thus, the surfactant loses its ability to template mesoporous silica. It is clear from our results that the morphology of silica particles synthesized in the aerosol-based process depends on the condition of the precursor solution.

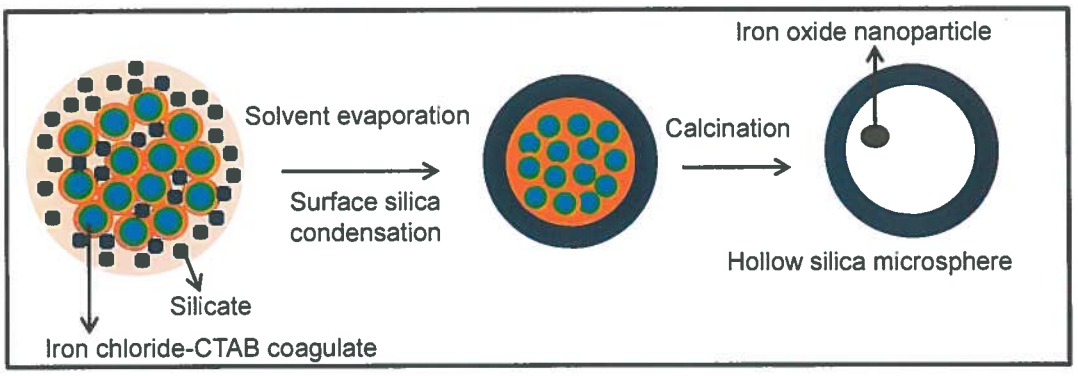

Figure 6.6: Colloidal aggregation and droplet transformation through aerosol process

6.3.3 Emulsion Stabilization Characteristics of Silica-Carbon Particles

The introduction of sucrose into the precursor solution leads to the formation of hollow structured silica-carbon particles on pyrolysis in an inert atmosphere.[30] In a recent work, we advanced that the carbonization procedure of hydrophilic particles is an effective technique for modifying particle wettability for optimal emulsion stabilization.[129] Here, the oil emulsification ability of the silica-carbon particles is investigated. Figure 6.7a shows the photograph of an isooctane-in-water emulsion stabilized by the silica-carbon composite particles and the control experiment with silica particles without carbon. The silica particles in the control experiment were prepared by calcination to remove the carbon and are unable to stabilize the emulsion.[30] The silica particles rapidly partition to the water phase after homogenization. The interfacial activity of the silica-carbon particles derives from the combination of hydrophobic carbon and hydrophilic silica moieties.[129] TEOS is the precursor for the hydrophilic silica while sucrose is the hydrophobic carbon source.[30]

Figure 6.7b shows optical micrographs of the emulsion stabilized by the silica-carbon particles. The stability of the emulsion was studied by analyzing a number of optical micrographs to obtain the droplet size distribution over 4 weeks (Figure 6.7c). Figure 6.7c shows the droplet size distribution after 48 hours of emulsion preparation and after 4 weeks. The average droplet size obtained were 137 μm after 48 hours and 179 μm after 4 weeks. The size distribution after one month indicates the stability of the emulsion. It is noteworthy that this effective silica-carbon particulate emulsifier can be produced in commercially viable quantities using the rapid and scalable aerosol process.

The emulsion phase was imaged with Cryo-SEM to reveal the structure of the silica-carbon particle assembly at the oil water interface (Figure 6.8). The particles form a closely-packed assembly at the oil-water interface. Cryo-SEM imaging clearly reveals the interfacial activity of particles across the whole range of sizes obtained in the aerosol-process.

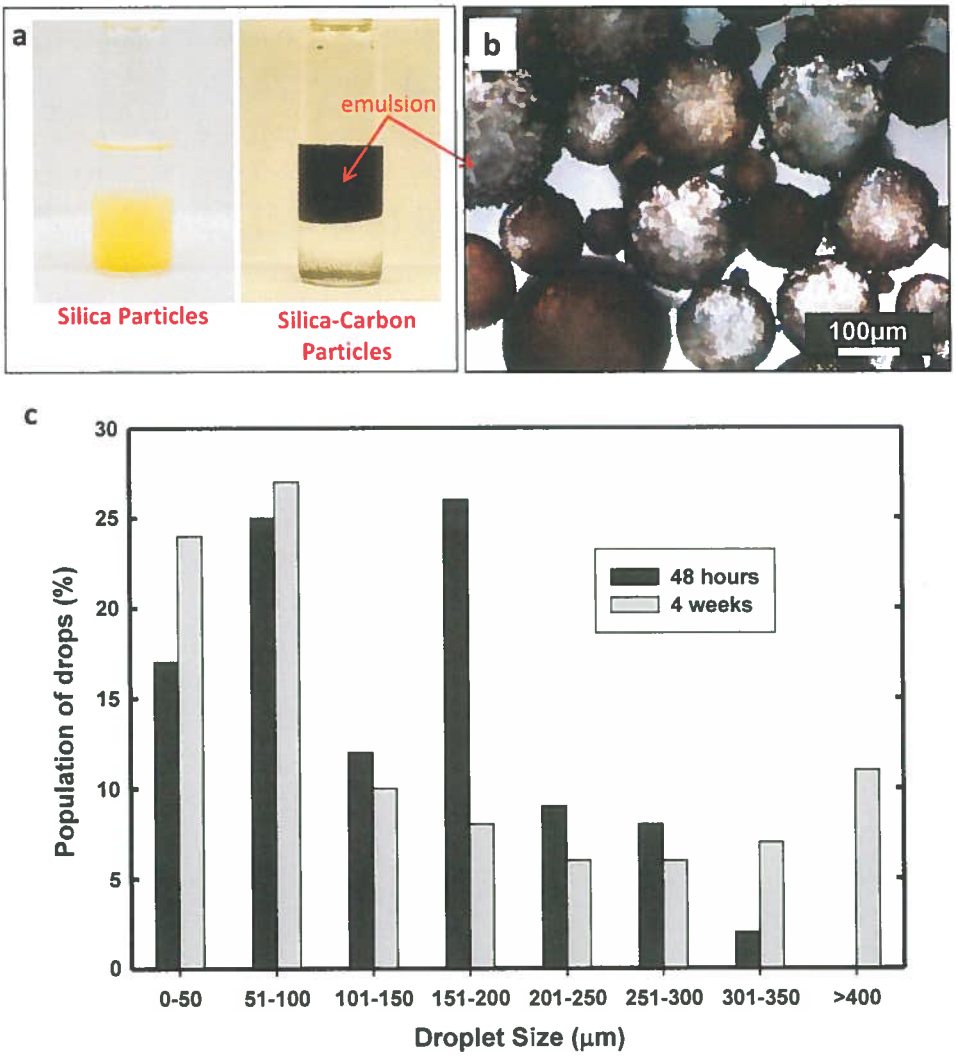

Figure 6.7: (a) Photograph showing emulsion stabilization ability of silica-carbon particles and inability of particles with silica alone to stabilize emulsions. (b) Optical microscopy image of isooctane-in-water emulsions stabilized by the silica-carbon particles. (c) Droplet size analysis showing emulsion stability with time.

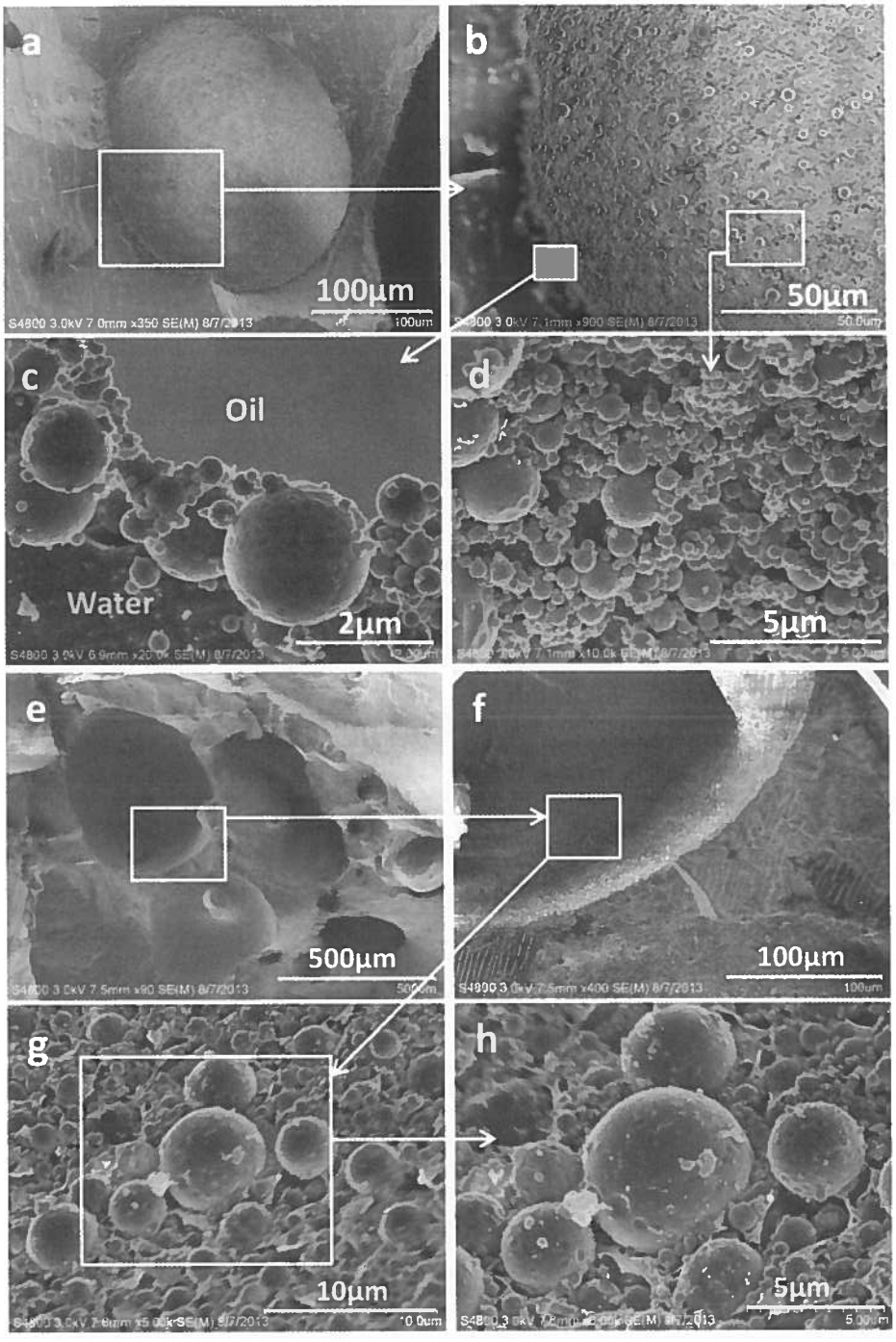

Figure 6.8: Cryo-SEM images of isooctane-in-water emulsion stabilized by silica-carbon. Panels (a) to (d) shows the interfacial adsorption of the particles from the aqueous side of the interface while panels (e) to (h) show the particles imaged from the inner surface of a fractured isooctane droplet.

The free energy change of detachment from the oil water interface for a small colloidal particle (ΔG) is given by:

$$\Delta G = \pi r^2 \gamma_{ow}(1 - cos\theta)^2 \qquad (6.2)$$

where r is the radius of the particle adsorbed at the interface, γ_{ow} is the interfaceial tension between the oil and the water phases, and θ is the contact angle of the particle at the oil water interface.[22] The interfacial tension of the isooctane–water interface was measured using the pendant drop method. A 20μL water droplet was suspended in isooctane with a measured interfacial tension of 50 mN/m in agreement with previously reported values.[162] For a water droplet of the same volume containing 0.3wt% silica-carbon particles, the measured interfacial tension was 49 mN/m. The interfacial adsorption of the particles did not lead to a significant change in the interfacial tension.

Figure 6.9a-c shows the three-phase contact angle on a silica-carbon film prepared by spray deposition of the precursor solution followed by pyrolysis in an inert atmosphere. In the presence of isooctane, the contact angle of water on the silica-carbon thin film surface was measured to be 74^0. Figure 6.9d shows the energy of attachment at the oil-water interface for a hollow particle and solid particle containing equal amount of solid material. For instance, a 200nm radius solid particle has the same amount of solid material as a hollow particle with external radius of 342nm and internal radius of about 274nm. For the hollow silica carbon particle here, the three phase contact angle is measured to be 74^0. From Figure 6.9d and equation 6.2, the energy required to detach the hollow particle is calculated to be $2.5 \times 10^6\ kT$ compared to $8.6 \times 10^5\ kT$ for the solid particle. This stability of the emulsion (Figure 6.7) is a result of the high energy of attachment of the hollow silica-carbon particles are held at the interface which is several

orders of magnitude higher than the kinetic energy of collision between droplets. Thus, the adsorption of the particles provides steric hindrance to droplet coalescence.

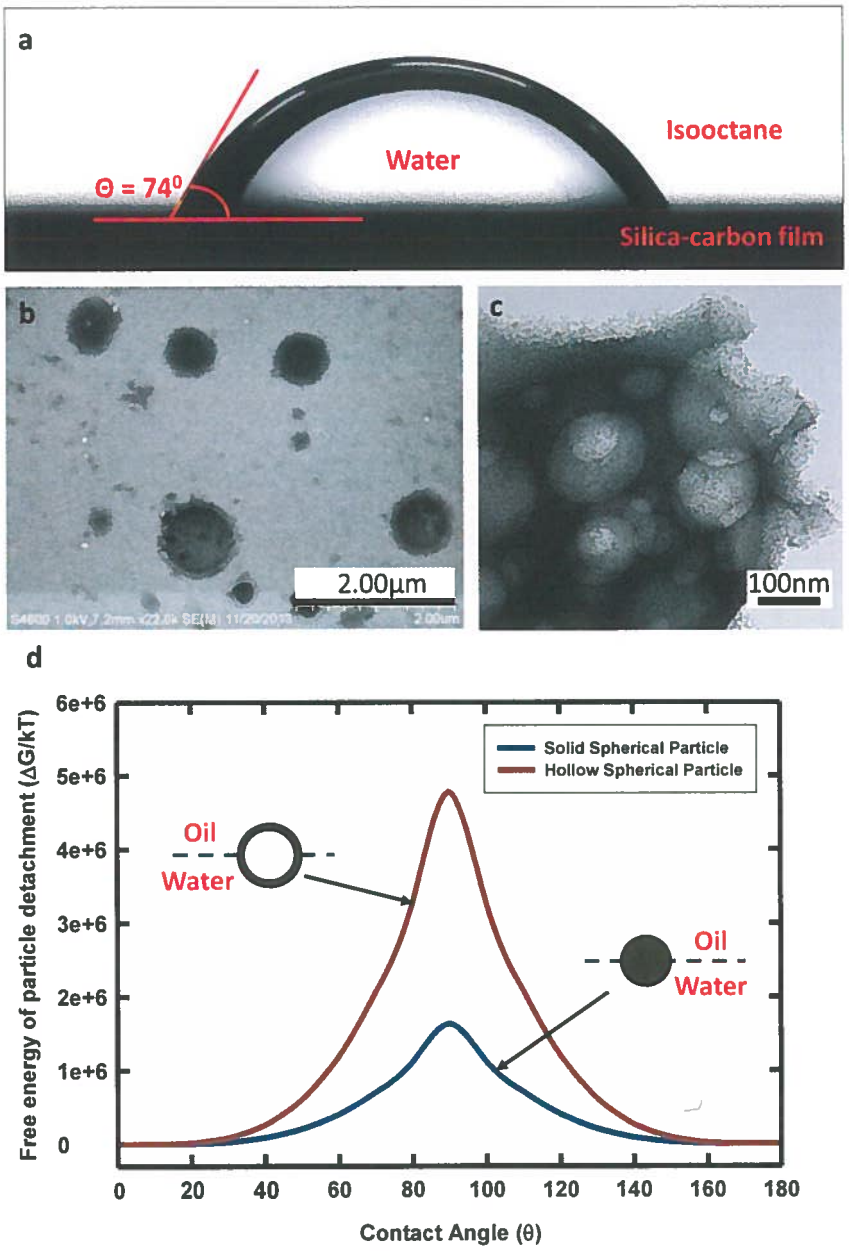

Figure 6.9: (a) Photograph showing contact angle of water drop on silica carbon film in an external isooctane phase. (b) SEM image of silica-carbon film (c) TEM image of silica carbon film (d) Free energy of particle detachment from the oil–water interface as a function of contact angle for a solid spherical particle (blue curve) and hollow spherical particle (red curve). All particles have the same amount of solid material and the oil–water interfacial tension is 49 mN/m.

6.4 Conclusions

The mechanisms governing the morphology of silica particles synthesized by the aerosol-based process has been elucidated by characterizing the interaction of salts and surfactant species in the precursor solution. Results of NMR spectroscopy, conductivity measurements, and light scattering experiments show that CTAB strongly interacts with positively charged ferric species from $FeCl_3$ by an anion mediated $S^+X^-I^+$ route under acidic conditions. Consequently, the CTAB is preferentially adsorbed onto ferric colloids and coagulates the colloids to form larger clusters. During the aerosol process, the silica shell is first formed due to the preferred silicate condensation on the gas–liquid interface of the aerosol droplet. Subsequent drying concentrated the ferric clusters inside the silica shell and resulted in a silica shell/ferric core particle. Amphiphilic silica-carbon particles can be prepared using a rapid and scalable aerosol-based process. The silica-carbon particles form emulsions of mutually immiscible phases that are stable over extended periods of time due to the integration of hydrophobic carbon into the hydrophilic silica particle. The concepts advanced here can be employed in the synthesis of hollow with through pores in the shell for encapsulation and release of materials such as nutrients and surfactant in oil spill treatment. Particles with ferromagnetic cores provide added incentives in the magnetic mobilization of oil spills and in synthesizing commercial quantities of supported metal oxide catalysts.

CHAPTER 7

NANOSTRUCTURED AMPHIPHILE MESOPHASES AS BUOYANT GEL DISPERSANTS

7.1 Introduction

Amphiphilic molecules spontaneously self-assemble into a range of nanoscale aggregates such as micelles, reverse micelles, fibrils, wormlike micelles, and vesicles.[16, 163, 164] At high concentrations, surfactant and lipids form liquid crystalline mesophases which can be arrays of cylinders (hexagonal or nematic), stacks of bilayers (lamellar, smectic, liposome) or a complex three dimensional network of interconnected structures (bicontinuous, tricontinuous).[16] The optimal aggregate formed in systems containing amphiphiles corresponds to the conditions of minimum free energy of self-assembly.[16, 164]

Surfactant assembly at the interface of multiphase systems is also exploited in the treatment of marine oil spills, where surfactant formulations known as dispersants are applied to lower the oil-water interfacial tension and facilitate oil dispersion into oil-in-water macroemulsions for subsequent biodegradation.[163, 165] Typical dispersant systems are liquid formulations of surfactant such as DOSS (dioctyl sulfosuccinate sodium salt), Tween 80 (polyoxyethylene (20) sorbitan monooleate) and Span 80 (sorbitan monooleate) in organic solvents, typically propylene glycol and petroleum distillates.[80] The synergy of surfactant components in dispersants facilitates the formation of very stable emulsions that are not readily obtained with a single surfactant.[80]

The DOSS component has been reported to help in stabilizing the oil-water interface formed during the breakup of dispersant treated oil,[166] while Tween 80 and Span 80 allow the attainment and retention of low interfacial tensions.[80, 166] In a recent collaborative work, a liquid formulation of two food grade amphiphiles, lecithin and Tween 80, was utilized for the stabilization of oil-in-water emulsions.[43] Lecithin or Tween 80 alone is ineffective in stabilizing crude oil-in-saline water emulsions, but oil emulsification with blends of lecithin and Tween 80 resulted in improved emulsion stability.[43] The synergistic mechanisms proposed for blends of Lecithin and Tween 80 include (i) a closer surfactant packing at the oil-water interface; (ii) fortification of the interfacial film by lecithin and (iii) steric resistance to droplet coalescence provided by the large headgroup of Tween 80. Nyankson et al. fractionated lecithin into the zwitterionic, phosphatidylcholine (PC) and anionic, phosphatidylinositol (PI) fractions and observed that the phosphatidylcholine fraction disperses oil more effectively compared to the native phosphatidylinositol fraction.[167] The integration of such environmentally friendly and non-toxic phospholipids into dispersants can improve the net environmental benefit of dispersant use in oil spill treatment.

A key challenge to the effective use of dispersants in the treatment of oil spills is that existing liquid dispersants suffer from spray drift and gets washed off by ocean currents, especially when applied onto heavy or weathered oils.[168] Nedwed and coworkers have advanced the development of gel-like dispersants to overcome the current limitations of existing liquid dispersants.[168] Key beneficial characteristics of gel type dispersants over traditional liquid dispersants include (a) close adherence to weathered oils without being washed off (b) buoyancy for extended periods allowing

more contact with oil (c) high surfactant concentrations (d) reduced solvent levels and (e) possibility of the gels providing some degree of visible feedback to oil spill responders.[168]

A gel mesophase consisting of the zwitterionic phospholipid, l-α-phosphatidylcholine (PC) and an anionic surfactant, DOSS, has previously been prepared in our laboratory for templated materials synthesis.[169, 170, 171] The addition of water to a solution of the PC and DOSS at a molar ratio of 1:2 in organic solvents such as paraffin leads to a transition from a microemulsion to a bicontinuous gel state that can incorporate very high water content.[169] The gel structure evolves from an inverse hexagonal mesophase consisting of randomly oriented cylinders at lower water content to a lamellar phase at high water content through an intermediate coexistence phase.[169, 172, 173]

Our objective in this work is to exploit the spontaneous self-assembly of the widely available double-tailed phospholipid PC and surfactant components of Corexit dispersants such as DOSS and Tween 80 into a buoyant, gel mesophase for potential application as gel dispersants. The chemical structures of the amphiphiles are presented in Figure 7.1. In this work, the gel mesophases are prepared with equimolar amounts of PC and DOSS to maximize the use of the innocuous PC phospholipid. We demonstrate that significant amounts of the non-ionic surfactant, Tween 80, can be incorporated into the gel system leading to a transition in gel structure and significant enhancement in oil emulsification characteristics. The structural transition was characterized by Small Angle Neutron Scattering (SANS), ^{31}P Nuclear Magnetic Resonance (NMR) Spectroscopy and Cryogenic Scanning Electron Microscopy (cryo-SEM). We demonstrate that the self-assembly of amphiphilic molecules into gel mesophases can be exploited in the design of effective dispersant systems for the treatment of oil spills.

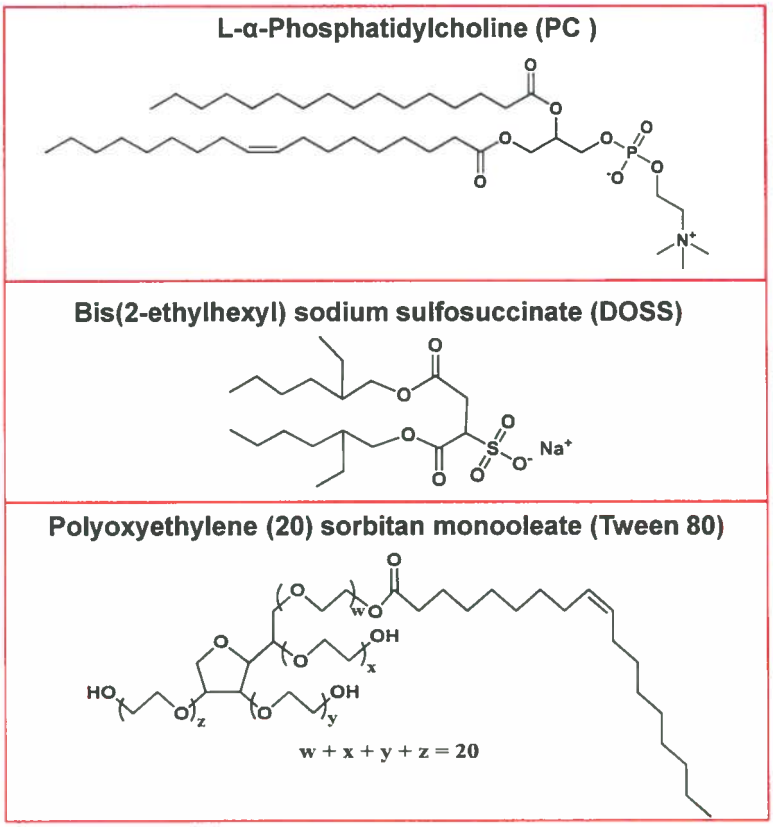

Figure 7.1: Molecular structures of amphiphiles (PC, DOSS and Tween 80) used in the synthesis of crystalline gel mesophases.

7.2 Experimental Procedures

7.2.1 Materials

Dioctyl sulfosuccinate sodium salt (DOSS, 98% purity), polyoxyethylene (20) sorbitan monooleate (Tween 80), deuterium dimethyl sulfoxide (DMSO-d6, 99.9%) and hexadecane were purchased from Sigma Aldrich. L-α-Phosphatidylcholine (95%) extracted from soybeans was purchased from Avanti Polar Lipids, Inc. Deuterium oxide (D_2O, 99.9%) was obtained from Cambridge Isotopes Laboratory. Deionized (DI) water, produced from an Elga water purification system (Medica DV25), with resistivity of 18.2 MΩ cm was used in all experiments. 0.6 M sodium chloride (Certified ACS grade, Fisher

Scientific) solution in deionized water was used as a substitute for seawater. Louisiana sweet crude oil with a viscosity of 0.01 Pa s and specific gravity 0.85 at 15 °C was obtained from British Petroleum's Macondo prospect (SOB-20100617032).[17] All chemicals were used as received.

7.2.2 Synthesis of Surfactant Gel Mesophases

In the preparation of the surfactant mesophases the PC to DOSS molar ratio was first varied from 0 to 1 with the total surfactant concentration fixed at 1.26M in hexadecane. The appropriate mass of each surfactant used in preparing the samples are summarized in Table 7.1. The surfactant components were dispersed into 5ml of hexadecane by intermittent sonication in a water bath and magnetic stirring at 50^0C until completely homogeneous solutions were obtained. Water was then gradually added into the system in 0.5 mL increments. The surfactant mesophase was mixed on a vortex mixer ((Thermolyne Maxi Mix II) after each addition of water until the mixture became homogeneous. As listed in Table 7.1, a gel mesophase forms above a threshold molar ratio of PC to DOSS of 2:5.

In this work, we focus on the system prepared with equimolar PC to DOSS content to maximize the use of the food grade phospholipid, PC. For the equimolar PC and DOSS micellar solution in hexadecane, the addition of 2.5ml of water marks the onset of gelation. Increasing Tween 80 amounts of 0.625g, 1.25g, 2.5g, 3.0g and 3.75g were then incorporated into the gel mesophase prepared with PC and DOSS. Tween 80 (Sigma Aldrich) was added dropwise into the PC-DOSS gel mesophase in 0.25g increments followed by vortex mixing until the mixture became homogeneous. The gel

system flows on tilting the vial at Tween 80 loadings greater than 3.75g indicating a breakdown of the gel system.

Table 7.1: Sample compositions prepared at varying PC to DOSS ratio

Molar ratio of PC to DOSS	Mass of Surfactant (g)		Surfactant Concentration in hexadecane (M)			Gel Formation (Yes/No)
	PC	DOSS	PC	DOSS	PC + DOSS	
0.00	0.00	2.80	0.00	1.26	1.26	No
0.14	0.60	2.45	0.16	1.10	1.26	No
0.20	0.80	2.33	0.21	1.05	1.26	No
0.33	1.19	2.10	0.32	0.95	1.26	No
0.40	1.36	2.00	0.36	0.90	1.26	Yes
0.50	1.59	1.87	0.42	0.84	1.26	Yes
0.60	1.79	1.75	0.47	0.79	1.26	Yes
0.67	1.91	1.68	0.50	0.76	1.26	Yes
0.80	2.12	1.56	0.56	0.70	1.26	Yes
1.00	2.39	1.40	0.63	0.63	1.26	Yes

7.2.3 SANS Data Collection and Reduction

Small Angle Neutron Scattering (SANS) characterization of gel microstructure was carried out at the extended-Q range small-angle neutron scattering (EQ-SANS) instrument of the Spallation Neutron Source at Oak Ridge National Laboratory. The gel

samples were prepared with D_2O (2.5ml) as the aqueous phase to provide contrast for the aqueous domains. The samples were loaded into 2mm path-length quartz cells (Hellma, Germany) and the SANS measurements were made at 25 °C. The scattering angle (θ) is related to the neutron wavelength (λ) and scattering vector (q) by the equation:[174]

$$q = \frac{4\pi}{\lambda}\sin\left(\frac{\theta}{2}\right) \qquad (7.1)$$

The time-of-flight EQ-SANS instrument was operated in 30 Hz mode with a minimum neutron wavelength, λ, of 2.5 Å in the first neutron band and a second neutron band starting at 9.4 Å. This provided an effective q-range of ~0.0035–0.45 $Å^{-1}$. The sample-to-detector distance was 4 m.

Standard SANS data reduction procedures were implemented in MantidPlot. The data was corrected for instrument dark current (cosmic radiation and electronic noise), detector sensitivity, background, incident beam normalization and sample transmission. A calibrated standard, Porasil B, was used to convert the data into absolute intensity units (1/cm). Reduced data were azimuthally averaged using MantidPlot to produce profiles of scattering intensity, $I(q)$ as a function of the scattering vector, q.

7.2.4 Cryo-Field Emission Scanning Electron Microscopy Imaging

Cryo-SEM imaging was performed using a Hitachi S-4800 field emission Scanning Electron Microscope operated at a voltage of 3 kV and a working distance of 9 mm. The samples were transferred into rivets mounted onto the cryo-SEM sample holder. The samples were then plunged into slushed liquid nitrogen to freeze the sample. This was followed by fracturing at −130 °C using a flat-edge cold knife and sublimation of the

solvent at −95 °C for 5 min. The temperature was lowered back to -130°C and the sample was then sputtered with a gold–palladium composite at 10 mA for 88 s before imaging.

7.2.5 ^{31}P Nuclear Magnetic Resonance (NMR) Spectroscopy

NMR spectra were acquired using a Bruker 500 MHz NMR spectrometer operating at 25^0C. The samples were held in coaxial NMR tubes. In a typical experiment, about 500μL of the gels were first transferred into an 8cm long, 5mm diameter NMR tube. The samples were transferred with the aid of a 1ml syringe fitted with a 15cm long needle with 2mm outer diameter and 1.5mm internal diameter. A 2.5mm diameter NMR tube containing DMSO lock agent was inserted into the 5mm NMR tube containing the gel samples. The samples were sealed and the NMR spectra were acquired after a 5 min equilibration time.

7.2.6 Rheological Measurements

Rheological properties of the gels were measured at room temperature on a TA instruments AR-2000 rheometer. The cone and plate geometry, with a cone angle of 1° and diameter 40 mm, was used. A solvent trap was used to mitigate solvent loss from the sample. The shear rate was varied from 0.0001 to $1s^{-1}$ in the steady stress measurement. The same trend was observed in the steady state rheological response of the gels for separate sample loadings, but the actual values of measured variables showed a large standard deviation of up to 50% in the viscosity values at low shear rates. The storage and loss moduli were measured by small amplitude oscillatory tests over an angular frequency range of 0.1-100 rad/s at 0.5% constant strain.

7.2.7 Oil Emulsification and Stability Characterization

The surfactant gel mesophase system was mixed with crude oil by vortex mixing and sonication. The mixture was then added to a 20ml vial containing saline water. The system was vortex mixed (Thermolyne Maxi Mix II, 37W) for 1minute at 3000 rpm. Emulsions were imaged on a Leica DMI REZ optical microscope and the images were analyzed to obtain the droplet sizes. Turbidity of emulsions was measured as a function of time to characterize the stability of the oil dispersion into the aqueous phase.[175] In the turbidimetric experiments the oil to water volume ratio was 0.003. An aliquot of the emulsion (~1.5 mL) was quickly transferred to a quartz cuvette (path length = 10 mm). The percentage light transmittance through the emulsion was then measured as a function of time using a UV–vis Spectrophotometer (Shimadzu UV-1700) at a wavelength of 400 nm.[17, 175] The UV Probe software (version 2.32) was used for data analysis.

7.3 Results and Discussion

7.3.1 Structural Analysis and Characterization of Gel Mesophases

Figure 7.2 shows the photograph of gels consisting of equimolar amounts of PC (2.39g) and DOSS (1.4g) with varying amounts of Tween 80. It is noteworthy that significant amounts of Tween 80 (up to 3.75g) can be successfully incorporated into the equimolar PC-DOSS gel mesophase. At these concentrations, the gel mesophases do not flow upon inverting the vial. The photograph reveals a visually observable swelling in the gel volume with increasing Tween 80 content as indicated by the dashed line in Figure 7.2.

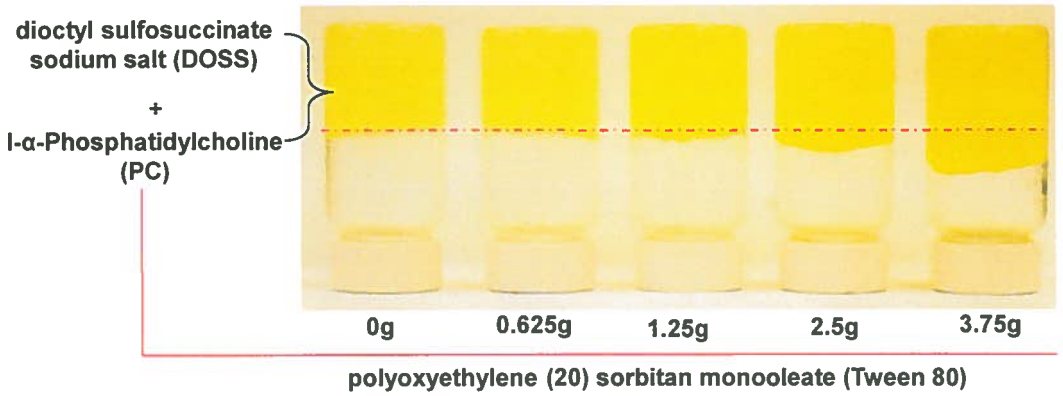

Figure 7.2: Photograph of gels prepared with equimolar amounts of PC (2.39g) and DOSS (1.4g) and varying amounts of Tween 80. The Tween 80 loadings are 0g, 0.625g, 1.25g, 2.5g and 3.75g respectively.

To understand the influence of Tween 80 loading on the characteristics of the gel systems; the PC, DOSS, and solvent levels were kept constant for all the gel systems reported in this work. The structure of the gels were characterized by a complementary combination of the analysis and modelling of SANS data, NMR spectroscopy as well as direct microscopic visualization by Cryo-SEM. SANS probes nanometer length scale structures and we exploit the significant difference in the neutron scattering properties of hydrogen and deuterium to provide scattering contrast for elucidating the structural features of the surfactant gel mesophase.[174]

Figure 7.3a shows the scattering curves of the gels with varying Tween 80 content. The plots of scattering intensity, I(q), versus scattering vector (q) for all the gel systems show the presence of at least one strong peak indicative of a periodic structure.[169] Overall the q position of the structure peak is higher for the gel prepared with PC and DOSS alone compared to all the gel systems containing Tween 80, corresponding to an increased periodicity (d-spacing) on addition of Tween 80. The maximum of the strong

structure peak shifts from 0.081Å^{-1} to lower q values of 0.072Å^{-1} and 0.069Å^{-1} on addition of 0.625g and 1.250g of Tween 80 to the gel mesophase respectively.

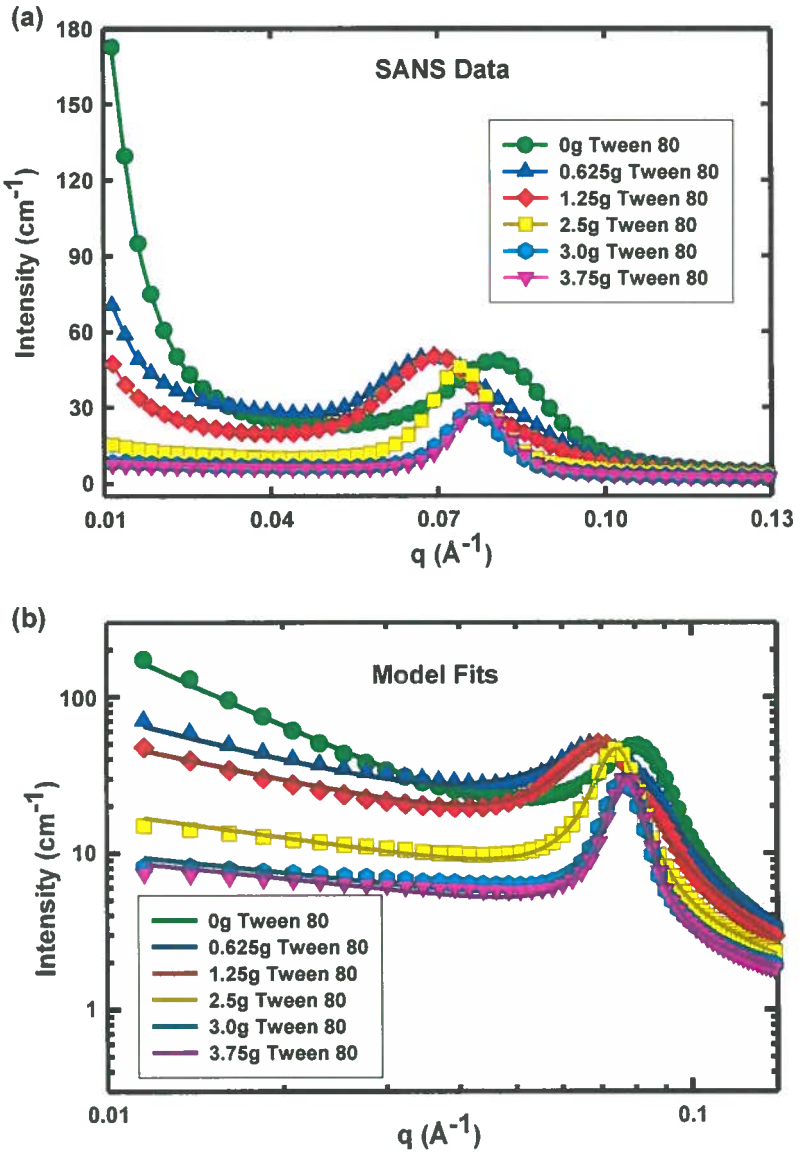

Figure 7.3: (a) SANS data on a linear scale for gel systems containing varying amounts of Tween 80 analyzed at 25^{0}C and (b) Model fits of the scattering data for the surfactant gel mesophases plotted on a log-log scale. The solid lines in Figure 7.3b are the model fits while the symbols are the experimental scattering data points at 25^{0}C from Figure 7.3a. The parameters for each fit in Figure 7.3b are listed in Table 7.2. All gels were prepared with 1.4g DOSS and PC (2.39g) to give equimolar amounts of DOSS and PC in hexadecane.

The q position of the scattering peak is inversely related to the experimentally observed d-spacing (d) by $q=2\pi/d$.[176] Thus, the peak shifts to lower q values on addition of 0.625g and 1.250g of Tween 80 into the gel system corresponds to an increase in the characteristic repeat distance of about 10Å and 13Å respectively between aqueous domains. This observed "swelling" effect in the aqueous domain size at constant D_2O content may be due to the partitioning of the water soluble surfactant, Tween 80, with large headgroups between the bulk aqueous domains and the amphiphilic layer separating the aqueous and organic domains.

At a higher Tween 80 loading of 2.5g, the structure peak shifts back to a higher q value of $0.074Å^{-1}$. Further increase of the Tween 80 content of the gel mesophase to 3.0g and 3.75g shifts the peak position to even higher values of $0.076Å^{-1}$ and $0.078Å^{-1}$ respectively. The reversal of the initial trend in which the structure peak shifts to low q values at the smaller Tween 80 loadings of 0.625 and 1.25g, suggests a significant transition in the gel structure at high Tween 80 content. The hypothesis of a structure transition with increasing Tween 80 content of the gel mesophase is corroborated by a progressive decrease in the intensity and decay characteristics of the scattering curves in the low q regime ($< 0.02A^{-1}$). The decrease in the scattering intensity is indicative of changes in the interparticle structure factor, S(Q)[177] while the significant change in the low q decay may correspond to a transition in the overall structure of the gel systems.[177, 178, 179]

To obtain quantitative structural information and understand of the influence of Tween 80 content on gel structure, the SANS data were fit by a sum of the power law and Teubner-Strey (TS) model functions using the sum model macro implemented in Igor

Pro.[180] The power law model function accounts for the decay in scattering intensity in the low q regime (< $0.02A^{-1}$) and the TS model function models the strong structure peak obtained in microemulsion-based systems.[181] Figure 7.3b shows that the SANS data is well fit by the summed model for all the gel systems. We note that the summed model is an approximation of the scattering spectra. However, the summation of the model functions allows the extraction of detailed structural information from the scattering profiles and this approach has been used to characterize gel-based microemulsion systems.[177, 182]

In applying the TS model, the scattering intensity of a structured two-phase system is calculated as the Fourier transform of the correlation function, $\gamma(r)$, in the form[181]

$$\gamma(r) = \frac{d}{2\pi r} e^{-r/\xi} sin\left(\frac{2\pi r}{d}\right) \qquad (7.2)$$

characterized by the periodic repeat distance (d) that is damped as a function of a correlation length (ξ) . In equation 7.2, r is a real space distance. The scattering intensity $I(q)$ of the two-phase system is then expressed in terms of the characteristic length scales of periodicity (d) and correlation length (ξ) by the equation:[181, 182]

$$I(q) = \frac{8\pi}{\xi}\left[\frac{\phi(1-\phi)(\Delta\rho)^2 c_2}{a_2 + c_1 q^2 + c_2 q^4}\right] \qquad (7.3)$$

where q is the scattering vector, ϕ is the volume fraction of the deuterated component; $\Delta\rho$ is the scattering contrast and a_2, c_1, c_2 are model coefficients.

The periodicity relates to the mean repeat distance between alternating water and oil domains. The correlation length is the length scale over which periodicity remains and

is a measure of the long range order in a system or the dispersion in the periodicity. An amphiphilicity factor (f_a), calculated from the TS model coefficients, provides a quantitative measure of the strength of the surfactant components to impart order on a system where f_a values close to 1 correspond to a disordered system and f_a close to -1 indicates a highly ordered lamellar morphology.[183] The periodic repeat distance (d), correlation length (ξ) and amphiphilicity factor (f_a) are related to the TS model coefficients by:[181]

$$d = 2\pi \left[\frac{1}{2}\left(\frac{a_2}{c_2}\right)^{1/2} - \left(\frac{c_1}{4c_2}\right)\right]^{-1/2} \qquad (7.4)$$

$$\xi = \left[\frac{1}{2}\left(\frac{a_2}{c_2}\right)^{1/2} + \left(\frac{c_1}{4c_2}\right)\right]^{-1/2} \qquad (7.5)$$

$$f_a = \frac{c_1}{\sqrt{4a_2c_2}} \qquad (7.6)$$

The power law model describes the scattering intensity simply in terms of a decay exponent (m) and a coefficient (A) by:

$$I(q) = Aq^{-m} \qquad (7.7)$$

Initial input parameters for the summed model were obtained by fitting the low q regime (< 0.02A^{-1}) and the q range around the structure peak (0.055$Å^{-1}$ - 0.140 $Å^{-1}$) separately by the power law and TS model functions respectively. The obtained values from the initial fits served as good estimates of the input parameters for the summed model, facilitating the fast and accurate model fitting of the SANS data (Figure 7.3b). Table 7.2 lists the fit parameters obtained for the SANS data. The model fits shows a low q power-law behavior with exponents (m) of 1.708, 1.020, 0.810 for gels containing 0g, 0.625g and

1.25g of Tween 80 respectively. At high Tween 80 loadings of 3.0g and 3.75g, the magnitude of the low q slope plateaus to smaller values of 0.210 and 0.188 respectively on a log-log scale.

Table 7.2: Fit parameters for the SANS data of the surfactant gel mesophases

Tween 80 in Gel (g)	**Low q Power Law Exponent (m)**	**Low q Power Law Coefficient (A)**	**Periodicity d (Å)**	**Correlation Length ξ (Å)**	**Amphiphilicity Factor (f_a)**
0	-1.708	0.076	78.029	91.553	-0.964
0.625	-1.020	0.621	87.593	62.000	-0.904
1.25	-0.810	1.193	88.537	93.710	-0.956
2.5	-0.410	3.362	84.400	170.983	-0.988
3.0	-0.210	6.700	82.051	192.675	-0.991
3.75	-0.188	7.300	80.871	212.148	-0.993

The low q region below the interaction peak can be considered as the Porod region of larger length scale structures or quasi periodically ordered domains in the gel mesophase. The slope is influenced by the structure factor, $S(q)$, of the assemblies within the domain. The small-q limit of the structure factor is given by:[184]

$$S(q = 0) = \rho k_B T \kappa_T \qquad (7.8)$$

where κ_T is the isothermal compressibility, $k_B T$ is the temperature in energy units and ρ is molecule number density. The progressive decrease of the low q slope suggests that the size of the quasi periodic domains increases until beyond the length scale of SANS

measurement and the compressibility between assemblies is severely decreased. The repulsive interactions between the large headgroups of Tween 80 on adjacent surfactant layers may contribute to the decreased compressibility. These effects can alter the spontaneous curvature of the surfactant film leading to structural changes in the gel system.

The periodicity is higher for the systems containing Tween 80 compared to the gel system with PC and DOSS alone (Table 7.2) in agreement with the peak shift to lower q values. At Tween 80 loadings of 2.5g and above, the SANS data fitting reveals a significant increase in the correlation length of the gel mesophase. The correlation length at Tween 80 loading of 3.75g is 212.148Å, more than double the correlation length of 91.553Å for the gel without Tween 80. The addition of Tween 80 significantly increases the length scale over which the quasi periodical order of the gel microstructure is retained. The sharpening of the structure peak with addition of Tween 80 (Figure 7.3a and 3b) also indicates a more well-defined repeat distance compared to the gel with PC and DOSS alone. The closeness of the amphiphilicity factors to -1 show that Tween 80, PC and DOSS act synergistically to impose a high degree of order on the gel mesophase.

^{31}P NMR provides a specific probe of the structure and molecular interactions in the mixed amphiphile mesophase as the gel system contains only a single phosphorus atom from the PC (Figure 7.1).[173] The ^{31}P nucleus has an electron shell that is not spherically symmetric.[173] Thus, the ^{31}P chemical shift is a tensor and depends on the orientation of the phosphorus group with respect to the external magnetic field.[173] In the ^{31}P NMR, the restricted motion of the phosphorus containing PC molecules in viscous

anisotropic assembly results in chemical shift anisotropy that reveals the phase characteristics and local environment of the ^{31}P nucleus.[173]

The value of the chemical shift anisotropy ($\Delta\sigma$) from the superposition of chemical shifts in various orientations relative to the magnetic field is given by:[173, 185]

$$\Delta\sigma = \sigma_{11} - (\sigma_{22} + \sigma_{33})/2 = \sigma_{\parallel} - \sigma_{\perp} \qquad (7.9)$$

where σ_{11}, σ_{22}, and σ_{33} are chemical shifts along three principal directions with σ_{11} defined as the unique axis. The chemical shift σ_{11} corresponds to the chemical shift when the magnetic field is parallel to the unique axis ($\sigma_{\parallel}$) while the average of σ_{22} and σ_{33} is defined as the chemical shift when the unique axis is perpendicular to the magnetic field ($\sigma_{\perp}$).[173, 185]

The NMR spectra for the PC-DOSS lecithin gel without Tween 80 in Figure 7.4 exhibits an upfield peak ($\sigma_{\perp}$) at -11.72ppm and a long downfield tail ($\sigma_{\parallel}$) at ~ 12.00ppm, a typical signature of a lipid lamellar structure.[173] The NMR spectrum exhibits a weak shoulder at about -1.0ppm indicative of some surfactant in an isotropic phase. Using equation 7.9, the ^{31}P chemical shift anisotropy of the lamellar phase is calculated to be ~ 23.72ppm. The gels with Tween 80 content of 1.25g and 3.75g also show the upfield peak and long downfield tail characteristics, indicative of a lamellar phase morphology.[173] The upfield peaks are sharper for the gels with Tween 80. The weak isotropic peak disappears on the addition of Tween 80, indicating that the gel system transitions into a more ordered lamellar phase. The upfield peak ($\sigma_{\perp}$) has a chemical shift of -11.72ppm, -11.53ppm and -11.05ppm at Tween 80 loadings of 0g, 1.25g and 3.75g respectively. The progressive shift of the peak ($\sigma_{\perp}$) downfield with increasing Tween 80

content suggests that the addition Tween 80 deshields the phosphorus nucleus and alters the local environment around the PC phospholipid.

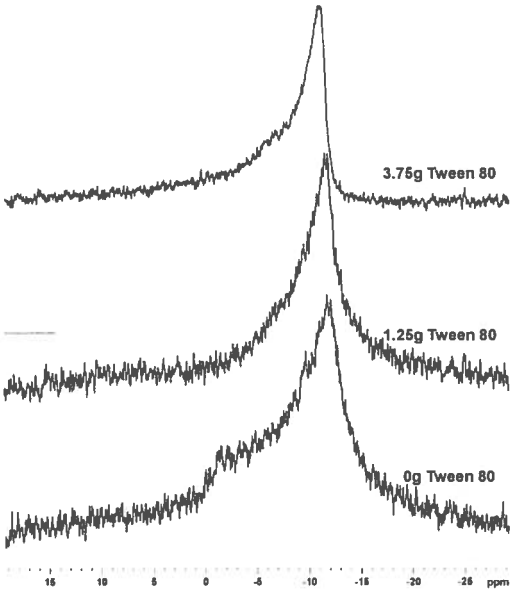

Figure 7.4: ^{31}P NMR spectra of PC-DOSS-Tween 80 gel systems measured at 25 °C. The mass of Tween 80 in the gels are 0g, 1.25g and 3.75g.

Cryo-SEM imaging allows a direct microscopic visualization of the gel microstructure (Figure 7.5). Figure 7.5a – 7.5b shows the lamellar phase morphology of the gel prepared with PC and DOSS alone. The overall lamellar microstructure is still observed in the gel system incorporating 1.25g of Tween 80 (Figure 7.5c, 7.5d). The lamellar phase shows some undulation on addition of 1.25g of Tween 80 compared to the relatively straight edged, lamellar morphology without Tween 80. The quasi periodic lamellar structures are about 100 - 200nm in diameter and span length scales of up to 2μm (Figure 7.5a – 7.5d). At a repeat distance of 78.029Å for the gel with PC and DOSS (Table 7.2), the number of unit cells across a 100 - 200nm quasi periodic domain is calculated to range from about 12 to 24. Cryo-SEM of the gel incorporating a higher Tween 80 loading of 3.75g shows discrete spherical structures (Figure 7.5e – 7.5h) in

agreement with the structural transition observed in the SANS data analysis and alteration of the local environment of the 31P nucleus in the NMR. The spherical domains range from about 1µm - 5µm. Cryo-SEM imaging reveals that the transition is likely due to the rolling of long, flexible and closely-packed lamellar assemblies into onion-like multilamellar structures at high Tween 80 loading (Figure 7.5e, 7.5f).

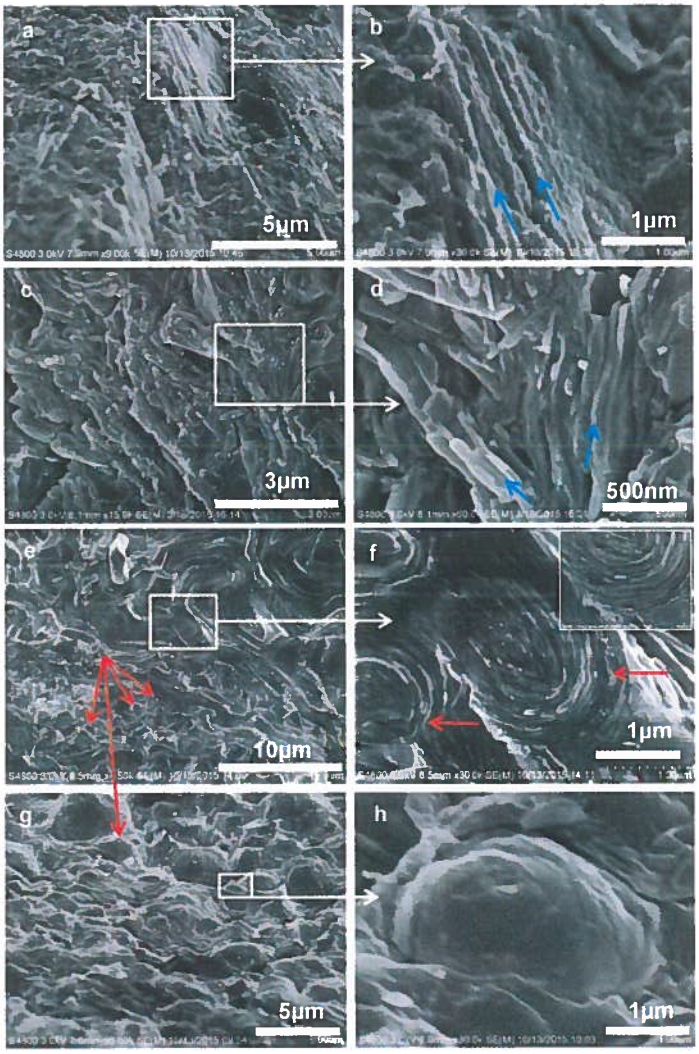

Figure 7.5: Representative cryo-scanning electron microscopy images of PC-DOSS gel mesophase with increasing Tween 80 loadings of 0g (a,b), 1.25g (c,d) and 3.75g (e-h). All gels were prepared with 1.4g DOSS and PC (2.39g) to give equimolar amounts of DOSS and PC in hexadecane. The lamellar and onion-like multilamellar structures are indicated by the blue and red arrows in Figures 7.5a – 7.5d and Figures 7.5e – 7.5h respectively.

The microstructural transition on addition of Tween 80 may be rationalized in molecular terms as a consequence of the change in the average packing parameter[16] of the surfactant mixture. The equilibrium structure of surfactant aggregates and the spontaneous interfacial curvature is described in terms of a molecular packing parameter ($P=v/al$) where v is the volume occupied by the surfactant tails, a is the effective headgroup cross-sectional area and l is the maximum effective tail length.[16] DOSS has a surfactant packing parameter (P) of 1.1, spontaneously adopting a concave curvature towards water resulting in the formation of spherical reversed micelles above the cmc.[186] The phospholipid, PC has a packing parameter of 0.6 and tends to form assemblies such as wormlike reverse micelles in non-polar solvents with interfaces of minimal curvatures.[186] The packing parameter of Tween 80 is about 0.07[187] due to the relatively large headgroup and short tail features. Surfactant with packing parameters $\leq$ 0.33 favorably form aggregates such as micelles with spherical curvatures.[164, 187]

Mixtures of amphiphilic molecules with different packing parameters may be described in terms of a mean packing parameter ($P_{mix} = \Sigma n_i P_i$) where n_i and P_i are the mole fraction and packing parameter of the individual surfactant in the mixture respectively.[16, 188] The gel prepared with equimolar concentrations of PC (2.39g) and DOSS (1.40g) has a calculated P_{mix} of 0.85. On incorporation of increasing amounts of Tween 80; 0.625g, 1.25g, 2.5g and 3.75g; the P_{mix} values are calculated to be 0.80, 0.75, 0.67, and 0.61 respectively. The incorporation of Tween 80 into the PC/DOSS surfactant mesophase alters the mean geometric packing characteristics of the mixed amphiphile aggregates and consequently the spontaneous curvature of the surfactant film. However, the equilibrium structure of the mesophases obtained at high surfactant concentration is

determined by the thermodynamics of surfactant self-assembly into aggregates as well as the interaggregate forces.[16]

Figure 7.6 shows the rheology of the gels in steady state shear flow. The gel systems show a non-Newtonian, shear-thinning response at all Tween 80 loadings. The shears stress versus shear rate curves show a stress plateau at low shear rates (0.001 and $0.01s^{-1}$). This rheological response is attributable to an early shift in the flow mechanism of the complex gel systems at low shear rates, with domains that may align and/or break down at very high shear rates.[189] The viscoelastic response of the gel system to dynamic oscillations is presented in Figure 7.7. The dynamic oscillatory measurements show frequency-independent moduli that do not cross over in the frequency range scanned. The elastic modulus (G′) is greater than the viscous modulus (G″) over the frequency range.

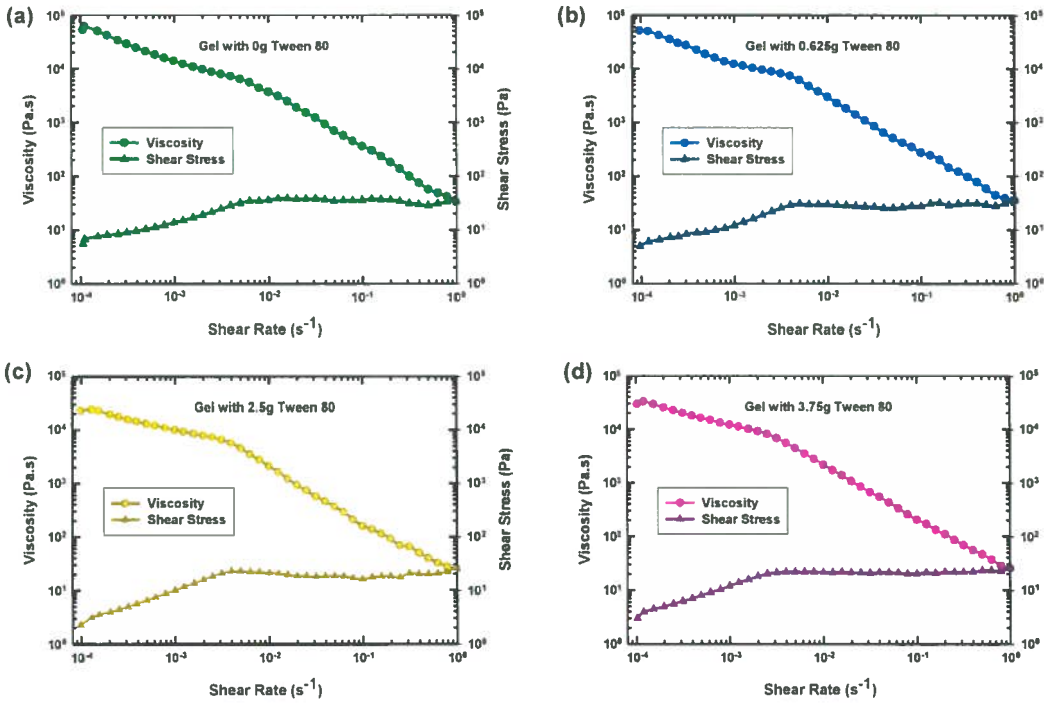

Figure 7.6: Steady flow viscosity and shear stress as a function of shear rate for gels with increasing Tween 80 content at 25 °C.

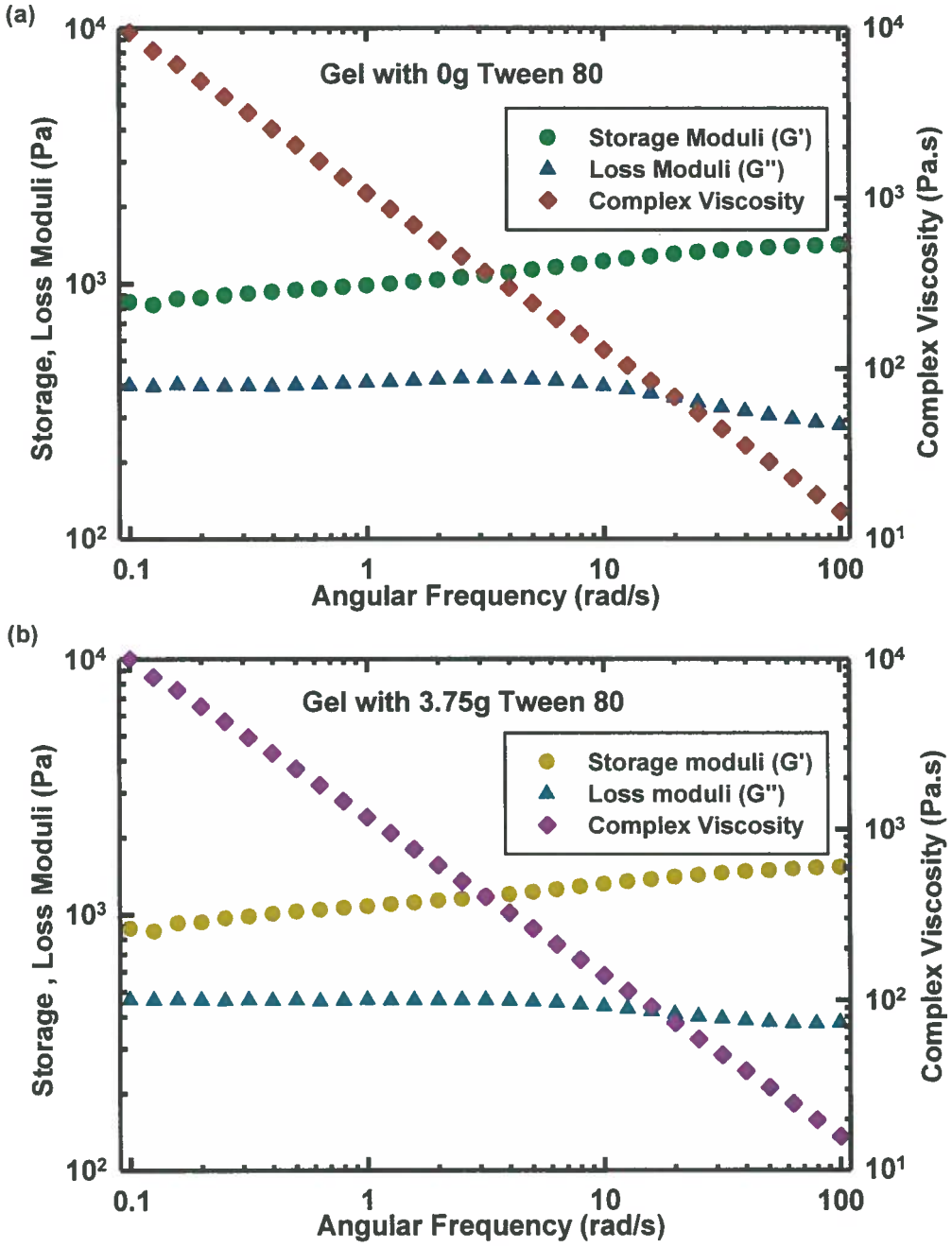

Figure 7.7: Storage (*G'*), loss moduli (*G"*) and complex viscosity as a function of angular frequency at T = 25 °C. The angular frequency range was 0.1-100 rad/s and the strain was kept constant at 0.5%.

7.3.2 Emulsion Stabilization Characteristics of Surfactant Gel Components

Motivated by the beneficial characteristics of gel dispersants in the treatment of oil spills, we characterize the oil emulsification characteristics of the surfactant gel mesophases for potential applications in oil spill remediation. We first characterized the oil emulsification ability of the PC-DOSS gel mesophase at a 1:1 molar ratio. Figure 7.8a shows that the crude-oil-in saline water emulsion prepared with the PC-DOSS amphiphile mixture is unstable and the oil phase completely resurfaces within 10 minutes. Incorporation of increasing amounts of Tween 80 into the DOSS-PC gel system results in a significant enhancement in emulsion stability over time (Figure 7.8a).

Turbidimetric measurements as a function of time provides a reasonable quantitative measure of the stability of the dispersed phase in emulsions systems.[17] Figure 7.8b presents the turbidity of emulsions stabilized by surfactant components of the gels at dispersant to oil mass ratios (DOR) of 1:20 and 1:100. The transmittance is highest in the oil-water system without dispersant (green curve), indicating that the dispersed oil rapidly rises to the surface. The rapid creaming and formation of the clear oil layer is driven by spontaneous tendency of the system to minimize the interfacial area between the hydrophobic oil phase and the water. The PC-DOSS-Tween 80 surfactant system at a DOR of 1:100 (red curve with open circles) is more efficient at stabilizing oil-in-water emulsions than the PC-DOSS system at DOR 1:20 (blue curve with filled squares). This suggests that the enhancement in oil emulsification in not just a sole function of surfactant concentration but is dependent on synergistic interactions of the surfactant components.[163, 166] The emulsion prepared with the PC-DOSS-Tween 80 surfactant

mixture shows a significantly improved stability at a DOR of 1:20 (Figure 7.8b red curve with filled circles).

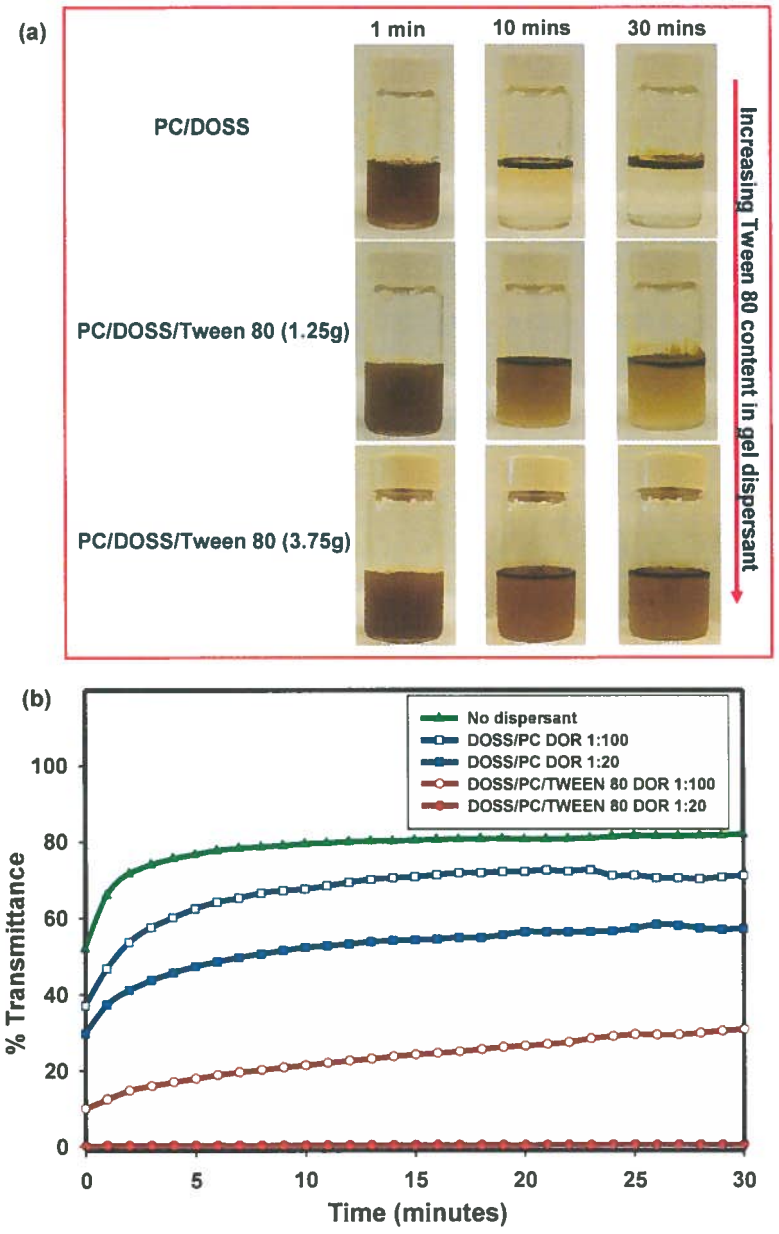

Figure 7.8: (a) Stability of crude oil-in-saline water emulsions prepared with PC/DOSS/Tween 80 gel mesophase with increasing Tween 80 content. Gel to oil mass ratio is 1:20 and oil to saline water ratio is 1:100. The gels were prepared with equimolar amounts of PC (2.39g) and DOSS (1.4g). (b) Turbidity of crude oil-in-saline water emulsions as a function of time and dispersant to oil mass ratio (DOR). The DOSS/PC/Tween 80 gel dispersant has a Tween 80 content of 3.75g.

Figure 7.9a shows a representative optical microscopy image of crude oil-in-saline water emulsion prepared with the gel dispersant. The oil is dispersed into droplets with average diameter of about 7μm. Figure 7.9b shows the mechanism of oil dispersion by the gel system. Crude oil is first applied to the water surface followed by the addition of the gel. Mixing energy was applied using a magnetic stirrer to facilitate breakdown of the gel and the emulsification of the surface oil layer. The side-view photograph in Figure 7.9b (v) shows that the gel is positively buoyant on water. The gel anchors to the surface oil layer, breaks down on input of mixing energy and facilitates oil dispersion into droplets that are suspended in the water column. The buoyancy of the gel can significantly enhance the encounter rates of the dispersant with the oil.[168] Although phospholipid based gels may be prepared with a range of organic solvents several of which are biocompatible,[190, 191] the gels with hexadecane are solidified at cold temperatures below the phase transition temperature of hexadecane (18^0C).[192] The solid nature of the gel dispersants in cold environment such as in arctic spills may further improve the oil-dispersant contact and prevent dispersant wastage.

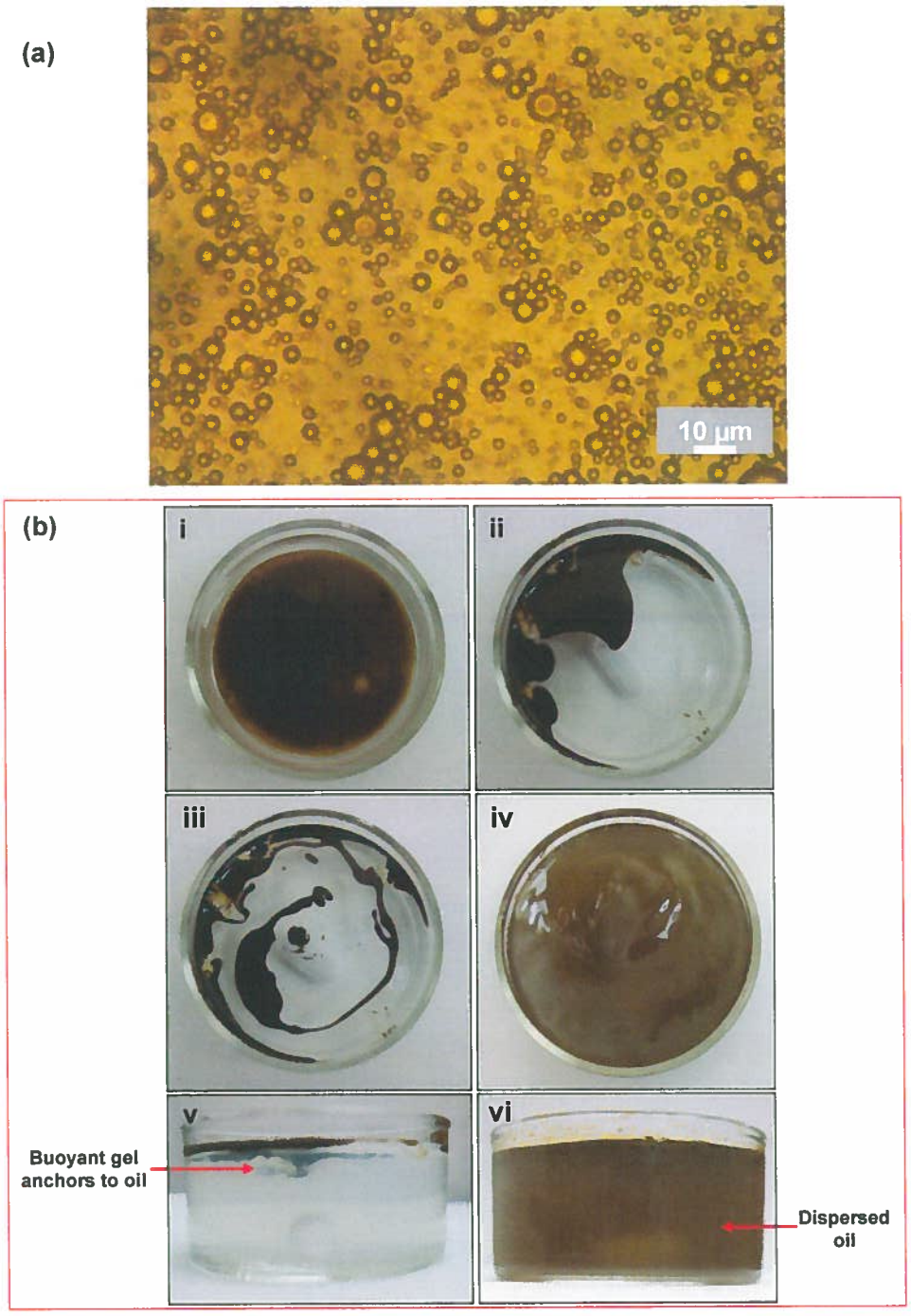

Figure 7.9: (a) Optical microscopy image of crude oil-in-saline water emulsion prepared with gel mesophases containing PC, DOSS and Tween 80. Tween 80 content in the gel is 3.75g. (b) Buoyancy and oil dispersion mechanism of PC/DOSS/Tween 80 gel. (i) Oil is added to water surface (ii) Dispersant gel is added to oil layer (iii) the system is mixed gently with a stirrer (iv) The oil is dispersed on input of sufficient mixing energy (v) Side-view of photograph in iii (f) Side-view of photograph in iv.

7.4 Conclusions

A surfactant gel system containing surfactant components of Corexit dispersants (DOSS, Tween 80) and a widely available double-tailed phospholipid, PC as zwitterionic surfactant has been developed for oil spill dispersion into small droplets. Above a threshold molar ratio of the environmentally friendly PC phospholipid to the DOSS of 2:5, a surfactant gel mesophase is formed on addition of appropriate amounts of water to the micellar solution of PC and DOSS. Significant Tween 80 amounts of up to 3.75g are successfully incorporated into the equimolar PC-DOSS gel mesophase. SANS analysis of the surfactant gel mesophase with equimolar amounts of PC and DOSS revealed a complex gel microstructure consisting of nanostructured aqueous and organic domains. The structural order of the gel mesophases produces very clear neutron scattering peaks. The scattering data was well fit by a sum of the power law and Teubner-Strey model functions. Increasing loading of Tween 80 leads to a structural transition from a gel system consisting of lamellar to spherical, onion-like multilamellar structures accompanied by a significant increase in the correlation length of the gel microstructure. Cryo-SEM imaging allowed the direct visualization of the rolling of the long, flexible and well-aligned lamellar structures into spherical multilamellar structures. The amphiphile mixture in the gel mesophase effectively disperses oil into small droplets that are stable for extended periods, leading to potential applications as a buoyant dispersant for oil spill remediation. The introduction Tween 80 into the gel mesophase significantly imparts the emulsion stabilization effectiveness of the gel. Aspects of continuing work include elucidating the synergistic emulsification mechanisms of the surfactant components, formulating gel dispersant systems with a range of non-ionic surfactant with varying

hydrophilic-lipophilic balance or molecular structures. The dispersion effectiveness of the gel dispersants on oils spanning a wide range of viscosities will be characterized using the baffled flask test. Spatial compartmentalization of nanoparticles in the gel mesophase or encapsulation of the gels within the tubular void volume of interfacially-adherent clay nanotubes can provide a unique approach to design mixed gel and particle emulsifier systems.[80, 97, 129] This work may be extended to new approaches in the design of nanostructured surfactant gel systems for the templated synthesis of functional nanocomposites that span large length scales, by combining materials synthesis in both the aqueous and organic domains.

CHAPTER 8

EMULSION STABILIZATION MECHANISMS AND EFFECTIVENESS OF BUOYANT GEL DISPERSANTS IN OIL SPILL TREATMENT

8.1 Introduction

The dispersion of crude oil spills into tiny droplets that mix vertically and horizontally in the water column is often employed in the treatment of oil spills.[1, 6, 80] The application of dispersants may reduce the possibility of shoreline impact, lessen the impact on marine life, increase oxygen transport to indigenous marine organisms and increase the available oil-water interfacial area for biodegradation.[5, 6, 7] Dispersants have been applied to treat major oil spills including Torrey Canyon, Santa Barbara Blowout, Ixtoc I blowout, Exxon Valdez and the Deepwater Horizon Blowout.[1]

The active surfactant components of dispersants diffuse through the bulk oil phase and preferentially adsorb at the oil-water interface to stabilize oil-in-seawater macroemulsions.[6, 43] Existing dispersant systems are liquid solutions of surfactant such as dioctyl sulfosuccinate sodium salt (DOSS) and polyoxyethylene (20) sorbitan monooleate (Tween 80) in hydrocarbon solvents.[6, 43, 80] The existing liquid dispersants are easily washed away by ocean current especially when applied to heavy or weathered oils and suffer from spray drift during aerial application.[168] Any dispersant not contacted with the spill oil is essentially wasted resulting in the application of large volume of dispersants in oil spill treatment. This consequently leads to the simultaneous introduction of large

volumes of hydrocarbon solvents into the marine ecosystem, generating issues regarding the potential toxicological impacts of existing dispersants.[12, 43, 193] Developing environmentally benign dispersant systems and efficiently targeting the dispersant to spill oils has huge economic and environmental significance.[97, 125, 129, 168]

Recently, we have advanced the potential application of a surfactant gel system consisting of the environmentally benign phospholipid, l-α-phosphatidylcholine (PC); anionic surfactant, DOSS; and nonionic surfactant, Tween 80, as a buoyant gel dispersant for the treatment of petroleum hydrocarbon spills. The gel is formed on addition of water and Tween 80 to a solution of PC and DOSS in a paraffin solvent such as hexadecane. Small Angle Neutron Scattering (SANS), Cryogenic Scanning Electron Microscopy (cryo SEM) and Nuclear Magnetic Resonance (NMR) techniques were used to characterize the structural transition of the gel from lamellar to spherical, onion-like multilamellar structures on addition of Tween 80. The large headgroups and small tail features of Tween 80 is proposed to modulate the spontaneous curvature[16] of the interface between the aqueous and organic domains of the gel resulting in the structural transition. The progressive incorporation of Tween 80 into the gel dispersant formulation significantly improves emulsion stability over extended time periods.

In this work, we elucidate the underlying mechanisms driving the emulsion stabilization characteristics of the gel dispersant. The dispersion effectiveness of the gel is also characterized using the standard baffled flask test[194] for varying oil phase viscosity and environmental temperature conditions. Small Angle Neutron Scattering (SANS) analysis and modelling provides quantitative structural features of the gel dispersant as a function of temperature conditions. We demonstrate that under varying temperature

conditions, the gel retains its structural integrity and positively buoyant characteristics on water, breaks down on contact with oil and release surfactant components that stabilize the crude oil-in-saline water macroemulsions.

8.2 Experimental Procedures

8.2.1 Materials

The phospholipid, l-α-phosphatidylcholine (95%, extracted from soybeans) was purchased from Avanti Polar Lipids. Dioctyl sulfosuccinate sodium salt (DOSS, 98%), polyoxyethylene (20) sorbitan monooleate (Tween 80), dichloromethane (≥99.8%) and hexadecane were purchased from Sigma Aldrich. Deionized (DI) water with resistivity of 18.2 MΩcm was produced using an Elga Medica DV25 Reverse Osmosis Water Purification System. A 0.6 M sodium chloride (Certified ACS grade, Fisher Scientific) solution in deionized water was used as a surrogate for seawater. Properties of the crude oils are listed in Table 8.1.[17, 195, 196] All chemicals were used as received.

Table 8.1: Crude oil Properties at 15^0C

Crude oil	Absolute Viscosity (cP)	Density (g/cm^3)	Kinematic Viscosity (cSt)
Louisiana sweet	10	0.856	11.682
Anadarko	10	0.906	11.038
Harmony	3588	0.942	3808.917
IFO 380	10490	0.966	10859.213

8.2.2 Preparation of Gel Dispersant

The gel mesophases were prepared according to a previously reported procedure. The amphiphiles, PC (2.39g) and DOSS (1.4g), were dispersed in 5ml of hexadecane by intermittent sonication in a water bath and magnetic stirring at 50^0C until a completely

homogeneous solution was obtained. Water was then added in 0.5 mL increments. The system was vortex mixed ((Thermolyne Maxi Mix II) after each addition of water until the mixture became homogeneous. At these compositions the system transitions from a microemulsion to a bicontinuous gel state at water content of 2.5ml. Tween 80 (Sigma Aldrich) was then added in 0.25g increments to the PC-DOSS gel mesophase followed by vortex mixing until the mixture became homogeneous. Gels were prepared with varying Tween 80 loadings of 0.625g, 1.25g, 2.5g, 3.0g and 3.75g. The synthesis procedure is illustrated schematically in Figure 8.1. The mass and volume fractions of the gels at the different Tween 80 loadings are presented in Table 8.2.

Table 8.2: Gel Sample Compositions [a]

Mass of Tween 80 in gel (g)	α_s	α_w	α_o	φ_s	φ_w	φ_o
0	0.374	0.247	0.380	0.213	0.310	0.477
0.625	0.410	0.232	0.358	0.236	0.255	0.510
1.25	0.442	0.219	0.338	0.279	0.240	0.481
2.5	0.498	0.198	0.305	0.352	0.216	0.432
3	0.517	0.190	0.293	0.378	0.207	0.415
3.75	0.543	0.180	0.277	0.412	0.196	0.392

[a] All gels were prepared with 2.39g of l-α-phosphatidylcholine (PC), 1.40g of dioctyl sulfosuccinate sodium salt (DOSS), 5 mL of hexadecane and 2.5ml of water. α_s, α_w and α_o represent the weight fractions of the three amphiphiles, aqueous phase and oil phase respectively. Assuming a total effective density of 2.2g/ml for the PC and DOSS; φ_s, φ_w and φ_o denote the corresponding volume fractions of the amphiphiles, aqueous phase and the oil phase respectively.

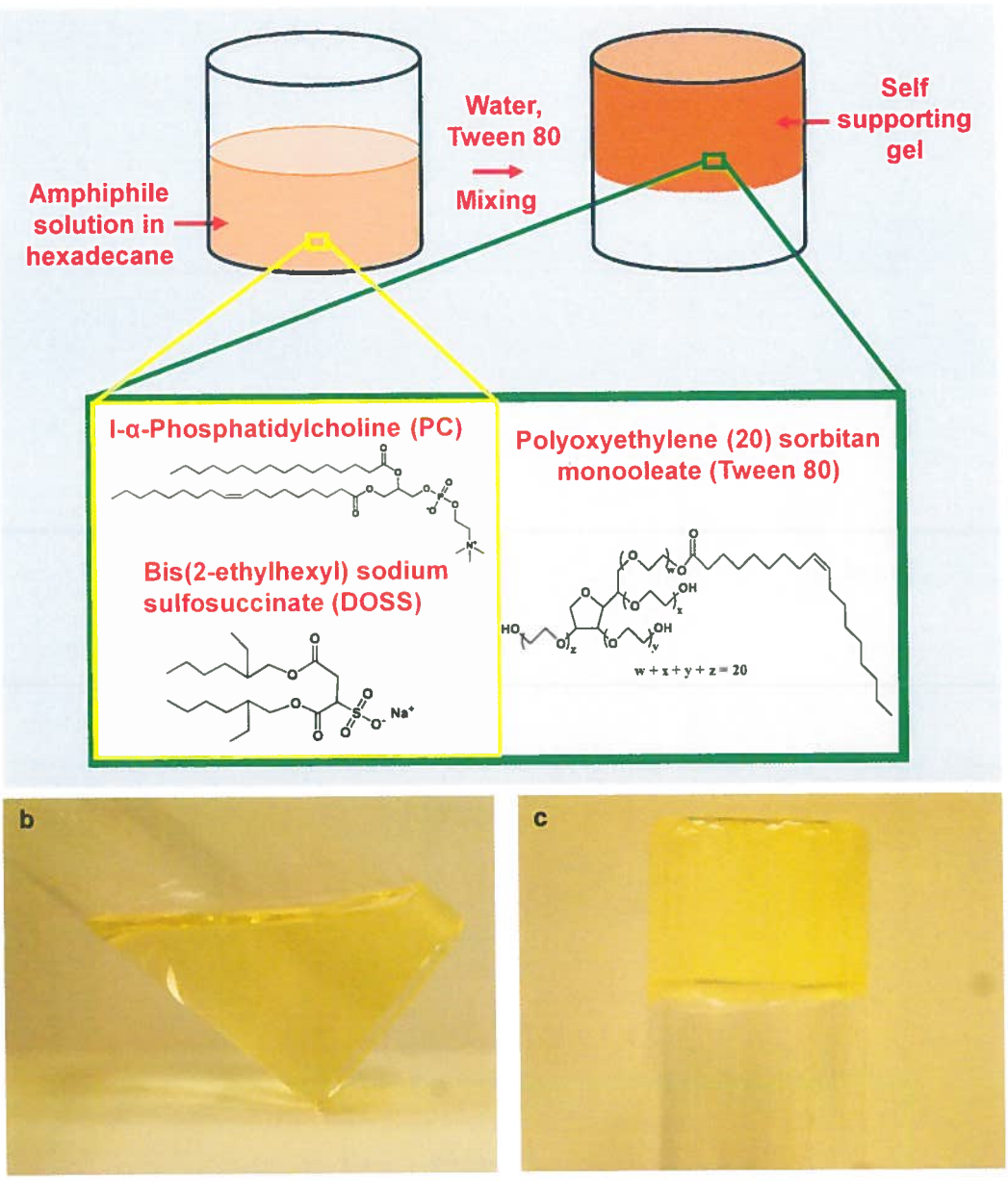

Figure 8.1: (a) Preparation of crystalline gel mesophases (b) photograph of the starting surfactant solution and (c) photograph of gel mesophase on addition of water

8.2.3 Emulsion Preparation and Optical Microscopy Imaging

The gel dispersant was uniformly mixed with the crude oil phase by vortex mixing and sonication. The mixture was then added to saline water in a 20ml scintillation vial. The system was vortex mixed at 3000 rpm (Thermolyne Maxi Mix II, 37W) for 1minute. The emulsions were imaged on a Leica DMI REZ optical microscope. The optical microscopy images were analyzed to obtain the droplet size distribution.

8.2.4 Interfacial Tension Measurements

Interfacial tensions were measured by the spinning drop and pendant drop techniques to span the range of crude oil-saline water interfacial tensions. For low interfacial tensions ($\leq$ 2mN/m) of the dispersant-oil mixtures, the interfacial tension was measured using the spinning drop technique (Grace Instruments model M6500 tensiometer). The tensiometer uses a rotating capillary of 2 mm inner diameter with total volume of 0.292 cm^3. The capillary was first filled with saline water and 0.001 cm^3 of the surfactant-oil mixtures were then injected using a micro syringe to create a small oil drop in the external saline water phase. The capillary tube was sealed and then rotated at a velocity in the range of 5000–6000 rpm. The capillary tube temperature was maintained at 25 °C by a cold water circulation around the tube.

Interfacial tensions were calculated using the Vonnegut's formula:[17, 66]

$$\gamma = \frac{\Delta\rho\omega^2 R^3}{4} \qquad (8.1)$$

where γ (mN m^{-1}) is the crude oil-saline water interfacial tension, $\Delta\rho$ (g cm^{-3}) is the density difference between the drop and the surrounding fluid, ω (rad s^{-1}) is the angular velocity, and R (cm) is the drop radius measured using an optical microscope fitted with a

digital output. The Vonnegut's formula is valid within 0.1% accuracy when the length of the oil drop exceeds four times its diameter.[17] Systems with high interfacial tensions that do not satisfy this condition were measured by the pendant drop method using a standard goniometer (ramé-hart Model 250) and the analysis was carried out using the DROPimage Advanced Software.

8.2.5 Characterization of Dispersant Effectiveness

Crude oil dispersion effectiveness of the gel was characterized using a baffled flask that generates breaking waves similar to that obtained on open ocean waters.[75, 95, 196] The dispersion effectiveness experiments were carried out with the gel system prepared with 2.39g of PC, 1.40G of DOSS and 3.75g of Tween 80. The organic and aqueous gel domains were 5ml of hexadecane and 2.5ml of water respectively. 100 µl of the gel dispersant and crude oil mixture at varying dispersant to oil mass ratios (DOR) was added to 120 ml of synthetic sea water in a baffled flask. The system was then agitated on a shaker (VWR advanced digital shaker, Model 3500) at 210 rpm for 10 minutes. After a settling time of 10 minutes, a 30 ml sample of the oil dispersion in the bulk aqueous phase was collected. The dispersed oil was then extracted with DCM and quantified with Ultraviolet–visible spectroscopy at 0.5nm intervals over the wavelength range of 360 - 400 nm.[75]

8.2.6 Small Angle Neutron Scattering (SANS) Experiments

The influence of temperature conditions on the gel microstructure was characterized by Small Angle Neutron Scattering (SANS). SANS measurements were carried out at the extended-Q range small-angle neutron scattering (EQ-SANS)

instrument of Oak Ridge National Laboratory's Spallation Neutron Source. The gel samples were prepared with D_2O (2.5ml) as the aqueous phase to provide neutron scattering contrast. The samples were loaded into 2mm path-length quartz cells (Hellma, Germany). SANS measurements were made in 10 °C increments between 15 °C and 55^0C to span a range of environmental temperature conditions. The EQ SANS instrument is equipped with a water bath for maintaining temperature.

The scattering vector (q) is related to the neutron wavelength (λ) and scattering angle (θ) by:[174]

$$q = \frac{4\pi}{\lambda}\sin\left(\frac{\theta}{2}\right) \qquad (8.2)$$

The SANS instrument was operated in 30 Hz frame-skipping mode with the first neutron band having a minimum neutron wavelength (λ) of 2.5 Å and a second neutron band starting at 9.4 Å. This provided an effective q-range of ~0.0035–0.45 $Å^{-1}$. Sample to detector distance was 4 m.

SANS data was reduced using the MantidPlot data analysis framework. The SANS data was corrected for detector sensitivity, background, instrument dark current (cosmic radiation and electronic noise), incident beam normalization and sample transmission. A calibrated Porasil B standard was used to convert the raw SANS data into absolute intensity units (1/cm). Reduced data were azimuthally averaged in MantidPlot to give the intensity, $I(q)$ versus scattering vector (q) profiles.

8.3 Results and Discussion

8.3.1 Emulsion Stabilization Mechanism of Gel System

The stability of emulsions prepared with surfactant depends on the characteristics of the stabilizing surfactant film at the oil-water interface.[164] Figure 8.2 shows optical microscopy images of crude oil-in saline water emulsions prepared with the PC-DOSS gel without Tween 80 (Figure 8.2a – 8.2d) and gel with 3.75g of Tween 80 (Figure 8.2e – 8.2f). Both systems were prepared at same dispersant to oil mass ratio (DOR) of 1:20. Optical microscopy images of the emulsion prepared with the PC-DOSS gel system reveals that the interfacial amphiphilic film is unable to provide required resistance to droplet coalescence over relatively short times (Figure 8.2a – 8.2d). Figure 8.2e – 8.2f reveals the significant influence of introducing Tween 80 into the gel on the resistance of the surfactant film at the crude oil-saline water interface to droplet coalescence. On addition of Tween 80 to PC and DOSS components, the surfactant film becomes effective in stabilizing the emulsion with the spherical shape and size of the droplets kept intact.

Figure 8.3a shows optical microscopy images of crude oil-saline water emulsions prepared with gels having increasing Tween 80 content. All emulsions were prepared at constant DOR of 1:20. Smaller droplet sizes are obtained with increasing Tween 80 content of the gel mesophase, with average droplet sizes of 41.04μm and 9.20μm at Tween 80 gel content of 0.625g and 3.75g respectively. In addition, about 99% of the droplets are in the 0-25μm range for the gel with 3.75g of Tween 80 compared to 49% for the gel system with 0.625g of Tween 80 (Figure 8.3b). The droplets transition for irregular shapes and droplets with flat interface curvatures to spherical droplets at high Tween 80 content of the amphiphilic gel system.

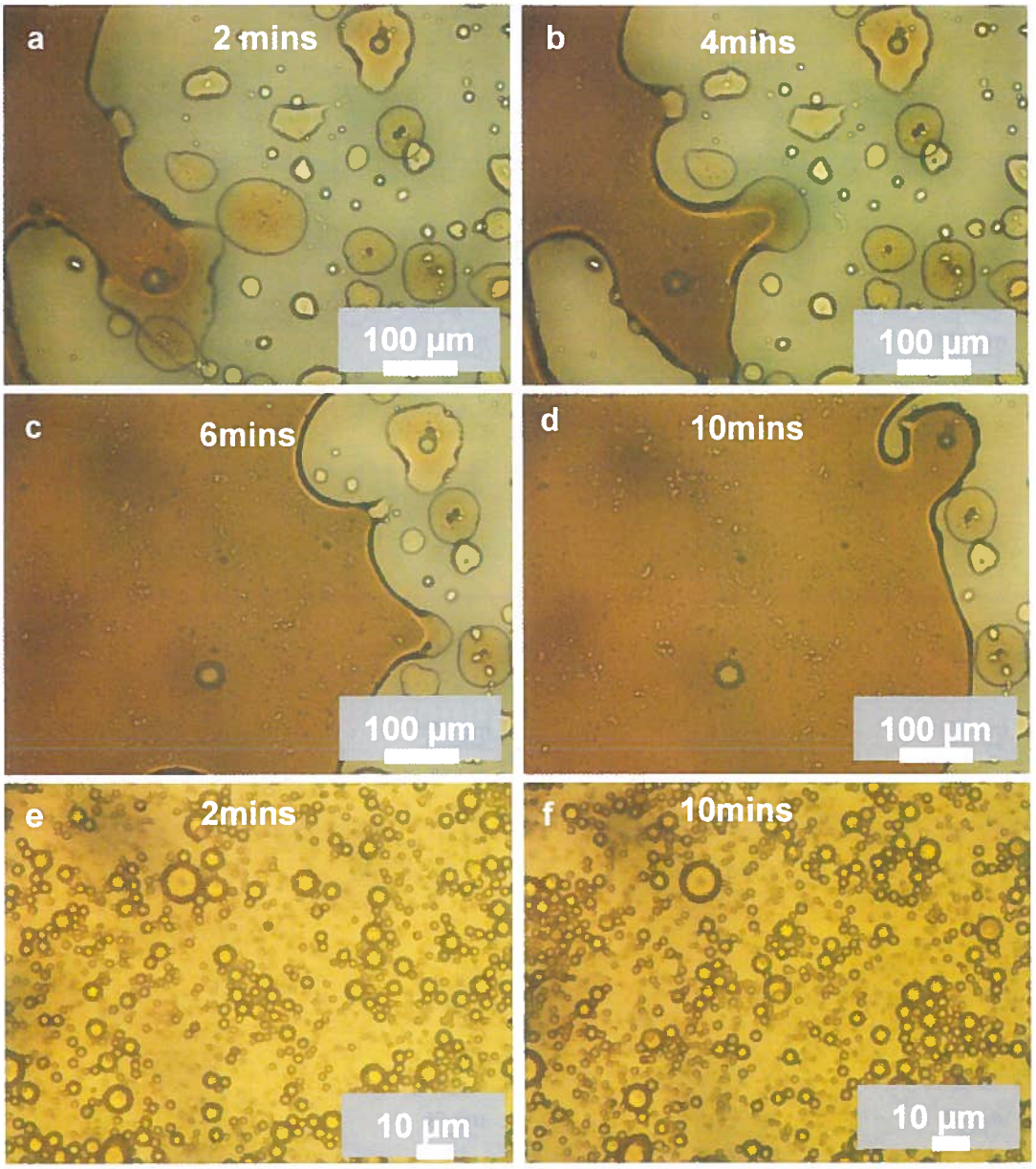

Figure 8.2: (a-d) Instability of the interfacial surfactant film to droplet coalescence for O/W emulsions prepared using surfactant gel containing PC and DOSS alone; (e-f) Influence of Tween 80 addition into surfactant gel system on the resistance of the surfactant film against droplet coalescence. Gel dispersant to oil mass ratio is 1:20 and oil to saline water ratio is 1:50.

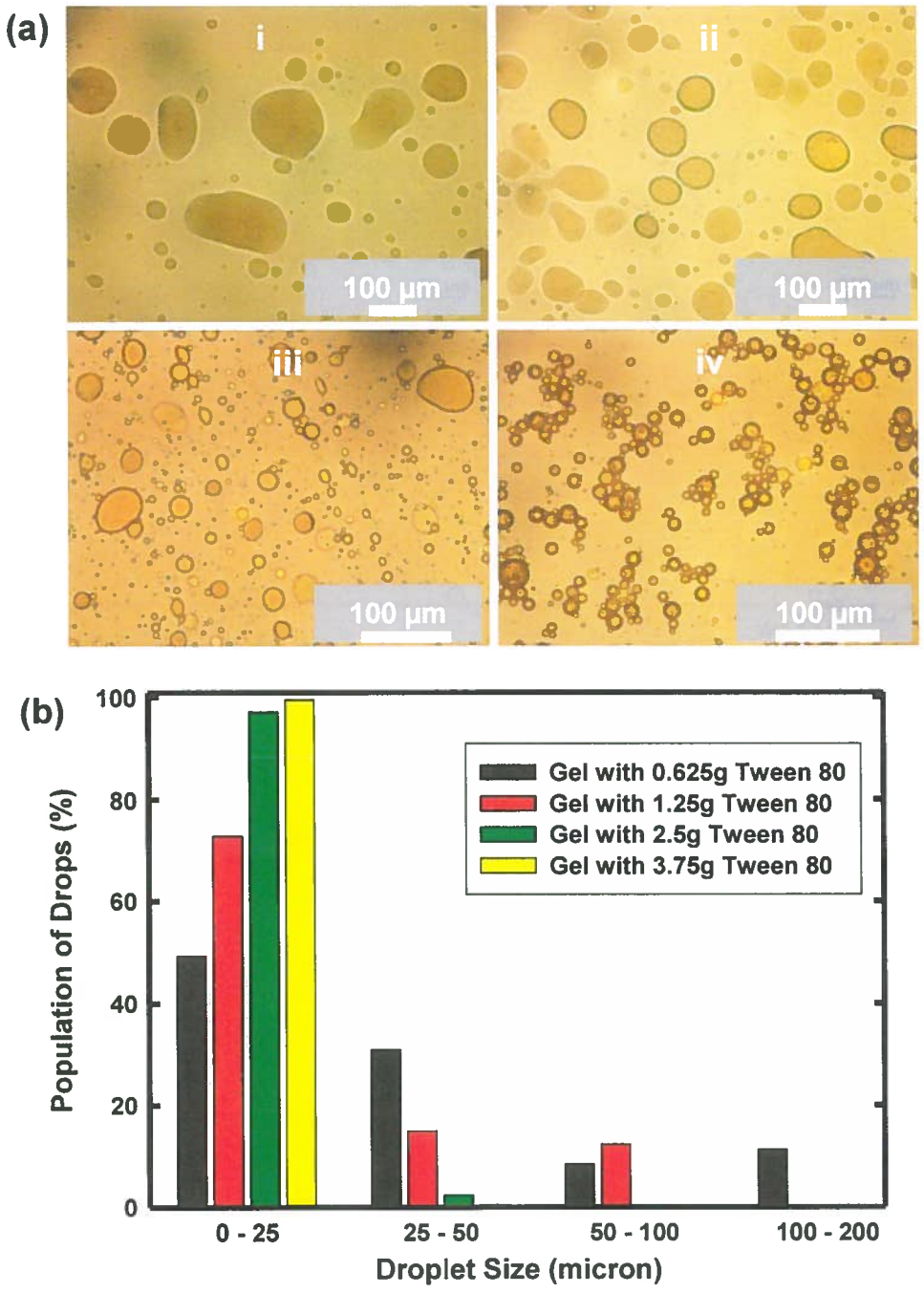

Figure 8.3: Optical microscopy images and droplet size distributions of crude oil-in-saline water emulsions prepared with gel mesophases containing PC, DOSS and increasing amounts of Tween 80. Optical microscopy images were taken immediately after emulsion preparation. In Panel a, the Tween 80 content of the gel dispersants were 0.625g (i), 1.25g (ii), 2.5g (iii) and 3.75g (iv). Gel dispersant to oil mass ratio is 1:20 and oil to saline water ratio is 1:50.

Neglecting energy losses as heat through viscous dissipation or during mixing, the work input required (W) to disperse a liquid of volume V with drops of radius R in an immiscible liquid is:[164]

$$W = \gamma * \frac{3V}{R} \qquad (8.3)$$

where γ is the interfacial tension.[172] From equation 8.3, the effectiveness of oil emulsification is strongly dependent oil-water interfacial tension. The reduction of the crude-oil saline water interfacial tension (IFT) by the gel systems were measured to characterize the role of the surfactant components in lowering the interracial excess free energy generated on oil emulsification.

The IFT curves in Figure 8.4 show that increasing Tween 80 loading leads to a progressive decrease in crude oil-saline water interfacial tension at all the dispersant to oil ratios. The impact of incorporating Tween 80 on interfacial tension (IFT) reduction is more pronounced at the lower DORs (1:100 and 1:50), yielding more than two orders of magnitude reduction in the IFT. At Tween 80 loading of 3.75g, the total surfactant concentration in the gel mesophase is calculated to be 54.3% (Table 8.2). The significant reduction in IFT at small DOR's is a beneficial characteristic of the concentrated surfactant gel system. Although the dispersant to oil ratio is an important parameter, the IFT measurements reveal that the synergistic interactions of the surfactant components plays the major role in reducing the interfacial tension and enhancing oil emulsification.

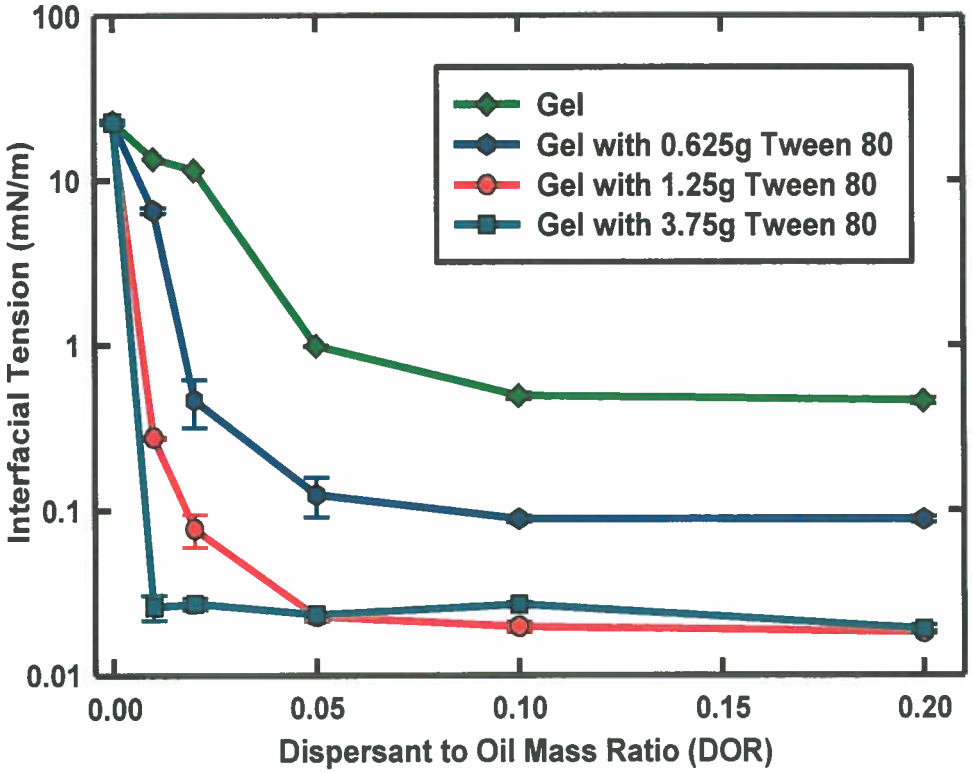

Figure 8.4: Crude oil–saline water interfacial tension measured by the pendant drop and spinning drop techniques

For two systems 1 and 2 with constant work input and liquid volumes,

$$\frac{\gamma_1}{R_1} = \frac{\gamma_2}{R_2} \qquad (8.4)$$

The emulsion stabilized by the gel with 1.25g Tween 80 has an average droplet size of 22.27μm with a measured interfacial tension of 0.077mN/m. Using equation 8.4, the decrease of interfacial tension to 0.027mN/m for the system stabilized by the gel with

3.75g Tween 80 translates to a theoretical average droplet size decrease to 7.81μm, close to the experimentally obtained average droplet size of 9.20μm.

The interfacial surfactant film adsorbs at the liquid-liquid interface to (i) reduce the interfacial tension and the thermodynamic instability of the system arising from the increase in the liquid-liquid interfacial area and (ii) provide a barrier to stabilize the dispersed droplets against coalescence.[197] The reduction in interfacial tension facilitates oil emulsification into tiny droplets with minimal wave energy input, as in oil spill remediation applications. The formation and stabilization of a large oil-water interfacial area makes the oil droplets readily available food sources for naturally occurring microorganisms.[198]

8.3.2 Gel Structure and Dispersion Characteristics at Varying Temperature Conditions

In practical oil spill treatment applications, the dispersant's effectiveness depends on several factors including the oil phase properties, dispersant to oil ratio (DOR) and environmental conditions such as temperature.[1, 195] It is noteworthy that the gels prepared with hexadecane as the organic solvent are in a partially solidified gel state at cold temperatures below the phase transition temperature of hexadecane (18^0C) and in a liquid crystalline gel state above 18^0C. We characterize the influence of temperature on the gel dispersant by microstructural analysis with SANS, visual observation of buoyancy characteristics and dispersion effectiveness using the standard baffled flask test. All the experiments are carried out with the gel system prepared with 3.75g of Tween 80.

Figure 8.5a shows the scattering curves of the gel dispersant with varying temperature. The scattering intensity, I(q), versus scattering vector (q) profiles for at the various temperatures show the presence of at least one strong peak indicating the retention of the periodic gel structure.[169] The SANS data is well fit by the equation:

$$I(q) = Aq^{-m} + \frac{8\pi}{\xi}\left[\frac{\phi(1-\phi)(\Delta\rho)^2 c_2}{a_2 + c_1 q^2 + c_2 q^4}\right] \qquad (8.5)$$

where ξ is the correlation length, q is the scattering vector, ϕ is the volume fraction of the deuterated component, $\Delta\rho$ is the scattering contrast and A, m, a_2, c_1, c_2 are model coefficients.

The first tem in equation 8.5 is a power law that accounts for the low q scattering and the second term is the Teubner Strey model[181] that accounts for the structure peak. The power law and Teubner-Strey (TS) model functions are combined using the sum model macro implemented in Igor Pro.[180] The low q regime ($< 0.02 Å^{-1}$) and the q range around the structure peak ($0.055 Å^{-1}$ - $0.140\ Å^{-1}$) were first fit separately and the obtained parameters were used as the initial input parameters for the summed model. This approach facilitates the fast and accurate model fitting of the SANS curves at various temperatures.

The correlation length (ξ) which is a measure of long range order in the gel microstructure is related to the model coefficients; a_2, c_1, c_2, by:[181]

$$\xi = \left[\frac{1}{2}\left(\frac{a_2}{c_2}\right)^{1/2} + \left(\frac{c_1}{4c_2}\right)\right]^{-1/2} \qquad (8.6)$$

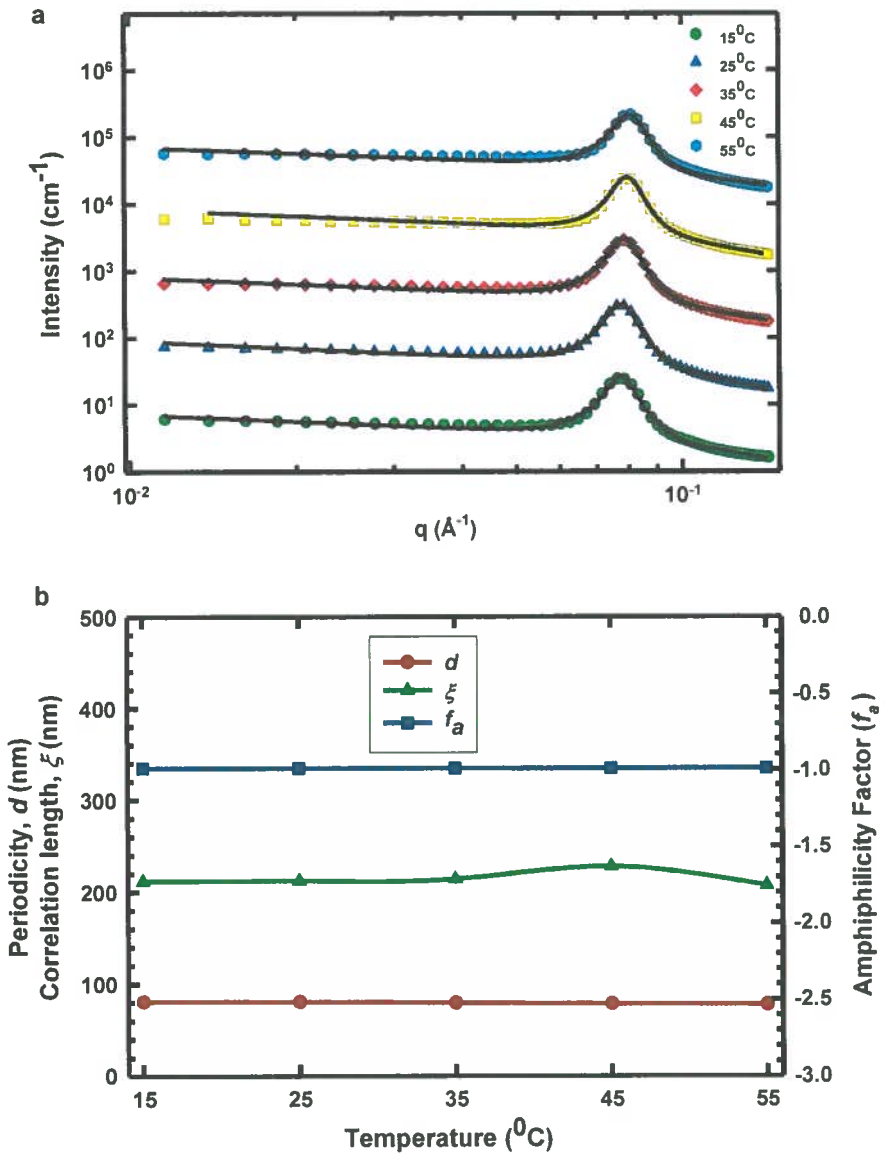

Figure 8.5: (a) Model fits of SANS data on a log-log scale for gel system containing 1.4g of DOSS, 2.39g of PC and 3.75g of Tween 80 at different temperatures. The plot at 15^{0}C is in absolute values but successive plots are scaled by an order of magnitude for clarity. The gel was prepared with hexadecane (5ml) as the organic domain and water (2.5ml) as the aqueous domain. The solid lines in Figure 8.5a are the model fits while the symbols are the experimental scattering data points. The complete parameters for each fit are listed in Table 8.3. (b) Plots of periodicity, correlation length and amphiphilicity factor of the gel dispersant as a function of temperature.

The periodic repeat distance (d) between alternating aqueous and organic domains in the gel is obtained from the model coefficients according to the equation:[181]

$$d = 2\pi \left[\frac{1}{2}\left(\frac{a_2}{c_2}\right)^{1/2} - \left(\frac{c_1}{4c_2}\right)\right]^{-1/2} \qquad (8.7)$$

A quantitative measure of the strength of the surfactant and phospholipid components to impart order on the gel system is expressed in terms of the amphiphilicity factor (f_a):[183]

$$f_a = \frac{c_1}{\sqrt{4a_2c_2}} \qquad (8.8)$$

where f_a values of 1 and -1 correspond to disordered and highly ordered lamellar systems respectively.[183] All the SANS model fit parameters of the gel system are listed in Table 8.3.

Table 8.3: SANS model fit parameters for gel dispersant [b]

Temperature (^{0}C)	Low q Power Law Exponent (m)	Low q Power Law Coefficient (A)	Periodicity d (Å)	Correlation Length ξ (Å)	Amphiphilicity Factor (f_a)
15	0.15	8.10	80.99	211.49	-0.99
25	0.19	7.30	80.87	212.15	-0.99
35	0.12	13.00	79.78	214.01	-0.99
45	0.05	40.28	78.73	227.77	-0.99
55	0.06	24.00	77.94	206.88	-0.99

[b] The gel system contains1.4g of DOSS, 2.39g of PC and 3.75g of Tween 80. The gel was prepared with hexadecane (5ml) as the organic domain and water (2.5ml) as the aqueous domain.

From the model fit parameters, the structural integrity of the gel dispersant is retained at the different temperatures (Table 8.3 and Figure 8.5b). However, there is a slight but progressive decrease of about 3.05 Å in the periodicity (*d*) with increasing temperature, from 80.99Å at 15^0C to 77.94Å at 55^0C. The amphiphilicity factor is retained at -0.99, indicative that amphiphiles act synergistically to impose a high level of order on the gel system under different temperature conditions. Figure 8.6 reveals that the gel retains positively buoyant characteristics on saline water under different temperature conditions which is a desirable characteristic for improved probability of the gel dispersant contact with spill oils compared to the easily washed away liquid dispersants.[168]

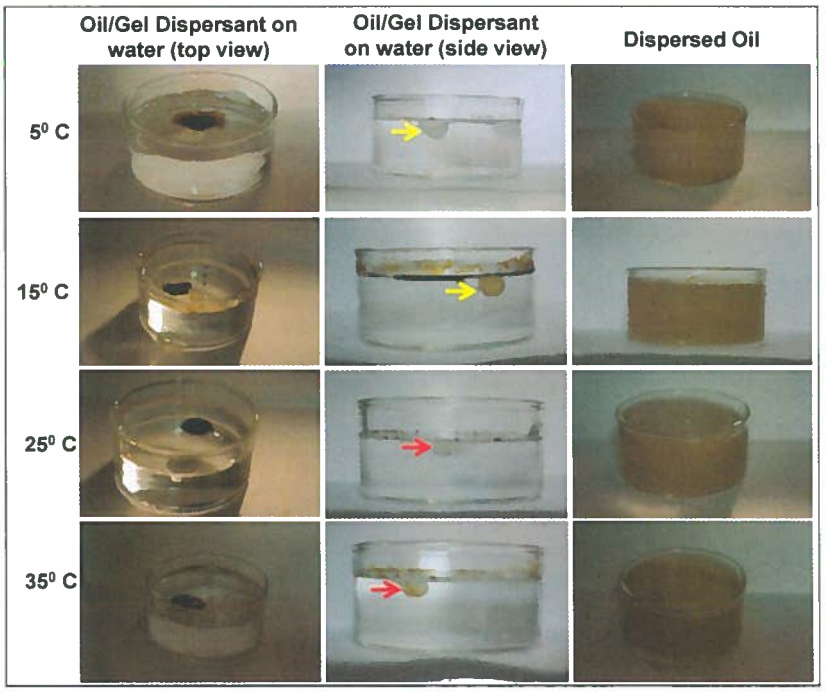

Figure 8.6: Buoyancy and oil emulsification mechanism of gel dispersant under varying temperature conditions. Organic domains of the gel are solidified below the phase transition temperature of hexadecane (18^0C). Yellow arrows indicate a partially solidified (frozen) dispersant in cold environment (< 18^0C) while red arrows indicate the liquid crystalline dispersant in warmer environment (>18^0C).

Figure 8.7 shows the crude oil dispersion effectiveness of the gel as a function of temperature (red bars). The control experiments (blue bars) were carried out without application of the gel dispersant. Insets to Figure 8.7 shows representative photograph of the dispersion experiment without and with application of the gel dispersant. Without the application of the gel dispersant, the oil is not readily dispersed into the water column.

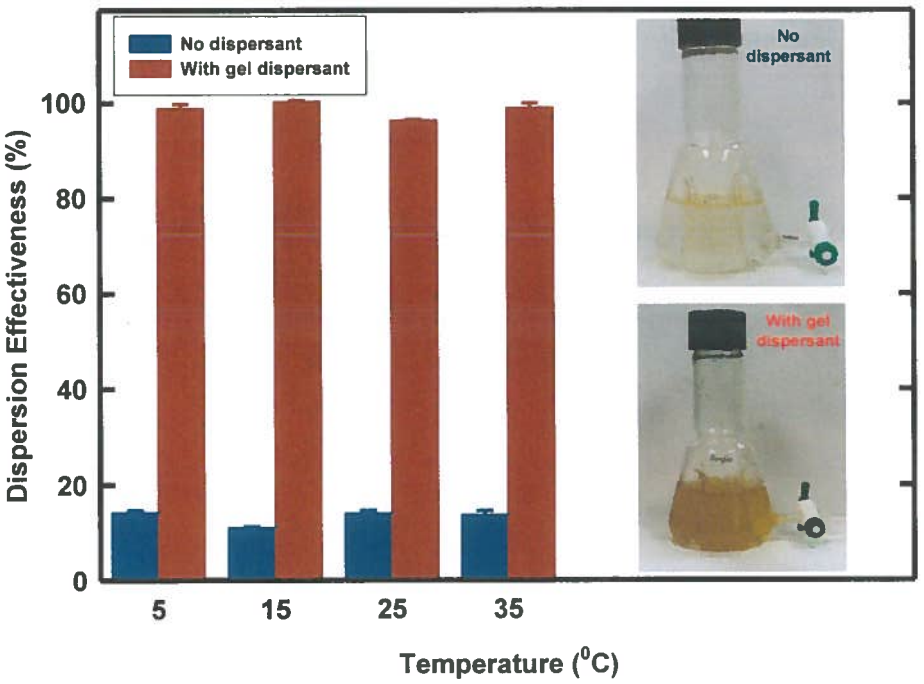

Figure 8.7: Dispersion effectiveness of gel dispersant at varying temperature conditions. The oil phase is the Louisiana Sweet Crude. The temperature conditions were simulated in a MicroClimate Environmental Chamber (Cincinnati Sub-zero). Insets are representative photographs of oil dispersion experiment without with gel dispersant application.

Neglecting contributions from the configurational entropy of the oil droplets, the free energy change on emulsification is given by:[13]

$$\Delta G^{emulsion} = \sigma \Delta A \qquad (8.9)$$

where σ is the interfacial tension and ΔA is the increase in interfacial area. Oil dispersion involves the creation of a significantly higher interfacial area between the oil and water phases. The spontaneous breakdown of the emulsions back to the separate parent bulk phases is therefore thermodynamically favorable necessitating the addition of emulsifying agents as stabilizers. The amphiphile components of the gel dispersant serve to lower the oil-water interfacial tension thereby stabilizing the oil droplets in the water column. The gel dispersant is structurally stable, remains buoyant and effectively disperses oil over a range of environmentally obtainable temperature conditions.

8.3.3 Influence of Oil Phase Properties on Gel Dispersant Effectiveness

The influence of oil phase viscosity on the dispersion effectiveness of the gel was characterized using the standard baffled flask test (Figure 8.8). Without the addition of dispersant, about 23% of the light Anadarko oil is suspended in the water by natural dispersion. This may indicate the presence of native surface active components in the crude oil. Natural dispersion has negligible effect in dispersing the heavier Harmony and IFO 380 oils. On application of the gel dispersant, there is a rapid increase in the dispersion of the light Anadarko oil with increasing DOR. The dispersion effectiveness also increases with the DOR for the heavier Harmony and IFO 380 oils. However, the increase in dispersion effectiveness is less rapid compared to the light Anadarko oil. This

indicates that the heavier oils are less amenable to dispersion into the water column and require higher amounts of the gel dispersant compared to the lighter Anadarko oil.

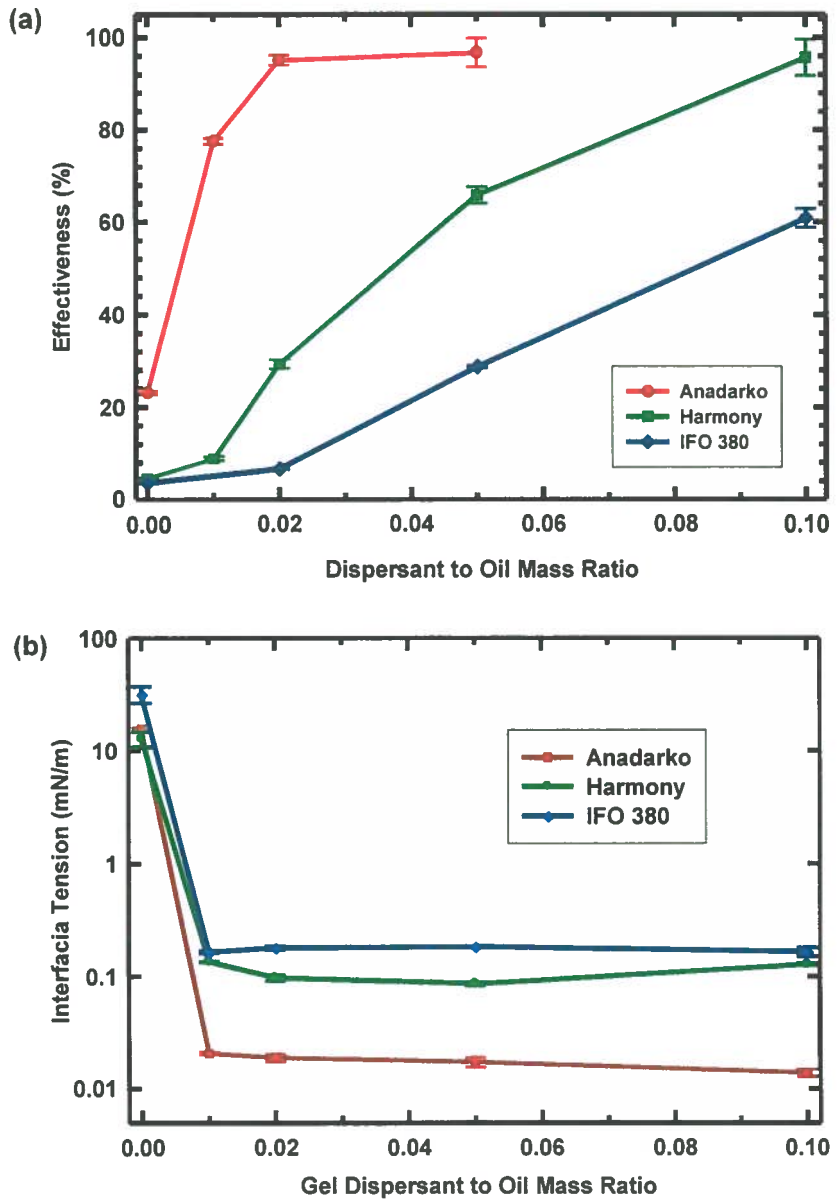

Figure 8.8: (a) Dispersion effectiveness of gel dispersant on oils of varying viscosities. (b) Crude oil- saline water interfacial tension measurements at varying gel to oil mass ratios. Interfacial tensions were measured by the pendant drop and spinning drop methods.

The dispersion effectiveness appears correlated with the reduction in the crude oil-saline water interfacial tension by the gel dispersant (Figure 8.8b). The gel dispersant is able to lower the interfacial tension for all crude oils. The IFT for the lighter Anadarko oil is about an order of magnitude smaller than for the heavier harmony and IFO 380 oils. For instance at DOR of 1:50, the interfacial tensions are ~ 0.018mN/m, 0.098mN/m and 0.182mN/m for Anadarko, Harmony and IFO 380 crude oils respectively. It is noteworthy that although there is no significant reduction in the interfacial tension for the heavier oils beyond a dispersant to oil ratio of 1:100 (Figure 8.8b), the dispersion effectiveness significantly increases with the DOR (Figure 8.8a). This indicates that the physicochemical mechanism of interfacial tension reduction is not the sole mechanism for oil dispersion. Low molecular amphiphiles such as surfactant and lipid molecules stabilize emulsions by physicochemical and mechanical mechanisms.[13] The ability of the surfactant components to provide a barrier to droplet coalescence by imparting viscoelastic properties on the oil-water interface may also play a key role in emulsion stabilization.[13] The results here underscore the influence of oil phase type on the effectiveness of the gel dispersant system.

8.4 Conclusions

The gel mesophase consisting of the phospholipid, l-α-phosphatidylcholine, dioctyl sulfosuccinate sodium salt and polyoxyethylene (20) sorbitan monooleate (Tween 80) is an effective gel dispersant for oil spill remediation. The introduction Tween 80 into the gel mesophase significantly imparts the interfacial tension reduction efficiency of the surfactant components of the gel to the 10^{-2} mN/m range. The incorporation of increasing Tween 80 loadings into the gel system leads to a progressive decrease in crude oil-saline

water interfacial tension at varying dispersant to oil ratios. Over a range of temperature conditions, the dispersant retains its gel characteristics, remains buoyant on water and effectively releases amphiphilic molecules that synergistically stabilize oil droplets. The gel disperses oils of varying viscosities. The dispersion of heavy oils increases with dispersant to oil ratio while lighter oils are effectively dispersed at low dispersant to oil ratios. A unique future direction to the gel dispersant system developed here is the spatial compartmentalization of particles, such as clay nanotubes,[80, 97, 129] into the nanostructured domains of the gel dispersant for mixed particle-surfactant stabilization of the crude oil-in-water emulsions. The amphiphile system in hexadecane may also be encapsulated in the tubular clay nanotubes for phase selective dispersant delivery to spill oils. Incorporation of water into the crude oil spills often forms water-in-oil emulsions, known as oil mousse.[6, 199] The gel-like characteristic of this dispersant may allow applications in the dispersion of oil mousses. These are aspects of our continuing work.

CHAPTER 9

CONCLUSIONS AND FUTURE DIRECTIONS

9.1 Conclusions

This dissertation has exploited the fundamental colloidal and interfacial phenomena of hollow particles, surfactant and polymers in designing synergistic systems for the effective treatment of oil spills.

Chapter 2 describes how naturally occurring halloysite clay nanotubes are effective in stabilizing oil-in-water emulsions and can serve as interfacially-active vehicles for delivering oil spill treating agents. Halloysite nanotubes adsorb at the oil-water interface and stabilize oil-in-water emulsions that are stable for months. Cryo-scanning electron microscopy (Cryo-SEM) imaging of the oil-in-water emulsions show that these nanotubes assemble in a side-on orientation at the oil-water interface and form networks on the interface through end-to-end linkages. For application in the treatment of marine oil spills, halloysite nanotubes were successfully loaded with surfactants and utilized as an interfacially-active vehicle for the delivery of surfactant cargo. The adsorption of surfactant molecules at the interface serves to lower the interfacial tension while the adsorption of particles provides a steric barrier to drop coalescence. Pendant drop tensiometry was used to characterize the dynamic reduction in interfacial tension resulting from the release of dioctyl sulfosuccinate sodium salt (DOSS) from halloysite nanotubes. At appropriate surfactant compositions and loadings in halloysite nanotubes, the crude oil-saline water interfacial tension is effectively lowered to levels appropriate

for the dispersion of oil. This work indicates a novel concept of integrating particle stabilization of emulsions together with the release of chemical surfactants from the particles for the development of an alternative, cheaper and environmentally-benign technology for oil spill remediation.

Chapter 3 presents the synergy of the unique nanotubular morphology and interfacial activity of halloysite with the magnetic properties of iron oxide nanoparticles for potential applications in oil spill dispersion, magnetic mobilization and detection using magnetic fields. Magnetically responsive oil-in-water emulsions are effectively stabilized by a halloysite nanotube supported superparamagnetic iron oxide nanoparticle system. The attachment of the magnetically functionalized halloysite nanotubes at the oil-water interface imparts magnetic responsiveness to the emulsion and provides a steric barrier to droplet coalescence leading to emulsions that are stabilized for extended periods. Interfacial structure characterization by cryogenic scanning electron microscopy reveals that the nanotubes attach at the oil-water interface in a side on-orientation. The tubular structure of the nanotubes is exploited for the encapsulation and release of surfactant species that are typical of oil spill dispersants such as dioctyl sulfosuccinate sodium salt and polyoxyethylene (20) sorbitan monooleate. The magnetically responsive halloysite nanotubes anchor to the oil-water interface stabilizing the interface and releasing the surfactants resulting in reduction in the oil-water interfacial tension. The synergistic adsorption of the nanotubes and the released surfactants at the oil-water interface results in oil emulsification into very small droplets (less than 20μm).

With a focus on halloysite in Chapter 4, the carbonization of hydrophilic particle surfaces is shown to be an effective route for tuning particle wettability in the preparation

of particle-stabilized emulsions. The wettability of naturally occurring halloysite clay nanotubes (HNT) is successfully tuned by the selective carbonization of the negatively charged external HNT surface. The positively charge chitosan biopolymer binds to the negatively charged external HNT surface by electrostatic attraction and hydrogen bonding, yielding carbonized halloysite nanotubes (CHNT) on pyrolysis in an inert atmosphere. Relative to the native HNT, the oil emulsification ability of the CHNT at intermediate levels of carbonization is significantly enhanced due to the thermodynamically more favorable attachment of the particles at the oil-water interface. Cryogenic Scanning Electron Microscopy (Cryo-SEM) imaging reveals that networks of CHNT attach to the oil-water interface with the particles in a side on-orientation. The concepts advanced here can be extended to other inorganic solids and carbon sources for the optimal design of particle-stabilized emulsions.

In chapter 5, the interaction of the cationic chitosan biopolymer with halloysite is extended to a surface active derivative of chitosan, hydrophobically modified chitosan (HMC) for synergistic emulsion stabilization with the HNT. The integration of cationic and hydrophobic functionalities into the surface active biopolymer, hydrophobically modified chitosan (HMC), facilitates synergistic emulsion stabilization with negatively charged halloysite clay nanotubes (HNT). The HMC biopolymer adsorbs on the negatively charged HNT by electrostatic attraction and anchors its hydrophobic residues into oil droplets by the hydrophobic effect. Emulsions with smaller droplet sizes and significantly improved interfacial resistance to droplet coalescence are obtained on synergistic emulsion stabilization by the HNT and HMC compared to the individual emulsifiers alone. Adsorption of the cationic HMC onto the negatively charged HNT

modifies the surface wettability of the nanotubes and cryo-SEM imaging reveals that the HMC locks the nanotubes together at the oil-water interface, creating a large barrier to coalescence. The emulsion stability is significantly enhanced for conditions in which the aqueous HNT dispersion is stabilized by the HMC rather than conditions where the negatively charged HNT is strongly flocculated by the cationic HMC. The electrostatic interactions of HMC and HNT, hydrophobic interaction between HMC chains, and the hydrophobic associations of HMC with the oil phase are proposed as key mechanisms driving the synergistic emulsion stabilization. The nanotubular morphology of halloysite is further exploited for the design of a mixed emulsifier system with inorganic micellar architecture having a Span 80 loaded HNT core stabilized in an aqueous HMC medium. In practical applications such as in oil spill dispersion, the HMC and HNT serves to strengthen the interfacial layer while release of the hydrophobic Span 80 surfactant from the HNT is crucial in lowering the interfacial tension to minimize the thermodynamic work of emulsification.

Chapter 6 presents a rapid and scalable aerosol approach for synthesizing hollow-structured particles by exploiting surfactant assembly and preferential partitioning between different species in solution. The introduction of a templating surfactant such as cetyl trimethyl ammonium bromide into a solution containing a silica precursor leads to the rapid formation of ordered mesoporous silica through an aerosol-based process. The addition of $FeCl_3$ into this precursor solution of CTAB leads to the rapid synthesis of submicrometer hollow silica particles encapsulating ferromagnetic iron oxide. However the addition of molar equivalents of other salts, $Fe(NO_3)_3$ and $CrCl_3$ into the precursor solution did not bring about the same change in morphology. The colloidal nature of the

solution that produces hollow particles through the aerosol-based process is characterized using transmission electron microscopy, light scattering, conductivity measurement and NMR spectroscopy techniques. The structural transition from mesoporous to hollow silica microspheres, results from the disruption of the co-assembly of silicate and CTAB by $FeCl_3$. Adding $FeCl_3$ into the precursor solution, results in the formation of colloidal aggregates with CTAB by salt bridging mechanism. Amphiphilic hollow silica-carbon particles are prepared using aerosol process by introducing a carbon source, sucrose, into the precursor solution. The combination of hydrophilic silica and hydrophobic carbon makes the particles partially wettable by oil and water stabilizing emulsions of the mutually immiscible phases over extended periods of time. This scalable aerosol based concept is significant in the scalable synthesis of hollow particles in commercially viable quantities for practical applications such as in oil spill dispersion.

Chapter 7 and 8 presents the synthesis of a nanostructured mesophase from the self-assembly of l-α-phosphatidylcholine (PC), dioctyl sulfosuccinate sodium salt (DOSS) and polyoxyethylene (20) sorbitan monooleate (Tween 80) as a buoyant and effective gel dispersant for oil spill remediation. The ordered mesophases were formed on addition of water and Tween 80 to an equimolar micellar solution of DOSS and PC in a paraffin solvent. Small Angle Neutron Scattering (SANS) analysis revealed the transition in gel microstructure with increasing Tween 80 content characterized by progressive decrease in low-q scattering intensity and power law decay characteristics, sharpened scattering maxima, amphiphilicity factors of about -0.99 and a significant increase in correlation length. Cryo-Scanning Electron Microscopy imaging allowed direct visualization of the structural transition with increasing Tween 80 content. The active

surfactant component of the gel dispersant effectively lowers the crude oil-saline water interfacial tension to the 10^{-2} mN/m range, appropriate for the dispersion of oil spills. The interfacial tension reduction facilitates the creation of new oil-water interfacial area producing crude oil-in- saline water emulsions with an average droplet size of about 7.81μm that are stable for extended periods. The gel is positively buoyant on water, breaks down on contact with oil and releases surfactant components that stabilize the oil-water interface. The efficacy and potential applications of the gel system in oi spill remediation is corroborated by dispersion effectiveness testing using the standard baffled flask method.

9.2 Future Directions

i. The interactions of oil degrading bacteria such as *Alcanivorax Borkumenis* with halloysite nanotubes may be characterized to understand the role of halloysite on bacterial adhesion, biofilm formation and biodegradation at the oil-water interface.

ii. Synergistic application of Span 80, halloysite and high molecular weight HMC for the herding, gelation and recovery of surface oil layers. As described in chapters 2, 3 and 5 the surfactant, Span 80 can be loaded onto the HNT. The HNT may also be functionalized by carbonization or with magnetic iron oxide nanoparticles for the sorption and magnetic mobilization of oil spills. The surfactant herding and magnetic mobilization concepts are described in Appendix B.

iii. Formulation of a dispersant system composed of particles and the buoyant surfactant gels. The particles may be incorporated into the gel structure (Figure 9.1) and the gels may be encapsulated within the tubular voids of halloysite. Preliminary experiments reveal that the gels retain their buoyancy on incorporation of particles.

Figure 9.1: Gel incorporating carbon particles

iv. Application of the nanostructured gel mesophases in templated materials synthesis at varying temperatures. The aqueous domains of the DOSS-PC gel may also be rigidified by addition of gelatin (Appendix C) for robust synthesis of nanostructured functional or composite materials. SANS analysis reveals that the gel structure varies with temperature, amphiphile molar ratio and solvents (Appendix D).

v. Halloysite-Carbon Nanotube-Titania (HCNT) composite can be synthesized for interfacial photocatalytic remediation of oil-contaminated water systems. The HCNT composite can be synthesized by in-situ growth of carbon nanotubes (CNT) from the iron oxide catalysts attached to halloysite (Figure 9.2), followed

by deposition of Titania nanoparticles. The wettability of the 'conanotubes' may be tuned by varying the grafting density of CNT's with growth time.

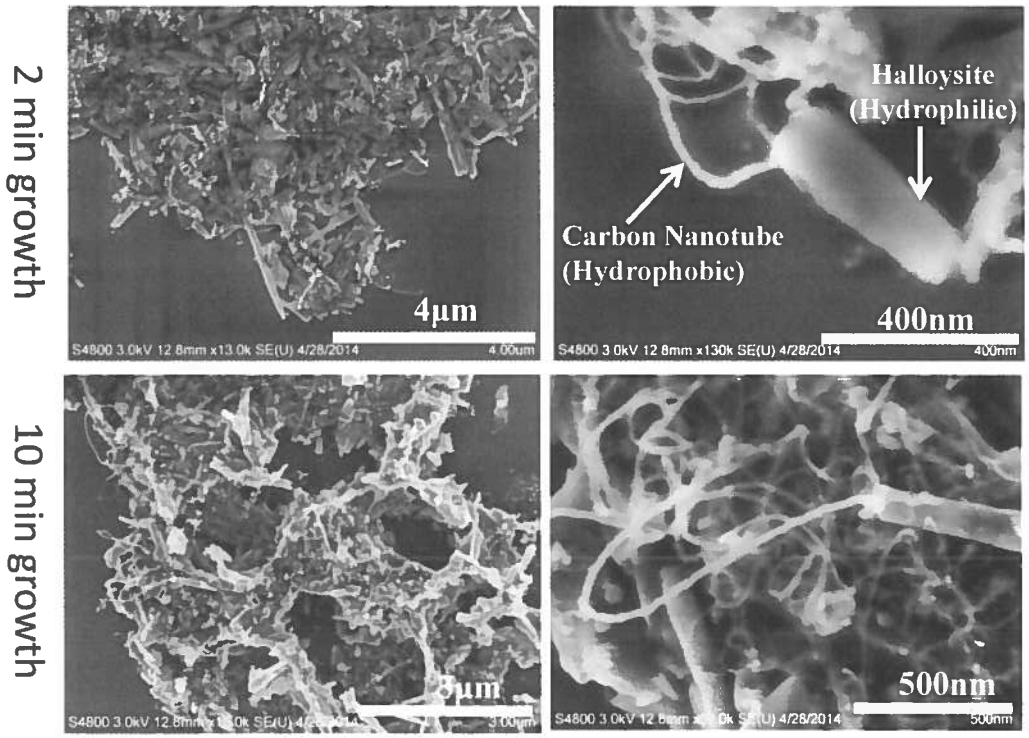

Figure 9.2: Transmission Electron Microscopy (TEM) image of carbon nanotubes grown from iron oxide nanoparticle catalyst supported on halloysite. Ethylene is used as carbon source.

APPENDIX A:

^{1}H NMR CHARACTERIZATION OF HYDROPHOBICALLY MODIFIED CHITOSAN

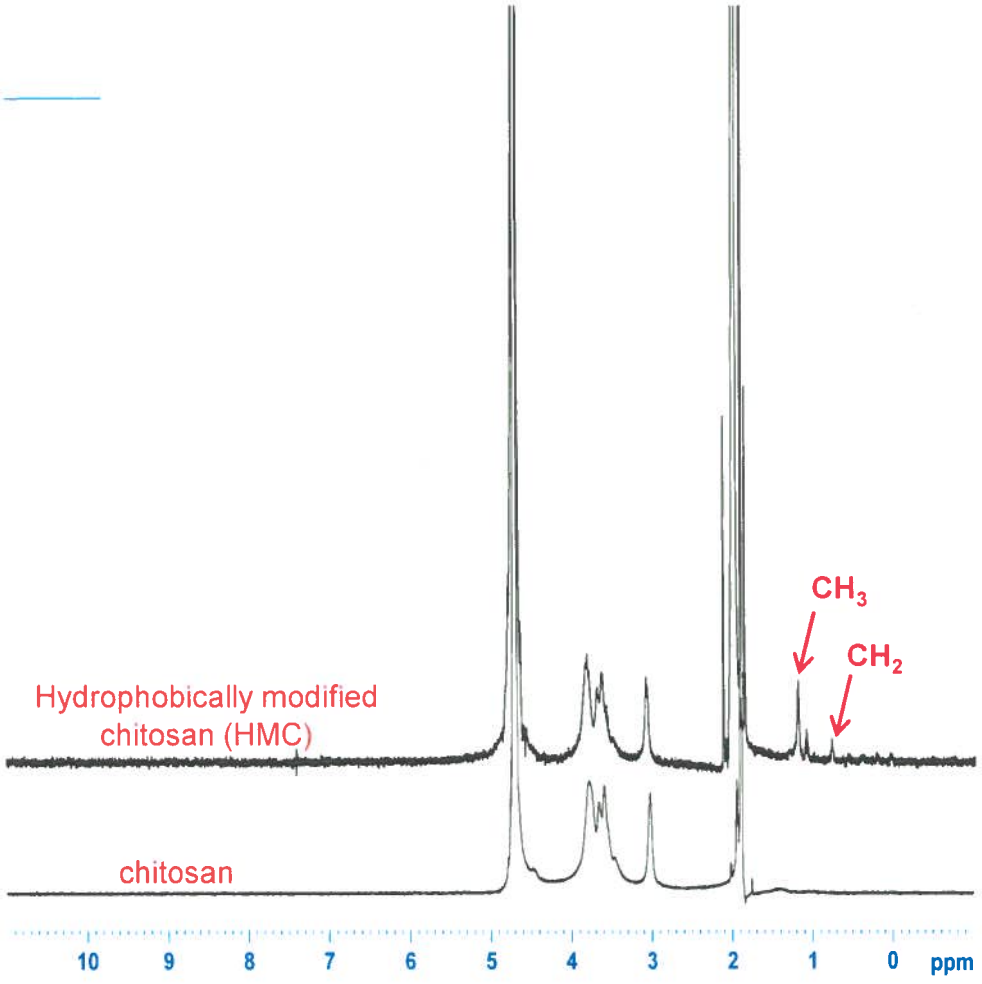

Figure A1. ^{1}H NMR spectra of native chitosan and hydrophobically modified chitosan (HMC). Alkyl groups are attached to the chitosan backbone in the HMC

APPENDIX B:

SYNERGISM OF FUNCTIONALIZED CLAY NANOTUBES AND WATER INSOLUBLE SURFACTANT IN THE HERDING AND MAGNETIC MOBILIZATION OF SURFACE OIL LAYERS

As described in Chapter 3, the attachment of the magnetically functionalized halloysite (M-HNT) to the surface of oil droplets makes the droplets magnetically responsive. Here, we advance the concept of the attachment of the particles at the curved interface of small oil droplets to the large scale interface of surfactant herded surface oil layers. We demonstrate that the synergistic application of a lipophilic nonionic surfactant, Span 80, surfactant and the magnetically functionalized halloysite nanotubes (MHNT) to surface oil layers allows the oil to be magnetically mobilized as a compact mass.

Figure B1 illustrates that the sequential application of Span 80 and M-HNT leads to the formation of a thickened and magnetically-responsive surface oil layer. First crude oil (~0.15 mL) was added to the surface of saline water. The oil spreads into a thin film on the surface of water (Figure B1, Panel a). The spreading of oil on water is typically described in terms of a spreading coefficient (S) which is related to the air-water surface tension (γ_{aw}), air-oil surface tension (γ_{ao}) and the oil-water interfacial tension (γ_{ow}) by the expression:

$$S = \gamma_{aw} - \gamma_{ao} - \gamma_{ow} \qquad \text{(B.1)}$$

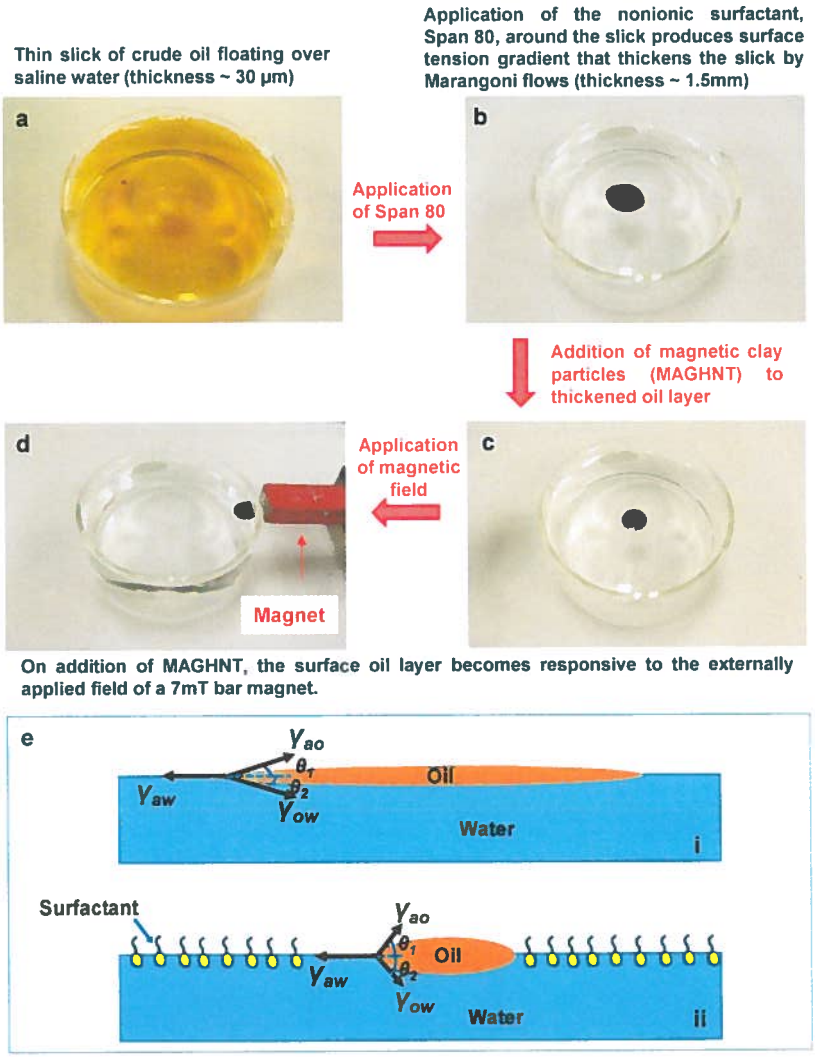

Figure B1: Experiment illustrating the synergistic roles of Span 80 and M-HNT in the chemical herding and magnetic mobilization of thickened surface oil layers (a-d). Panel e shows force balance analysis of the spread of an oil lens on water (i) and a surfactant thickened oil layer (ii).

The spreading phenomena can be explained through simple force balance concepts presented schematically in Figure B1, Panel e. A force balance for an oil lens on water gives:

$$\gamma_{aw} = \gamma_{oa}\cos\theta_1 + \gamma_{ow}\cos\theta_2 \qquad \text{(B.2)}$$

where θ_1 *and* θ_2 are contact angles as defined in Figure B1, Panel e. For typical surface tension values of γ_{aw} = 72mN/m, γ_{ow} = 23mN/m, and γ_{oa} = 29mN/m; the air-water surface tension is greater than the sum of the oil-water and air-oil surface tensions even for zero contact angles. This implies that there will be a net force driving the spread of the oil into a thin film since:

$$\gamma_{aw} > \gamma_{oa}cos\theta_1 + \gamma_{ow}cos\theta_2 \qquad \text{(B.3)}$$

The lipophilic surfactant, Span 80, was then quickly applied along the edges of the Petri dish. The volume ratio of Span 80 to crude oil used was about 0.02. The introduction of the water insoluble surfactant to the air-water interface reduces the air-water surface tension leading to a retraction of the oil layer (Figure B1, Panel b). The lowering of the air-water surface tension (γ_{aw}) leads to an imbalance in the components of the three surface tensions with:

$$\gamma_{aw} < \gamma_{oa}cos\theta_1 + \gamma_{ow}cos\theta_2 \qquad \text{(B.4)}$$

The surfactant generates surface tension gradients resulting in surface convective flow and thickening of the oil layer by the Marangoni effect. The surfactant alters the balance of surface tension forces in equation B.4, ultimately generating a negative spreading pressure that contracts the surface oil layer (Figure B1, Panel e). Based on the volume of oil added, the thin oil slick of about 30.0 μm thickness spread over a circular cross-sectional area of about 50.3cm^2 is thickened to about a 1.50mm thick oil layer spread over an area of about 1.02cm^2. M-HNT powder (15mg) was then carefully applied to the thickened oil phase (Figure B1, Panel d). Figure B1, Panel d shows that the addition of the magnetic clay particles to the oil layer imparts magnetic responsiveness to the applied magnetic field from a 7mT bar magnet.

APPENDIX C:

INCORPORATION OF GELATIN IN AQUEOUS DOMAINS OF A NANOSTRUCTURED GEL MESOPHASE

The structural effects of incorporating gelatin in to the aqueous domains of a reverse hexagonal gel mesophase consisting of l-α-phosphatidylcholine (PC) and dioctyl sulfosuccinate sodium salt (DOSS) at a molar ratio of 1:2 is characterized by small angle neutron scattering (SANS). The SANS procedure is as described in Chapters 7 and 8. The SANS data is presented in Figure C1 and Table C1. The systems are hexagonal when the ratio of the higher order (q_{ho}) to structure peak (q_m) positions is $\approx \sqrt{3}$ (Table C1).

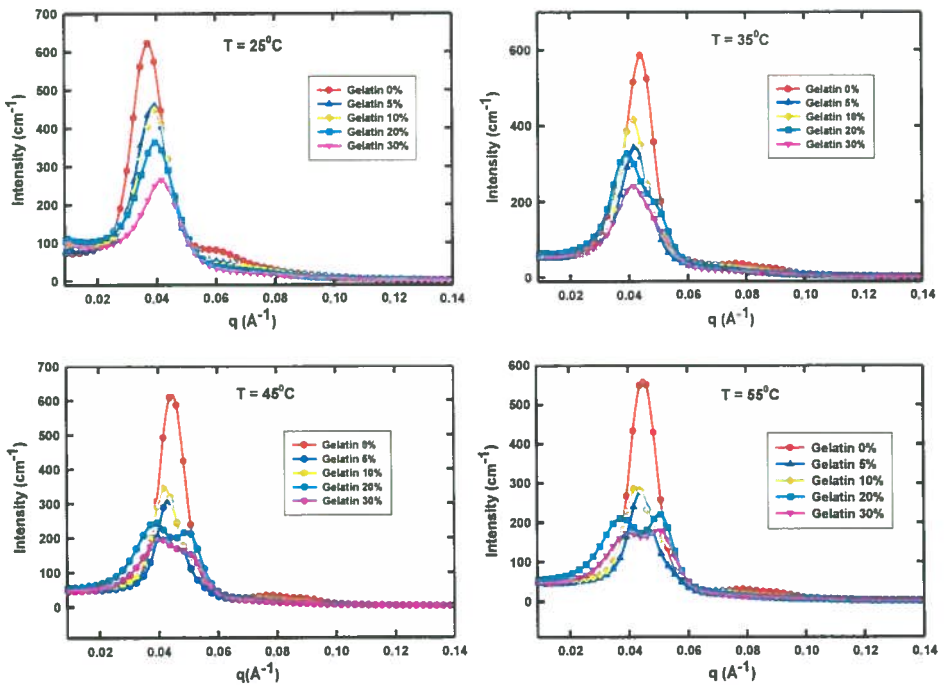

Figure C1: SANS data on a linear scale for PC-DOSS gel systems with increasing gelatin loading in the aqueous phase analyzed at 25°C, 35°C, 45°C and 55 °C.

Table C1: Peak positions as a function of gelatin loading in the aqueous phase and temperature

Temperature (^{0}C)	Gelatin (wt% in D_2O)	Primary Reflection q_m (Å^{-1})	Higher q Reflection q_h (Å^{-1})	Ratio (q_h /q_m)
25	0	0.037	0.065	1.749
	5	0.039	0.067	1.705
	10	0.039	0.072	1.823
	20	0.039	0.074	1.881
	30	0.042	0.076	1.833
35	0	0.044	0.079	1.789
	5	0.042	0.076	1.836
	10	0.042	0.074	1.781
	20	0.039	0.074	1.881
	30	0.042	0.074	1.777
45	0	0.044	0.079	1.789
	5	0.044	0.074	1.684
	10	0.042	0.072	1.722
	20	0.039		
	30	0.039		
55	0	0.046	0.079	1.699
	5	0.044	0.076	1.736
	10	0.042		
	20	0.037		
	30	0.039		
65	0	0.046	0.079	1.699
	5	0.046	0.079	1.699
	10	0.044		
	20	0.037		
	30	0.039		
25R	0	0.037	0.062	1.687
	5	0.039	0.072	1.823
	10	0.039	0.069	1.764
	20	0.039	0.069	1.764
	30	0.042	0.074	1.777

APPENDIX D:

SMALL ANGLE NEUTRON SCATTERING STUDY OF STRUCTURAL TRANSITIONS WITH GEL COMPOSITION AND TEMPERATURE

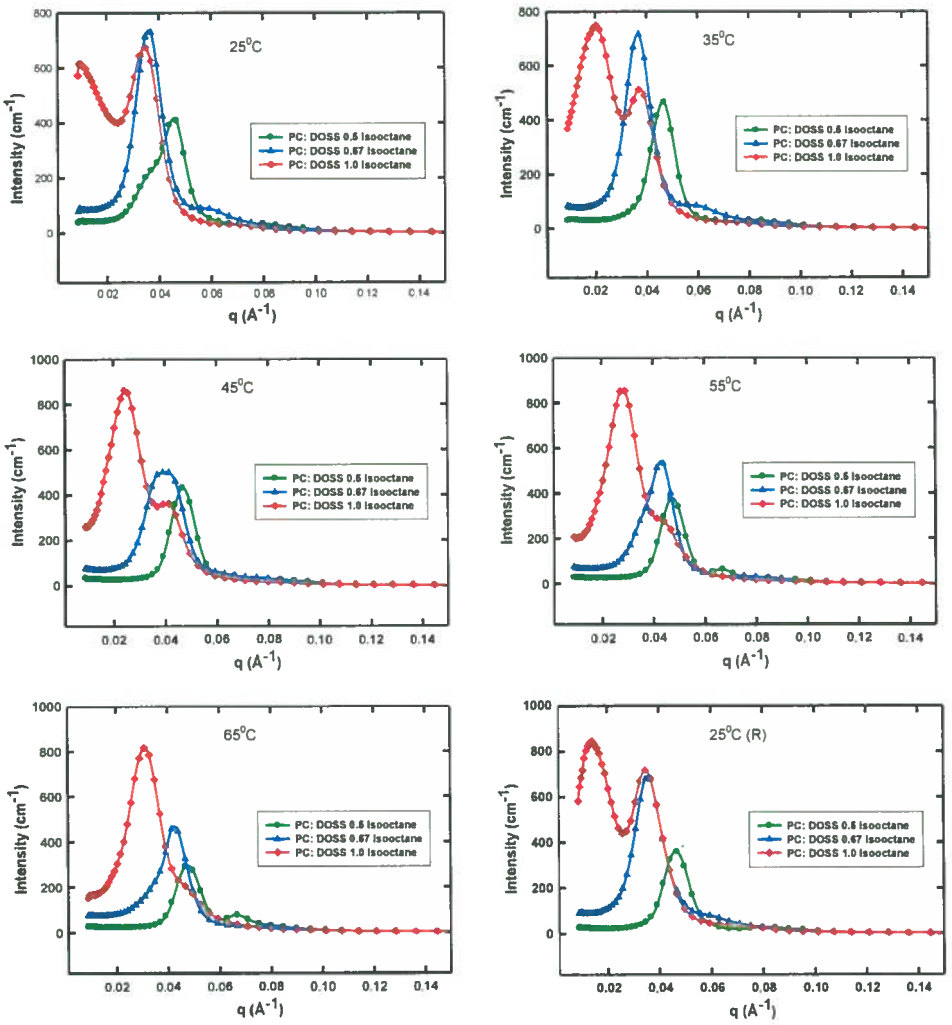

Figure D1: SANS data on a linear scale for gel systems with varying PC-DOSS molar ratio analyzed at 25°C, 35°C, 45°C , 55°C and 65 °C. The aqueous phase is D_2O (6.902ml) and organic phase is isooctane (5ml). The mass of PC and DOSS at the molar ratios 0.5, 0.67 and 1.0 are as presented in Table 7.1 (Chapter 7).

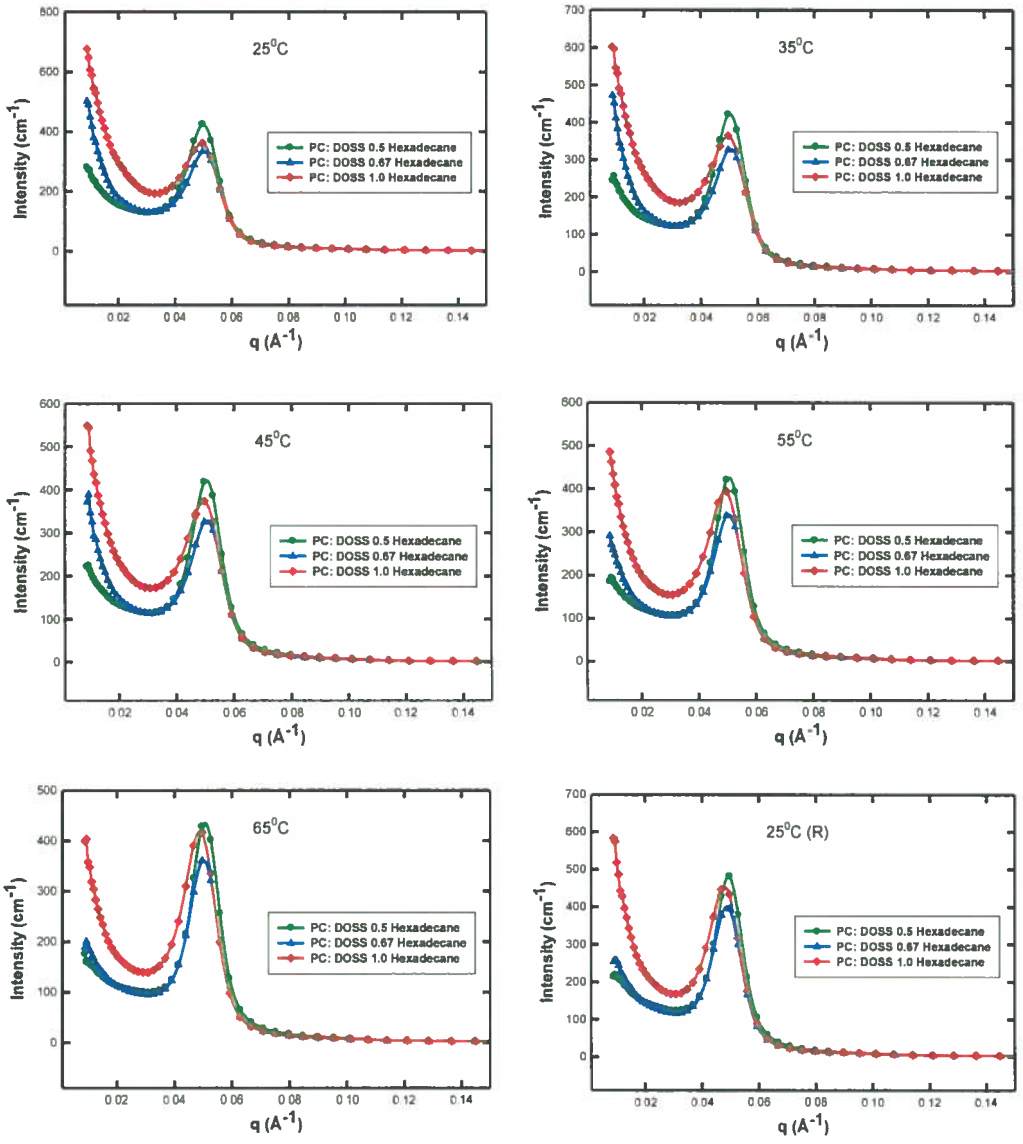

Figure D2: SANS data on a linear scale for gel systems with varying PC-DOSS molar ratio analyzed at 25°C, 35°C, 45°C , 55°C and 65 °C. The aqueous phase is D_2O (6.902ml) and organic phase is hexadecane (5ml). The mass of PC and DOSS at the molar ratios 0.5, 0.67 and 1.0 are as presented in Table 7.1 (Chapter 7).

Table D1: Gel Structure as a function of Composition and Temperature

PC to DOSS Molar Ratio	Organic Solvent (5ml)	Water Content (ml)	Temperature ^{0}(C)	q_m	q_s	q_{ho}	q_{ho}/q_m	Structure
0.5	Isooctane	6.902	25	0.047		0.080	1.710	Hexagonal
			35	0.047		0.080	1.710	Hexagonal
			55	0.047	0.067	0.085	1.926	Coexisting
			25R	0.047		0.080	1.710	Hexagonal
1	Isooctane	6.902	25	0.035		0.071	2.044	Lamellar
0.5	Hexadecane	6.902	25	0.050		0.101	2.044	Lamellar
			35	0.050		0.101	2.044	Lamellar
			55	0.050		0.101	2.044	Lamellar
			25R	0.050		0.101	2.044	Lamellar

LIST OF REFERENCES

1. Fingas, M.; Brown, C. E. *Handbook of Oil Spill Science and Technology*; John Wiley & Sons, Inc2014.

2. Clark, K. How Do Oil Spills out at Sea Typically Get Cleaned Up?

3. Somasundaran, P.; Patra, P.; Farinato, R. S.; Papadopoulos, K. *Oil Spill Remediation: Colloid Chemistry-Based Principles and Solutions*. 1st ed.; John Wiley & Sons, Inc: 2014.

4. Goldstein, B. D.; Osofsky, H. J.; Lichtveld, M. Y. Current Concepts the Gulf Oil Spill. *New Engl J Med* **2011,** *364* (14), 1334-1348.

5. Kanicky, J. R. L.-M., J. C.; Pandey, S.; Shah, O. D. . *Surface Chemistry in the Petroleum Industry. In Handbook of Applied Surface and Colloid Chemistry*; John Wiley & Sons: New York, 2001.

6. Fingas, M. *Oil Spill Science and Technology*. Gulf Professional Publishing: Boston, 2011.

7. Lessard, R. R.; Demarco, G. The significance of oil spill dispersants. *Spill Sci Technol B* **2000,** *6* (1), 59-68.

8. Buist, I.; Nedwed, T. In *Using Herders for Rapid In Situ Burning Of Oil Spills on Open Water*, International Oil Spill Conference, 2011.

9. Chapman, H.; Purnell, K.; Law, R. J.; Kirby, M. F. The use of chemical dispersants to combat oil spills at sea: A review of practice and research needs in Europe. *Mar Pollut Bull* **2007,** *54* (7), 827-838.

10. Nikolopoulou, M.; Kalogerakis, N. Enhanced bioremediation of crude oil utilizing lipophilic fertilizers combined with biosurfactants and molasses. *Mar Pollut Bull* **2008,** *56* (11), 1855-1861.

11. Hemmer, M. J.; Barron, M. G.; Greene, R. M. Comparative Toxicity of Eight Oil Dispersants, Louisiana Sweet Crude Oil (Lsc), and Chemically Dispersed Lsc to Two Aquatic Test Species. *Environ Toxicol Chem* **2011,** *30* (10), 2244-2252.

12. Prince, R. C.; Parkerton, T. F. Comment on "Toxicity and Mutagenicity of Gulf of Mexico Waters During and After the Deepwater Horizon Oil Spill". *Environ Sci Technol* **2014,** *48* (6), 3591-3592.

13. Berg, J. C. *An Introduction to Interfaces & Colloids: The Bridge to Nanoscience*; 1st ed.; World Scientific Publishing: Hackensack, NJ, 2010.

14. Kronberg, B.; Holmberg, K.; Lindman, B. *Surface Chemistry of Surfactants and Polymers*; John Wiley & Sons: Chichester, United Kingdom, 2014.

15. Rosen, M. J. *Surfactants and interfacial phenomena*; 3rd ed.; Wiley-Interscience: Hoboken, N.J., 2004. p xiii, 444 p.

16. Israelachvili, J. N. *Intermolecular and Surface Forces*; 3rd ed.; Elsevier: London, 2010.

17. Venkataraman, P.; Tang, J. J.; Frenkel, E.; McPherson, G. L.; He, J. B.; Raghavan, S. R.; Kolesnichenko, V.; Bose, A.; John, V. T. Attachment of a Hydrophobically Modified Biopolymer at the Oil-Water Interface in the Treatment of Oil Spills. *Acs Appl Mater Inter* **2013,** *5* (9), 3572-3580.

18. Desbrieres, J.; Babak, V. Interfacial properties of chitin and chitosan based systems. *Soft Matter* **2010,** *6* (11), 2358-2363.

19. Raffa, P.; Wever, D. A.; Picchioni, F.; Broekhuis, A. A. Polymeric Surfactants: Synthesis, Properties, and Links to Applications. *Chem Rev* **2015,** *115* (16), 8504-63.

20. Ngai, T.; Bon, S. A. F. *Particle-Stabilized Emulsions and Colloids*; The Royal Society of Chemistry2015.

21. Pickering, S. U. Emulsions. *Journal of the Chemical Society, Transactions* **1907,** *91* 2001.

22. Binks, B. P.; Horozov, T. S. *Colloidal Particles at Liquid Interfaces*; Cambridge University Press: Cambridge, U.K., 2006.

23. Binks, B. P.; Lumsdon, S. O. Influence of particle wettability on the type and stability of surfactant-free emulsions. *Langmuir* **2000,** *16* (23), 8622-8631.

24. Chen, H. M.; He, J. H.; Tang, H. M.; Yan, C. X. Porous silica nanocapsules and nanospheres: Dynamic self-assembly synthesis and application in controlled release. *Chem Mater* **2008,** *20* (18), 5894-5900.

25. Cao, F.; Li, D. X. Morphology-controlled synthesis of SiO2 hollow microspheres using pollen grain as a biotemplate. *Biomed Mater* **2009,** *4* (2).

26. Ding, S. J.; Chen, J. S.; Qi, G. G.; Duan, X. N.; Wang, Z. Y.; Giannelis, E. P.; Archer, L. A.; Lou, X. W. Formation of SnO2 Hollow Nanospheres inside Mesoporous Silica Nanoreactors. *Journal of the American Chemical Society* **2011,** *133* (1), 21-23.

27. Ge, C.; Zhang, D. Z.; Wang, A. L.; Yin, H. B.; Ren, M.; Liu, Y. M.; Jiang, T. S.; Yu, L. B. Synthesis of porous hollow silica spheres using polystyrene-methyl acrylic acid latex template at different temperatures. *J Phys Chem Solids* **2009,** *70* (11), 1432-1437.

28. Keene, M. T. J.; Gougeon, R. D. M.; Denoyel, R.; Harris, R. K.; Rouquerol, J.; Llewellyn, P. L. Calcination of the MCM-41 mesophase: mechanism of surfactant thermal degradation and evolution of the porosity. *J Mater Chem* **1999,** *9* (11), 2843-2850.

29. Lu, Y. F.; Fan, H. Y.; Brinker, C. J.; Ward, T. L.; Rieker, T. Aerosol-assisted self-assembly of mesostructured spherical nanoparticles. *Abstr Pap Am Chem S* **1999,** *218*, U426-U426.

30. Wang, Y. Q.; Sunkara, B.; Zhan, J. J.; He, J. B.; Miao, L. D.; McPherson, G. L.; John, V. T.; Spinu, L. Synthesis of Submicrometer Hollow Particles with a Nanoscale Double-Layer Shell Structure. *Langmuir* **2012,** *28* (39), 13783-13787.

31. Zheng, T. H.; Pang, J. B.; Tan, G.; He, J. B.; McPherson, G. L.; Lu, Y. F.; John, V. T.; Zhan, J. J. Surfactant templating effects on the encapsulation of iron oxide nanoparticles within silica microspheres. *Langmuir* **2007,** *23* (9), 5143-5147.

32. Liu, J.; Xue, D. F. Hollow Nanostructured Anode Materials for Li-Ion Batteries. *Nanoscale Res Lett* **2010,** *5* (10), 1525-1534.

33. Stoffyn-Egli, P.; Lee, K. Formation and characterization of oil-mineral aggregates. *Spill Sci Technol B* **2002,** *8* (1), 31-44.

34. Binks, B. P.; Rodrigues, J. A.; Frith, W. J. Synergistic interaction in emulsions stabilized by a mixture of silica nanoparticles and cationic surfactant. *Langmuir* **2007,** *23* (7), 3626-3636.

35. Dong, J. N.; Worthen, A. J.; Foster, L. M.; Chen, Y. S.; Cornell, K. A.; Bryant, S. L.; Truskett, T. M.; Bielawski, C. W.; Johnston, K. P. Modified Montmorillonite Clay Microparticles for Stable Oil-in-Seawater Emulsions. *Acs Appl Mater Inter* **2014,** *6* (14), 11502-11513.

36. Skelhon, T. S.; Grossiord, N.; Morgan, A. R.; Bon, S. A. F. Quiescent water-in-oil Pickering emulsions as a route toward healthier fruit juice infused chocolate confectionary. *J Mater Chem* **2012,** *22* (36), 19289-19295.

37. Hsu, M. F.; Nikolaides, M. G.; Dinsmore, A. D.; Bausch, A. R.; Gordon, V. D.; Chen, X.; Hutchinson, J. W.; Weitz, D. A. Self-assembled shells composed of colloidal particles: Fabrication and characterization. *Langmuir* **2005,** *21* (7), 2963-2970.

38. Joussein, E.; Petit, S.; Churchman, J.; Theng, B.; Righi, D.; Delvaux, B. Halloysite clay minerals - A review. *Clay Miner* **2005,** *40* (4), 383-426.

39. Abdullayev, E.; Price, R.; Shchukin, D.; Lvov, Y. Halloysite Tubes as Nanocontainers for Anticorrosion Coating with Benzotriazole. *Acs Appl Mater Inter* **2009,** *1* (7), 1437-1443.

40. Cavallaro, G.; Lazzara, G.; Milioto, S. Exploiting the Colloidal Stability and Solubilization Ability of Clay Nanotubes/Ionic Surfactant Hybrid Nanomaterials. *J Phys Chem C* **2012,** *116* (41), 21932-21938.

41. Atlas, R. M. Petroleum biodegradation and oil spill bioremediation. *Mar Pollut Bull* **1995,** *31* (4-12), 178-182.

42. Allan, S. E.; Smith, B. W.; Anderson, K. A. Impact of the Deepwater Horizon Oil Spill on Bioavailable Polycyclic Aromatic Hydrocarbons in Gulf of Mexico Coastal Waters. *Environ Sci Technol* **2012,** *46* (4), 2033-2039.

43. Athas, J. C.; Jun, K.; McCafferty, C.; Owoseni, O.; John, V. T.; Raghavan, S. R. An Effective Dispersant for Oil Spills Based on Food-Grade Amphiphiles. *Langmuir* **2014**.

44. Aveyard, R.; Binks, B. P.; Clint, J. H. Emulsions stabilised solely by colloidal particles. *Adv Colloid Interfac* **2003,** *100*, 503-546.

45. Saha, A.; Nikova, A.; Venkataraman, P.; John, V. T.; Bose, A. Oil Emulsification Using Surface-Tunable Carbon Black Particles. *Acs Appl Mater Inter* **2013,** *5* (8), 3094-3100.

46. Ramsden, W. Separation of solids in the surface-layers of solutions and 'suspensions' (observations on surface-membranes, bubbles, emulsions, and mechanical coagulation). - Preliminary account. *Proceedings of the Royal Society of London, Series A: Mathematical, Physical and Engineering Sciences* **1903,** *72*, 156-164.

47. Ingram, D. R.; Kotsmar, C.; Yoon, K. Y.; Shao, S.; Huh, C.; Bryant, S. L.; Milner, T. E.; Johnston, K. P. Superparamagnetic nanoclusters coated with oleic acid bilayers for stabilization of emulsions of water and oil at low concentration. *J Colloid Interf Sci* **2010,** *351* (1), 225-232.

48. Katepalli, H.; John, V. T.; Bose, A. The Response of Carbon Black Stabilized Oil-in-Water Emulsions to the Addition of Surfactant Solutions. *Langmuir* **2013,** *29* (23), 6790-6797.

49. Kraft, D. J.; de Folter, J. W. J.; Luigjes, B.; Castillo, S. I. R.; Sacanna, S.; Philipse, A. P.; Kegel, W. K. Conditions for Equilibrium Solid-Stabilized Emulsions. *J Phys Chem B* **2010,** *114* (32), 10347-10356.

50. Vergaro, V.; Abdullayev, E.; Lvov, Y. M.; Zeitoun, A.; Cingolani, R.; Rinaldi, R.; Leporatti, S. Cytocompatibility and Uptake of Halloysite Clay Nanotubes. *Biomacromolecules* **2010,** *11* (3), 820-826.

51. Wei, W. B.; Minullina, R.; Abdullayev, E.; Fakhrullin, R.; Mills, D.; Lvov, Y. Enhanced efficiency of antiseptics with sustained release from clay nanotubes. *Rsc Adv* **2014,** *4* (1), 488-494.

52. Qi, R. L.; Cao, X. Y.; Shen, M. W.; Guo, R.; Yu, J. Y.; Shi, X. Y. Biocompatibility of Electrospun Halloysite Nanotube-Doped Poly(Lactic-co-Glycolic Acid) Composite Nanofibers. *J Biomat Sci-Polym E* **2012,** *23* (1-4), 299-313.

53. Liu, M. X.; Zhang, Y.; Wu, C. C.; Xiong, S.; Zhou, C. R. Chitosan/halloysite nanotubes bionanocomposites: Structure, mechanical properties and biocompatibility. *Int J Biol Macromol* **2012,** *51* (4), 566-575.

54. Lvov, Y. M.; Shchukin, D. G.; Mohwald, H.; Price, R. R. Halloysite clay nanotubes for controlled release of protective agents. *Acs Nano* **2008,** *2* (5), 814-820.

55. Levis, S. D., P. . Use of coated microtubular halloysite for the sustained release of diltiazem hydrochloride and propranolol hydrochloride. *International Journal of Pharmaceutics* **2003,** *253*, 145-157.

56. Liu, H.; Wang, C. Y.; Zou, S. W.; Wei, Z. J.; Tong, Z. Facile fabrication of polystyrene/halloysite nanotube microspheres with core-shell structure via Pickering suspension polymerization. *Polym Bull* **2012,** *69* (7), 765-777.

57. Lin, Y.; Ng, K. M.; Chan, C. M.; Sun, G. X.; Wu, J. S. High-impact polystyrene/halloysite nanocomposites prepared by emulsion polymerization using sodium dodecyl sulfate as surfactant. *J Colloid Interf Sci* **2011,** *358* (2), 423-429.

58. Wei, Z. J.; Wang, C. Y.; Liu, H.; Zou, S. W.; Tong, Z. Halloysite nanotubes as particulate emulsifier: Preparation of biocompatible drug-carrying PLGA microspheres based on pickering emulsion. *J Appl Polym Sci* **2012,** *125*, E358-E368.

59. Singh, B.; Mackinnon, I. D. R. Experimental transformation of kaolinite to halloysite. *Clay Clay Miner* **1996,** *44* (6), 825-834.

60. Soma, M.; Churchman, G. J.; Theng, B. K. G. X-Ray Photoelectron Spectroscopic Analysis of Halloysites with Different Composition and Particle Morphology. *Clay Miner* **1992,** *27* (4), 413-421.

61. Cavallaro, G.; Lazzara, G.; Milioto, S.; Parisi, F.; Sanzillo, V. Modified Halloysite Nanotubes: Nanoarchitectures for Enhancing the Capture of Oils from Vapor and Liquid Phases. *Acs Appl Mater Inter* **2014,** *6* (1), 606-612.

62. Ward, C. J.; Song, S.; Davis, E. W. Controlled Release of Tetracycline-HCl from Halloysite-Polymer Composite Films. *J Nanosci Nanotechno* **2010,** *10* (10), 6641-6649.

63. Jurado, E.; Fernandez-Serrano, M.; Nunez-Olea, J.; Luzon, G.; Lechuga, M. Simplified spectrophotometric method using methylene blue for determining anionic

surfactants: Applications to the study of primary biodegradation in aerobic screening tests. *Chemosphere* **2006,** *65* (2), 278-285.

64. Mata-Sandoval, J. C.; Karns, J.; Torrents, A. Influence of rhamnolipids and Triton X-100 on the biodegradation of three pesticides in aqueous phase and soil slurries. *J Agr Food Chem* **2001,** *49* (7), 3296-3303.

65. Crabb, N. T. P., H. E. The determination of polyoxyethylene nonionic surfactants in water at the parts per million level. *Journal of the American Oil Chemists' Society* **1964,** *41*, 752–756.

66. Vonnegut, B. Rotating Bubble Method for the Determination of Surface and Interfacial Tensions. *Review of Scientific Instruments* **1942,** *13*, 6-9.

67. Tambe, D. E.; Sharma, M. M. Factors Controlling the Stability of Colloid-Stabilized Emulsions .1. An Experimental Investigation. *J Colloid Interf Sci* **1993,** *157* (1), 244-253.

68. Lewandowski, E. P.; Searson, P. C.; Stebe, K. J. Orientation of a nanocylinder at a fluid interface. *J Phys Chem B* **2006,** *110* (9), 4283-4290.

69. Fournier, J. B.; Galatola, P. Anisotropic capillary interactions and jamming of colloidal particles trapped at a liquid-fluid interface. *Phys Rev E* **2002,** *65* (3).

70. Loudet, J. C.; Alsayed, A. M.; Zhang, J.; Yodh, A. G. Capillary interactions between anisotropic colloidal particles. *Phys Rev Lett* **2005,** *94* (1).

71. Cheng, H. F.; Liu, Q. F.; Yang, J.; Zhang, J. S.; Frost, R. L. Thermal analysis and infrared emission spectroscopic study of halloysite-potassium acetate intercalation compound. *Thermochim Acta* **2010,** *511* (1-2), 124-128.

72. Brochu, C. P., E.; Caron, G.; Desnoyers, J. E. Dispersion of crude oil in seawater: The role of synthetic surfactants. *Oil and Chemical Pollution* **1986,** *3*, 257– 279.

73. McClements, D. J. *Food Emulsions: Principles, Practice, and Techniques*; CRC Press: Boca Raton, FL, 1999.

74. Alexandridis, P.; Holzwarth, J. F.; Hatton, T. A. Thermodynamics of Droplet Clustering in Percolating Aot Water-in-Oil Microemulsions. *J Phys Chem-Us* **1995,** *99* (20), 8222-8232.

75. Riehm, D. A.; McCormick, A. V. The role of dispersants' dynamic interfacial tension in effective crude oil spill dispersion. *Mar Pollut Bull* **2014,** *84* (1-2), 155-63.

76. Lin, K. Y. A.; Yang, H. T.; Petit, C.; Lee, W. D. Magnetically controllable Pickering emulsion prepared by a reduced graphene oxide-iron oxide composite. *J Colloid Interf Sci* **2015,** *438*, 296-305.

77. Ryoo, S.; Rahmani, A. R.; Yoon, K. Y.; Prodanovic, M.; Kotsmar, C.; Milner, T. E.; Johnston, K. P.; Bryant, S. L.; Huh, C. Theoretical and experimental investigation of the motion of multiphase fluids containing paramagnetic nanoparticles in porous media. *J Petrol Sci Eng* **2012,** *81*, 129-144.

78. Paunov, V. N.; Cayre, O. J.; Noble, P. F.; Stoyanov, S. D.; Velikov, K. P.; Golding, M. Emulsions stabilised by food colloid particles: Role of particle adsorption and wettability at the liquid interface. *J Colloid Interf Sci* **2007,** *312* (2), 381-389.

79. Morgan, A. R.; Ballard, N.; Rochford, L. A.; Nurumbetov, G.; Skelhon, T. S.; Bon, S. A. F. Understanding the multiple orientations of isolated superellipsoidal hematite particles at the oil-water interface. *Soft Matter* **2013,** *9* (2), 487-491.

80. Owoseni, O.; Nyankson, E.; Zhang, Y. H.; Adams, S. J.; He, J. B.; McPherson, G. L.; Bose, A.; Gupta, R. B.; John, V. T. Release of Surfactant Cargo from Interfacially-Active Halloysite Clay Nanotubes for Oil Spill Remediation. *Langmuir* **2014,** *30* (45), 13533-13541.

81. Binks, B. P. Particles as surfactants - similarities and differences. *Curr Opin Colloid In* **2002,** *7* (1-2), 21-41.

82. Hu, Z.; Ballinger, S.; Pelton, R.; Cranston, E. D. Surfactant-enhanced cellulose nanocrystal Pickering emulsions. *J Colloid Interf Sci* **2015,** *439*, 139-148.

83. Pichot, R.; Spyropoulos, F.; Norton, I. T. Mixed-emulsifier stabilised emulsions: Investigation of the effect of monoolein and hydrophilic silica particle mixtures on the stability against coalescence. *J Colloid Interf Sci* **2009,** *329* (2), 284-291.

84. Nyankson, E.; Ober, C. A.; DeCuir, M. J.; Gupta, R. B. Comparison of the Effectiveness of Solid and Solubilized Dioctyl Sodium Sulfosuccinate (DOSS) on Oil Dispersion Using the Baffled Flask Test, for Crude Oil Spill Applications. *Ind Eng Chem Res* **2014,** *53* (29), 11862-11872.

85. Nedwed, T. S., L.; Thomann, H. . In *Remote detection of oil spilled under ice and snow using nuclear magnetic resonance.* , 31st Arctic Marine Oil Spill Program Technical Seminar, , Ottawa, Canada, , 2–5 June 2008; 2008; Environment Canada, Ottawa, Canada, pp 693–702.

86. Keating, K.; Knight, R. A laboratory study to determine the effect of iron oxides on proton NMR measurements. *Geophysics* **2007,** *72* (1), E27-E32.

87. Xie, Y. F.; Qian, D. Y.; Wu, D. L.; Ma, X. F. Magnetic halloysite nanotubes/iron oxide composites for the adsorption of dyes. *Chem Eng J* **2011,** *168* (2), 959-963.

88. Levis, S. R.; Deasy, P. B. Characterisation of halloysite for use as a microtubular drug delivery system. *International Journal of Pharmaceutics* **2002,** *243* (1-2), 125-134.

89. Wang, L.; Chen, J. L.; Ge, L.; Zhu, Z. H.; Rudolph, V. Halloysite-Nanotube-Supported Ru Nanoparticles for Ammonia Catalytic Decomposition to Produce COx-Free Hydrogen. *Energ Fuel* **2011,** *25* (8), 3408-3416.

90. Kucheryavy, P.; He, J. B.; John, V. T.; Maharjan, P.; Spinu, L.; Goloverda, G. Z.; Kolesnichenko, V. L. Superparamagnetic Iron Oxide Nanoparticles with Variable Size and an Iron Oxidation State as Prospective Imaging Agents. *Langmuir* **2013,** *29* (2), 710-716.

91. Tcholakova, S.; Denkov, N. D.; Ivanov, I. B.; Campbell, B. Coalescence in beta-lactoglobulin-stabilized emulsions: Effects of protein adsorption and drop size. *Langmuir* **2002,** *18* (23), 8960-8971.

92. Hua, X. Y.; Rosen, M. J. Dynamic Surface-Tension of Aqueous Surfactant Solutions .1. Basic Parameters. *J Colloid Interf Sci* **1988,** *124* (2), 652-659.

93. Weissleder, R.; Stark, D. D.; Engelstad, B. L.; Bacon, B. R.; Compton, C. C.; White, D. L.; Jacobs, P.; Lewis, J. Superparamagnetic Iron-Oxide - Pharmacokinetics and Toxicity. *Am J Roentgenol* **1989,** *152* (1), 167-173.

94. Abdullayev, E.; Lvov, Y. Halloysite clay nanotubes as a ceramic "skeleton" for functional biopolymer composites with sustained drug release. *J Mater Chem B* **2013,** *1* (23), 2894-2903.

95. Nyankson, E.; Owoseni, O.; John, V. T.; Gupta, R. B. Surfactant-Loaded Halloysite Clay Nanotube Dispersants for Crude Oil Spill Remediation. *Ind. Eng. Chem. Res.* **2015,** *54* (38), 9328–9341.

96. Worthen, A. J.; Foster, L. M.; Dong, J.; Bollinger, J. A.; Peterman, A. H.; Pastora, L. E.; Bryant, S. L.; Truskett, T. M.; Bielawski, C. W.; Johnston, K. P. Synergistic formation and stabilization of oil-in-water emulsions by a weakly interacting mixture of zwitterionic surfactant and silica nanoparticles. *Langmuir* **2014,** *30* (4), 984-94.

97. Owoseni, O.; Nyankson, E.; Zhang, Y. H.; Adams, D. J.; He, J. B.; Spinu, L.; McPherson, G. L.; Bose, A.; Gupta, R. B.; John, V. T. Interfacial adsorption and surfactant release characteristics of magnetically functionalized halloysite nanotubes for responsive emulsions. *J Colloid Interf Sci* **2016,** *463*, 288-298.

98. Creighton, M. A.; Ohata, Y.; Miyawaki, J.; Bose, A.; Hurt, R. H. Two-Dimensional Materials as Emulsion Stabilizers: Interfacial Thermodynamics and Molecular Barrier Properties. *Langmuir* **2014,** *30* (13), 3687-3696.

99. Madivala, B.; Vandebril, S.; Fransaer, J.; Vermant, J. Exploiting particle shape in solid stabilized emulsions. *Soft Matter* **2009,** *5* (8), 1717-1727.

100. Yuan, P.; Southon, P. D.; Liu, Z. W.; Green, M. E. R.; Hook, J. M.; Antill, S. J.; Kepert, C. J. Functionalization of halloysite clay nanotubes by grafting with gamma-aminopropyltriethoxysilane. *J Phys Chem C* **2008,** *112* (40), 15742-15751.

101. Zhou, J.; Wang, L. J.; Qiao, X. Y.; Binks, B. P.; Sun, K. Pickering emulsions stabilized by surface-modified Fe3O4 nanoparticles. *J Colloid Interf Sci* **2012,** *367*, 213-224.

102. Foster, L. M.; Worthen, A. J.; Foster, E. L.; Dong, J. N.; Roach, C. M.; Metaxas, A. E.; Hardy, C. D.; Larsen, E. S.; Bollinger, J. A.; Truskett, T. M.; Bielawski, C. W.; Johnston, K. P. High Interfacial Activity of Polymers "Grafted through" Functionalized Iron Oxide Nanoparticle Clusters. *Langmuir* **2014,** *30* (34), 10188-10196.

103. Hou, Y. F.; Jiang, J. Q.; Li, K.; Zhang, Y. W.; Liu, J. D. Grafting Amphiphilic Brushes onto Halloysite Nanotubes via a Living RAFT Polymerization and Their Pickering Emulsification Behavior. *J Phys Chem B* **2014,** *118* (7), 1962-1967.

104. Lu, J.; Zhou, W.; Chen, J.; Jin, Y. L.; Walters, K. B.; Ding, S. J. Pickering emulsions stabilized by palygorskite particles grafted with pH-responsive polymer brushes. *Rsc Adv* **2015,** *5* (13), 9416-9424.

105. Zhu, Y.; Jiang, J. Z.; Liu, K. H.; Cui, Z. G.; Binks, B. P. Switchable Pickering Emulsions Stabilized by Silica Nanoparticles Hydrophobized in Situ with a Conventional Cationic Surfactant. *Langmuir* **2015,** *31* (11), 3301-3307.

106. Cavallaro, G.; Lazzara, G.; Milioto, S.; Parisi, F. Hydrophobically Modified Halloysite Nanotubes as Reverse Micelles for Water-in-Oil Emulsion. *Langmuir* **2015,** *31* (27), 7472-7478.

107. Williams, M.; Armes, S. P.; York, D. W. Clay-Based Colloidosomes. *Langmuir* **2012,** *28* (2), 1142-1148.

108. Yan, N. X.; Masliyah, J. H. Effect of pH on adsorption and desorption of clay particles at oil-water interface. *J Colloid Interf Sci* **1996,** *181* (1), 20-27.

109. Jada, A.; Debih, H. Hydrophobation of Clay Particles by Asphaltenes Adsorption. *Compos Interface* **2009,** *16* (2-3), 219-235.

110. Yu, G. Z.; Dong, J. N.; Foster, L. M.; Metaxas, A. E.; Truskett, T. M.; Johnston, K. P. Breakup of Oil Jets into Droplets in Seawater with Environmentally Benign Nanoparticle and Surfactant Dispersants. *Ind Eng Chem Res* **2015,** *54* (16), 4243-4251.

111. Liu, Y. Y.; Tang, J.; Chen, X. Q.; Xin, J. H. Decoration of carbon nanotubes with chitosan. *Carbon* **2005,** *43* (15), 3178-3180.

112. Bengisu, M.; Yilmaz, E. Oxidation and pyrolysis of chitosan as a route for carbon fiber derivation. *Carbohyd Polym* **2002,** *50* (2), 165-175.

113. Chen, Y. J.; Javvaji, V.; MacIntire, I. C.; Raghavan, S. R. Gelation of Vesicles and Nanoparticles Using Water-Soluble Hydrophobically Modified Chitosan. *Langmuir* **2013,** *29* (49), 15302-15308.

114. Chen, L.; Tang, C. Y.; Ning, N. Y.; Wang, C. Y.; Fu, Q.; Zhang, Q. Preparation and Properties of Chitosan/Lignin Composite Films. *Chinese J Polym Sci* **2009,** *27* (5), 739-746.

115. Ding, Y.; Gu, G.; Xia, X. H.; Huo, Q. Cysteine-grafted chitosan-mediated gold nanoparticle assembly: from nanochains to microcubes. *J Mater Chem* **2009,** *19* (6), 795-799.

116. Hertl, W. Infrared frequency shifts due to hydrogen bonding of surface amino groups on silica. *J Phys Chem-Us* **1973,** *77*, 1473.

117. Kaczmarek, H.; Zawadzki, J. Chitosan pyrolysis and adsorption properties of chitosan and its carbonizate. *Carbohyd Res* **2010,** *345* (7), 941-947.

118. Sevilla, M.; Fuertes, A. B. The production of carbon materials by hydrothermal carbonization of cellulose. *Carbon* **2009,** *47* (9), 2281-2289.

119. Schulman, J. H.; Leja, J. Control of contact angles at the oil–water–solid interfaces. *Trans Faraday Soc* **1954,** *50*, 598–605.

120. Yan, N. X.; Masliyah, J. H. Characterization and Demulsification of Solids-Stabilized Oil-in-Water Emulsions .1. Partitioning of Clay Particles and Preparation of Emulsions. *Colloid Surface A* **1995,** *96* (3), 229-242.

121. Desbrieres, J.; Martinez, C.; Rinaudo, M. Hydrophobic derivatives of chitosan: characterization and rheological behaviour. *Int J Biol Macromol* **1996,** *19* (1), 21-8.

122. Lee, J. H.; Gustin, J. P.; Chen, T. H.; Payne, G. F.; Raghavan, S. R. Vesicle-biopolymer gels: Networks of surfactant vesicles connected by associating biopolymers. *Langmuir* **2005,** *21* (1), 26-33.

123. St Dennis, J. E.; Meng, Q. K.; Zheng, R. N.; Pesika, N. S.; McPherson, G. L.; He, J. B.; Ashbaugh, H. S.; John, V. T.; Dowling, M. B.; Raghavan, S. R. Carbon microspheres as network nodes in a novel biocompatible gel. *Soft Matter* **2011,** *7* (9), 4170-4173.

124. Chandler, D. Interfaces and the driving force of hydrophobic assembly. *Nature* **2005,** *437* (7059), 640-647.

125. Pi, G. L.; Mao, L. L.; Bao, M. T.; Li, Y. M.; Gong, H. Y.; Zhangt, J. R. Preparation of Oil-in-Seawater Emulsions Based on Environmentally Benign Nanoparticles and Biosurfactant for Oil Spill Remediation. *Acs Sustain Chem Eng* **2015,** *3* (11), 2686-2693.

126. Velev, O. D.; Furusawa, K.; Nagayama, K. Assembly of latex particles by using emulsion droplets as templates .1. Microstructured hollow spheres. *Langmuir* **1996,** *12* (10), 2374-2384.

127. Gong, H. Y.; Li, Y. M.; Bao, M. T.; Lv, D.; Wang, Z. N. Petroleum hydrocarbon degrading bacteria associated with chitosan as effective particle-stabilizers for oil emulsification. *Rsc Adv* **2015,** *5* (47), 37640-37647.

128. Wongkongkatep, P.; Manopwisedjaroen, K.; Tiposoth, P.; Archakunakorn, S.; Pongtharangkul, T.; Suphantharika, M.; Honda, K.; Hamachi, I.; Wongkongkatep, J. Bacteria Interface Pickering Emulsions Stabilized by Self-assembled Bacteria-Chitosan Network. *Langmuir* **2012,** *28* (13), 5729-5736.

129. Owoseni, O.; Zhang, Y.; Su, Y.; He, J.; McPherson, G. L.; Bose, A.; John, V. T. Tuning the Wettability of Halloysite Clay Nanotubes by Surface Carbonization for Optimal Emulsion Stabilization. Langmuir, 2015, 31 (51), pp 13700–13707

130. Yah, W. O.; Takahara, A.; Lvov, Y. M. Selective modification of halloysite lumen with octadecylphosphonic acid: new inorganic tubular micelle. *J Am Chem Soc* **2012,** *134* (3), 1853-9.

131. Cavallaro, G.; Lazzara, G.; Milioto, S.; Parisi, F.; Sanzillo, V. Modified halloysite nanotubes: nanoarchitectures for enhancing the capture of oils from vapor and liquid phases. *ACS Appl Mater Interfaces* **2014,** *6* (1), 606-12.

132. Zheng, R.; Arora, J.; Boonkaew, B.; Raghavan, S. R.; Kaplan, D. L.; He, J.; Pesika, N. S.; John, V. T. Liposomes tethered to a biopolymer film through the hydrophobic effect create a highly effective lubricating surface. *Soft Matter* **2014,** *10* (46), 9226-9229.

133. Marinova, K. G.; Alargova, R. G.; Denkov, N. D.; Velev, O. D.; Petsev, D. N.; Ivanov, I. B.; Borwankar, R. P. Charging of oil-water interfaces due to spontaneous adsorption of hydroxyl ions. *Langmuir* **1996,** *12* (8), 2045-2051.

134. Benner, S. W.; John, V. T.; Hall, C. K. Simulation Study of Hydrophobically Modified Chitosan as an Oil Dispersant Additive. *J Phys Chem B* **2015,** *119* (23), 6979-6990.

135. Piculell, I.; Thuresson, K.; Lindman, B. Mixed solutions of surfactant and hydrophobically modified polymer. *Polym Advan Technol* **2001,** *12* (1-2), 44-69.

136. Bratskaya, S.; Avramenko, V.; Schwarz, S.; Philippova, I. Enhanced flocculation of oil-in-water emulsions by hydrophobically modified chitosan derivatives. *Colloid Surface A* **2006,** *275* (1-3), 168-176.

137. Binks, B. P.; Lumsdon, S. O. Stability of oil-in-water emulsions stabilised by silica particles. *Phys Chem Chem Phys* **1999,** *1* (12), 3007-3016.

138. Ashby, N. P.; Binks, B. P. Pickering emulsions stabilised by Laponite clay particles. *Phys Chem Chem Phys* **2000,** *2* (24), 5640-5646.

139. Javvaji, V.; Dowling, M. B.; Oh, H.; White, I. M.; Raghavan, S. R. Reversible gelation of cells using self-assembling hydrophobically-modified biopolymers: towards self-assembly of tissue. *Biomater Sci-Uk* **2014,** *2* (7), 1016-1023.

140. Li, X. L.; Lou, T. J.; Sun, X. M.; Li, Y. D. Highly sensitive WO3 hollow-sphere gas sensors. *Inorg Chem* **2004,** *43* (17), 5442-5449.

141. Park, J. C.; Bang, J. U.; Lee, J.; Ko, C. H.; Song, H. Ni@SiO2 yolk-shell nanoreactor catalysts: High temperature stability and recyclability. *J Mater Chem* **2010,** *20* (7), 1239-1246.

142. Yamada, Y.; Mizutani, M.; Nakamura, T.; Yano, K. Mesoporous Microcapsules with Decorated Inner Surface: Fabrication and Photocatalytic Activity. *Chem Mater* **2010,** *22* (5), 1695-1703.

143. Yang, J.; Lee, J.; Kang, J.; Lee, K.; Suh, J. S.; Yoon, H. G.; Huh, Y. M.; Haam, S. Hollow silica nanocontainers as drug delivery vehicles. *Langmuir* **2008,** *24* (7), 3417-3421.

144. Wang, S. Q.; Zhang, J. Y.; Chen, C. H. Dandelion-like hollow microspheres of CuO as anode material for lithium-ion batteries. *Scripta Mater* **2007,** *57* (4), 337-340.

145. Lou, X. W.; Archer, L. A.; Yang, Z. C. Hollow Micro-/Nanostructures: Synthesis and Applications. *Adv Mater* **2008,** *20* (21), 3987-4019.

146. Cheng, X. J.; Li, J. P.; Li, X. H.; Zhang, D. H.; Zhang, H. J.; Zhang, A. Q.; Huang, H.; Lian, J. S. A highly sensitive sensor based on hollow particles for the detection, adsorption and removal of Hg2+ ions. *J Mater Chem* **2012,** *22* (45), 24102-24108.

147. Brinker, C. J.; Lu, Y. F.; Sellinger, A.; Fan, H. Y. Evaporation-induced self-assembly: Nanostructures made easy. *Adv Mater* **1999,** *11* (7), 579-+.

148. Drenski, M. F.; Reed, W. F. Simultaneous multiple sample light scattering for analysis of polymer solutions. *J Appl Polym Sci* **2004,** *92* (4), 2724-2732.

149. Lu, Y. F.; McCaughey, B. F.; Wang, D. H.; Hampsey, J. E.; Doke, N.; Yang, Z. Z.; Brinker, C. J. Aerosol-assisted formation of mesostructured thin films. *Adv Mater* **2003,** *15* (20), 1733-+.

150. Kresge, C. T.; Leonowicz, M. E.; Roth, W. J.; Vartuli, J. C.; Beck, J. S. Ordered Mesoporous Molecular-Sieves Synthesized by a Liquid-Crystal Template Mechanism. *Nature* **1992,** *359* (6397), 710-712.

151. Cornell, R. M. S., U. . *The Iron Oxide: Structure, Properties, Reactions, Occurrences, and Uses*; Wiley-VCH: Weinheim2003. p 4.

152. Lin, H. P.; Mou, C. Y. Salt effect in post-synthesis hydrothermal treatment of MCM-41. *Micropor Mesopor Mat* **2002,** *55* (1), 69-80.

153. Huo, Q. S.; Margolese, D. I.; Ciesla, U.; Demuth, D. G.; Feng, P. Y.; Gier, T. E.; Sieger, P.; Firouzi, A.; Chmelka, B. F.; Schuth, F.; Stucky, G. D. Organization of Organic-Molecules with Inorganic Molecular-Species into Nanocomposite Biphase Arrays. *Chem Mater* **1994,** *6* (8), 1176-1191.

154. Dominguez, A.; Fernandez, A.; Gonzalez, N.; Iglesias, E.; Montenegro, L. Determination of critical micelle concentration of some surfactants by three techniques. *J Chem Educ* **1997,** *74* (10), 1227-1231.

155. Li, W.; Han, Y. C.; Zhang, J. L.; Wang, B. G. Effect of ethanol on the aggregation properties of cetyltrimethylammonium bromide surfactant. *Colloid J+* **2005,** *67* (2), 159-163.

156. Huang, J. B.; Mao, M.; Zhu, B. Y. The surface physico-chemical properties of surfactants in ethanol-water mixtures. *Colloid Surface A* **1999,** *155* (2-3), 339-348.

157. Sammalkorpi, M.; Karttunen, M.; Haataja, M. Ionic Surfactant Aggregates in Saline Solutions: Sodium Dodecyl Sulfate (SDS) in the Presence of Excess Sodium Chloride (NaCl) or Calcium Chloride (CaCl2). *J Phys Chem B* **2009,** *113* (17), 5863-5870.

158. Zhang, Y. J.; Cremer, P. S. Interactions between macromolecules and ions: the Hofmeister series. *Curr Opin Chem Biol* **2006,** *10* (6), 658-663.

159. Yang, J. Viscoelastic wormlike micelles and their applications. *Curr Opin Colloid In* **2002,** *7* (5-6), 276-281.

160. Zhang, L.; Somasundaran, P.; Maltesh, C. Electrolyte effects on the surface tension and micellization of n-dodecyl beta-D-maltoside solutions. *Langmuir* **1996,** *12* (10), 2371-2373.

161. Yu, D. F.; Huang, X.; Deng, M. L.; Lin, Y. Y.; Jiang, L. X.; Huang, J. B.; Wang, Y. L. Effects of Inorganic and Organic Salts on Aggregation Behavior of Cationic Gemini Surfactants. *J Phys Chem B* **2010,** *114* (46), 14955-14964.

162. Freitas, A. A.; Quina, F. H.; Carroll, F. A. Estimation of water-organic interfacial tensions. A linear free energy relationship analysis of interfacial adhesion. *J Phys Chem B* **1997,** *101* (38), 7488-7493.

163. Rosen, M. J. *Surfactants and Interfacial Phenomena*; 3rd ed.; John Wiley & Sons: Hoboken, NJ, 2004.

164. Evans, F.; Wennerstrom, H. *The Colloidal Domain: Where Physics, Chemistry, Biology, and Technology Meet*; Wiley VCH New York, NY, 1999.

165. Kirby, S. M.; Anna, S. L.; Walker, L. M. Sequential Adsorption of an Irreversibly Adsorbed Nonionic Surfactant and an Anionic Surfactant at an Oil/Aqueous Interface. *Langmuir* **2015,** *31* (14), 4063-4071.

166. Riehm, D. A.; McCormick, A. V. The role of dispersants' dynamic interfacial tension in effective crude oil spill dispersion. *Mar Pollut Bull* **2014,** *84* (1-2), 155-163.

167. Nyankson, E.; DeCuir, M. J.; Gupta, R. B. Soybean Lecithin as a Dispersant for Crude Oil Spills. *Acs Sustain Chem Eng* **2015,** *3* (5), 920-931.

168. Nedwed, T.; Canevari, G. P.; Clark, J. R.; Belore, R. In *New dispersant delivered as a gel*, International Oil Spill Conference, 2005; American Petroleum Institute: Washington, DC, pp 121–125.

169. Simmons, B. A.; Irvin, G. C.; Agarwal, V.; Bose, A.; John, V. T.; McPherson, G. L.; Balsara, N. P. Small angle neutron scattering study of microstructural transitions in a surfactant-based gel mesophase. *Langmuir* **2002,** *18* (3), 624-632.

170. Li, X. C.; John, V. T.; He, G. H.; Zhan, J. J.; Tan, G.; McPherson, G.; Bose, A.; Sarkar, J. Shear Induced Formation of Patterned Porous Titania with Applications to Photocatalysis. *Langmuir* **2009,** *25* (13), 7586-7593.

171. Li, S. C.; Irvin, G. C.; Simmons, B.; Rachakonda, S.; Ramannair, P.; Banerjee, S.; John, V. T.; McPherson, G. L.; Zhou, W. L.; Bose, A. Structured materials syntheses in a self-assembled surfactant mesophase. *Colloid Surface A* **2000,** *174* (1-2), 275-281.

172. Tan, G.; Xu, P.; John, V. T.; He, J.; McPherson, G. L.; Agarwal, V.; Bose, A. Cryo-field emission scanning electron microscopy imaging of a rigid surfactant mesophase. *Langmuir* **2008,** *24* (19), 10621-10624.

173. Liu, L.; Tan, G.; McPherson, G.; John, V. T.; Maskos, K.; Bose, A. High-resolution NMR characterization of a gel-like surfactant mesophase. *Langmuir* **2008,** *24* (17), 9286-9294.

174. Goodwin, J. W. *Colloids and Interfaces with Surfactants and Polymers—An Introduction*; John Wiley & Sons Ltd: New York, 2004.

175. Zattoni, A.; Piccolomini, E. L.; Torsi, G.; Reschiglian, P. Turbidimetric detection method in flow-assisted separation of dispersed samples. *Anal Chem* **2003,** *75* (23), 6469-6477.

176. Higgins, J. S.; Benoit, H. C. *Polymers and Neutron Scattering*; Oxford University Press1994.

177. Atkinson, P. J.; Robinson, B. H.; Howe, A. M.; Heenan, R. K. Structure and stability of microemulsion-based organogels *J. Chem. Soc. Faraday Trans.* **1991,** *87*, 3389-3397.

178. Lee, H. Y.; Diehn, K. K.; Ko, S. W.; Tung, S. H.; Raghavan, S. R. Can Simple Salts Influence Self-Assembly in Oil? Multivalent Cations as Efficient Gelators of Lecithin Organosols. *Langmuir* **2010,** *26* (17), 13831-13838.

179. Hatzopoulos, M. H.; Eastoe, J.; Dowding, P. J.; Grillo, I. Cylinder to sphere transition in reverse microemulsions: the effect of hydrotropes. *J Colloid Interface Sci* **2013,** *392*, 304-10.

180. Kline, S. R. Reduction and analysis of SANS and USANS data using IGOR Pro. *J Appl Crystallogr* **2006,** *39*, 895-900.

181. Teubner, M.; Strey, R. Origin of the Scattering Peak in Microemulsions. *J Chem Phys* **1987,** *87* (5), 3195-3200.

182. Laupheimer, M.; Sottmann, T.; Schweins, R.; Stubenrauch, C. Studying orthogonal self-assembled systems: microstructure of gelled bicontinuous microemulsions. *Soft Matter* **2014,** *10* (43), 8744-8757.

183. Schubert, K. V.; Strey, R.; Kline, S. R.; Kaler, E. W. Small-Angle Neutron-Scattering near Lifshitz Lines - Transition from Weakly Structured Mixtures to Microemulsions. *J Chem Phys* **1994,** *101* (6), 5343-5355.

184. Hansen, P.; McDonald, I. R. *Theory of Simple Liquids*; 3rd ed.; Elsevier: New York, 2006.

185. Smith, I. C. P.; Ekiel, I. H. *Phosphorus-31 NMR: Principles and Applications*; Academic Press: New York: , 1984.

186. Simmons, B. A.; Li, S. C.; John, V. T.; McPherson, G. L.; Bose, A.; Zhou, W. L.; He, J. B. Morphology of CdS nanocrystals synthesized in a mixed surfactant system. *Nano Lett* **2002,** *2* (4), 263-268.

187. Amani, A.; York, P.; de Waard, H.; Anwar, J. Molecular dynamics simulation of a polysorbate 80 micelle in water. *Soft Matter* **2011,** *7* (6), 2900-2908.

188. Manohar, C.; Narayanan, J. Average packing factor approach for designing micelles, vesicles and gel phases in mixed surfactant systems. *Colloid Surface A* **2012,** *403*, 129-132.

189. Singh, M.; Agarwal, V.; De Kee, D.; McPherson, G.; John, V.; Bose, A. Shear-induced orientation of a rigid surfactant mesophase. *Langmuir* **2004,** *20* (14), 5693-5702.

190. Angelico, R.; Ceglie, A.; Colafemmina, G.; Lopez, F.; Murgia, S.; Olsson, U.; Palazzo, G. Biocompatible lecithin organogels: Structure and phase equilibria. *Langmuir* **2005,** *21* (1), 140-148.

191. Scartazzini, R.; Luisi, P. L. Organogels from Lecithins. *J Phys Chem-Us* **1988,** *92* (3), 829-833.

192. Zheng, R. T.; Gao, J. W.; Wang, J. J.; Chen, G. Reversible temperature regulation of electrical and thermal conductivity using liquid-solid phase transitions. *Nat Commun* **2011,** *2*.

193. Paul, J. H. Response to Comment on "Toxicity and Mutagenicity of Gulf of Mexico Waters During and After the Deepwater Horizon Oil Spill". *Environ Sci Technol* **2014,** *48* (6), 3593-3594.

194. Venosa, A. D.; King, D. W.; Sorial, G. A. The baffled flask test for dispersant effectiveness: A round robin evaluation of reproducibility and repeatability. *Spill Sci Technol B* **2002,** *7* (5-6), 299-308.

195. Wang, Z.; Hollebone, B. P.; Fingas, M.; Fieldhouse, B.; Sigouin, L.; Landriault, M.; Smith, P.; Noonan, J.; Thouin, G.; Weaver, J. J. *Characteristics of Spilled Oils, Fuels, and Petroleum Products: 1. Compositions and Properties of Selected Oils*: Research Triangle Park, NC2003.

196. Venosa, A. D.; Holder, E. *Laboratory-Scale Testing of Dispersant Effectiveness of 20 Oils Using the Baffled Flask Test*2011.

197. Fingas, M. *Oil Spill Science and Technology*. Gulf Professional Publishing: Boston, MA, 2011; p 444.

198. Prince, R. C. Oil Spill Dispersants: Boon or Bane? *Environ Sci Technol* **2015,** *49* (11), 6376-6384.

199. Kilpatrick, P. K. Water-in-Crude Oil Emulsion Stabilization: Review and Unanswered Questions. *Energ Fuel* **2012,** *26* (7), 4017-4026.

BIOGRAPHY

Sehinde is a native of Erijiyan Ekiti in Ekiti State of Nigeria and grew up in Akure, Ondo State. He received a B.Sc with First Class Honors in Chemical Engineering from Obafemi Awolowo University, Ile-Ife Nigeria in 2008. Following his undergraduate career, Sehinde worked in the petroleum chemistry laboratory of the American University of Nigeria during his National Youth Service Corps (NYSC) year in Yola, Adamawa State. He then held a Management Trainee position at PZ Cussons PLC. Sehinde was enrolled into the graduate program in Chemical and Biomolecular Engineering at Tulane University in Fall 2011 and joined Prof. Vijay John's research group. His doctoral research involved the integrative engineering of surfactant, multifunctional particles and polymers; for applications in oil spill remediation, design of optimally stable colloidal systems, magnetic field-enhanced fluid separation and synthesis of nanostructured materials. Sehinde's research led to several peer-reviewed publications in scientific journals and conference presentations. Working at the Sullivan Park Research Center of Corning Incorporated in New York in the summer of 2015, Sehinde helped to develop a robust technique for the design and fabrication of glass microfluidics as potential keystone components in high-technology applications. Sehinde led the effort to re-charter the Tulane National Society of Black Engineers (NSBE) chapter after 6 years of inactivity, serving as Chapter President and Programs Chairperson. He successfully raised funds for programs focused on academic excellence, professional development and community service including implementing the 'Engineering the Future program' for pre-

collegiate students. He has won prestigious awards from the American Institute of Chemical Engineers (AIChE), American Chemical Society (ACS), the Gulf of Mexico Research Initiative (GoMRI), Department of Chemical and Biomolecular Engineering and School of Science and Engineering at Tulane University. Sehinde has also been inducted into the Golden Key International Honor Society and Tau Beta Pi Engineering Honor Society in recognition of excellent academic and service achievements.